Institut für Biophysik
Fachrichtung Physik
Fakultät Mathematik und Naturwissenschaften
der Technischen Universität Dresden

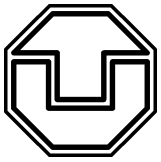

DNA Unwinding by Helicases Investigated on the Single Molecule Level

Dissertation

zur Erlangung des akademischen Grades

Doctor rerum naturalium

(Dr. rer. nat.)

vorgelegt von

Daniel Klaue

geboren in Lübben am 18. November 1979

März 2012

1. Gutachter: Prof. Dr. Petra Schwille

2. Gutachter: Prof. Dr. Holger Puchta

Die Arbeit wurde eingereicht am: 30. März 2012

Kurzfassung

Jeder Organismus ist bestrebt, die genetischen Informationen intakt zu halten, die in seiner DNA gespeichert sind. Dies wird durch präzise gesteuerte zelluläre Prozesse wie DNA-Replikation, -Reparatur und -Rekombination verwirklicht. Ein wesentlicher Schritt ist dabei das Entwinden von DNA-Doppelsträngen zu Einzelsträngen. Diese chemische Reaktion wird von Helikasen durch die Hydrolyse von Nukleosidtriphosphaten katalysiert. Obwohl bei allen Helikasen bestimmte Aminosäuresequenzen hoch konserviert sind, können sie sich in Eigenschaften wie Struktur, Funktion oder DNA Substratspezifität stark unterscheiden.

Gegenstand der vorliegenden Arbeit ist es, die Entwindungsmechanismen von drei verschieden Helikasen aus zwei unterschiedlichen Organismen zu untersuchen, die sich in ihrer Struktur sowie ihrer Funktion unterscheiden. Es handelt sich dabei um die replikative, hexamerische Helikase Large Tumor-Antigen (T-Antigen) vom Simian-Virus 40 und die DNA-Reparatur-Helikasen RecQ2 und RecQ3 der Pflanze *Arabidopsis thaliana*.

Um DNA-Entwindung in Echtzeit zu untersuchen, wird eine biophysikalische Einzelmolekültechnik, die "Magnetische Pinzette", verwendet. Mit dieser Technik kann man ein DNA-Molekül, das an ein magnetisches Partikel gebunden ist, strecken und gleichzeitig dessen Gesamtlänge messen. Mit speziellen DNA-Konstrukten kann man so bestimmte Eigenschaften der Helikasen bei der DNA-Entwindung, wie z.B. Geschwindigkeit, Länge der entwundenen DNA (Prozessivität) oder den Einfluß von Kraft, ermitteln.

Es wird gezeigt, dass T-Antigen eine der langsamsten und prozessivsten Helikasen ist. Im Gegensatz zu prokaryotischen Helikasen ist die Entwindungsgeschwindigkeit von T-Antigen kaum kraftabhängig. Aktuelle Modelle sagen dieses Verhalten nicht vorraus, weshalb ein alternatives Modell entwickelt wird.

Die untersuchten RecQ-Helikasen zeigen ein Entwindungsverhalten bei dem permanent kurze Abschnitte von DNA entwunden und wieder zusammengeführt werden. Dieses Verhalten wird hier zum ersten Mal unter dem Einfluß externer Kräfte gemessen. Es wird gezeigt, dass die permanente Entwindung auf die Fähigkeit beider Helikasen, von einem einzelen DNA-Strang auf den anderen zu wechseln, zurückzuführen ist. Obwohl RecQ2 und RecQ3 beide das Verhalten des permanenten Entwindens aufzeigen, unterscheiden sie sich stark in anderen Eigenschaften. Der gravierendste Unterschied ist, dass RecQ2 wie eine klassische Helikase die DNA entwindet, während RecQ3 eher bestrebt ist, die DNA-Einzelstränge wieder zusammenzuführen. Die unterschiedlichen Eigenschaften könnten die verschieden Aufgaben beider Helikasen während DNA-Reparaturprozessen widerspiegeln.

Weiterhin werden die experimentellen Methoden optimiert, um möglichst hohe Auflösungen der Daten zu erreichen. Dazu zählen der Aufbau einer verbesserten und stabileren "Magnetischen Pinzette" mit sub-nanometer Auflösung und die Entwicklung neuer Methoden, um DNA Konstrukte herzustellen. Außerdem wird die Torsionssteifigkeit von magnetischen Partikeln in externen magnetischen Feldern untersucht. Dabei finden sich Auswahlkriterien für DNA-gebundene magnetische Partikel, durch die eine hohe Auflösung erreicht wird.

Abstract

Each organism has to maintain the integrity of its genetic code, which is stored in its DNA. This is achieved by strongly controlled and regulated cellular processes such as DNA replication, -repair and -recombination. An essential element of these processes is the unwinding of the duplex strands of the DNA helix. This biochemical reaction is catalyzed by helicases that use the energy of nucleoside triphophate (NTP) hydrolysis. Although all helicases comprise highly conserved domains in their amino acid sequence, they exhibit large variations regarding for example their structure, their function and their target nucleic acid structures.

The main objective of this thesis is to obtain insight into the DNA unwinding mechanisms of three helicases from two different organisms. These helicase vary in their structures and are involved in different pathways of DNA metabolism. In particular the replicative, hexameric helicase Large Tumor-Antigen (T-Antigen) from Simian virus 40 and the DNA repair helicases RecQ2 and RecQ3 from *Arabidopsis thaliana* are studied.

To observe DNA unwinding by these helicases in real-time on the single molecule level, a biophysical technique, called magnetic tweezers, was applied. This technique allows to stretch single DNA molecules attached to magnetic particles. Simultaneously one can measure the DNA end-to-end distance. Special DNA hairpin templates allowed to characterize different parameters of the DNA unwinding reaction such as the unwinding velocity, the length of unwound DNA (processivity) or the influence of forces. From this mechanistic models about the functions of the helicases could be obtained.

T-Antigen is found to be one of the slowest and most processive helicases known so far. In contrast to prokaryotic helicases, the unwinding velocity of T-Antigen shows a weak dependence on the applied force. Since current physical models for the unwinding velocity fail to describe the data an alternative model is developed.

The investigated RecQ helicases are found to unwind and close short stretches of DNA in a repetitive fashion. This activity is shown for the first time under external forces. The experiments revealed that the repetitive DNA unwinding is based on the ability of both enzymes to switch from one single DNA strand to the other.

Although RecQ2 and RecQ3 perform repetitive DNA unwinding, both enzymes differ largely in the measured DNA unwinding properties. Most importantly, while RecQ2 is a classical helicase that unwinds DNA, RecQ3 mostly rewinds DNA duplexes. These different properties may reflect different specific tasks of the helicases during DNA repair processes.

To obtain high spatial resolution in DNA unwinding experiments, the experimental methods were optimized. An improved and more stable magnetic tweezers setup with sub-nanometer resolution was built. Additionally, different methods to prepare various DNA templates for helicase experiments were developed. Furthermore, the torsional stability of magnetic particles within an external field was investigated. The results led to selection rules for DNA-microsphere constructs that allow high resolution measurements.

Contents

1 Basic principles

This chapter provides some basic principles of the object of interest, the helicase. A short overview of the structure and function of helicases is given in the first section followed by a brief review of the current understanding of DNA unwinding by helicases in the second section. Further introduction to helicases can be found in the following reviews: [1, 2] for history, classification and function, [3, 4, 5] for motifs, structure and mechanisms, [6] for regulation by helicases and [7] for physical models to describe DNA unwinding. The third section will briefly review some single molecule techniques to study helicases. More techniques can be found in [8]. Finally, the last section provides the outline of this thesis.

1.1 Helicases

1.1.1 Motor proteins fueled by NTP hydrolysis

Helicases are a large group of multifunctional enzymes that can be found in all organisms. They fulfill key roles in almost every part of nucleic acid metabolism e.g. replication, repair or recombination and therefore exist in large diversity depending on their explicit function. Most commonly helicases separate (unwind) duplex strands of desoxyribonucleic (DNA) and ribonucleic acids (RNA) (Fig. 1.1a).

These enzymes are also part of the larger class of motor proteins, because they are all driven by the hydrolysis of nucleoside triphosphate (NTP) and/or deoxynucleoside

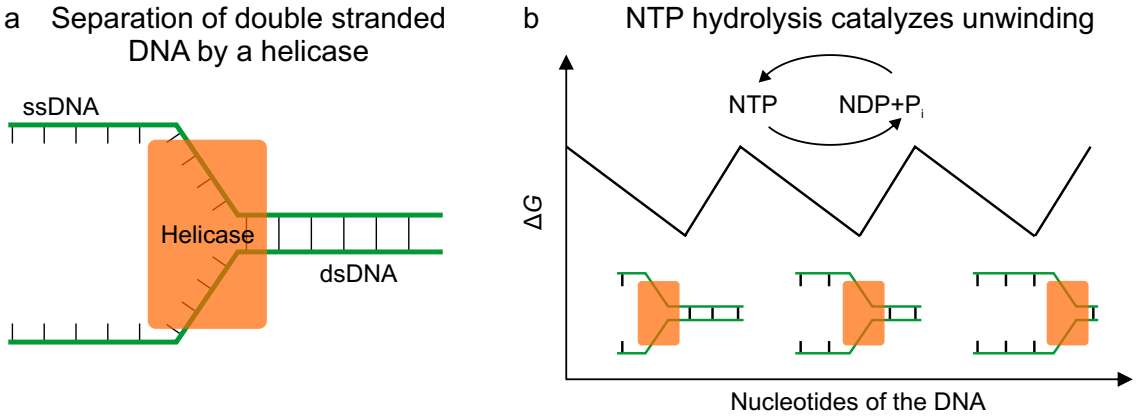

Figure 1.1 Sketch of DNA unwinding by helicases. (**a**) Sketch of the most common task of helicases: Separation of double stranded DNA (dsDNA) into single stranded DNA (ssDNA) during various cellular processes (see main text). (**b**) Schematic plot of the free energy of the barrier provided by paired bases. The cycle of NTP binding, hydrolysis and release lowers the free energy, i.e. catalyzes the DNA/RNA unwinding reaction.

triphosphate (dNTP) fueling the helicases "engine", the NTPase domain. During NTP hydrolysis chemical energy stored in the phophate bonds is released, by separating the gamma phosphate from the NTP [9]. The products are a nucleoside diphosphate (NDP) and an inorganic phosphate (P_i).

The exergonic reaction releases $\Delta G \approx -25\ k_BT$ [9] and changes the affinity of the motor to its substrate (the DNA) as well as the whole conformation of the enzyme, therby forcing the helicase to conduct a step forward, also called power stroke (see Figure 1.1b). In addition to the substrate- and NTP-dependence all helicases require divalent cations to coordinate the phosphates of the NTPs during the hydrolysis reaction (mostly magnesium).

In the following DNA will be referred to as template and adenosin triphosphate (ATP) as nucleoside triphosphate, because these are the most common interaction partners and were also exclusively used in the experiments presented here.

Presence and organization of conserved motifs in the amino acid sequence assigns most of the helicases to one of six superfamilies (SF). These conserved motifs constitute domains of the enzyme which participate in ssDNA binding, ATP binding and ATP hydrolysis [8]. Non-conserved domains are responsible, for example, for DNA sequence recognition or protein-protein interaction sites. The appearance and arrangement of different domains cause the variety of operations helicases are able to perform and their diversity. In the following section the main structure of helicases is presented.

1.1.2 Structure of helicases

All of the helicases have the same "engine". The "engines" are folded proteins containing an essential motif for ATP binding and hydrolysis called Walker A (for phosphate interaction) and Walker B (for magnesium interaction) [10] according to the finder John E. Walker. Two groups of the folded proteins are distinguished: the RecA-like-folds and the AAA+ folds. The RecA-like folds (first found in the enzyme RecA and named thereafter) are typical for SF 1 and SF 2 helicases. The AAA+ fold (ATPases Associated with diverse cellular Activities) is typical for SF 3 helicases.

The crystal structure of a typical SF 2 helicase with DNA and without ATP or ADP is shown in Figure 1.2a (Hel308 from Archaeoglobus fulgidus) [11]. The two RecA-like folds and the ATP binding pocket are highlighted. The 3´ ssDNA overhang of the cocrystalized DNA is in contact with the RecA-like folds. The crystal structure helps to derive the mechanism of the movement of the helicase along ssDNA and will be explained in more detail in the next section.

A representative of SF 1 helicases with DNA and without ATP or ADP is shown in Figure 1.2b (UvrD from E.coli) [12]. As for Hel308 the RecA-like folds and ssDNA are found to be in contact, although the crystal structures of both enzymes are largely different. The structure of UvrD with DNA reveals that, beside the contact of the RecA-like folds to the ssDNA, another part of the enzyme makes a direct contact to the dsDNA. This leads to a different mechanism of movement of the helicase on the DNA (see next section).

Despite the structural differences, helicases occur also in different oligomerization states. UvrD, for example, is able to move along ssDNA (translocation) as a monomer,

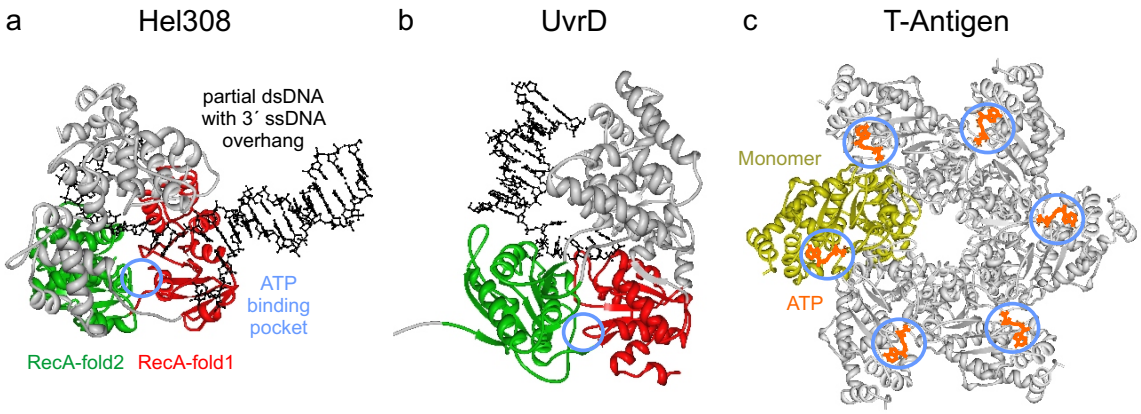

Figure 1.2 Crystal structures of different helicases. All structures are visualized with proteinworkshop [20]. (**a**) SF 2 helicase Hel308 [11] (PDB:2P6R). The two RecA-like parts of the "engine" are green and red. Cocrystalized DNA is shown in black. DNA is partially double stranded, with a 3´ single stranded overhang. Position of the ATP binding pocket (ATP is not shown) is indicated by a blue circle. (**b**) E.coli SF 1 helicase UvrD cocrystalized with partially dsDNA and without ATP [12] (PDB:2IS1). Colour coding is the same as in a. (**c**) Viral SF 3 helicase T-Antigen. Amino acids 251-627 of 708 (the helicase domain) are shown. [21] (PDB: 1SVM). One monomer is highlighted in dark yellow. Bound ATP is shown in orange in all of the monomers.

but needs to form a dimer to unwind dsDNA [13]. The oligomerization state can depend on enzyme concentration as well as the concentration of additional ligands such as the DNA or ions [14]. Helicases of the SF 1 and 2 mostly form homo- or hetero-dimers (E.coli UvrD [13], Rep [15], PcrA [16]) as well as monomers (BLM [17], PriA [18], T4 Dda [19]).

SF 3 helicases form ring shaped hexamers (T-Antigen [22], T4 gp41 [23], E.coli DnaB [24], E1 [25]). Figure 1.2c shows the crystal structure of the hexameric SF 3 helicase Large Tumor-Antigen (T-Antigen) cocrystalized with ATP. T-Antigen is able to unwind DNA as single hexamer. One strand of the DNA is suggested to pass through the inner channel while the second strand is sterically sheared off the dsDNA. *In vivo* T-Antigen even works as a double hexamer, which will be described in more detail in chapter 4. All of the monomers can hydrolyze ATP and interact with the DNA. How the hydrolysis is coordinated between the monomers will be discussed in the next section.

Crystal structures reveal the interaction sites of helicases with the DNA and the ATP and the enzyme configurations in presence and absence of DNA, ATP and ADP. To derive the mechanism of translocation of helicases additional results of dynamic single molecule or kinetic bulk experiments are required. Current models for the mechanism of helicase translocation along ssDNA and unwinding of dsDNA, will be presented in the next section.

Finally it should be noticed that *in vivo* helicases are parts of large protein complexes which mutual interacts with and influence the helicase. Additional proteins may change the conditions for oligomerization or other properties of the helicase.

Helicase	Organism	Superfamily	Activity	NTPs	Polarity
UvrD	E.coli	SF 1	DNA Repair	ATP	3´-5´
Rep	E.coli	SF 1	DNA Repair	(d)ATP	3´-5´
AtRecQ2	Arabidopsis thaliana	SF 2	DNA Repair	(d)ATP, (d)GTP, (d)CTP, UTP, dTTP	3´-5´
RecD	E.coli	SF 2	Recombination	(d)ATP	5´-3´
HPV E1	Human papilloma virus	SF 3	DNA Replication	(d)ATP, UTP, GTP	3´-5´
Large Tumor Antigen	Simian virus 40	SF 3	DNA Replication, (RNA unwinding)	(d)ATP, (d)GTP, (d)UTP, (d)CTP	3´-5´

Table 1.1 Examples of helicases with some of their most important properties. (d)NTP means the helicase can hydrolyze the NTP and the dNTP.

Some examples of helicases with their main properties are shown in table 1.1.

1.2 DNA unwinding by helicases

1.2.1 How a helicase steps forward

It is important to distinguish between ssDNA translocation and dsDNA unwinding. Translocation on ssDNA is always required, though not sufficient for most helicases to processively unwind dsDNA. The mechanisms presented in the following can be applied for ssDNA translocation as well as dsDNA unwinding.

Figure 1.3 sketches three proposed ssDNA translocation/ dsDNA unwinding models for SF 1 and 2 helicases. Omitting the displaced strand in the images, each mechanism provides a model for pure ssDNA translocation. For dsDNA unwinding always one subunit of a monomer (or at least one monomer of an oligomer) is translocating along ssDNA, while another subunit/monomer is responsible for base pair opening.

The inchworm mechanism in Figure 1.3a can be applied to a monomer with two DNA binding sites or a dimer which moves by alternating binding of the monomers. It was suggested, for example, for the movement of Rep monomers [28] and PcrA monomers [26]. The two RecA-like folds bind to ssDNA (independent of the ssDNA sequence). To translocate along the ssDNA, the following cycle is passed [14]: 1. Without ATP the leading subunit is tightly bound to the ssDNA while the lagging one is weakly bound to the ssDNA and both subunits are distant. 2. Upon ATP binding conformational changes shift the lagging subunit towards the leading one and the affinity for ssDNA of both units change (now the leading one is weakly and the lagging one is now tightly bound). 3. When ATP is hydrolyzed the leading subunit opens a base pair, such that the distance between the subunits increases. 4. Upon

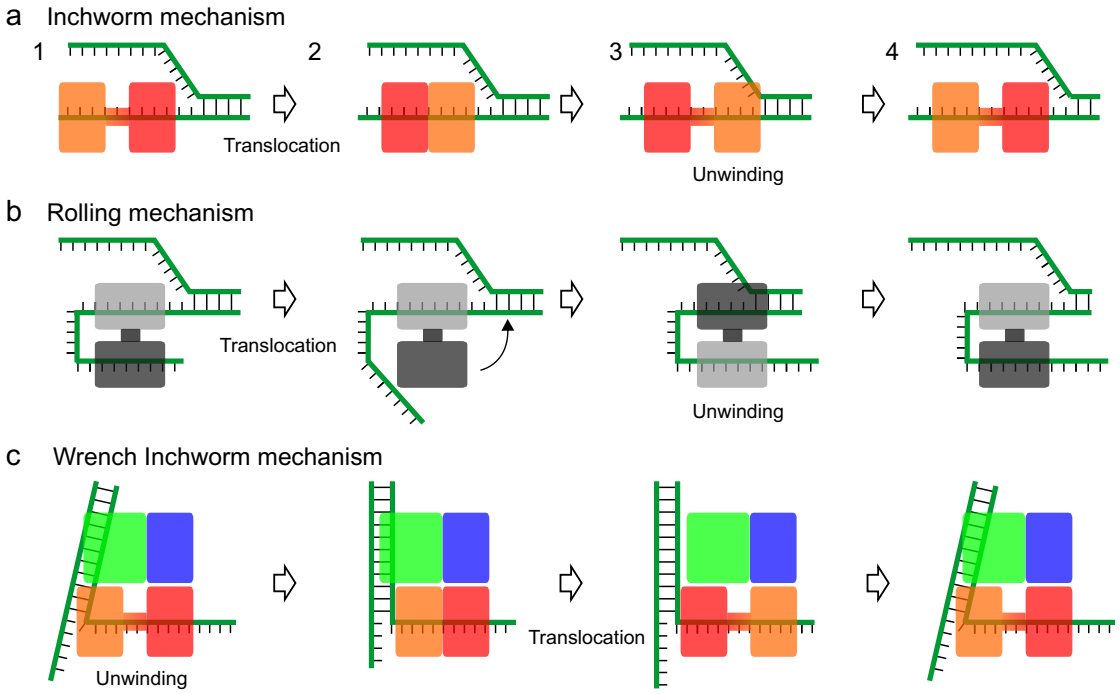

Figure 1.3 Different unwinding mechanisms of SF 1 and -2 helicases. (**a**) Inchworm mechanism can be used to describe the movement of monomers and dimers [26]. Alternating tight (dark orange) and loose (light orange) binding of the subunits in monomers (or the monomers in dimers) drives the helicase along the DNA. The leading subunit (monomer) interacts with the DNA junction to open a base pair. (**b**) Rolling mechnism for helicases which act as dimers (monomer 1: light gray, monomer 2:dark gray) [15]. The monomers alternate in binding of ssDNA and unwinding the dsDNA region. (**c**) Wrench inchworm mechanism is proposed for UvrD which is a monomer composed of four subunits [27]. Two subunits mainly move like an inchworm (same colors as in a), while another subunit tightly binds to dsDNA to support the inchworm movement. All of these mechanisms include also translocation on ssDNA. Sizes of the enzymes are not to scale. The different steps present certain states of the ATP hydrolysis cycle.

ADP release the starting conformation is reset.

Figure 1.3b shows the active rolling mechanism, proposed for dimeric helicases like RepA [29]. One monomer binds to the ssDNA while the other one binds to the dsDNA junction. Upon ATP hydrolysis in the monomers, allosteric effects (one monomer regulates the other) cause alternating binding of the monomers to ssDNA and the dsDNA junction. While the monomer attached to ssDNA translocates, the monomer at the dsDNA junction opens a base pair.

Figure 1.3c shows a more complicated model suggested for UvrD monomers [27, 12]. UvrD has four subunits. Three of the subunits form a rigid body while one subunit is flexible (when UvrD is attached to DNA) [5]. Upon ATP binding the flexible subunit undergoes a 20° rotation, bringing it closer to the other three domains. This step opens a base pair. ATP hydrolysis followed by ADP release rotates the subunit 20° in the opposite direction. This step is accompanied by translocation of UvrD along

the DNA. In contrast to the inchworm mechanism (with its two alternating contacts to the ssDNA), UvrD has four contact points to the DNA. One of these contact points is to the dsDNA, one contact point is to the DNA junction (i.e. to ssDNA and dsDNA) and two contact points are to the ssDNA which exits the enzyme. The dsDNA contact and one ssDNA contact are tightly bound upon binding of ATP, while the contact to the DNA junction and the other ssDNA contact are weak. When ATP is hydrolyzed and released, the formerly tight bindings become weak, while the weak

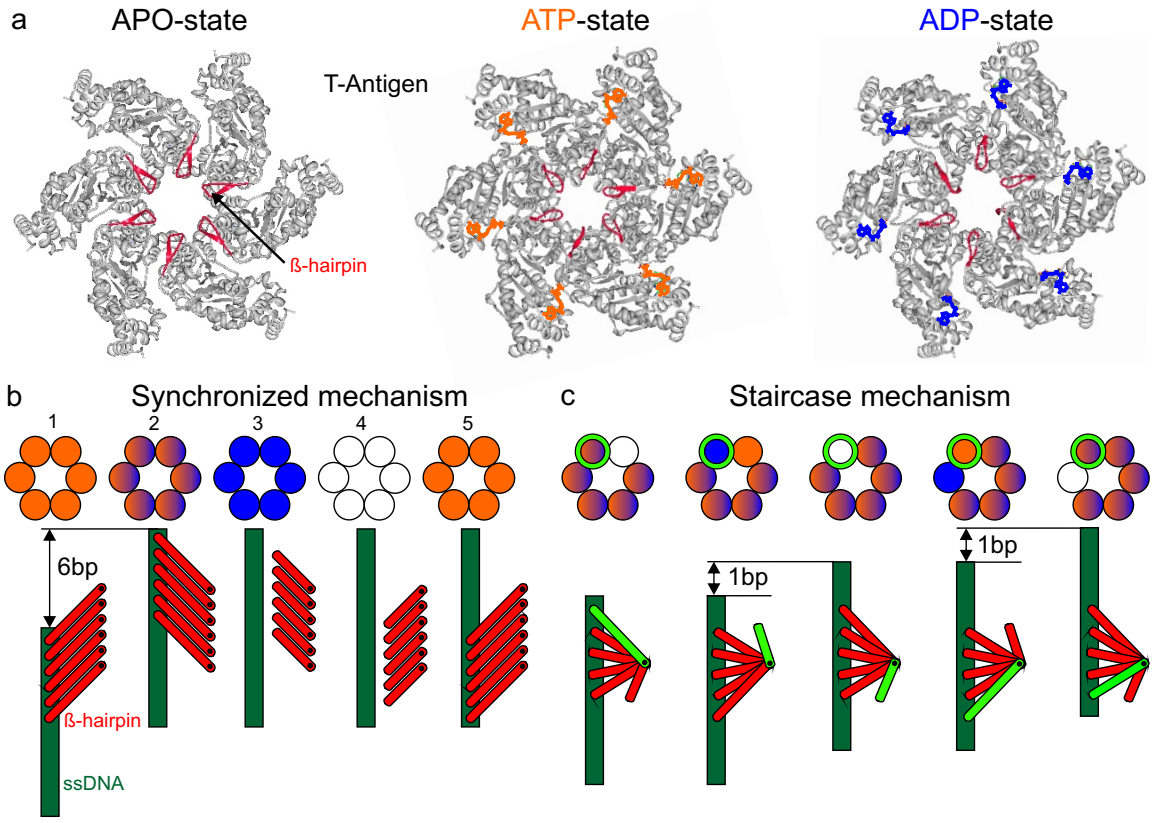

Figure 1.4 Different unwinding mechanisms of SF 3 helicases. (**a**) Crystal structures of T-Antigen (amino acids 251-627) without nucleoside triphosphate (APO), with ATP (orange) and with ADP (purple) [21]. The DNA binding site aa 508-517 (beta-hairpin) is shown in red. (**b**) T-Antigen hexamer is sketched by six circles (one for each monomer) in the same view as in (a). The nucleotide binding state of each monomer is shown by the corresponding color as in (a). The gradient from orange to blue indicates ATP hydrolysis. Below each sketch, the corresponding reaction of the beta-hairpin (red elements) and its effect on the DNA (green) is shown. Binding of ATP couples the DNA beta-hairpins to the DNA (1). ATP hydrolysis results in a large conformational change and translocates the bound DNA (2). Bound ADP releases the binding loop (3). Dissociation of ADP resets the conformational change (4). Binding of ATP results in binding of the next six base pairs (5). The synchronized translocation results in 6 basepair (bp) steps. (**c**) The staircase model suggests subsequent translocation of single base pairs of the DNA. Color coding is as in (b). One helicase monomer and its corresponding DNA binding loop is highlighted in green. Successive translocation results in 1 bp steps.

binding become tight. [8]. This movement converts the subunit-rotation into linear translocation along the DNA. This causes a spiral movement similar to a ratchet wrench [12]. The resulting movement in all mechanisms is always unidirectional with respect to the ssDNA backbone the helicase translocate on (unwinding polarity, either 3´ to 5´ or 5´ to 3´ direction)

In monomeric helicases tight and loose binding of the two binding sites is controlled by one ATP hydrolyzation procedure. Oligomeric helicases have accordingly more ATPases which need to be coordinated to result in a unidirectional unwinding process [30]. How the hydrolysis is coordinated between the monomers can be revealed by investigating the step size of a helicase, corresponding to the number of nucleotides a helicase overcomes per ATP hydrolysis cycle while unwinding or translocating. This mechano-chemical coupling is defined either as physical, i.e. average distance the helicase travels relative to the DNA backbone per working step or as kinetic, i.e. the average number of base pairs unwound (nucleotides translocated) between two rate limiting steps of the cycle [8]. These steps can further be composed of several substeps. A large physical step might be the result of several accumulated small steps. A large kinetic step might occur as a result of several fast steps interrupted by a rate limiting step [31, 32]. Two different models of ATP hydrolysis coordination in hexameric T-Antigen are depicted in Figure 1.4. The crystal structure without ATP (APO), in presence of ATP and in presence of ADP revealed different conformational states of T-Antigen, especially of the DNA binding hairpins (beta-hairpin) [21] (Fig. 1.4a). Upon ATP hydrolysis, these beta-hairpins translocate the DNA along the inner channel of the enzyme. All ATP binding pockets were found to symmetrically bind the nucleoside triphosphate, implying a synchronized hydrolysis of all monomers. The step size of T-Antigen would therefore be expected to be 6 basepair (bp) for dsDNA unwinding or 6 nucleotides (nt) for the DNA translocation (Fig. 1.4b). However, the shown structures were recorded in absence of DNA [21]. In contrast, in high resolution optical tweezers studies on hexameric T7gp4 1 bp steps have been detected [33]. Also studies of the crystal structures of the E1 helicase in presence of DNA suggest a a smaller step size. For these enzymes a staircase mechanism was suggested where the DNA is transported sequentially (Fig. 1.4c).

As mentioned above translocation on ssDNA is not necessarily sufficient for dsDNA unwinding. Some purely translocating helicases are strong enough to shear the second strand away if encountering dsDNA. Other purely translocating helicases are too weak, so that their progress depends on thermal fluctuations of the DNA junction in front of the enzyme. Other helicases actively interacts with the base pair at the leading subunit (or monomer) while translocating. Those mechanisms will be discussed in the next section.

1.2.2 Active and passive DNA unwinding

DNA unwinding can be classified as active or passive [3, 34]. A passive helicase diffuses along ssDNA. However, the diffusion is blocked in one direction by an intrinsic mechanism of the helicase, which can be illustrated as a ratchet (Fig. 1.5a). The ratchet-system translates the diffusive movement in a directed movement, i.e.

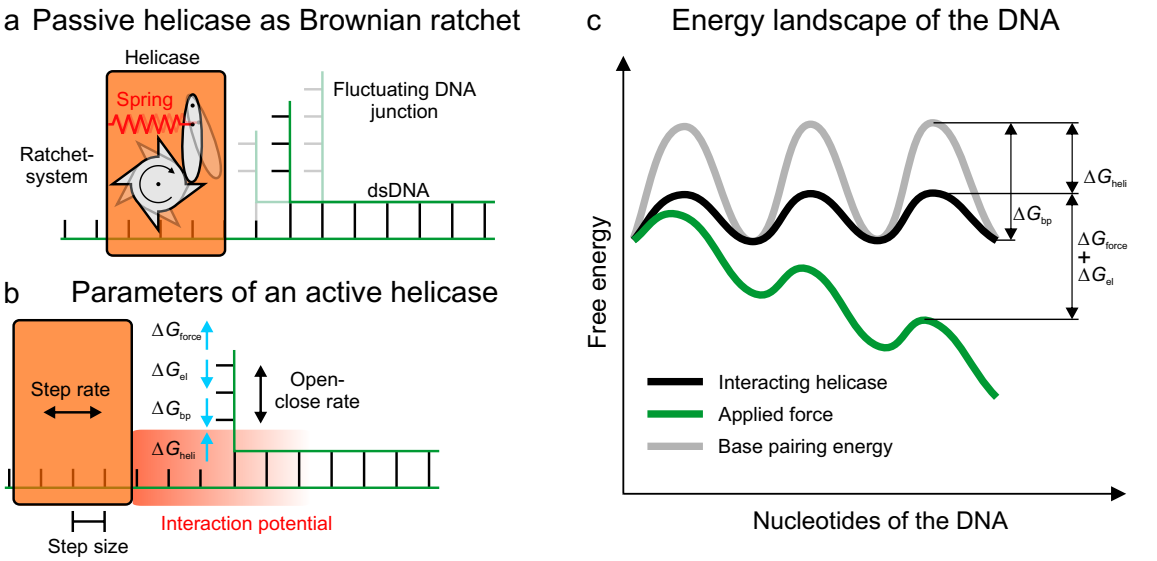

Figure 1.5 Active and passive unwinding mechanisms. (**a**) A passive helicase (orange) sketched as a Brownian ratchet. The helicase translocates along ssDNA (from left to right). The cogwheel can rotate only clockwise, because a pawl circumvents counter-clockwise rotation. Several base pairs at the DNA junction (in front of the helicase) fluctuate between an open and closed state due to thermal excitation. (**b**) Parameters required to describe helicase unwinding with an active model [38]. The helicase interaction potential is shown as a red gradient. The rate of the helicase movement (back and forward) as well as the rate of the fluctuations of the DNA junction (open and close) are indicated by black arrows. Energies influencing the fluctuations of the DNA junction are indicated by blue arrows (free energy from the applied magnetic (external) force $\Delta G_{\mathrm{force}}$, free energy from the elastic force of the free ssDNA ΔG_{el}, base pairing energy ΔG_{bp}, interaction potential of the helicase ΔG_{heli}). The step size and the shape of the interaction potential (how the potential decays) are further parameters. (**c**) Energy landscape of the DNA in the hairpin and the influences of the different contributions of the free energies as indicated.

translocation of the helicase with a strand polarity (either 3´to 5´ or vice versa). The potential energy of the ratchet is represented by the spring in Figure 1.5a. Althoug the movement of the helicase is driven by thermal energy, the system is not a perpetuum mobile, because the energy generated during ATP hydrolysis is potential energy of the ratchet. When the helicase encounters the DNA junction, it cannot perform sufficient work to open a base pair. The first base pairs at the junction undergo fast open-close fluctuations induced by thermal energy. This provides temporarily new ssDNA in front of the helicase, so that the enzyme can step forward. With this mechanism a passive helicase progresses through dsDNA, as shown for T4 gp41 [35], T7 gp4 [36] or hepatitis C virus helicase [37]. This mechanistic behavior is also called a Brownian ratchet.

In contrast an active helicase directly interacts with the dsDNA junction and lowers the free energy of the base pairs ΔG_{bp}. The free energy of the base pairs is composed of the free energy of guanin-cytosin base pairs, adenin-thymin base pairs and base pair stacking. The amount of free energy reduction caused by the helicase ΔG_{heli} can

be used to describe the degree of activity of an active helicase [39]:

$$\Delta G_{\text{heli}} = 0 \qquad \text{purely passive helicase} \tag{1.1}$$

$$\Delta G_{\text{heli}} = \Delta G_{\text{bp}} \qquad \text{purely active helicase} \tag{1.2}$$

$$0 < \Delta G_{\text{heli}} > \Delta G_{\text{bp}} \qquad \text{active helicase} \tag{1.3}$$

Generally active helicases have been found to be neither purely passive nor purely active. The observable parameter to estiamte the free energy reduction caused by the helicase is its unwinding velocity. This velocity depends on several parameters, which are described by a physical model developed by Betterton and Jülicher [34, 38] (Fig. 1.5b). This model will be described in more detail in section 4.3. The main parameters of this model are the back and forward translocation rate of the helicase and its dependence on the open-close rate of the DNA junction. Both rates are coupled via the distance between the helicase and the DNA junction [40] and depend on the acting forces (indicated in Figure 1.5b). These forces change the energy landscape of the DNA hairpin (Fig. 1.5c), i.e. the activation barrier and consequently the step rate is changed. Thus the helicase unwinding velocity is influenced by the acting forces. The applied external forces (and the energy of the ssDNA elaticity) can be measured in magnetic tweezers measurements as will be shown in section 2.3.2. Also the DNA base pairing energy can be determined, shown in section 3.3.2. The technique used here allows to observe the unwinding velocity of the helicase and simultaneously change the base pairing energy by applying forces which act on the DNA junction. However, the model still depends on the shape, the range and the strength of the helicase potential which reduces the base pairing energy as well as the step size and the back and the forward rate of the helicase. Combination of different parameters can lead to similar unwinding velocities and thus to contradicting results [7]: For instance, a passive helicase with a step size of 1 bp and a small backward translocation rate results in the same unwinding velocity as an active helicase with $\Delta G_{\text{heli}} = 2\ \text{k}_\text{B}\text{T}$ and a step size of 2 bp, without backward translocation and an interaction range of 1 bp.

Alternatively the ratio of unwinding velocity v_{unw} to ssDNA translocation velocity v_{trans} can be used to classify the helicase as active or passive [40]:

$$v_{\text{unw}}/v_{\text{trans}} << 1 \qquad \text{purely passive helicase} \tag{1.4}$$

$$v_{\text{unw}}/v_{\text{trans}} = 1 \qquad \text{purely active helicase} \tag{1.5}$$

$$0 < v_{\text{unw}}/v_{\text{trans}} < 1 \qquad \text{active helicase.} \tag{1.6}$$

Thereby the parameters of step size and backward translocation cancel each other.

However, the force-dependence of the helicase unwinding velocity determined in this thesis (for T-Antigen) cannot be described by the current physical model using any physical relevant combination of parameters (see section 4.3). An alternative model will be introduced in chapter 4. While the current model assigns a closed base pair in front of the helicase as an insuperable obstacle, i.e. the helicase has to "wait" for the next base pair to open, the alternative model describes the helicases as a base pair breaker, i.e. the helicase opens the next base pair, for the price of a reduced unwinding velocity.

To determine the molecular mechanism of dsDNA unwinding by a helicase, certain properties like the conformational states, velocities, affinities to DNA and ATP need to be observed in parallel. The results of current methods like ensemble averaged assays (bulk experiments), static crystal structure analysis and dynamic single molecule measurements are reqired to be combined to give a much more detailed molecular picture of helicase unwinding and translocation mechanisms. Especially with dynamic single molecule techniques important results have been achieved recently. The next section briefly introduces the advantages and disadvantages of different single molecule techniques.

1.3 Single molecule techniques

Bulk assays deliver kinetic results, crystal structures reveal conformations and single molecule experiments can generate dynamic unwinding data, e.g. step sizes, unwinding- and translocation velocities as well as rates of conformational changes [41]. Furthermore single molecule techniques allow to detect reaction intermediates, which are invisible in bulk experiments, such as pausing of the enzyme, stepping back or repetitve behaviour [8]. Another advantage is the ability to detect heterogenetic behaviour of single enzymes within one population, e.g. different ssDNA translocation between two enzymes of the same kind. Heterogenity broadens statistical averages in bulk experiments and lead to misinterpretation of the investigated property [42]. For example, ensemble transient kinetic experiments on UvrD showed a step size of 4 nt [32]. The results were based on meauring variances, which hide the individual events [43]. Single molecule Förster resonance energy transfer (FRET) experiments revealed a step size of 1 nt and also a large molecular heterogenities between individual molecules [42].

Figure 1.6a shows how single molecule FRET experiments can be used to study DNA unwinding by helicases. A fluorescence microscope, an exciting lasers and a detection system for the emitted light is required. A DNA molecule is attached to a surface of a fluidic chamber. Fluorescent labels are attached to the DNA and to the helicase. The fluorophores are special a pair of donor and acceptor dyes, i.e. the wavelengths of absorption or excitation of the acceptor need to overlap the wavelengths of emission of the donor and the dipol orientations of donor and acceptor need to be approximately parallel. Upon approach of the dyes, a radiation-free energy transfer from the donor to the accceptor changes the fluorescence intensities of both dyes (dipol-dipol interaction). The donor emission intensity decreases, because the energy is transfered to the acceptor, whose emission intensity increases. The ratio of donor- to acceptor intensity defines the FRET efficiency. This method is applied to probe helicase-DNA interaction (left sketch) or internal conformational changes in the helicase (right sketch). The advantage of FRET is the high sensitivity of the signal depending on the distance R between the dyes (R^6). This results in a resolution of $2 - 8$ nm [8]. It is also possible to detect multimerization of enzymes, a very important property in determining the mechanism of a helicase. Additionally a high number of molecules can be observed at a time (usually 200-400) [8]. A disadvantage is that the

signal is only detectable in very short ranges (max. 8 nm) and it changes non linear. Furthermore no forces are applicable in FRET assays.

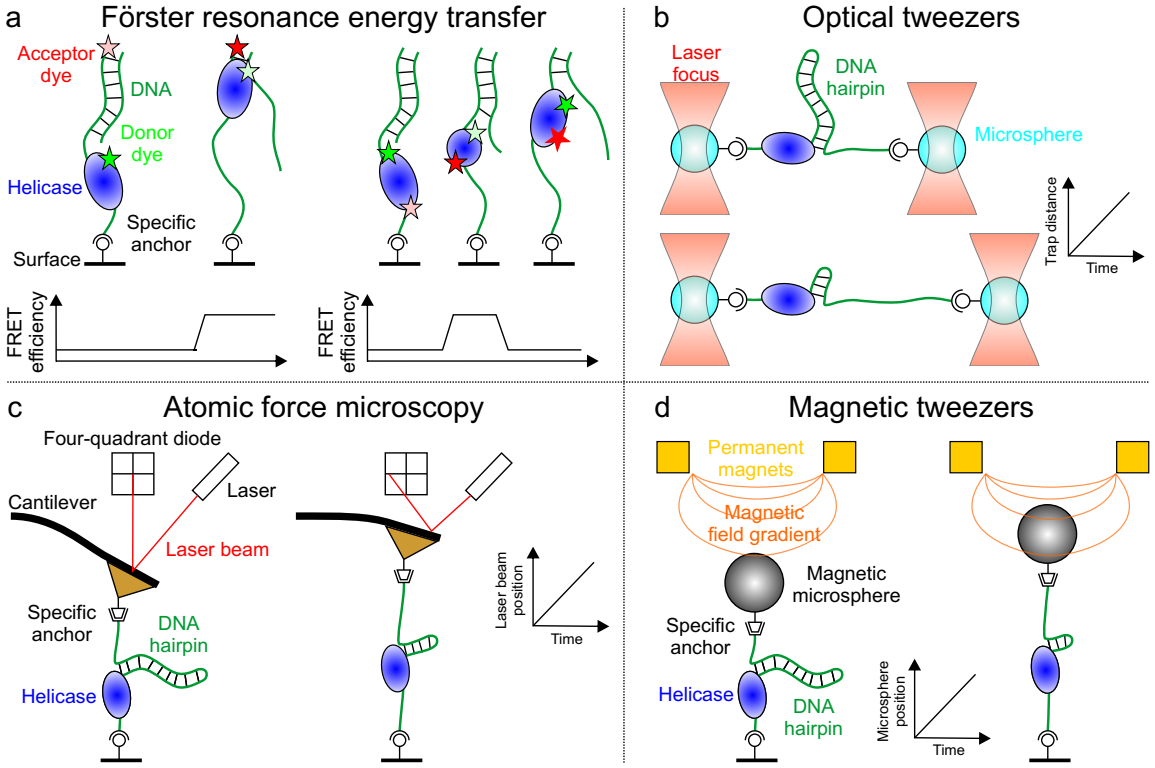

Figure 1.6 Single molecule techniques to probe helicases. The graph within each sketch indicates the measured signal of the techniques. (**a**) Sketch of single molecule FRET experiments to probe the helicase-DNA interactions (left side) or intrinsic conformational changes of a helicase (right side). (**b**) Assay to measure helicase activity with optical tweezers. Two laser foci trapping two microspheres connected with a DNA hairpin. The left laser focus is held at a fixed position. Upon DNA hairpin unwinding the distance between the microspheres increases, because a feedback maintains a constant force between the microspheres. (**c**) Sketch of an AFM experiment to detect DNA hairpin unwinding. Activity of the helicase causes a deflection of the cantilever which is detected by a changing laser beam position. (**d**) Magnetic tweezers are a passive force clamp, where DNA hairpin unwinding is observed by tracking the magnetic microsphere position in real time.

Atomic force microscopy (AFM) as well as optical- and magnetic tweezers allow to apply forces to the DNA. The dynamics of unwinding can be directly influenced by tilting the energy landscape of the unwinding reaction (see last section). These force-dependent experiments deliver important information on the occuring energies. Passive helicases, for example, highly speed up upon increasing the force acting on the DNA.

Figure 1.6b shows two configurations used in optical tweezers experiments. The upper sketch is a dual trap [44] where two dielectric microspheres are trapped in the strong gradient of focussed laser beams. The sample is located in a chamber filled with a liquid. To probe helicase activity a modified DNA hairpin is used, which

is attached to the microspheres at both ends. One trap holds the position of the microsphere, the other can be used to exert forces and measure changes in the DNA length. Unwinding of the DNA hairpin by a helicase will cause either an increase of DNA extension or decrease of trapping force. The dual trap guarantees a very high subnanometer resolution [44] (e.g. 1 bp in [45]), because of the uncoupled drift between setup and laserbeam. A disadvantage of optical tweezers is that only one molecule can be measured at a time.

In Figure 1.6c an AFM experiment is sketched. The sample is a DNA hairpin, attached on one end to a substrate surface. On the other end the DNA is attached to a functionalized AFM cantilever. The deflection of the cantilever, which is measured with a reflected laser beam on a four-quadrant diode, is the signal that can be converted to force. These AFM experiments allow measuring with a low spatial resolution (> 5 bp), but a high temporal resolution (1 ms) [46]. However, it is difficult to functionalize the tip of the cantilever. The throughput is also limited to one measurement at a time.

In Figure 1.6d the method used in this thesis, magnetic tweezers [47], is shown. This single molecule force spectroscopy technique will be introduced in detail and characterized in chapter 2. Briefly, a magnetic field gradient generates a force onto a magnetic microsphere, which is attached to a DNA hairpin. Helicase activity can be observed in real-time by tracking the spatial position of the microsphere.

1.4 Objectives and outline

One of the objectives of this thesis is to understand what causes the large differences in DNA unwinding mechanisms of helicases, although all of them are based on the same motor unit. Some helicases are capable to resolve elaborate DNA structures like holiday junctions, D-loops or G-quadruplexed DNA [48], while others are not able to unwind DNA at all (EcoR124I) [49]. The herein investigated helicases T-Antigen from Simian virus 40, RecQ2 and AtRecQ3 from Arabidopsis thaliana (AtRecQ2) differ in their specific tasks (T-Antigen: DNA replication, RecQ: DNA repair) and their classification (T-Antigen: SF 3, RecQ: SF 2). T-Antigen and AtRecQ are active in eukaryotic cells, so that their behavior can be compared to the one of prokaryotic helicases (e.g. T4, T7). Furthermore the different molecular activities between two RecQ helicases of the same organism will be investigated (AtRecQ2 and AtRecQ3).

Helicase acitvity for T-Antigen was shown in bulk already in 1986 [50]. Structural analysis refined the picture of T-Antigen [51, 52, 21]. The experimental results presented in this thesis will show the first single molecule, real-time DNA unwinding data of T-Antigen.

Additionally, mechanistic questions, like the classification concerning active or passive behavior will be addressed. Since the unwinding velocity data from our magnetic tweezers experiments cannot be described by current models, an alternative model will be presentd, which might be applicable to other eukaryotic helicases as well. For AtRecQ2 we find repetitive unwinding behaviour under external forces, as shown, for example, in FRET experiments for the NS 3 helicase [31]. Repetitive

means that a single helicase unwinds and closes a DNA hairpin several times. The suggested mechanism for NS 3 cannot explain our observations, also leading to a new model for repetitve unwinding.

To obtain high spatial resolution the experimental methods were optimized, including improvement of the DNA hairpin substrates (chapter 3), published in NAR Methods [53]. Also systematic investigation of the physics of magnetic microspheres attached to DNA in magnetic tweezers were conducted (sections 2.3.4, 2.3.5, 2.4). The results concerning the vertical resolution of magnetic tweezers were published in PRL [54]. The high spatial resolution obtained with the setup was also used to investigate initiation DNA supercoiling, published in Biophysical Journal [55].

2 Magnetic tweezers

The first section of this chapter decribes the concept of magnetic tweezers and contains material and methods about the design and construction of the magnetic tweezers.

The second section describes the method of tracking the spatial position of the microspheres with sub-nanometer resolution.

In the third section it is explained how to extract the applied magnetic forces from the fluctuations of a DNA tethered microsphere. For verification the magnetic forces are also determined from the properties of the used magnets and microspheres. Force experiments will be presented using pure dsDNA, DNA hairpin constructs and a DNA Holliday junction construct. Additionally the microspheres will be characterized concerning their torsional properties, i.e. how torque can influences a general force measurement. Finally, force experiments reveal that the determined forces can be underestimated due to a wrong determination of the DNA length.

The last section shows that the axial (along z direction) resolution of magnetic tweezers can become limited by rotational fluctuations which largely vary between individual microspheres. This is caused by the off-center attachment between DNA molecule and microsphere, which originates from the alignment of the magnetic microsphere with the external field.

contains measurements revealing that the resolution in z position can become limited, caused by misalignment of the DNA axis and the microsphere center which leads to rotational fluctuations. Characterization of the microspheres torsional stiffnesses uncovered the reason for rotational fluctuations. By solving the set of differential equations describing the coupled linear and rotational microsphere motions, we are able to directly quantify the torsional stiffness from the measured fluctuations. These results were published in Physical Review Letters [54].

2.1 The Setup

2.1.1 The basic concept of magnetic tweezers

Magnetic tweezers are a detection and manipulation tool that allows to stretch single molecules (commonly DNA) [56]. Figure 2.1 sketches the setup used in this thesis. A DNA molecule is attached on one end to a substrate surface and on the other end to a microsphere. The attachment is realized by implementing biotin- and digoxigenin-labeled bases to the DNA´s ends (see chapter 3). The substrate surface and the microsphere are coated with the corresponding antigene, anti-digoxigenin and streptavidin, respectively. The microsphere consists of superparamagnetic nanoparticles, i.e. in absence of an external magnetic field, the microsphere is non-magnetic (no remanence). However, in presence of an external magnetic field the microsphere becomes a magnetic dipol. The interaction of the external magnetic field on the

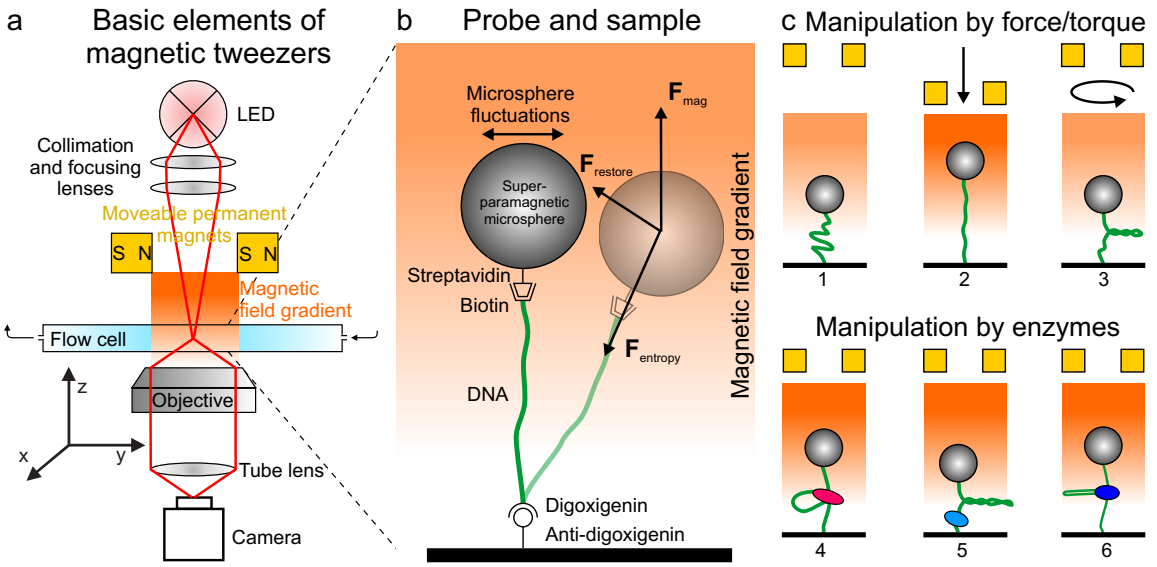

Figure 2.1 Main components, basic principle and applications of magnetic tweezers. (**a**) Scheme of the basic elements of the magnetic tweezers setup (red lines indicate the beam path). The orientation of the magnetic dipol of each permanent magnet is indicated with S-N. The direction of the external magnetic field lines is defined as the y-direction (see coordinate system). The magnetic field is indicated by the orange color gradient. (**b**) The magnetic field gradient causes an upward force (F_{mag}) acting on the superparamagnetic microsphere, which stretches the tethered DNA (F_{entropy}). Brownian motion permanently disrupts the positional equilibrium (recovered by F_{restore}) causing small displacements. (**c**) Common applications of magnetic tweezers. Magnetic tweezers can be used to stretch and twist DNA (upper row) or to observe DNA manipulations of enzymes (lower row).

magnetic dipole results in a force acting on the microsphere (along the magnetic field gradient). The DNA tethered microsphere is located in a thin (≈ 150 μm inner distance) flow cell filled with liquid medium. Above the flow cell two permanent magnets in close proximity to each other (≈ 1 mm), with a high remanence provide a strong magnetic field gradient. The vertical force traps the tethered microsphere and stretches the DNA. The two permanent magnets can be moved vertically. The closer the magnets to the flow cell, the higher the magnetic field gradient experienced by the microsphere and thus the higher the applied force acting on the microsphere.

A light emitting diode (LED) illuminates the microsphere through the gap between the two permanent magnets. The microsphere is imaged with an objective onto a camera. Three dimensional tracking of the microsphere enables to determine the length of the attached DNA and to calculate the applied force (explained in detail in sections 2.2 and 2.3).

Additionally to the force, the external magnetic field can also exert torque on the microsphere. Due to magnetic polarization anisotropy the microsphere is torsionally trapped. This allows to rotate the microsphere by rotating the two permanent magnets, which results in twisting of the DNA [55].

The properties of magnetic tweezers to stretch and twist DNA are well suited for DNA manipulation experiments (Fig. 2.1c). For example magnetic tweezers were

used to investigate the force-extension behaviour of DNA [56], supercoiling of DNA [57, 58, 59, 55] or intramolecular DNA mechanics [60].

In contrast to manipulating DNA by external force and torque, one can observe the influence on DNA by an enzyme. By keeping the external forces constant one can follow changes in the DNA topology. For example, DNA loop formation by the restriction enzyme EcoR124I [61], DNA supercoil relaxation by the E.coli gyrase [62] or branch migration of a DNA holliday junction by the enzyme RuvAB can be observed [63]. Magnetic tweezers have also been used to study DNA unwinding by helicases [64, 39]. One method, which was also used in this thesis, is to observe DNA hairpin unwinding (see Figure 1.6d). In such a configuration unwinding of one base pair leads to a DNA length extension of two nucleotides, which can be observed in real time by following the resulting positional changes of the microsphere.

A reason to choose magnetic tweezers as a single molecule detection method is the non-invasive measurements of forces and positions avoiding heating or photodamage of the sample. Another advantage is the throughput of up to several 10s of DNA hairpin samples simultaneously. Usually the spatial- and temporal resolution of magnetic tweezers is limited to 10 bp and 50 ms, respectively. Several improvements on the self-made magnetic tweezers setup and the tracking algorithm used in this thesis result in 3 ms temporal and ≈ 3 bp spatial resolution in helicase experiments (see section 2.2.1). In the following section the setup design is presented in detail.

2.1.2 Setup design

The setup is based on a self-made inverted microscope (see photograph in Figure 2.2). Two permanent rare earth magnets (NeFeB) with a large remanence of 1.4 T (W-05-N50-G, Supermagnete, Uster, Switzerland) placed 0.7 mm apart within an iron holder provide a magnetic field of several 100 mT and a strong magnetic field gradient. The magnets are connected to motorized stages for translational and rotational movements (M126.PD1 and C150.PD, PI, Karlsruhe, Germany). The range of vertical forces these magnets exert onto superparamagnetic microspheres with a diameter of $d = 2.8$ μm (M280 streptavidin coated beads, Invitrogen, San Diego, USA) is between ≈ 10 fN and 100 pN.

The illumination of the microsphere is realized by a red LED (625nm, CR5111A-WY, Roithner Lasertechnik GmbH, Vienna, Austria). The emitter of the LED is imaged into the flow cell to obtain a high light intensity. The light is collected by a high numerical aperture (NA=1.25) oil-immersion objective (Achn 100xOP, Olympus, Hamburg, Germany). The images are recorded with a high speed CMOS camera (EoSens CL MC1360-63, Mikrotron, Unterschleissheim, Germany) with 8 bit gray scale.

Optomechanical elements (lens mounts, mirror mount, lens tubes, etc.) are from Thorlabs (Newton, NJ, USA) or manufactured by workshops of the TU-Dresden (Labor- und Versuchsfeldverbund Zeunerbau, Kutzbachbau, Dresden). Optical elements (lenses, mirror) are from Newport (Irvine, CA, USA).

The flow cell is assembled of two glass cover slides (No.1, Menzel Gläser, Braunschweig, Germany) which are spaced by parafilm to ≈ 300 μm distance of the inner

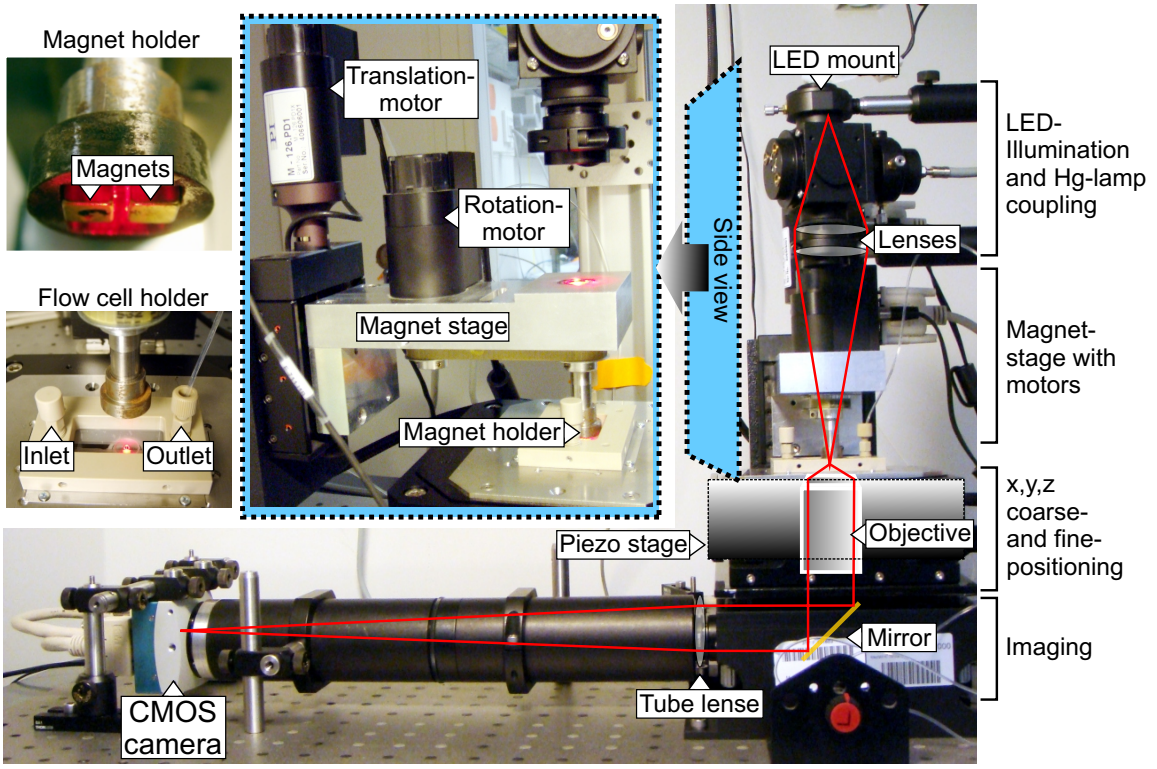

Figure 2.2 Photograph of the magnetic tweezers setup. On the right side the main body of the magnetic tweezers is shown with the illumination pathway through the magnet stage. Red lines indicate the beam path. A side view shows the motor which moves the magnet stage vertically and the motor that turns the iron magnet holder. The holder with the pair of permanent magnets and the flow cell holder are shown on the left side.

surfaces (protocol in appendix 6.2.1). The cover slide on top has an in- and an outlet hole to exchange the solution. The cover slide at the bottom is coated with the anti-digoxigenin to attach DNA with digoxigenin labeled bases. The flow cell is mounted into a holder, with an in- and outlet connector, so that the outlet can be connected via tubings to a syringe pump system to provide a constant, slow flow during the exchange of the solutions.

The flow cell holder is mounted on a piezo-driven nano positioning stage (P-517.3CD, PI, Karlsruhe, Germany). The stage has a large opening in the center for the objective. The stage is used to control the distance between the focus of the objective and the microsphere with high precision . The whole setup is placed on a heavy bread board on a passive damping table (63-500 Series, TMC, Peabody, MA 01960 USA).

2.2 Data aquisition

The key idea of magnetic tweezers is to extract information about the DNA from the response of an attached microsphere to acting forces. Variations in the DNA length (e.g. caused by DNA hairpin unwinding of a helicase) directly changes the vertical position z of the microsphere. Additionally the fluctuations of the microsphere in

the horizontal x and y direction carry information about the applied force (higher forces decrease the fluctuations and vice versa), because the force determines the trap stiffness of the system (usually around 10^{-6} pNnm^{-1}).

Thus the position of the microsphere in all three dimensions (x,y,z) of the microsphere needs to be determined with high accuracy to guarantee high spatial- and force-resolution. The tracking procedure is described in the following section.

2.2.1 Tracking the vertical and horizontal position of a microsphere

As mentioned earlier, the illumination of the microsphere is realized with a distant LED. The focussing lens is located 150 mm above the flow cell to guarantee an approximatelly parallel illumination. Scattered light from the microsphere interferes with unscattered light. This creates a defined diffraction pattern of symmetric ring images of the microspheres (Fig. 2.3a). The high numerical aperture objective is required to image many diffraction rings onto the CMOS camera. The profile of the diffraction ring pattern is used to track the position of the microsphere in all three dimensions. Thus, several well defined diffraction rings increase the stability of the tracking. Therefore, the stage is positioned such that the focus of the objective is above the microsphere (overfocus) (Fig. 2.3a).

The x and y tracking is based on an algorithm previously described [47, 65]. Briefly, the image on the camera sensor is cropped to a region of interest (ROI) around the microsphere before the measurement. Figure 2.3b shows a part of the ROI (the center is indicated). The sketch shows the procedure for the position determined in the x direction. Firstly an intensity profile along the center x axis (the axis through the center of the ROI) is recorded. The intensity is an average of the 10 pixels to the left and 10 pixels to the right of the center x axis. A mirror image of this profile is produced by flipping the image along the center y axis (Fig. 2.3b). These two profiles are convoluted by a cross-correlation algorithm (this is possible due to the symmetry of the microsphere). The maximum of the resulting cross-correlation corresponds to twice the distance between the microsphere center and the center y axis. This procedure is done for x and y separately and results in the horizontal position determination with a nanometer tracking accuracy. Before the next image is recorded the ROI center is reset to the just determined center of the microsphere (only with pixel resolution).

The tracking in the z direction relies on the proportional dependence of the radii of the diffraction rings on the focus position. An increasing distance between the focus and the microsphere results in larger radii of the diffraction rings (Fig. 2.3d). To determine the z position, a set of reference images of the diffraction ring pattern at defined focal positions has to be taken. In order to obtain this so called look-up table (LUT) the flow cell mounted on the piezo stage is moved vertically in discrete steps of 150 nm. Every 150 nm the diffraction ring pattern is recorded. For each aquired image the tracking software calculates a radial intensity profile. Hence, for every pixel the intensity and distance R to the microsphere center needs to be determined (Fig. 2.3c). For higher accuracy the intensity of each pixel is devided and assigned partially to $\bar{R}_{\mathrm{i}}$ and $\bar{R}_{\mathrm{i+1}}$. Then number of pixels with distance $\bar{R}$ ($\bar{R}$ is a multiple integer of

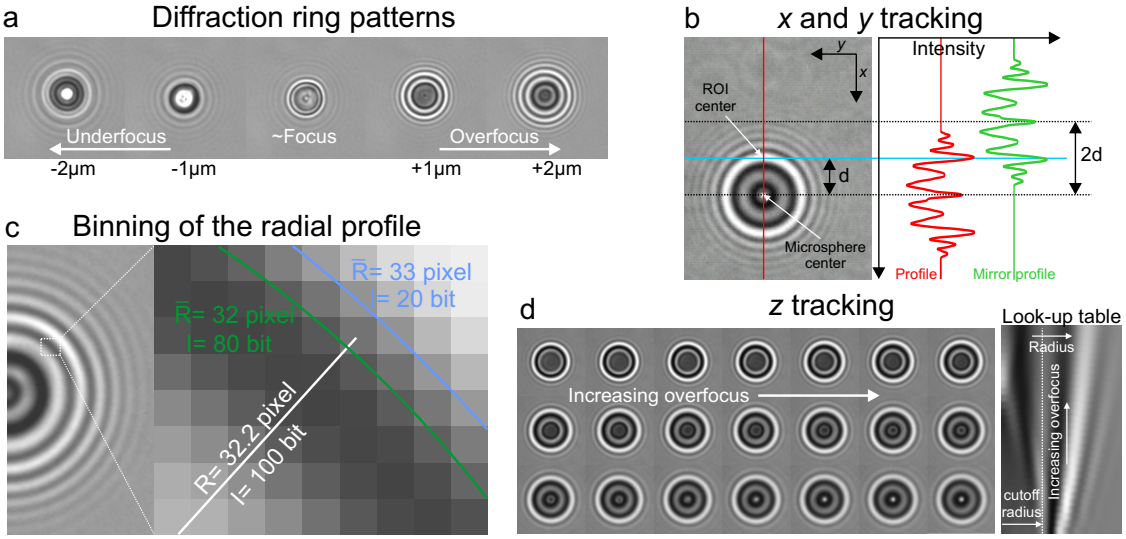

Figure 2.3 Tracking of the microsphere in x, y and z. (**a**) Unfocussed images of the microsphere produce a diffraction ring pattern. The numbers indicate the distance between focus and microsphere center. The well defined rings in overfocus are used for the tracking. (**b**) *left*: The image sketches the method to determine the coordinates of the horizontal position (here the x position). The image shows a part of the ROI (its center and the x and y axis are indicated), with a microsphere (center is indicated). The intensities of 10 pixels to the left and right of the red line are averaged to obtain the intensity profile. *right*: The intensity profile (red line) of the image is mirrored across the y axis (blue line) and results in the mirrored intensity profile (green line). The distance $2d$ between both profiles is found by cross-correlation. The distance d correspond to the new x coordinate of the microsphere. (**c**) Right image is a magnification of the indicated area on the left image. The radial intensity profile is obtained by calculating the distance R of each pixel to the microsphere center. If R is not an integer number of pixels, the intensity of this pixel is devided into a bin of $\bar{R}_\mathrm{i}$ and $\bar{R}_{\mathrm{i}+1}$ (see text). (**d**) The rows show increasingly overfocussed microsphere images with a step size of 150 nm. Only rings larger than the cutoff radius are used for the radial profile. The right image shows a stack of radial profiles, obtained from the method shown in c.

pixels) are grouped. This binning can cause artifacts and will be later discussed in detail. Finally, for every distance $\bar{R}$ the intensities are summed up to result in the radial profile. The first 25 pixels of the profile are neglected, because the the radii of the diffraction pattern in this area do not depend proportionally on the focus position (see cutoff radius in Figure 2.3d).

During an experiment the radial profile of the microsphere obtained during tracking is always compared to each of the radial profiles in the LUT by subtracting each pixel. The absolute values of these differences are summed up. This sum is a measure for the difference between measured radial profile and a profile of the LUT. Around the least deviating profile of the LUT ($\pm$ six profiles) a weighted fit with a quadratic function is performed. The minimum of this quadratic function determines the z position with sub-nanometer accuracy.

The general tracking procedure is to aquire an image of the microsphere, calculate

the x and y coordinates of the center position and lastly to determine its z coordinate. This is usually done simultaneously for two microspheres, where one is tethered to the DNA and another is fixed to the substrate surface. During the tracking thermal drift causes all components of tthe setup to expand and/ shrink. This produces a shift of the microsphere image. To compensate for drift-induced positional movements, a second fixed microsphere (reference microsphere) serves as a benchmark.

In the following sources of noise caused by the tracking are discussed. Beside the thermal noise another source is the electronical shot noise in the pixels of the CMOS sensor in the camera. To lower this noise the signal (microsphere image) is distributed over a large area of pixels in order to gain a higher averaging of the noise. This can be achieved by magnifying the microsphere image. Another source of noise are binning artifacts caused by the z tracking (Fig. 2.3c). The image magnification will also reduce these binning artifacts, because the intensity difference between adjancent pixels is reduced. The magnification is limited by the sensor size (the images of both microspheres have to fit onto the sensor) and the number of photons (a higher magnification reduces the imaged intensity of the light source). Additionally the size of the ROI limits the aquisition rate of the camera (e.g. 500 Hz for 1280x1024 pixels - the full sensor, $\approx$ 4.5 kHz for two ROIs with 160x160, 100 kHz for one pixel). Therefore a good compromise between magnification, ROI size and light intensity has to be found. In the setup described here a magnification was used that resulted in a resolution of 62 nm/pixel. This was achieved by using a 400 mm tube lens instead of the standard 160 mm one recommended for the used objective. The resulting magnification reduces the tracking noise and produces a sufficient photon density. It also allows to choose a field of view including several microspheres in order to track

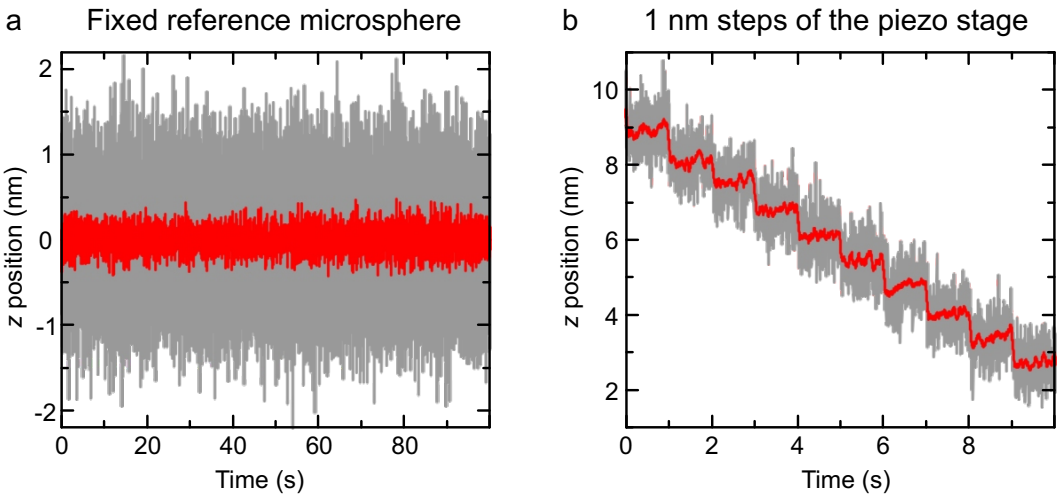

Figure 2.4 Tracking and detection accuracy of the microspheres. (**a**) 300 Hz tracking data in z direction of a non-magnetic microsphere (3.2 μm diameter) fixed to the surface. The noise (gray) sets the maximal tracking accuracy (standard deviation 0.54 nm). The red line presents 15 Hz filtered data. To reduce the long term drift, the data was subtracted from a average of the data (adjacent average, 0.5 Hz). (**b**) 1 nm steps induced by moving the piezo stage every 1 s can clearly be distinguished.

multiple molecules in parallel.

The setup design and the tracking algorithm allow to achieve sub-nanometer tracking resolution (Fig. 2.4a) in z direction. Figure 2.4 shows the achieved tracking accuary in z direction on a fixed reference microsphere (3.2 μm diameter, tosly activated). The temporal resolution of the setup is limited by the light intensity of the LED. In this thesis tracking was performed in ROIs of 160x160 pixels at 300 Hz if not indicated otherwise.

Recent reviews assign magnetic tweezers a temporal resolution of 50 ms [8] and a spatial resolution of 10 nm in the z direction [66]. The instrumental design and the tracking algorithm of the setup used in this thesis improves the temporal resolution as well as the spatial resolution in the z direction by a factor of 10 compared to specifications given in recent reviews [8].

2.3 Measuring forces with Magnetic tweezers

2.3.1 From Brownian motion to forces - theory

The physical system of a tethered particle which is trapped by force, damped in a viscous medium and constantly pushed out of equilibrium by impacting molecules can be treated as an inverted pendulum (see Figure 2.1b). The length of the pendulum is the mean length of the tether $L = \langle z \rangle$. For small displacements the applied force F_{mag} restores the deflected microsphere with a lateral stiffness k_{y}:

$$F_{\mathrm{mag}} = k_{\mathrm{y}} \cdot L. \tag{2.1}$$

Here the y direction is defined along the magnetic field lines (see Figure 2.1a for coordinates). In the y direction the movement of the microsphere is restricted, because the microsphere is pinned in the field, i.e. no rotation around the x axis is possible (explained in more detail in Figure 2.6 at the end of this section). Therefore, the pendulum length corresponds to the DNA length. In the x direction the rotational movement of the microsphere around the y axis needs to be considered seperately. This will be discussed in section 2.3.5.

The trap stiffness k_{y} depends on the transverse fluctuations (mean square displacements) given by the equipartition theorem [56]:

$$k_{\mathrm{y}} \cdot \left\langle \delta y^2 \right\rangle = k_{\mathrm{B}} T, \tag{2.2}$$

where k_{B} is the Boltzmann constant and T the temperature. Therefore by recording the microspheres fluctuations in the y direction and the tether´s mean length $\langle z \rangle$ on can determine the force (insert eq. 2.2 into eq. 2.1):

$$F_{\mathrm{mag}} = k_{\mathrm{B}} T \cdot \langle z \rangle / \left\langle \delta y^2 \right\rangle. \tag{2.3}$$

The mean-square displacement $\langle \delta y^2 \rangle$ arises from a random force (Brownian motion). The equation of motion for a tethered point mass, which is exposed to force and damped in a viscous medium corresponds to (Langevin-equation [67]):

$$m\ddot{y}(t) = -\gamma \dot{y}(t) - k_{\mathrm{y}} y(t) + f_{\mathrm{therm}}(t). \tag{2.4}$$

The inertial forces acting on a microsphere of mass m are caused by random thermal forces $f_{\mathrm{therm}}(t)$. They are acting against the friction with a drag coefficient γ and the restoring magnetic force, which was described as a harmonic potential with the trap stiffness $k_{\mathrm{y}}(t)$.

The random nature of the thermal forces can only be described in statistical manner. The properties of the random force f_{therm} are [9]:

$$\langle f_{\mathrm{therm}}(t)\rangle = 0 \quad \text{and} \quad \langle f_{\mathrm{therm}}(t) f_{\mathrm{therm}}(\bar{t})\rangle = 2k_{\mathrm{B}}T\gamma \cdot \delta(t-\bar{t}) \tag{2.5}$$

where δ is the Dirac-delta function. The first equation guarantees that the motion is random, because the force disappears on average. The second equation shows that the random forces are uncorrelated in time. The Dirac-delta function for the auto-correlation of f_{therm} at two different times is exact, because the time scale of the microsphere motion is much larger than the collision time of the water molecules with the microsphere. To solve the equation of motion (equation 2.4) the Einstein–Ornstein–Uhlenbeck theory [67] is applied. This theory requires the determination of the fourier transformed equation of motion [68]:

$$Y(\omega) = \frac{F_{\mathrm{therm}}(\omega)}{-m\omega^2 - \gamma i\omega + k_{\mathrm{y}}} = \frac{\sqrt{2k_{\mathrm{B}}T\gamma}}{-m\omega^2 - \gamma i\omega + k_{\mathrm{y}}}, \tag{2.6}$$

where $Y(\omega)$ and $F_{\mathrm{therm}}(\omega)$ are the Fourier transforms of $y(t)$ and $f_{\mathrm{therm}}(t)$, respectively. Equation 2.6 describes an oscillator, whose solution depends on the damping [9]. If $\gamma^2 < 4mk_{\mathrm{y}}$, the system is underdamped, while for $\gamma^2 > 4mk_{\mathrm{y}}$ it is overdamped. The actual values for a typical tweezers experiment ($\gamma = 10^{-9}$ Ns/m, $m = 10^{-15}$ kg, $k = 10^{-9}$ N/m) reveal that the system is highly overdamped [47, 56]. The characteristic time constant (τ) for the inertial forces m/γ is in the range of picoseconds, while the time constant for the damping γ/k_{y} is in the range of nanoseconds. Therefore it is reasonable to neglect the term for inertial forces $-m\omega^2$ in equation 2.6 [9].

The square of the absolute value of $Y(\omega)$ yields the power spectrum of the microsphere motion:

$$|Y(\omega)|^2 = \frac{4k_{\mathrm{B}}T\gamma}{k_{\mathrm{y}}^2} \frac{1}{1 + \left(\frac{w}{w_{\mathrm{c}}}\right)^2}, \tag{2.7}$$

with the characteristic cutoff frequency (inverse of the characteristic time constant τ):

$$w_{\mathrm{c}} = k_{\mathrm{y}}/\gamma = 2\pi f_{\mathrm{c}} = 2\pi/\tau. \tag{2.8}$$

Frequencies larger than the cutoff frequency are dominated by the brownian motion ($1/f^2$-noise). For $f < f_{\mathrm{c}}$ the damping of the system results in constant amplitudes. This so called Lorenzian curve describes the theoretically expected movement of the microsphere in the frequency space.

Parseval's theorem connects the mean-squared displacements $\langle \delta y^2 \rangle$ in real space with its power spectrum $|Y(f)|^2$ [68]:

$$\left\langle \delta y^2 \right\rangle = \int_{-\infty}^{\infty} |y(t)|^2 \, d\omega = \int_{-\infty}^{\infty} |Y(f)|^2 \, df = \frac{1}{2\pi} \int_{-\infty}^{\infty} |Y(\omega)|^2 \, d\omega \tag{2.9}$$

with the frequency f and the angular frequency $\omega = 2\pi f$. The integral of the power spectrum is the power spectral density (PSD) of the fluctuations. Using Parseval's theorem (equation 2.9) and considering the one-sided PSD (factor 2) and the symmetry of the power spectrum (another factor 2) the mean-square displacements can be calculated [9]:

$$\left\langle \delta y^2 \right\rangle = \frac{2}{\pi} \int_0^\infty |Y(\omega)|^2 \, d\omega = \frac{2k_\mathrm{B}T}{\pi w_\mathrm{c} k_\mathrm{y}} \int_0^\infty \frac{1}{1 + \left(\frac{w}{w_\mathrm{c}}\right)^2} d\omega. \tag{2.10}$$

The solution for the integral in 2.10 is an arctan function:

$$\left[\omega_\mathrm{c} \cdot \arctan\left(\frac{\omega}{\omega_\mathrm{c}}\right) \right]_0^\infty = \frac{\pi}{2}\omega_\mathrm{c}. \tag{2.11}$$

Applying 2.11 to 2.10 yields the same result as equation 2.2, as required from equipartition theorem:

$$\left\langle \delta y^2 \right\rangle = \frac{k_\mathrm{B}T}{k_\mathrm{y}}. \tag{2.12}$$

Integrating equation 2.10 from 0 to x creates a function A:

$$A(f) = \frac{2\left\langle \delta y^2 \right\rangle}{\pi} \cdot \arctan\left(\frac{1}{2\pi f_\mathrm{c}} \cdot f\right). \tag{2.13}$$

This function is fitted to the PSD of the recorded microsphere fluctuations, to obtain the cutoff frequency f_c and $\langle \delta y^2 \rangle$. However, the recorded fluctuations depend on the camera aquisition and need to be corrected before fitting equation 2.13.

The difference between the recorded fluctuations and the theory (equation 2.10) to describe the brownian motion can be contributed primarily to the camera, which acts as a filter of the real signal. Two effects occur when recording the motion of the microsphere with a camera. Firstly, the finite aquisition time of the camera causes an averaging of the real signal (windowing effect). The averaging reduces the amplitude of the signal (Fig. 2.5a). This can mathematically be described as a convolution of the signal with a box function. A convolution in the real space corresponds to a point wise multiplication in the frequency space. Thus, the windowing effect is incorporated in the theory by multiplying equation 2.7 with the fourier transformed box function, which corresponds to a sinc^2 function [69]:

$$|Y(f)|^2 = \frac{k_\mathrm{B}T\gamma}{\pi^2 k_\mathrm{y}^2} \frac{1}{1 + \left(\frac{f}{f_\mathrm{c}}\right)^2} \cdot \frac{\sin^2(\pi f / f_\mathrm{cam})}{(\pi f / f_\mathrm{cam})^2}, \tag{2.14}$$

with f_cam being the camera acquisition rate.

Additionally the finite acquisition frequency produces the so called aliasing effect (seen in the PSD). The Nyquist-Shannon sampling theorem explains that a signal needs to be sampled with at least twice its frequency ($f_\mathrm{cam} \geq 2f_\mathrm{signal}$) to be able to reconstruct it (Fig. 2.5b). This critical frequency is called Nyquist frequency (f_Ny).

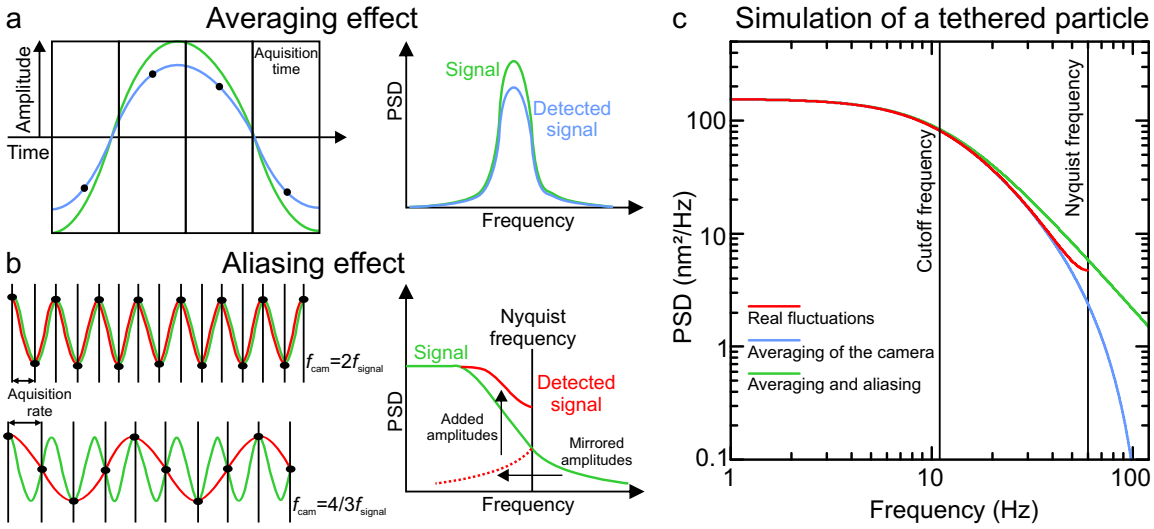

Figure 2.5 Effects of signal sampling with the camera. (**a**) The sketch is adapted from [69]. *left*: The signal (green solid line) is averaged (black dots) due to the finite aquisition time symbolized by the boxes. The signal will be detected with reduced amplitude (blue solid line). *right*: Thus, the amplitudes in the PSD are reduced. (**b**) The sketch is adapted from [69]. *left, top*: Minimal sampling frequency to avoid aliasing ($f_{\mathrm{cam}} = 2f_{\mathrm{signal}}$). *left, bottom*: f_{signal} is the same as above, but sampled with only 4/3 of the signal frequency. The red solid line is the detected signal. *right*: In the PSD amplitudes of frequencies higher than the Nyquist frequency (vertical black line) will be mirrored back at the Nyquist frequency (as indicated by the horizontal black arrow). There, these amplitudes (red dashed line) add up to the existing ones (as indicated by the vertical black arrow). (**c**) Effect of averaging only (blue line) and averaging plus aliasing (red line) on a simulated PSD signal (green line) of a 10 μm dsDNA molecule tethered to a microsphere of 1 μm radius at 5 pN applied force, recorded with 120 Hz. The cutoff frequency of this system is 11.8 Hz.

If $f_{\mathrm{cam}} < f_{\mathrm{Ny}}$ high frequencies appeaer as low frequencies (aliasing effect). In the frequency space the amplitudes of these higher frequencies are mirrored at f_{Ny} and contribute to the amplitudes of lower frequencies [69]. Since the signal of a tethered microsphere always contains frequencies larger than half of the camera aquisition frequency aliasing is inherent. However, this effect can be incorporated in the theory by numerically flipping the frequencies larger than f_{Ny}.

The consequenses of both effects are presented in Figure 2.5c. Windowing causes a reduction of the PSD amplitude resulting in an underestimation of the mean-square displacement, which corresponds to the area under the PSD curve (see equation 2.9). Aliasing shifts amplitudes to wrong frequencies and causes a shift of the cutoff frequency (f_{c}), which is used to calculate properties of the system (see equation 2.8). Additionally, aliasing causes the PSD to end at the Nyquist frequency. Therefore, acquisition frequency should be be chosen so that the Nyquist frequency is well above the cutoff frequency of the experimental data to be able to fit equation 2.13.

By considering both effects the real mean-squared displacement and cutoff frequency can be reconstructed from the observed fluctuations. The mean-squared displacement is used to determine the force (equation 2.3), while the cutoff frequency is used

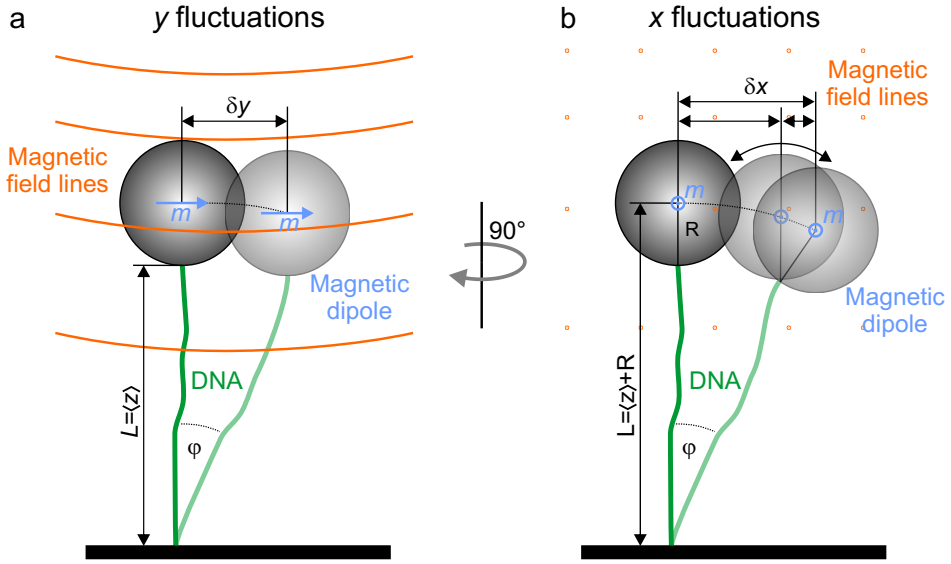

Figure 2.6 Differences in force determination using x and y fluctuations. (**a**) The magnetic field lines (orange) orient the dipole (blue) along the field. The fluctuations of the microsphere $\langle \delta y \rangle$ are only translational. The pendulum length is the DNA length. (**b**) The magnetic field lines (orange dots) are perpendicular to the image plane (b is rotated 90° against a). The fluctuations of the microsphere $\langle \delta x \rangle$ are a combination of translational and rotational movement. The pendulum length is the DNA length and the microsphere radius.

to calculate the properties of the system (drag coefficient and microsphere radius, presented in section 2.3.5).

Due to the orientation of the magnetic field and the magnetic anisotropy of the microspheres rotations around the x-axis are inhibited (Figure 2.6a). Therefore, the pendulum length is equal to the DNA length and does not require determination of the radius of the microsphere. As a control one can additionally determine the forces from the fluctuations, perpendicular to the magnetic field lines, (x direction) (instead of the y fluctuations). In the x direction the rotational movement of the microsphere is not constrained by the field, so that the bead can rotate around the y-axis (Figure 2.6b). To calculate the force from the fluctuations in the x direction (F_x) one can use the derived force equation (2.3). One needs to consider that the pendulum is now extended by the radius R of the microsphere so that the force calculated from $\langle \delta x^2 \rangle$ is:

$$F_\mathrm{x} = \frac{k_\mathrm{B}T \cdot (\langle z \rangle + R)}{\langle \delta x^2 \rangle}. \tag{2.15}$$

The determination of the radius will be shown in section 2.3.5.

2.3.2 From Brownian motion to forces - experiment

The need for the force calibration of every DNA-microsphere system arises from large variations of the saturation volume magnetization M_s and the radius R among microspheres of the same type. These variances cause large differences in the applied

Name	M_s (kA/m)	R (μm)	Company
M 280	10	1.4	Invitrogen, San Diego, CA, USA
MyOne	40	0.505	
MagSense	130	0.6	MagSense Life Sciences, W. Lafayette, IN, USA

Table 2.1 The microspheres used in this thesis [70, 71].

force resulting from a certain external magnetic field gradient. Throughout this thesis the microspheres shown in table 2.1 were used.

For example, the volume magnetization of M280 microspheres shows 72% standard deviation [71]. The radius of MagSense microspheres was found to show appoximately 20% standard deviation. A smaller radius of a microsphere was found to increase the spatial resolution in the z direction (explained in detail in section 2.4.1): A smaller radius increases the resolution. On the other hand a smaller volume corresponds to less magnetic particles in the microsphere and hence a smaller applicable force. Therefore the requirements of each experiment define the used type of microspheres.

A protocol how to set up a force calibration experiment (i.e. how to connect the DNA with the microsphere and the flow cell surface) is explained in the appendix 6.2.3. After choosing an appropriate DNA microsphere system (see 6.2.3), the LUTs for the DNA microsphere and the reference microsphere are recorded. In order to minimize the fluctuations of the microsphere during recording the LUT the DNA is stretched with maximum force (corresponds to the shortest distance between magnets and microsphere) and every profile of the LUT is additionally averaged over several images to reduce the occuring fluctuations.

Then the microsphere is tracked at various magnet positions. The time of a measurement T at each magnet position depends on the desired accuracy of the determination of the mean-square displacements. The relative statistical error of the mean-square displacements decreases with increasing measurement time. The statistical error can be calculated with :

$$\epsilon = 1/\sqrt{N} = 1/\sqrt{T/\tau} \tag{2.16}$$

where τ is the characteristic time constant of the microsphere fluctuations, which is the inverse of the cutoff frequency (see equation 2.8). Thus the desired measurement time can be calculated according to [47]:

$$T = \frac{1}{f_c \epsilon^2} = \frac{2\pi\gamma}{k_y \epsilon^2} = \frac{2\pi \cdot 6\pi\eta R \cdot L_0}{F_{mag}\epsilon^2}, \tag{2.17}$$

with the cutoff frequency f_c (introduced in equation 2.7) and assuming a stokes drag with a drag coefficient of $\gamma = 6\pi\eta R$. In the range of 1 to 50 pN stretching force the DNA will approximatelly keep its contour length L_0 (enthalpic regime). For example, a 10 μm long DNA molecule, attached to a microsphere of 500 nm radius, in water ($\eta = 0.001$) at a force of 10 pN and a desired error of $\epsilon = 10\%$, requires a measurement time of about $T = 1$ min. In the force range below 1 pN the DNA will adapt the form of an entropic coil (entropic regime). The stiffness of the DNA in this regime can be

approximated to be constant [58] with $F/L = 3k_BT/2pL_0$ (p is the DNA persistence length). Thus, with the same parameters as used in the example above below 1 pN an accuracy of 90% requires a measurement time of approximately nine minutes.

At each magnet position, the mean-square displacement is determined as explained in the last section. To calculate the force, additionally the DNA length needs to be determined. Since the spatial position is always determined relative to the reference microsphere, the absolute length of the DNA molecule can only be calculated knowing the position of the flow cell surface. This is found by lowering the force (moving the magnets more than 6 mm away from the sample). At this distance the microsphere is not subjected to any significant magnetic field. Next, the z position is recorded for several seconds. The lowest z position defines the location of the flow cell surface. This offset allows to determine the absolute mean DNA length.

In Figure 2.7 a typical DNA stretching experiment of an approximately 11 kbp dsDNA molecule attached to a MagSense microsphere is shown. Some representative time traces in the y direction showing the movement of the microsphere are presented in Figure 2.7a. The larger the applied force is, the higher is the trap stiffness and the smaller are the fluctuations, which are significantly above the detection noise (compare to Fig. 2.4). The corresponding PSDs (averaged) in Figure 2.7b are shown with the calculated power spectrum using equation 2.7 with the fitvalues for the cutoff frequency determined using equation 2.13. The low frequency limit is determined by the measurement time (not shown in the plot), the high frequency limit is the Nyquist frequency. The expected shape of a Lorenzian curve can be seen with a plateau for frequencies below the cutoff frequency and $1/f^2$-behaviour for frequencies above. Additionally the aliasing effect due to the camera acquisition can be observed as a slight increase of the $1/f^2$ decay close to the Nyquist frequency (where the PSD ends).

The plots of force versus DNA extension (force-extension) can be seen in Figure 2.7c. Beside the forces determined from the y fluctuations also force values from the x fluctuations are shown. These forces coincide within error.

To verify the correct determination of the forces, the force-extension curves are fitted with the extensible worm-like chain model [72] comprising an improved formula of the inextensible worm-like-chain model (WLC) [73]:

$$F(z_{\mathrm{entr}}) = \frac{k_BT}{p}\left[\frac{1}{4\left(1 - z_{\mathrm{entr}}/L\right)^2} - \frac{1}{4} + \left(\frac{z_{\mathrm{entr}}}{L}\right) + \sum_{i=2}^{7} a_i \left(\frac{z_{\mathrm{entr}}}{L}\right)^i\right] \tag{2.18}$$

where the entropic part of the DNA extension z_{entr} is given by:

$$z_{\mathrm{entr}} = z_{\mathrm{DNA}} - \frac{L_0 F}{S}. \tag{2.19}$$

L_0 denotes the DNA contour length in the absence of force, z_{DNA} the DNA end-to-end distance at a given force F. S corresponds to the DNA stretching modulus for which 530 pN was taken throughout the analysis, p denotes the DNA persistence length and k_BT is the thermal energy at room temperature. The used coefficients a_i are:

$a_2 = -0.5164228$; $a_3 = -2.737418$; $a_4 = 16.07497$; $a_5 = -38.87607$; $a_6 = 39.49944$; $a_7 = -14.17718$ [73].

The WLC model including the correction terms (equation 2.18) cannot be solved analytically for the force. Therefore, equation 2.18 is first solved without the correction terms, which is a 3rd order polynom. The solution is found using Cardano's method to solve a cubic equation [74]. The solution is:

$$F = \sqrt[3]{\frac{-q}{2} + \frac{1}{18}\sqrt{81q^2 + 12p^3}} + \sqrt[3]{\frac{-q}{2} - \frac{1}{18}\sqrt{81q^2 + 12p^3}}. \tag{2.20}$$

The coefficients depend on the persistence length, the DNA extension, the contour length and the stretching modulus and are given in the appendix 6.4.1. The data

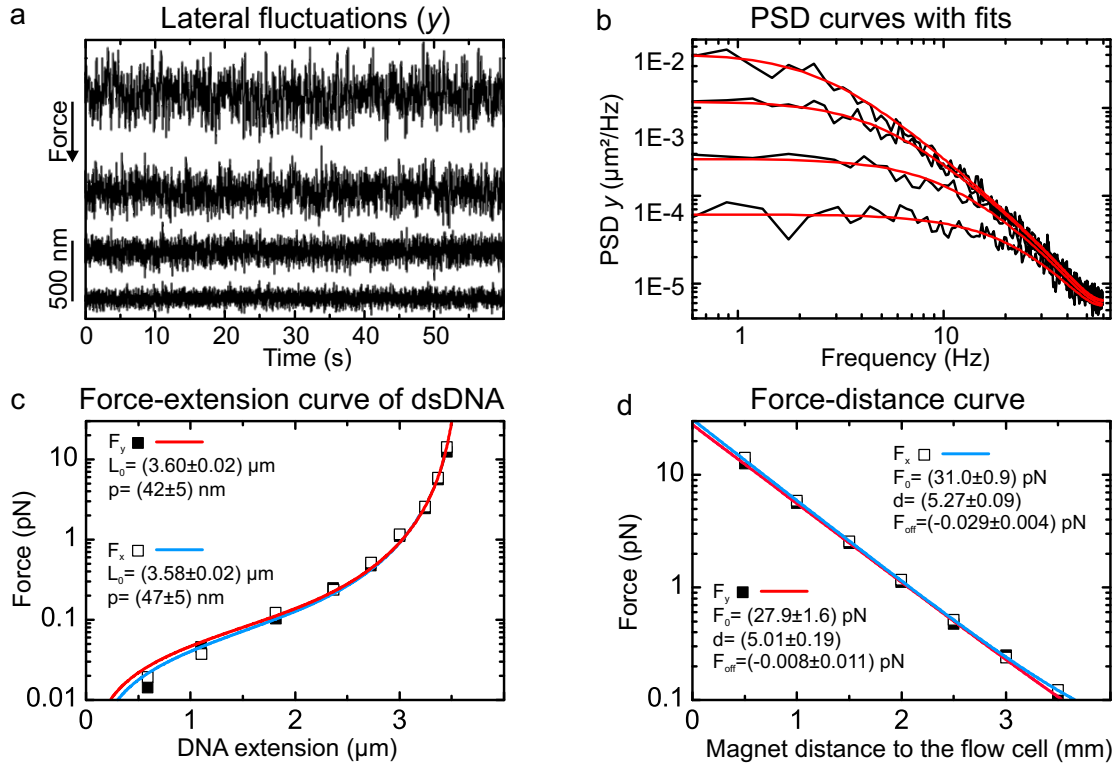

Figure 2.7 Force measurements on an 11 kbp dsDNA molecule attached to a MagSense microsphere, tracked at 120 Hz in phosphate buffer (see appendix 6.2.2. (**a**) Tracking data in y direction for four different forces (from top to bottom: 7.4, 3.5, 1.7 and 0.8 pN). (**b**) Averaged PSD (black lines) of the fluctuations shown in a obtained by dividing the trace into 40 equally long pieces and averaging the results. Red lines are the calculated PDSs using the cutoff frequency determined by fitting equation 2.13 to the PSDs calculated and corrected from the measured fluctuations using equation 2.14. (**c**) Force-extension curve. Filled squares show forces determined using y fluctuations with the corresponding WLC fit (red line). Open squares and the blue lines represent forces calculated by integrating the PSDs using x fluctuations. The fit parameters (persistence length and contour length) are indicated. (**d**) Force versus distance of the magnets to the flow cell with the fit of equation 2.21. The fit parameters are indicated. Colors are as in c.

are fitted with Equation 2.20 to obtain the force and calculate the DNA extension including the actual stretching. Finally the full WLC (equation 2.18) is fitted using the calculated extension. Additionally the fits are weighted with the force since larger forces increase the trap stiffness and result in a higher force resolution [66]. The force-extension curves using x and y fluctuations are well fitted by equation 2.18 and display the expected contour length for an ≈ 11 kbp dsDNA molecule (contour length $L_0 = 0.34$ nm/bp $\cdot$ 10600 bp $= 3.6$ μm) and persistence length p for dsDNA ($p = \approx 50$ nm [73]).

Another consistency check for correctly determined forces is the force-magnet position (force-distance), which is the distance of the magnets to the flow cell (the top cover slide of the flow cell) (Fig. 2.7d). The force-distance curve is expected to display an exponential behavior and will be explained in more detail in 2.3.3. The data is fitted with:

$$F(h) = F_0 \cdot \exp(-h \cdot \ln(d)) - F_{\text{off}} = F_0 \cdot d^{-h} - F_{\text{off}} \tag{2.21}$$

where h is the distance of the magnet to the flow cell and is d the factor of force decrease per change of the distance h. F_{off} is a force offset that accounts for volume exclusion effects which appear at low DNA-extensions [75], because the surface acts as a boundary for the free movement of the microsphere. F_0 is the maximum force that can be achieved in this configuration (when the magnets touch the flow cell). The factor d is determined by the properties of the permanent magnets and the used microsphere and was found to be well reproducable. Additionally, equation 2.21 is used to calibrate the system, i.e. to determine the corresponding magnet positions to apply a certian force.

In conclusion, the forces can be well determined for a long dsDNA molecule attached to a MagSense microsphere. However, the large variations of the maximum force among different microspheres requires a force calibration for each DNA-microsphere system. The acting forces can also be predicted from the magnetic properties of the microsphere and the permanent magnets. This is shown in the next section.

2.3.3 Determining the magnetic field and predicting the forces

As mentioned above the microspheres consist of superparamagnetic nanoparticles embedded in a polymer matrix, i.e. small dipoles which show a high magnetic moment that freely rotates at energies of $k_{\text{B}}T$ without any externally applied field [76]. The force $\vec{F}_{\text{i}}$ acting on a superparamagnetic nanoparticle i with magnetic moment $\vec{m}_{\text{i}}$ in a magnetic field $\vec{B}$ can be calculated acording to:

$$\vec{F}_{\text{i}} = (\vec{m}_{\text{i}} \cdot \nabla)\, \vec{B}, \tag{2.22}$$

in the absence of currents and time-dependend fields [76]. Note that in this thesis the magnetic flux density is refered to as magnetic field. The force acting on the nanoparticle varies in time due to thermal rotational fluctuations of the dipole moment. If the dipole is free to rotate within the nanoparticle, the following expression for the average force acting on the dipole along the magnetic field gradient can be derived:

$$\left\langle \vec{F}_{\text{i}} \right\rangle = m_{\text{i}} \left(\overline{\cos \vartheta} \right) \nabla |\vec{B}|, \tag{2.23}$$

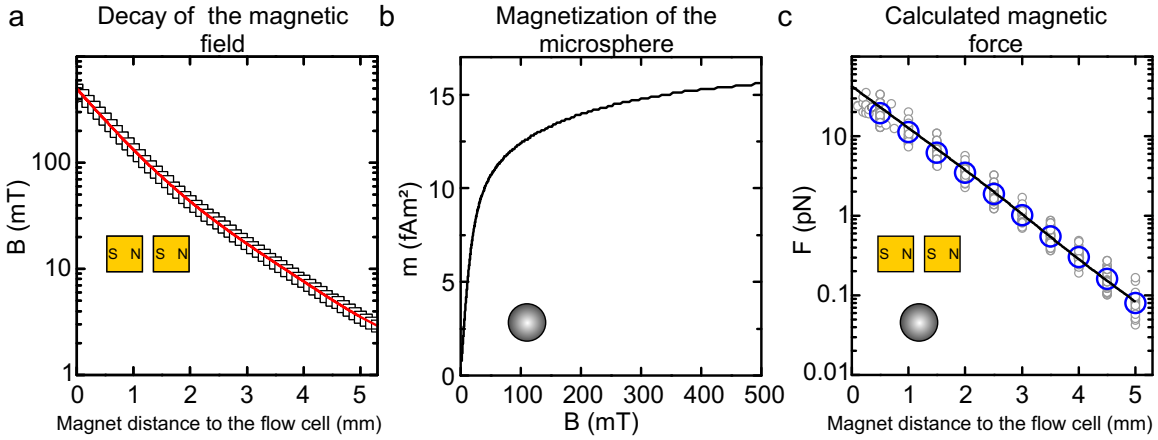

Figure 2.8 Magnetic properties of M 280 microspheres and NeFeB magnets. (**a**) The strength of the magnetic field B (black squares) as a function of distance from the flow cell. B was measured using a Hall probe and approximated with an analytical function (red curve). (**b**) Field-dependent magnetization of a single M 280 microsphere as inferred from bulk magnetization curves [70]. (**c**) The forces acting on a single M 280 microsphere as a function of distance of the magnets are represented by a solid black line. Measured forces of individual microspheres calculated from y fluctuations are shown as gray cicles. Average forces are shown as blue circles.

with ϑ being the angle between dipole moment and magnetic field. Using Boltzmann statistics an analytical expression for the average angle can be derived [76] and the upper equations turns into:

$$\left\langle \vec{F}_{\mathrm{i}} \right\rangle = m_{\mathrm{i}} L \left(\frac{m_{\mathrm{i}} B}{k_{\mathrm{B}} T} \right) \nabla |\vec{B}|, \tag{2.24}$$

in which L is the Langevin function, k_{B} the Boltzmann constant and T the temperature. For the whole superparamagnetic microsphere comprising many small particles the magnetic force is obtained from the sum of the individual forces:

$$\left\langle \vec{F}_{\mathrm{mag}} \right\rangle = \left(\sum_{\mathrm{i}} m_{\mathrm{i}} L \left(\frac{m_{\mathrm{i}} B}{k_{\mathrm{B}} T} \right) \right) \nabla |\vec{B}| = m(B) \nabla |\vec{B}|. \tag{2.25}$$

Thus by knowing the field-dependent apparent magnetic moment $m(B)$ of the microsphere, one can calculate the force acting on the microsphere from the gradient of the magnetic field. The magnetic field $\vec{B}$ along the y-direction was measured using a small Hall probe (CY-P3A, Chen Yang Technologies GmbH & Co. KG, Germany) at various distances along the z-direction (Fig. 2.8a).

Figure 2.8b shows the apparent magnetic moment in the microsphere [70]. Both, the magnetic field decay and the magnetization curve were approximated by analytical functions. Using equation 2.25 the magnetic force acting on the microsphere was calculated. The resulting forces decay approximately exponentially with a constant which is characteristic for the used combination of microsphere and permanent magnets, as mentioned in the last section (Equation 2.21). We find a good agreement of the calculated forces with the average measured forces using y fluctuations (Fig. 2.8c).

2.3.4 Force measurements on DNA hairpin constructs

Various DNA hairpin constructs were used in this thesis and will be briefly introduced. These constructs contain hairpins of 2000, 500, 90 and 40 bp, with different attachments to the flow cell surface and to the microsphere (Fig. 2.9a-c).

The preparation of these constructs will be presented in chapter 3, the specific usage will be explained in the chapters 4 and 5. In this section only the distances between flow cell surface and microsphere are of interest (Fig. 2.9). The 2000 bp hairpin (P2000) has only ssDNA spacers (spacers are stretches of ssDNA between the hairpin and the microsphere as well as the flow cell surface). When the hairpin is closed the microsphere is very close to the surface (the distance is shorter than the microsphere´s radius) and when the hairpin is open it is more than twice the microsphere diameter away (Figure 2.9a). The 500 bp hairpin (P500) has a 1000 bp dsDNA handle and an 80 nt ssDNA spacers surrounding the hairpin, is also close to the surface when the hairpin is closed and nearly one microsphere diameter away when it is open (Figure 2.9b). The 40 and 90 bp hairpins exist in two versions each: One version with a 600 bp dsDNA handle (P40 and P90ATmGC, Fig. 2.9c left), the other one with a 3000 bp dsDNA handle (P40long and P90ATmGClong, Fig. 2.9c right). All of the short haipin constructs contain 44 nt ssDNA spacer between the hairpin and the handle as well as 5 nt spacers between the hairpin and the micrsphere. The short versions always have a small distance between the microsphere and the flow cell surface independent of the state of the hairpin (closed or open). The long version have a correspondingly long distance between the microsphere and the flow cell surface.

In general the force measurements are executed as shown in section 2.3.2. Three aspects need to be considered when measuring forces on the DNA hairpin constructs: Firstly, when the hairpin is closed, the short distance between the microsphere and

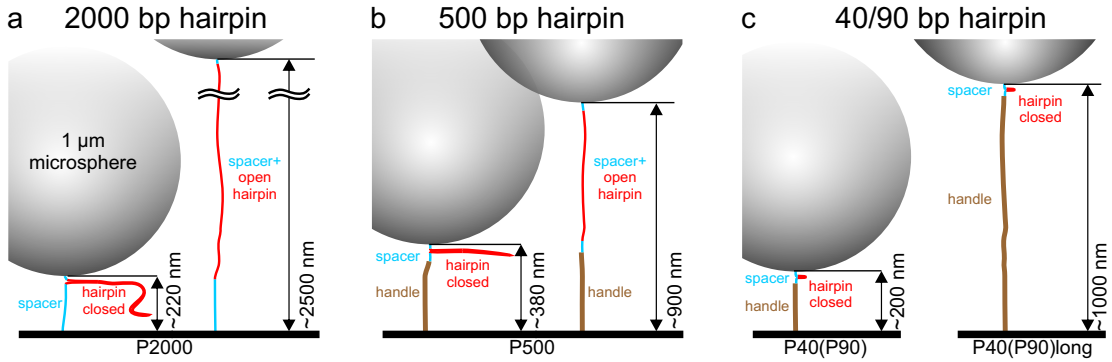

Figure 2.9 Overview of the used DNA hairpin constructs. Blue lines are ssDNA spacers, brown lines are dsDNA handles and red lines represent the hairpin DNA. Distance between microsphere and flow cell surface are drawn to scale. (**a**) Sketch of the 2000 bp DNA hairpin construct in closed (left) and open (right) state. The black line-breaks indicate that the open hairpin is much longer than the image size. (**b**) Sketch of the 500 bp DNA hairpin construct in closed (left) and open (right) state. (**c**) Sketch of the 40 bp and the 90 bp DNA hairpin construct with a short handle (left) and a long handle (right).

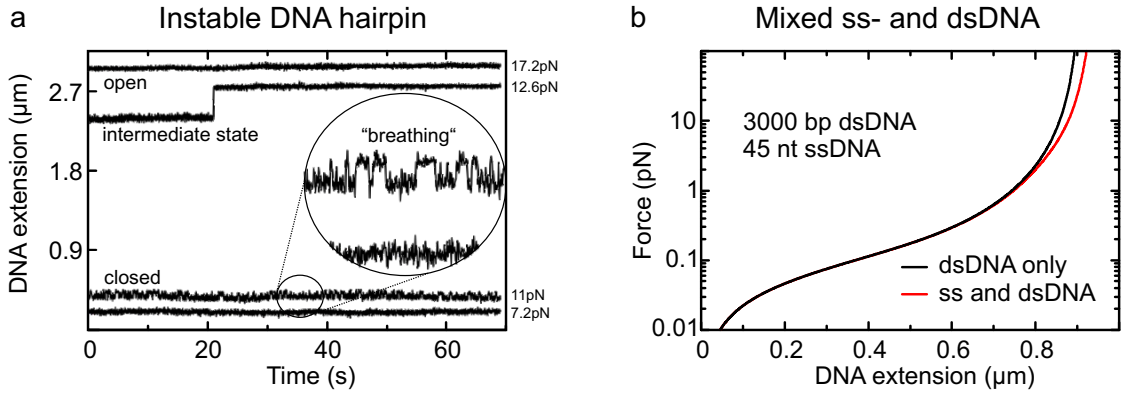

Figure 2.10 Critical properties of DNA hairpin constructs for force measurements. (**a**) Length of the 2000 bp DNA hairpin construct in PBS buffer (see Appendix 6.2.2) at four different forces (indicated next to the graph). The hairpin is closed below 11 pN (lower two traces) and open above 12 pN (upper two traces). The inset indicates a magnification of the lower traces. The jump at 12.6 pN is caused by an intermediate stable state. (**b**) Simulated force-extension curve for pure 3000 bp dsDNA (black line) and mixed 3000 bp dsDNA and 45 nt ssDNA (red line).

the flow cell surface can cause sticking of the microsphere to the surface or volume exclusion effects [75, 77, 78]. For P500 and P2000 this distance is extended by applying forces at which the hairpin is open, because it prolongs the DNA to more than the microsphere´s radius. This distance was found to be mostly sufficient to produce reliable results. For P40 and P90ATmGC the open hairpin does not contribute much to the DNA extension, such that the additional constructs P40long and P90ATmGClong (with more than a microsphere radius distance between the microsphere and the flow cell surface) were prepared for calibration purposes only as explained at the end of this section.

Secondly, at the critical force F_{unzip} the hairpin gets unstable and opens (unzips). The instability of the hairpin at forces close to F_{unzip} induce "breathing" at the junction of the DNA hairpin, i.e. a few base pairs can fluctuate between an open and a closed state. Additionally, the hairpin can have intermediate stable states between completely open and closed (Fig. 2.10a). Both effects over- or underestimates the mean DNA length $\langle z \rangle$ and result in wrong forces according to equation 2.3. Therefore, forces are determined only well below or above F_{unzip}.

Thirdly, verifying the determined force-extension curve with the WLC model is impossible, because the WLC only describes dsDNA [73], while the used DNA hairpin constructs all contain ssDNA. When the hairpin is closed the "spacers" (Fig. 2.9a-c), contribute only a few percent to the DNA extension (except for P2000, which is completely ssDNA). However, the impact of only a few nucleotides of ssDNA causes already deviations from the WLC behaviour at forces larger than a few pN (Fig. 2.10b).

Figure 2.11a shows the force-extenion curve of the 500 bp DNA hairpin construct (P500, Fig. 2.9b). Several forces with open and closed hairpin were recorded. No sticking was observed at the low DNA extension, forces around the unzipping force,

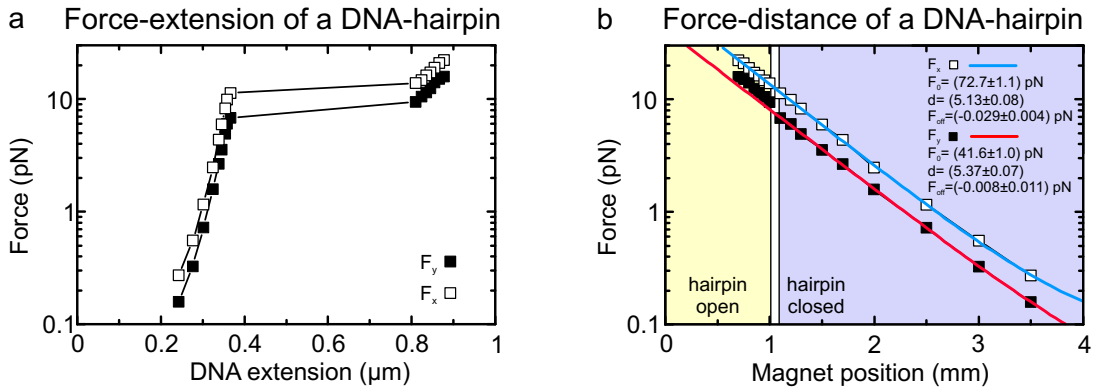

Figure 2.11 Force measurements on a 500 bp DNA hairpin construct attached to a MagSense microsphere, tracked at 300 Hz. (**a**) Force-extension curve. Filled squares show forces determined using y fluctuations, open squares represent forces calculated from the x fluctuations. (**b**) Force-distance curve. The squares show the forces calculated from x and y fluctuations as in (a). The blue line is a fit of equation 2.21 to the forces using x fluctuations, the red line to the forces using y fluctuations. The fit to the forces using y fluctuations includes just the data points when the hairpin is closed (> 1.1 mm magnet position). Fit parameters are indicated.

where the hairpin is instable, were excluded. The curve shows the expected transition from the closed to the open hairpin state, seen as an abrupt jump in the extension (Fig. 2.11a). To verify the results the forces were calculated using x and y fluctuations (F_x, F_y). Interestingly F_x is always significantly higher than F_y, such that the question arises which coordinate provides the correct force. In Figure 2.11b the forces are plotted against the distance of the magnets from the top of the flow cell (force-distance). The decay of F_x exhibts the expected exponential decay, as shown for a long dsDNA construct (compare to Figure 2.7b). In contrast, F_y exhibits an abrupt at the hairpin open-close transition. The force-extension experiments for P500 were repeated several times with different molecules to ensure reproducability. However, the disagreement between F_x and F_y persited. Also, the force-distance curve of the 2000 bp DNA hairpin construct (P2000, Fig. 2.9a) shows a deviation between the forces determined from the x and y fluctuations (Fig. 2.12a). When the 2000 bp hairpin is open, the deviations between F_x and F_y are smaller than the deviations for the open 500 bp construct. Since P2000 is much longer than P500 when the hairpin is open, the difference in the deviations between F_x and F_y are suggested to be DNA length dependent. This is also consistent with vanishing deviations between F_x and F_y for long dsDNA as shown in the previous section. Since the abrupt jump in the force decay upon DNA hairpin unzipping is unexpected and only detected using the y fluctuations, F_y is suggested to be erroneous determined. The discrepancy between F_x and F_y and its length dependence will be discussed in more detail in section 2.7.

Figure 2.12b shows the force measurements with the 40 bp DNA hairpin construct and the long dsDNA handle (P40long, Fig. 2.9c right side). Only F_x is plotted. The jump in the force-extension curve indicates the transition from closed to open state. In contrast to the 500 bp and 2000 bp DNA hairpin constructs, this DNA hairpin

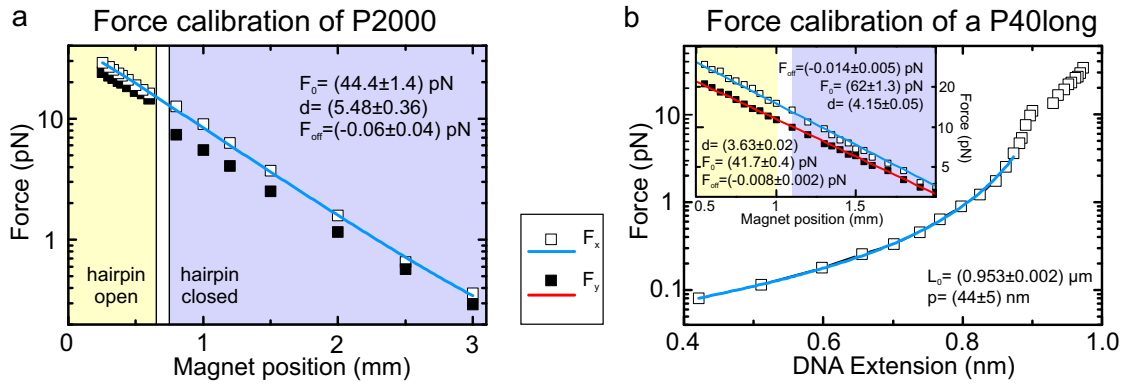

Figure 2.12 Force measurements on a 2000 bp and a 40 bp DNA hairpin construct recorded with 300 Hz. (**a**) Force-distance curve of the 2000 bp DNA hairpin construct using MagSense microspheres. Filled squares are forces using the y fluctuations (F_y), open squares correspond to forces from the x fluctuations (F_x). The blue line is a fit to F_x with equation 2.21. Fit parameters are indicated. The yellow area shows forces at which the hairpin is open, the purple area at which the hairpin is closed. (**b**) Force-extension curve of the 40 bp DNA hairpin construct (P40long) using M280 microspheres. Symbols correspond to F_x as in (a). The blue line is a fit to the WLC model (equation 2.18) for forces below 3 pN resulting in the indicated fitting values. The inset shows the force-distance curve, with fits according to equation 2.21 for F_x and F_y.

construct contains a large part of dsDNA. In this case it is possible to fit the data with the WLC model (equation 2.18) for low forces where the influence of the ssDNA spacers is negligible. The simulation in Figure 2.10 was calculated for the ratio of ss- to dsDNA as it is present in 40 bp DNA hairpin with the long dsDNA handle. The influence of the ssDNA for this construct is negligible at forces below 3 pN, i.e. the WLC fitting was performed only at forces below 3 pN. The force-distance curve shows again that F_x is larger than F_y (inset in Fig. 2.12). No jump between open and closed DNA hairpin is seen because the extension upon DNA hairpin opening is very small (compared to the DNA extension upon unzipping of P500 or P2000). The force measurements for the 90 bp DNA hairpin construct with the long dsDNA handle (P90ATmGClong, Fig. 2.9c right side) are similar to the 40 bp DNA hairpin construct in Figure 2.12b, only the force where the hairpin opens is different (data not shown).

Having all four DNA hairpin constructs (P2000, P500, P40long, P90ATmGClong) calibrated allows to determine the force at which the DNA hairpins unzips (F_{unzip}). This force is quite reproducable for each DNA hairpin sequence under the same conditions (ionic strength of the buffer, temperature, etc. [79]). Therefore, once the unzipping force is known for certain experimental conditions, it can be used to quickly find the force-distance dependence for the actual experiment, instead of recording the force at several positions prior to each experiment. Once the unzipping force is found, one point of the force-distance calibration curve is known. Together with the average decay d (equation 2.21) of the used magnet-microsphere combination allows to determine the full force-distance calibration curve. In section 3.3.2 the exact

procedure for the determination of the unzipping force will be shown.

However, the question of the origin of the deviations between forces determined from the x and the y fluctuations remains unanswered. In particular it is necessary to determine which coordinate provides the correct forces. The abrupt force jump of the forces determined from the y fluctuations in the force-distance curves for 500 bp DNA hairpin (Fig. 2.11b) and the 2000 bp DNA hairpin (Fig. 2.12a) upon hairpin unzipping suggested that this force is incorrectly determined, because the force-distance was shown to develop exponentially (section 2.3.3). As mentioned before, a major difference between the 11 kbp dsDNA construct measured in section 2.3.2 and the DNA hairpin constructs is the distances between the microsphere and the flow cell surface (independent of the state of the hairpins). Therefore, force measurements from x and y fluctuations will be investigated in dependence on the pendulum length (distance between the microsphere and the flow cell surface). The idea is to use five dsDNA constructs with different contour lengths ranging from $500 - 2000$ nm and compare the determined forces using x and y fluctuations. Since the force decreases with a decay length in the range of several mm (e.g. Figure 2.7d), the force change in the range of $500 - 2000$ nm is not even 1%. Thus, if the experimental conditions which determines the force (magnetic material, microsphere, buffer, temperature, etc.) remain constant, the measured forces of different DNA constructs with different contour lengths should as well coincide. Keeping the experimental conditions constant however is problematic. As mentioned in section 2.3.2 the microspheres exhibit a large variation of the radius and saturation magnetization among individual microspheres. Thus, forces for different DNA-microsphere systems are incomparable. Therefore, an assay was developed, where a single DNA-microsphere system is used for which the DNA length can be changed. The results are presented in the following section.

2.3.5 Accuracy of the determined force depends on the DNA length

To use one DNA-microsphere and obtain different DNA lengths an assay including a DNA Holliday junction was developed (Fig. 2.13). A Holliday junction is a four-arm DNA junction (Fig. 2.13a). The used DNA construct consists of ≈ 5.5 kbp with the Holliday junction in the center. If the contributing sequences upstream and downstream of this center position are homologous to each other, the junction can move (branch migration) (Fig. 2.13b). This branch migration can be driven by introducing negative twist into the DNA. One turn of the attached microsphere reduces the DNA length by one helical pitch (3.4 nm). This property allows to stably set different DNA lengths and perform force-extension measurements for each extension.

In Figure 2.13c traces for induced branch migration at 0.8 pN and 1.7 pN are presented. The linearly fitted slopes are expected to reflect the length of one DNA helical pitch moved, per magnet rotation added [80]. Corrected for the relative extension of the molecule at the applied force ($L_{\mathrm{rel}} = 0.85$ for 0.8 pN, $L_{\mathrm{rel}} = 0.92$ for 1.7 pN), the slope indeed corresponds to ≈ 3.4 nm/rotation.

Positive magnet rotations induce plectoneme formation, which decreases the length much faster. This configuration is, however, less controlable to set precisely a certain DNA length. The construct was set to five different magnet rotations (0 , -70 ,

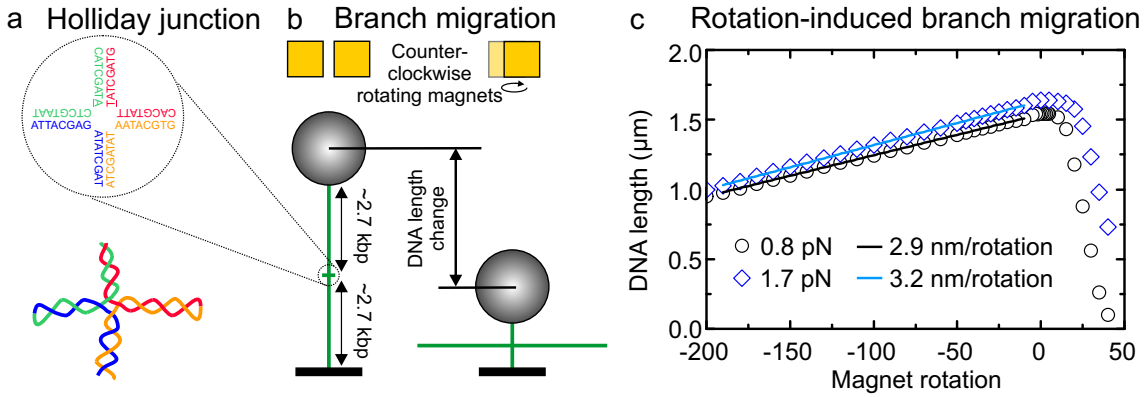

Figure 2.13 Magnet-rotation induced branch migration. (**a**) First bases of the used Holliday junction. A 1 bp mismatch (underlined) stabilizes the structure. (**b**) Illustration that demonstrates how negative (counter clockwise) rotations reduce the DNA length by branch migration. (**c**) The plot shows DNA length versus magnet rotations for a Holliday junction construct at forces of 0.8 pN and 1.7 pN. The slope of the DNA length for negative magnet rotations was linearly fitted, resulting in the indicated fitting values.

-140 , -280 and -360 magnet rotations) resulting in five initial DNA lenghts of the construct. Then force-extension curves for each initial DNA length were recorded. The forces were calculated with equation 2.15 using the x fluctuations and with equation 2.3 using the y fluctuations. Figure 2.14a shows the force-extension curves and corresponding WLC fits (equation 2.18) for the five different initial DNA lengths. The values of the WLC fit (Contour length L_0 and persistence lenght p) are shown in Figure 2.14b,c. The fit values of the contour lenghts for the forces calculated from the x fluctuations and the y fluctuations deviate maximal by 1.7%. Its mean is shown in Figure 2.14b. The slope of the linear fit of the mean contour length corresponds to the expected length change of one helical pitch (3.4 nm) per rotation of the magnets. The fit values of the persistence lengths p are slightly overestimated for short contour length (Fig. 2.14c). Accordingly to theory volume exclusion- and boundary-effects of a microsphere close to the surface should cause a decreasing effective persistence length [77, 78]. Most importantly an increasing deviation between forces calculated from the x fluctuations and forces from the y fluctuations is seen for decreasing initial DNA lengths (Fig. 2.14a).

These differences in the forces are also well seen in the force-distance plots in Figure 2.13d. The individual force-distance curves were fitted with equation 2.21, the fit results (force decay d and maximum applicable force F_0) are presented in Figure 2.14e,f. The fit values of the force decays are comparable to the decay on long dsDNA molecules. The maximum applicable force drops strongly for forces determined from the y fluctuations with decreasing DNA length, while it remains constant for forces determined from the x fluctuations.

This DNA length dependent decrease of forces is, however, unexpected: It could arise from sudden inhomogenities of the magnetic field or the short distance between microsphere and flow cell surface (electrostatic interaction and volume exclusion forces [75]). Inhomogenities of the magnetic field are excluded, based on the measurements

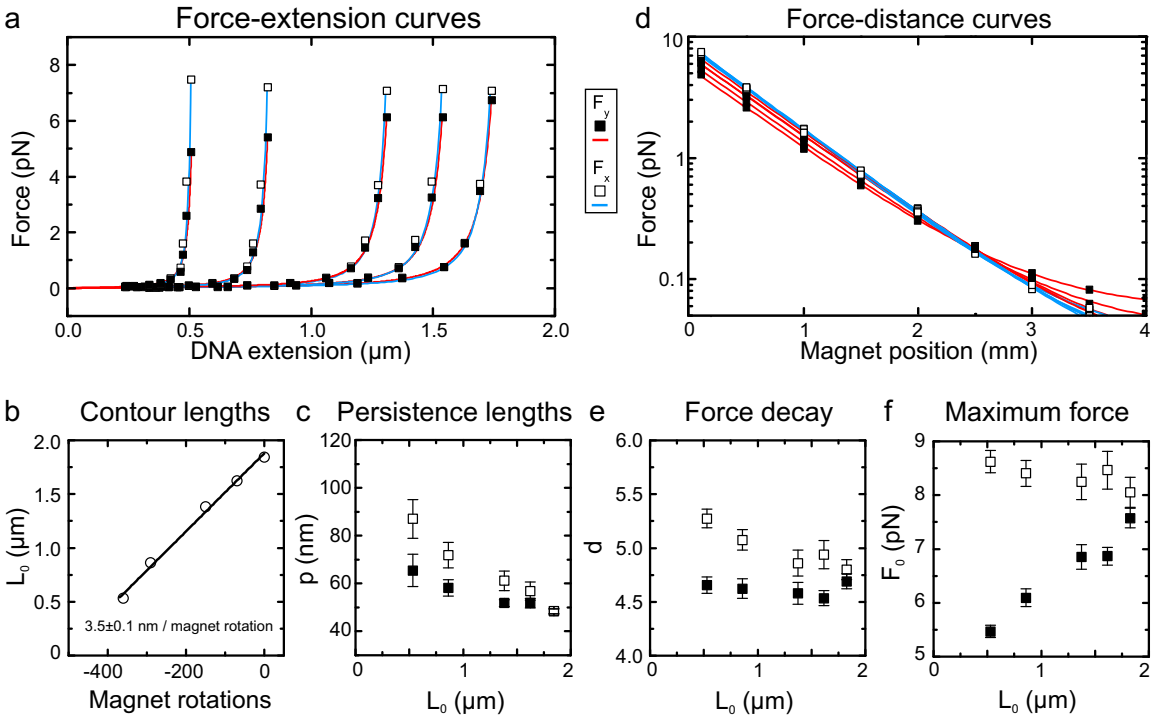

Figure 2.14 Force measurements for various DNA contour lengths. The MyOne microsphere was tracked with 300 Hz. Filled squares are forces using the y fluctuations (F_y), open squares correspond to forces calculated from the x fluctuations (F_x). The blue lines are fits to F_x, red lines to F_y. (**a**) Force-extension curves and WLC fits using equation 2.18. (**b**) Open circles are the WLC fit values of the contour length L_0 from the data in (a) (mean of x and y). Black line is a linear fit with the indicated slope. (**c**) Values of the persistence lengths p of the WLC fit from a. (**d**) Force-distance curves and corresponding fits using equation 2.21. (**e**) Force change per distance between magnets and flow cell. Values are taken from the force-distance fits in b. (**f**) Maximum applicable force F_0 from the force-distance fits in b.

in section 2.3.3 and simulations of the magnetic field using finite element analysis software [81] (COMSOL, Hersham, UK). Influences of the nearby flow cell surface contributing to the magnetic forces should be detected for both the x and the y coordinates equally and should also be measured for long DNA molecules at a low extension. As this is not observed, this strongly indicate that F_y is underestimated.

The forces applied to the microsphere are inverese proportional to the mean-square displacements and proportional to the pendulum length (see equations 2.3 and 2.15 for F_y and F_x respectively). To find the origin of the underestimation of the forces along the y coordinate, the determination of the mean-square displacements is considered in more detail in the following.

As mentioned earlier, the lateral movement of the DNA tethered microsphere in the x direction has a translational and a rotational component, while in the y direction the alignment of the magnetic field and the magnetic dipole of the microsphere restricts rotational movement (see Fig. 2.6). In the following section it will be shown, that the restriction of rotational movements in the y direction can be annihilated such that,

i.e. rotational movement can occur.

Similar to the translational fluctuations also the rotational fluctuations are decribed by a harmonic potential. The restoring torque is due to a torsional spring constant k_{tor}:

$$T = k_{\mathrm{tor}} \cdot \delta\varphi \tag{2.26}$$

for small angular displacements $\delta\varphi$. These angular displacements correspond to linear displacements $\delta y = R\delta\varphi$ (with the microsphere radius R), while the torque corresponds to a force $T = F_{\mathrm{rot}} \cdot R$. Therefore the linear spring constant of the rotational movement k_{rot} can be expressed by the torsional spring constant k_{tor}:

$$k_{\mathrm{rot}} = k_{\mathrm{tor}}/R^2. \tag{2.27}$$

Using the equipartition theorem this yields (similar to the translational mean-square displacements, see equation 2.2):

$$\left\langle \delta y_{\mathrm{rot}}^2 \right\rangle = \frac{k_{\mathrm{B}}T}{k_{\mathrm{rot}}} = \frac{k_{\mathrm{B}}T \cdot R^2}{k_{\mathrm{tor}}}. \tag{2.28}$$

The physical system of translational and rotational fluctuations is described as two springs in series. The reciprocal spring constants of translation and rotation add up and result in a smaller total spring constant, i.e. a larger mean-square displacement. These rotational displacements have not been considered in the calculation of the forces along the y direction, in other words the mean-square displacements in equation 2.3 are purely translational ($\langle \delta y^2 \rangle = \langle \delta y_{\mathrm{trans}}^2 \rangle$). Additionally occuring rotational fluctuations cause an overestimation of $\langle \delta y^2 \rangle = \langle \delta y_{\mathrm{trans}}^2 \rangle + \langle \delta y_{\mathrm{rot}}^2 \rangle$ and consequently an underestimation of the force

$$F_{\mathrm{y}} = \frac{k_{\mathrm{B}}T \cdot \langle z \rangle}{\langle \delta y_{\mathrm{trans}}^2 \rangle + \langle \delta y_{\mathrm{rot}}^2 \rangle}. \tag{2.29}$$

In the following section the torsional spring constant of M280 microspheres will be determined to be $k_{\mathrm{tor}} \approx 100$ pNμm. Assuming the same order of magnitude of the torsional spring constant for a MyOne microsphere with 500 nm radius, yields additional rotational mean-square displacements of $\langle \delta y_{\mathrm{rot}}^2 \rangle = k_{\mathrm{B}}T \cdot 0.4$ pN/nm≈ 10 nm^2. The smallest mean-square displacement determined in the Holliday junction experiments is achieved when the highest force (7.4 pN) is applied to the shortest DNA length (500 nm). The estimated contribution of rotational mean-square displacements of ≈ 10 nm^2 are 2% of the recorded mean-square displacements of $\langle \delta y^2 \rangle = 426$ nm^2. However, the deviation of the forces calculated from the x and y fluctuations is 35%. In conclusion, although rotational fluctuations occur in the y direction, their estimated contribution to the translational fluctuations cannot explain the large deviations between F_{x} and F_{y}. Another check to find the origin of the deviations between F_{x} and F_{y} is to test the consistency of the two system properties which can be calculated from the fluctuation, drag coefficient and the microsphere radius.

In the following the drag coefficient will be calculated from the cutoff frequency for the highest force values of the data presented in Figure 2.14. Additionally, the

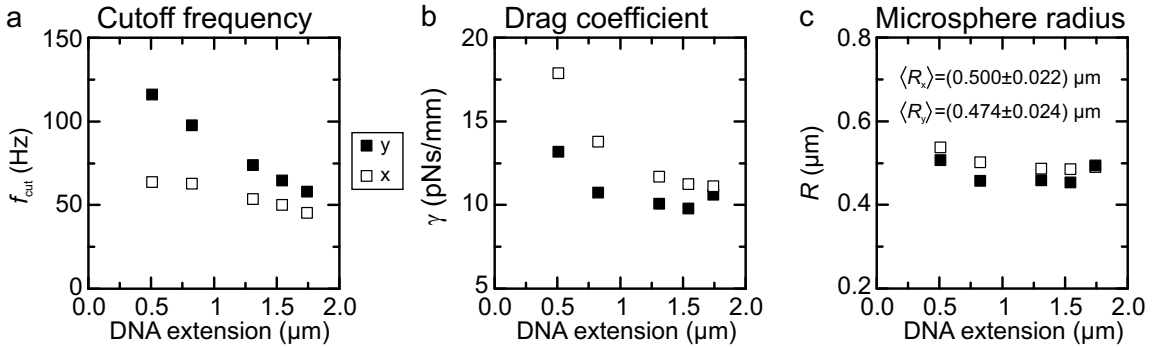

Figure 2.15 Cutoff frequency, drag coefficient and microsphere radius determined as from the x and y fluctuations at high forces for different DNA contour lengths. Filled squares are values determined from the y, open squares from the x fluctuations. The parameters were calculated for the highest applied forces of each force-extension measurement from Figure 2.14. (**a**) Cutoff frequencies f_{cut} as function of the DNA extension as obtained from fits of the PSD of the x and y fluctuations using equation 2.13. (**b**) Drag coefficients as function of DNA extension as obtained from f_{cut} according to equation 2.8. (**c**) Obtained microsphere radius versus DNA extension. The mean values for the radii using x and y fluctuations are indicated.

microsphere radius will be successively determined from the drag coefficient to test wether the values are in agreement with theoretical expectations. Therefore, the mean-square displacements are determined from fits the power spectral density (PSD) of the fluctuations with equation 2.13 (see section 2.3.1). The PSD fitting also the yields the cutoff frequency, which provides the drag coefficient of the microsphere (see equation 2.8). The fit provides a correct result only if the cutoff frequency is well below the Nyquist frequency, which is 150 Hz for the current measurement (300 Hz aquisition frequency). Figure 2.15a shows the cutoff frequencies determined by fitting the PSD of the x and y fluctuations. The cutoff frequencies are below the Nyquist frequency. The values for the y fluctuations are higher than for the x ones and increase for shorter molecules, while the values for x fluctuations stay almost constant. The drag coefficient can directly be calculated from the cutoff frequency (see chapter 2.3.1) using

$$k_{\mathrm{x}} = \frac{k_{\mathrm{B}}T}{\langle x^2 \rangle}, \qquad \gamma_{\mathrm{x}} = \frac{k_{\mathrm{B}}T}{\langle x^2 \rangle \, 2\pi f_{\mathrm{cut}}} \tag{2.30}$$

$$k_{\mathrm{y}} = \frac{k_{\mathrm{B}}T}{\langle y^2 \rangle}, \qquad \gamma_{\mathrm{y}} = \frac{k_{\mathrm{B}}T}{\langle y^2 \rangle \, 2\pi f_{\mathrm{cut}}} \tag{2.31}$$

with the cutoff frequencies of the corresponding coordinate. Figure 2.15b shows the length dependence of the drag coefficients. As expected γ increases for decreasing distances between microsphere and flow cell surface, due to the so called wall-effect, which influences the hydrodynamic properties of the microsphere [82]. The values of the drag coefficient for the x fluctuations are higher, because translational and rotational friction occurs. For the y fluctuations only translational friction occurs.

Furthermore, the microsphere radius R is extracted from the drag coefficient γ to test wether theory and experiment are in agreement. The close distance between

themicrosphere and the flow cell surface affects the drag coefficient, i.e. close to the surface the microsphere radius is no longer equal to the hydrodynamic radius far away from surfaces (Stokes' law). The translational drag coefficient γ_{trans} in the absence of a nearby surface is [83]:

$$\gamma_{\text{trans}} = 6\pi\eta R \tag{2.32}$$

with the viscosity η of the surrounding medium (10^{-3} kg s^{-1} m^{-1}). Correction terms for the drag coefficient in lateral direction close to the flow cell surface are given by Faxén's law [84]:

$$C_{\text{trans}}(z,R) = \frac{1}{1 - \frac{9R}{16z} + \frac{R^3}{8z^3} - \frac{45R^4}{256z^4} - \frac{R^5}{16z^5}} \tag{2.33}$$

with the distance z between the microsphere and the flow cell surface. Therefore the drag coeffiecient of the microsphere fluctuating in the y direction (γ_{y}) with pure translational friction is given by:

$$\gamma_{\text{y}} = \gamma_{\text{trans}} \cdot C_{\text{trans}}(z,R) = \frac{6\pi\eta R}{1 - \frac{9R}{16z} + \frac{R^3}{8z^3} - \frac{45R^4}{256z^4} - \frac{R^5}{16z^5}}. \tag{2.34}$$

The microsphere fluctuations in the x direction are accompanied by a rotational movement (see Figure 2.6). The rotational drag coefficient in the absence of a surface is [83]:

$$\gamma_{\text{rot}} = 8\pi\eta R^3. \tag{2.35}$$

The correcting term for the rotational drag coefficient close to the flow cell surface is given by [85]:

$$C_{\text{rot}}(z,R) = 1 + \frac{5R^3}{16z^3} \tag{2.36}$$

To obtain the drag coefficient in the x direction (γ_{x}) the work of the combined friction for tranlation and rotation is derived. This will provide the correct drag coefficient:

$$W_\gamma^x = F_\gamma \delta x = \gamma_{\text{x}} \dot{x} \delta x = W_{\gamma,\text{trans}} + W_{\gamma,\text{rot}}. \tag{2.37}$$

The work for translational ($W_{\gamma,\text{trans}}$) and rotational displacements ($W_{\gamma,\text{rot}}$) are:

$$W_{\gamma,\text{trans}} = F_{\gamma,\text{trans}}\, \delta x = \gamma_{\text{trans}} \dot{x}\, \delta x = 6\pi\eta R\, \dot{x}\, \delta x\, C_{\text{trans}}(z,R) \tag{2.38}$$

$$W_{\gamma,\text{rot}} = F_{\gamma,\text{rot}}\, \delta\varphi = \gamma_{\text{rot}} \dot{\varphi}\, \delta\varphi = 8\pi\eta R^3\, \frac{\dot{x}}{R+z}\, \frac{\delta x}{R+z}\, C_{\text{rot}}(z,R) \tag{2.39}$$

with the angle of displacement φ (see Figure 2.6). The sum of $W_{\gamma,\text{trans}}$ and $W_{\gamma,\text{rot}}$ will provide the work of the friction for the combined motion:

$$W_\gamma^x = 6\pi\eta R \dot{x}\delta x C_{\text{trans}}(z,R) + 8\pi\eta R^3 \frac{\dot{x}}{R+z} \frac{\delta x}{R+z} C_{\text{rot}}(z,R) \tag{2.40}$$

$$= \left(6\pi\eta R\, C_{\text{trans}}(z,R) + \frac{8\pi\eta R^3}{(R+z)^2}\, C_{\text{rot}}(z,R)\right) \dot{x}\delta x \tag{2.41}$$

where the term in parentheses is the drag coefficient for the x fluctuation γ_{x} (see equation 2.37):

$$\gamma_{\mathrm{x}} = 6\pi\eta R \left(C_{\mathrm{trans}}(z,R) + \frac{8R^2}{6(R+z)^2} C_{\mathrm{rot}}(z,R) \right) \tag{2.42}$$

The microsphere radius is determined by iteratively finding the best fit of the derived equations for the drag coefficients for the x and y fluctuations (equations 2.42 and 2.34 respectively) to the apparent drag coefficients in Figure 2.15b. The determined values for the radius and their mean are presented in Figure 2.15c. Within error the theory is in agreement of the radius given by the manufacturer: $R_{\mathrm{MyOne}} = 0.525\ \mu\mathrm{m}$. In conclusion, the fitted cutoff frequencies and the calculated drag coefficients are reliable, because the subsequently determined microsphere radii were found with high precision.

Neither the lateral fluctuations nor an erroneous fit of the cutoff frequency explains the large deviations between the forces determined from the x and y coordinates and the underestimation of the forces using the y fluctuation. This suggests that the differences in the force determination depend less on the mean-square displacements, than on the pendulum length (the applied force is proportional to the length, see equations 2.3 and 2.15 for F_{y} and F_{x}, respectively). Therefore an underestimation of the forces in the y direction corresponds to an underestimation of the pendulum length. In the case of the y coordinate the pendulum length is the DNA length and for the x coordinate it is the DNA length extended by the microsphere radius. Thus an incorrect determined DNA length has a larger impact in the y coordinate, than on the x coordinate. Underestimation of the DNA length can be due to a misalignment of the attachment point of the DNA to the microsphere (attachment point not vertically aligned with the microsphere center). This can be caused by a non-spherical shape of the microspheres or the misaligment is caused by the torsional pinning of the microshpere. In the latter case one needs to consider that the DNA is attached to the microsphere in the absence of the magnetic field. When the DNA-microsphere system is subjected to forces the magnetic dipole is aligned in the magnetic field, independent of the attachment point of the DNA. This so called off-center attachment will be discussed in detail in the next section.

Another reason for the underestimation of the DNA length is the attachment of the DNA to the microsphere and the flow cell surface both using long anchor segments (see chapter 3). Several DNA bases can bind to the flow cell surface or the microsphere causing bent DNA at the attachment points. Because of its bending rigidity the DNA between the attachment on the surface (horizontal) will display a curvature compared to the DNA between the surface and the microsphere (vertical). Thus a shorter DNA length will be observed.

Although the microsphere radius can be determined with high precision the incorrect determined DNA length might result in erroneously calculated forces. The "hidden" DNA length might be as large as the radius of the microsphere (imagine the DNA attachment point at the equator of the microsphere), i.e. the relative error of the DNA length decreases with increasing DNA contour length. Therefore the long dsDNA in section 2.3.2 shows no deviation between the forces determined from the x and y

coordinates. Since the force determination using the x coordinate is based on a longer pendulum compared to the y coordinate, the impact of the incorrect DNA length is less pronounced. Hence for short DNA molecules as used in this thesis, it is important to determine forces using the x coordinate to achieve high resolution.

2.4 Limited vertical resolution of magnetic tweezers

2.4.1 Rotational fluctuations and off-center attached microspheres

For the helicase experiments in this thesis it is important to achieve high spatial resolution (in the vertical direction) to gain information about the mechanics underlying the DNA unwinding process. The spatial resolution limits of magnetic tweezers arise from the thermal fluctuations, which can be decreased, for example, by applying higher forces. Figure 2.16 shows the recorded vertical positions of two individual M280 microspheres attached to a 5.7 kbp dsDNA construct. The vertical fluctuations are reduced with increasing forces. However, the fluctuations of the microsphere recorded in Figure 2.16a are larger than the fluctuations of the microsphere recorded in Figure 2.16b.

To identify the origin of the additional fluctuations we characterized 27 DNA-microsphere systems. One property, which largely varies between the individual DNA-microsphere systems, is the off-center attachment $R_\perp$ of the DNA to the microsphere. This means that the attachment point of the DNA to the microsphere is not vertically aligned to the DNA axis and the microsphere center (compare sketches in Figure 2.17a and b). Off-center attachment can be detected by slowly rotating the magnets and following the induced microsphere rotation in the x, y plane. Since the microsphere rotates around its DNA attachment point a large off-center $R_\perp$ will cause a large radius (Fig. 2.17c,d). The tracking data of the vertical fluctuations of the investigated DNA-microsphere systems revealed that a larger off-center attachment results in larger

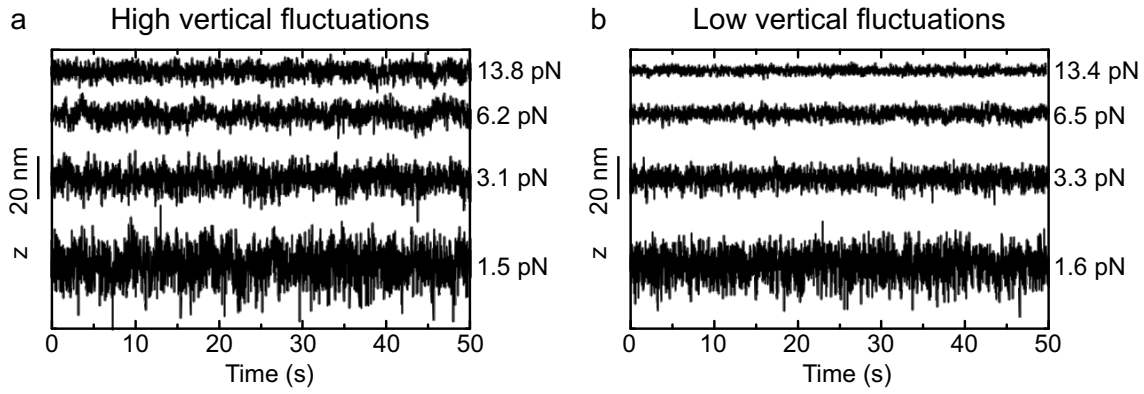

Figure 2.16 Axial microsphere position (z direction) with high and low fluctuations. (**a**) Time traces of the z position of a magnetic microsphere at different forces. The fluctuations at 13.8 pN are nearly not reduced compared to 6.2 pN, which would be expected due to the higher trap stiffness. (**b**) Time traces of the z position of a magnetic microsphere at similar forces as shown in (a). The fluctuations decrease with increasing force as expected.

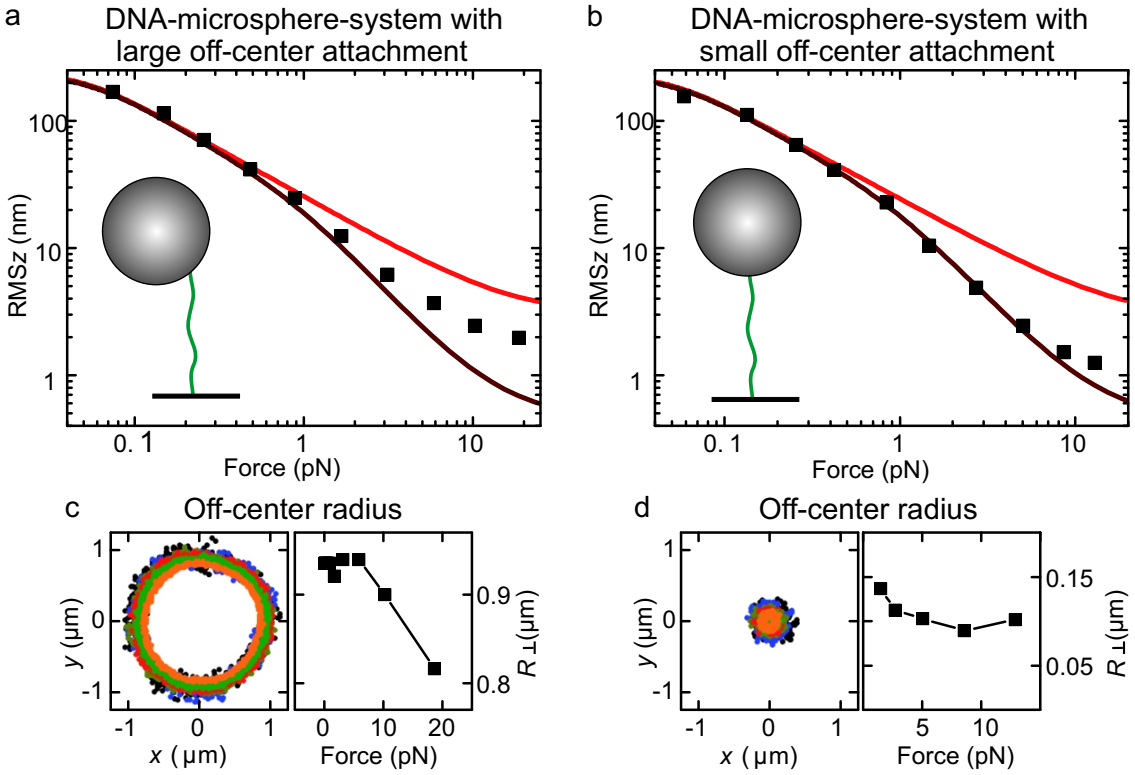

Figure 2.17 Expected and measured noise along the vertical direction for a microsphere with large and small off-center attachment $R_\perp$. (a,b) Measured root-mean-squared displacements in vertical direction (RMSz) as a function of force (black squares). Solid lines are the calculated RMSz with (brown) and without correction (red) for low-pass filtering by the camera using equation 2.43. (c,d) Off-center attachment $R_\perp$ measured at different forces by slowly rotating the magnetic field and following the circular track of the microsphere in the x, y plane.

fluctuations.

To compare the data to theoretical predictions an analytic expression for the expected noise can be derived. Similar to the fluctuations in the horizontal direction (see section 2.3) the system can be assumed to be overdamped. The DNA can be approximated, in the limit of small displacements, as a linear spring with a constant $k_{\mathrm{DNA}} = dF_{\mathrm{DNA}}/dz_{\mathrm{DNA}}$, which is given by the WLC model (see section 2.3.2, equation 2.18). The measured dynamics of the system of a linear spring k_{DNA} and a viscous damping element is described by a PSD equivalent to equation 2.7 [69]:

$$Z(f) = \frac{4k_{\mathrm{B}}T\gamma_{\mathrm{trans}}}{k_{\mathrm{DNA}}^2}\frac{1}{1+(f/f_{\mathrm{c}})^2}\frac{\sin^2(\pi f/f_{\mathrm{cam}})}{(\pi f/f_{\mathrm{cam}})^2}, \tag{2.43}$$

where k_{B} is the Boltzmann constant, T the temperature and $f_{\mathrm{c}} = k_{\mathrm{DNA}}/2\pi\gamma_{\mathrm{trans}}$ the cut-off frequency. The translational drag coefficient perpendicular to the surface γ_{trans} is given by an interpolation [82] of Brenner's formula [83]:

$$\gamma_{\mathrm{z}} = \frac{6\pi\eta R}{1 - \frac{9R}{8h} + \frac{R^3}{2h^3} - \frac{57R^4}{100h^4} + \frac{R^5}{5h^5} + \frac{7R^{11}}{200h^{11}} - \frac{R^{12}}{25h^{12}}} \tag{2.44}$$

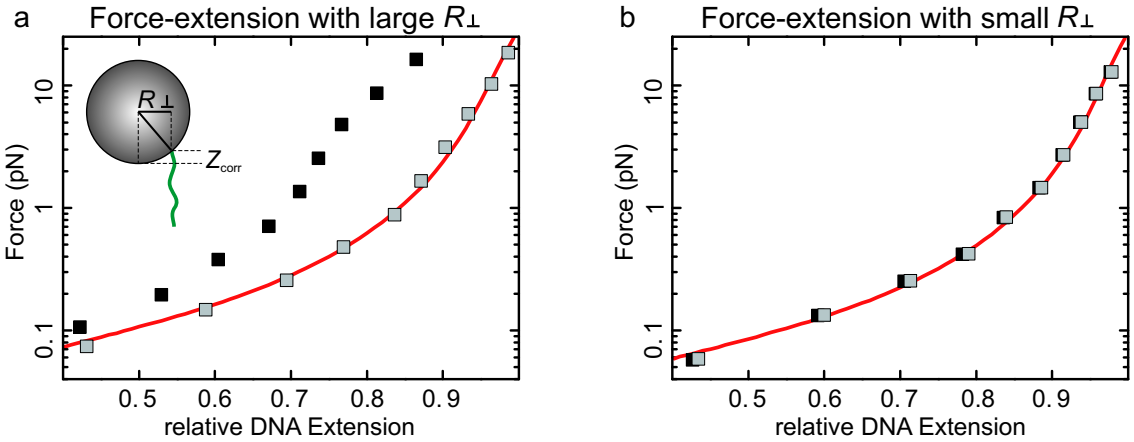

Figure 2.18 Force-extension relations for a microsphere with (a) large and (b) small off-center attachment $R_\perp$. (**a**,**a**) Measured data (black squares) and after correction by Z_{corr} (see sketch) due to the off-center attachment (gray squares). The red line is a fit with the extensible WLC model (equation 2.18) with a persistence length of $p = 45 \pm 5$ nm.

The first two terms of equation 2.43 describe the real occurring fluctuations, whereas the right part corrects for low-pass filtering by the camera with acquisition frequency f_{cam} [69]. Integrating the PSD (equation 2.43) from zero to infinity provides the expected mean-squared fluctuations $\langle z^2 \rangle$. Aliasing causes shifts of high frequency components (see section 2.3.1, Figure 2.5), which is not included in equation 2.43. However, they are included in the mean-squared displacements $\langle z^2 \rangle$ due to the integration from from zero to infinity.

Comparing the measured and the expected root-mean-squared displacements in the vertical direction (RMSz), we find an excellent agreement at forces below 2 pN (see Figure 2.17a), whereas at larger forces a significantly higher noise can be found. Figure 2.17a,b shows the differing results for small and large off-center attached microspheres. Additionally Figure 2.17c,d shows that the off-center attachment decreases with increasing force. This can be explained by rotational displacements of the microsphere out of its preferred orientation. Such a rotational displacement should also be observed along the vertical direction for large off-center attachment, i.e. providing a wrong DNA extension.

Indeed, force-extension curves for microspheres with a large off-center attachment did not show the expected WLC behavior (Fig. 2.18a). The correction for rotational displacements in the vertical direction as calculated from the measured off-center attachment and the microsphere radius, the force distance curves could be remarkably restored (Fig. 2.18a).

These rotational displacements suggest a relatively low torsional spring constant k_{tor} of the microspheres within the magnetic field and might explain the observed increase in the noise at large forces. Indeed, we observe a strong correlation of the observed noise (RMSz) at high stretching forces and the off-center attachment (Fig. 2.19a). Additionally, the deviations in DNA length between high forces (20 pN) and low forces (where the off-center attachment maximizes) were evaluated (Fig. 2.19b).

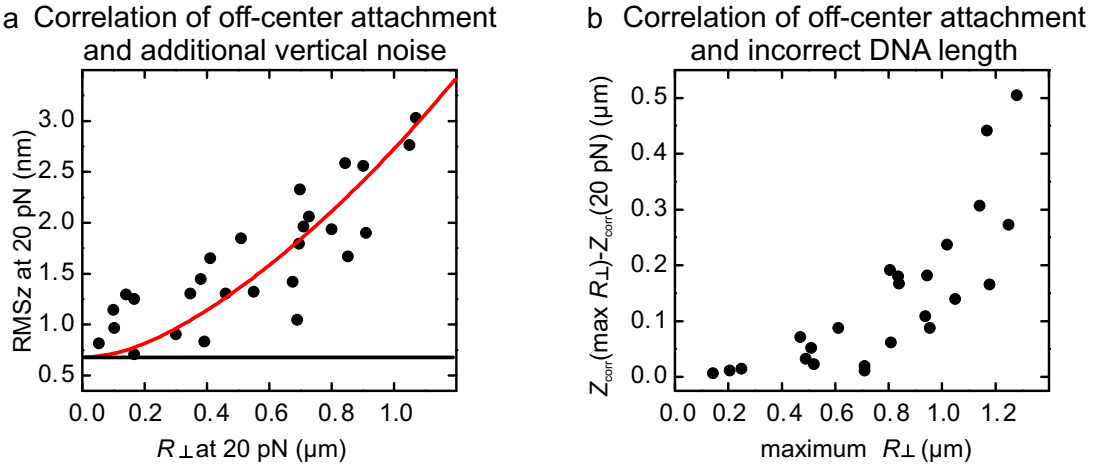

Figure 2.19 Noise and corrections for the DNA extension are proportional to the off-center attachment. (**a**) Measured RMSz at 20 pN versus the off-center attachment $R_\perp$. Solid lines represents the expected noise in the absence (black) and presence (red) of rotational fluctuations of the microspheres. A torsional spring constant of $k_{\mathrm{tor}} = 100$ pN μm rad^{-1} was chosen. (**b**) Deviations in the DNA extension due to rotational displacements (see Figure 2.18 sketch) at 20 pN calculated from the difference in Z_{corr} at 20 pN and at low force where the off-center attachment $R_\perp$ maximizes.

The results show a strong correlation with the off-center attachment.

In conclusion, these results indicate that the magnetic microspheres can exhibit significant rotational displacements and fluctuations. To provide a quantitative basis and a qualitative understanding of the torsional forces within the applied field the torsional spring constant of a single microsphere is determined in the next section.

2.4.2 Coupled rotational and translational displacements

Quantifying the measured fluctuations should allow to determine the torsional spring constant of a single microsphere. To obtain a relation between the torsional spring constant of a magnetic microsphere and the measured mean-squared displacements in the vertical direction, we derive the power spectrum of the system, in which translational and rotational fluctuations are coupled (see Figure 2.20).

We approximate the magnetic potential counteracting the rotational displacements as a harmonic with torsional spring constant k_{tor}. The back driving torque is then given by:

$$T_{\mathrm{mag}} = -k_{\mathrm{tor}} \Delta\varphi \tag{2.45}$$

for small displacements $\Delta\varphi$. The rotational drag torque is given by:

$$T_{\mathrm{D}} = -\gamma_{\mathrm{torque}} \dot{\varphi} \tag{2.46}$$

with the rotational drag coefficient γ_{torque}, which is given by equation 2.35 with the correction in equation 2.36 [83]. T_{mag} and T_{D} originate from the corresponding linear forces along the DNA axis (Figure 2.20a):

$$F_{\mathrm{torque}} = -k_{\mathrm{tor}}/R_\perp^2 \, \Delta z_{\mathrm{rot}} \qquad \text{and} \qquad F_{\mathrm{D,torque}} = -\gamma_{\mathrm{torque}}/R_\perp^2 \, \dot{z}_{\mathrm{rot}}. \tag{2.47}$$

The distance z_{rot} denotes the height of the microsphere center above the DNA attachment point (Figure 2.20a) with $\Delta z_{\mathrm{rot}} = R_{\perp}\Delta\varphi$ for small $\Delta\varphi$. With the acting random forces $F_{\mathrm{trans}}(t)$ and $F_{\mathrm{rot}}(t)$, one can derive an analytic expression for the coupled noise power spectrum $Z^{\mathrm{c}}(f)$ [44]. The index c refers to the coupled system. From the the coupled noise power spectrum the mean-squared displacements are obtained by integration of the PSD (similar to the horizontal mean-squared displacements in section 2.3.1). The equations are a set of coupled linear Langevin equations:

$$\begin{aligned} -\gamma_{\mathrm{rot}}\dot{z}_{\mathrm{rot}} - k_{\mathrm{rot}}\Delta z_{\mathrm{rot}} + k_{\mathrm{DNA}} z_{\mathrm{DNA}} &= F_{\mathrm{rot}}(t) \\ -\gamma_{\mathrm{trans}}\dot{z} - k_{\mathrm{DNA}} z_{\mathrm{DNA}} &= F_{\mathrm{trans}}(t) \end{aligned} \tag{2.48}$$

with $k_{\mathrm{rot}} = k_{\mathrm{tor}}/R_{\perp}^2$, $\gamma_{\mathrm{rot}} = \gamma_{\mathrm{torque}}/R_{\perp}^2$ and $z_{\mathrm{DNA}} = z - z_{\mathrm{rot}}$. The translational drag coefficient γ_{trans} is given by equation 2.34 in section 2.3.5. This set of linear, coupled Langevin equations describing the coupling between translational and rotational Brownian fluctuations of the magnetic microsphere can be written in the following matrix form:

$$-\boldsymbol{\gamma}\dot{\boldsymbol{z}} - \boldsymbol{\kappa}\boldsymbol{z} = \boldsymbol{F}(t) \tag{2.49}$$

$$\boldsymbol{\gamma} = \begin{bmatrix} \gamma_{\mathrm{rot}} & 0 \\ 0 & \gamma_{\mathrm{trans}} \end{bmatrix},\ \boldsymbol{z} = \begin{bmatrix} z_{\mathrm{rot}} \\ z \end{bmatrix},\ \boldsymbol{\kappa} = \begin{bmatrix} k_{\mathrm{DNA}} + k_{\mathrm{rot}} & -k_{\mathrm{DNA}} \\ k_{\mathrm{DNA}} & k_{\mathrm{DNA}} \end{bmatrix},\ \boldsymbol{F}(t) = \begin{bmatrix} F_{\mathrm{rot}}(t) \\ F_{\mathrm{trans}}(t) \end{bmatrix}$$

To solve this equation set we find a linear transformation $\boldsymbol{z} = \boldsymbol{A}\cdot\boldsymbol{\zeta}$ that decouples these equations, i.e. resulting in: $-\dot{\boldsymbol{\zeta}} - \boldsymbol{\lambda}\boldsymbol{\zeta} = \boldsymbol{\Phi}(t)$ (see appendix 6.4.2). Here, $\boldsymbol{\lambda}$ is the diagonal matrix with the eigenvalues $\lambda_{\pm}$ of the matrix $\boldsymbol{\gamma}^{-1}\boldsymbol{\kappa}$ with $\boldsymbol{\lambda} = \boldsymbol{A^{-1}}\boldsymbol{\gamma}^{-1}\boldsymbol{\kappa}\boldsymbol{A}$, where $\boldsymbol{A}$ is formed by a set of eigenvectors. $\boldsymbol{\Phi}(t)$ are the transformed Langevin forces. Choosing a normalization for $\boldsymbol{A}$ for which $\boldsymbol{A^{-1}}(\boldsymbol{\gamma}^{-1})^T(\boldsymbol{A^{-1}})^T = \boldsymbol{I}$, the following

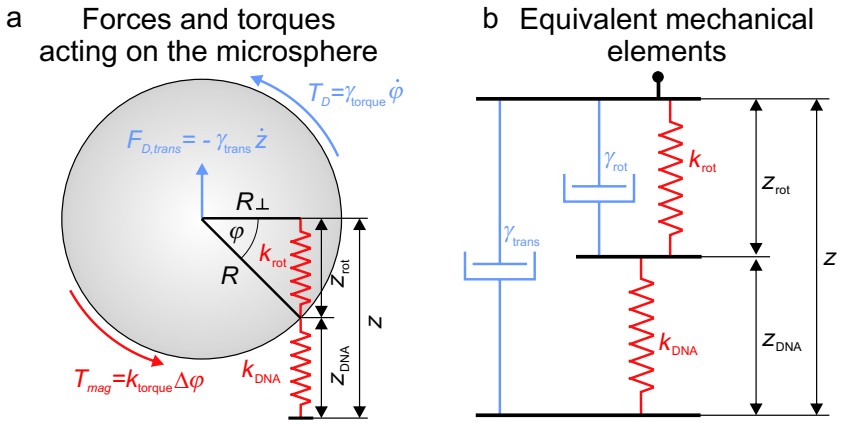

Figure 2.20 Coupled translational and rotational fluctuations. (**a**) Sketch of linear, torsional and drag forces acting on the magnetic microsphere. (**b**) Alternative representation of the model shown in a, describing the idealized system with basic mechanical elements. The drag is modeled by a dashpot such that the force scales linear with velocity. The stiffness of the spring is expected to be constant in the range of movement and can be modeled by a spring, such that the force scales linear with the displacement. The mass can be neglected because the system is overdamped [9].

expression can be derived for the power spectrum (see appendix 6.4.2):

$$Z^{\mathrm{c}}(f) = 2k_{\mathrm{B}}T\boldsymbol{A}(\boldsymbol{\lambda}^2 + (2\pi f)^2\boldsymbol{I})^{-1}\boldsymbol{A}^T \tag{2.50}$$

with the unit matrix $\boldsymbol{I}$. For our system the eigenvalues are:

$$\lambda_{\pm} = \frac{k_{\mathrm{DNA}} + k_{\mathrm{rot}}}{2\gamma_{\mathrm{rot}}} + \frac{k_{\mathrm{DNA}}}{2\gamma_{\mathrm{trans}}} \pm \frac{1}{2}\sqrt{\left(\frac{k_{\mathrm{DNA}} + k_{\mathrm{rot}}}{\gamma_{\mathrm{rot}}} + \frac{k_{\mathrm{DNA}}}{\gamma_{\mathrm{trans}}}\right)^2 - \frac{4k_{\mathrm{DNA}}k_{\mathrm{rot}}}{\gamma_{\mathrm{trans}}\gamma_{\mathrm{rot}}}} \tag{2.51}$$

and for the power spectrum we obtain:

$$Z^{\mathrm{c}}(f) = \frac{4k_{\mathrm{B}}T}{1 + C^2\gamma_{\mathrm{trans}}\gamma_{\mathrm{rot}}} \begin{bmatrix} \frac{1}{\gamma_{\mathrm{rot}}(\lambda_+^2 + (2\pi f)^2)} + \frac{\gamma_{\mathrm{trans}}C^2}{\lambda_-^2 + (2\pi f)^2} & \frac{C}{\lambda_+^2 + (2\pi f)^2} + \frac{C}{\lambda_-^2 + (2\pi f)^2} \\ \frac{C}{\lambda_+^2 + (2\pi f)^2} + \frac{C}{\lambda_-^2 + (2\pi f)^2} & \frac{\gamma_{\mathrm{rot}}C^2}{\lambda_+^2 + (2\pi f)^2} + \frac{1}{\gamma_{\mathrm{trans}}(\lambda_-^2 + (2\pi f)^2)} \end{bmatrix} \tag{2.52}$$

with

$$C = \left(\lambda_- - \frac{k_{\mathrm{DNA}} + k_{\mathrm{rot}}}{\gamma_{\mathrm{rot}}}\right) k_{\mathrm{DNA}}^{-1}. \tag{2.53}$$

In the matrix of the PSD (equation 2.52), the first diagonal expressions contain the PSD for rotational fluctuations of the microsphere (z_{rot}) and the second diagonal entry contains the PSD for the fluctuations of the DNA and the microsphere rotation ($z = z_{\mathrm{DNA}} + z_{\mathrm{rot}}$). Low pass filtering due to the finite exposure time of the camera is considered in analogy to the case without rotational fluctuations by multiplying the power spectrum with the sinc^2 function (compare to section 2.3.1, equation 2.14). This provides the following expression for the low-pass corrected power spectrum of the z fluctuation of the magnetic microsphere:

$$Z^{\mathrm{c}}_{\mathrm{corr}}(f) = \frac{4k_{\mathrm{B}}T}{1 + C^2\gamma_{\mathrm{trans}}\gamma_{\mathrm{rot}}} \left(\frac{\gamma_{\mathrm{rot}}C^2}{\lambda_+^2 + (2\pi f)^2} + \frac{1}{\gamma_{\mathrm{trans}}(\lambda_-^2 + (2\pi f)^2)}\right) \frac{\sin^2(\pi f/f_{\mathrm{cam}})}{(\pi f/f_{\mathrm{cam}})^2}. \tag{2.54}$$

Numeric integration of the spectrum from zero to infinity provides the mean-squared displacements in the vertical direction for the coupled translational and rotational fluctuations corrected for the low pass filtering of the camera. f_{cam} is the reciprocal value of the exposure time.

Using the derived expression for the mean-squared displacements in vertical direction, we determined the rotational spring constant k_{rot} for each microsphere as a function of force. This was done by iteratively finding the rotational spring constant, which would generate the observed mean-squared displacements in the vertical direction at a given force. For a given force, the rotational spring constant is decreasing with increasing off-center attachment following the expected $1/R_{\perp}^2$ dependence within error (Fig. 2.21a).

We also determined the torsional spring constant k_{tor} and its dependence on the magnetic field B (Fig. 2.21b inset). The magnetic field was measured with a small hall probe (see chapter 2.3.3). At a given field strength, the torsional spring constant exhibits a significant variability between different microspheres (Fig. 2.21a inset). We

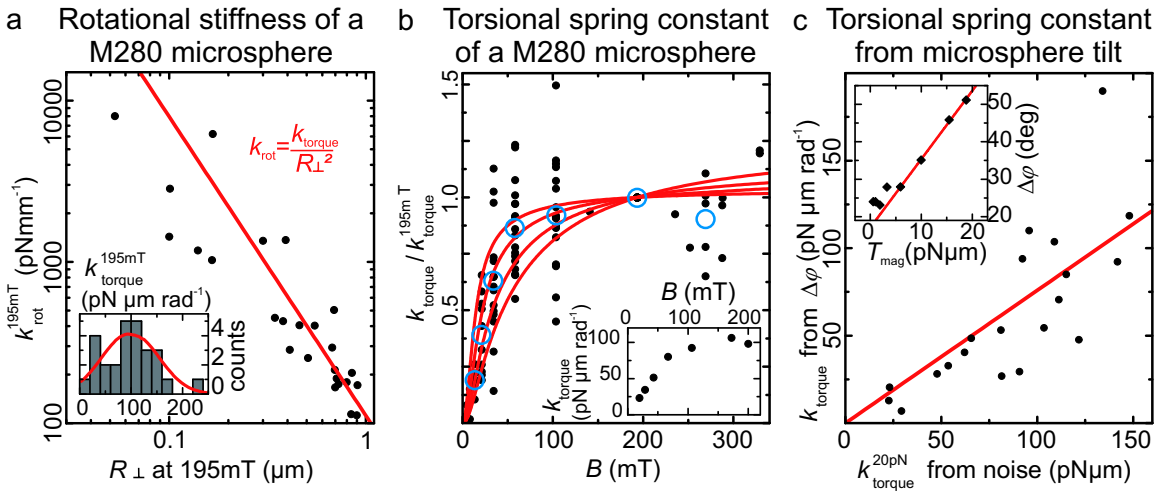

Figure 2.21 Torsional spring constant of M280 microspheres. (**a**) The torsional spring constant k_{rot} at 195 mT as function of the off-center attachment $R_\perp$ (black dots). The red line is a fit to the data with $k_{\mathrm{rot}} = k_{\mathrm{tor}}/R^n$ with $k_{\mathrm{tor}}^{195\mathrm{mT}} = 111 \pm 4$ pN μm rad^{-1} and n=1.9±0.2. Inset: histogram of $k_{\mathrm{tor}}^{195\mathrm{mT}}$ with a mean of 94 ± 10 pN μm rad^{-1}. (**b**) Overlay of all torsional spring constant curves as a function of B normalized at $B = 195$ mT (black dots). Blue circles represent the mean for a given B. Red lines: calculations of the magnetic anisotropy constant C of 1, 2, 4 and 7 kJ m^{-3} (see next section 2.4.3). Inset: k_{tor} curve of a representative microsphere. (**c**) The torsional spring constant k_{tor} estimated from the angular tilt of the microsphere versus k_{tor} from noise measurements. The red line is a linear fit with a fixed intersection at zero to show the correlation between the two methods to determine k_{tor} (slope: 0.76). Inset: Angular displacement as function of the applied torque for a single microsphere. k_{tor} is estimated from a linear fit to the data at higher forces (red line).

normalized the torsional spring constant curves from all microspheres at $B = 195$ mT (Fig. 2.21b). Whereas the torsional spring constant initially increases monotonously with force, it saturates at higher forces, suggesting that it becomes independent of the applied field. The mean torsional spring constant at $B = 195$ mT (at which the torsional spring constant already saturates) equals to 94 ± 10 pN μm rad^{-1} (Fig. 2.21a inset). Calculating the expected noise as a function of the off-center attachment for the obtained mean torsional spring constant well describes the experimental noise (see Figure 2.19a).

A saturation of the torsional spring constant is also observed when examining the microsphere´s angular displacements (angular tilt) $\Delta\varphi$ since they arise only when the torsional spring constant saturates. To quantitatively correlate angular displacements with the obtained torsional spring constant, we estimated the saturation value of the torsional spring constant from plotting $\Delta\varphi$ over the applied torque T_{mag} (Fig. 2.21c inset). The slope of the increasing part of this data at high fields provides then an estimate for the saturating torsional spring constant. We find a good correlation between the torsional spring constant values determined by the two independent concepts (Fig. 2.21b). In the next section the origin of the saturating torsional spring constant will be discussed.

2.4.3 Magnetization anisotropy causes saturation of the torsional spring constant

The torque experienced by a magnetic dipole within the magnetic field B is given by $\vec{T}_{\mathrm{mag}} = \vec{m} \times \vec{B}$, where $\vec{m}$ denotes the magnetic moment. In contrast to our observations, one would therefore expect a linear increase of the torsional spring constant with the magnetic field if the magnetic moment has saturated ($B > 100$ mT, Figure 2.22a). This assumes that the magnetization direction is perfectly aligned with the dipole axis, i.e. the anisotropy axis. Superparamagnetic microspheres consist however of many iron oxide nanoparticles, dispersed in a polymer matrix. Each nanoparticle displays a certain magnetization anisotropy [86]. The magnetization anisotropy of the whole microsphere likely arises from a slight preferential angular orientation of the nanoparticles. Within a single particle the magnetization vector $\vec{m}$ can, however, be misaligned from the particle anisotropy axis (Fig. 2.22b). For this, an energetic penalty given by the anisotropy constant C has to be paid and the free energy density for the particle magnetization within a homogeneous field B can be written as [87]:

$$U_{\mathrm{mag}} = \frac{1}{2} C \sin^2 \alpha - BM \cos(\varphi - \alpha) \tag{2.55}$$

where M denotes the volume magnetization. φ is the angle between the anisotropy axis and magnetic field, α is the angle between the anisotropy axis and the magnetic moment (Fig. 2.22b). Equation 2.55 can be used to calculate the torsional spring constant assuming a parallel alignment of all nanoparticles of a microsphere. Whereas for small fields the magnetic moment is aligned with the anisotropy axis, high fields

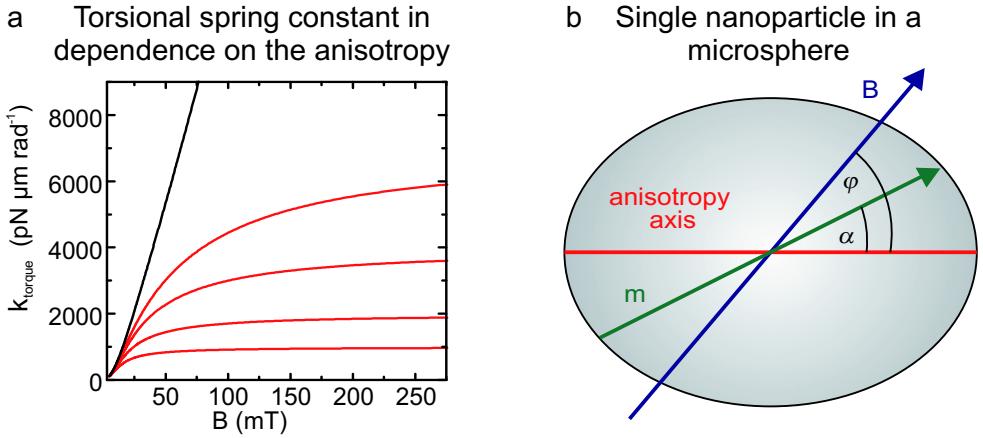

Figure 2.22 (**a**) Torsional spring constant k_{tor} as function of the magnetic field calculated for different values of the magnetic anisotropy constant C with $C = 7000, 4000, 2000$ or $1000\ \mathrm{Jm}^{-3}$ (red lines from top to bottom). Calculations were performed assuming perfect parallel alignment of the anisotropy axis of all nanoparticles of the microsphere. The black line is the expected k_{tor} for a microsphere with fixed orientation of the magntic dipole moment, i.e. with an infinitly high anisotropy. (**b**) Sketch of an anisotropic iron oxide nanoparticle within a magnetic field (blue arrow) and with a magnetic moment (green arrow). The red line shows the anisotropy axis resulting from shape- and crystalline anisotropy.

force an alignment of the magnetic moment with the field causing the torsional spring constant to saturate. A good qualitative agreement with the experimentally observed behavior is obtained for values of the anisotropy constant between 1000 and 7000 J m^{-3} (Fig. 2.22a) in agreement with the bulk crystalline anisotropy constant of γFe_2O_3 of 4.7 kJ m^{-3} [86]. Thus, the material properties of the magnetic particles can provide an explanation for the saturation of the torsional spring constant. However, other effects, such as dipole interactions between nanoparticles, may also contribute.

Superparamagnetic microspheres have become a valuable tool for applying force in fundamental biophysical experiments. Despite the wide application of torsion and twist generation using magnetic microspheres, the torsional forces and their origin remain inadequately characterized. Depending on the application, torsional forces are either neglected [88] or assumed to be larger than any other acting force [68]. The significant rotational fluctuations displayed by magnetic microspheres can be used to calculate their torsional spring constant as a function of the magnetic field. Generally, magnetic measurements of single small particles still remain a challenging topic [89]. With our measurements we provide a basis for using DNA to carry out magnetic measurements on such systems. Torsion magnetometry is a powerful technique in order to characterize small magnetic samples down to torque values of $\approx 10^{-13}$ Nm [90]. Here the measurements were performed with a sensitivity of $\approx 10^{-13}$ Nm. However, even more sensitive measurements can potentially be achieved by using the torsional spring constant of DNA directly. Therefore, DNA-based magnetic tweezers might become a new tool in ultrasensitive torsion magnetometry.

3 DNA hairpin constructs for magnetic tweezers

DNA hairpin constructs are widely used to study DNA unwinding by helicases [35, 91, 92, 93] or nucleic acid folding [94]. An advantage of DNA hairpins is the loop at the end of the dsDNA region, so that neither unzipping by force nor unwinding of the hairpin by a helicase results in lost of one of the ssDNA strands and therewith loss of the attached microsphere. This allows for example for simple force calibration of the magnetic tweezers by determining the hairpin unzipping force.

To achieve high spatial resolution in vertical direction, a high stiffness of the DNA hairpin constructs is required. This is achieved by keeping the overall length of the construct short and including dsDNA instead of ssDNA where possible.

Different DNA hairpin lengths are required, depending on the specific question the experiment adresses. For example long DNA hairpin constructs are desired for high statistical confidence in experiments where the microsphere is sheared off the DNA by a helicase after unwinding, i.e. the construct is intact for just one helicas run. Additionally different base pair content (AT/GC-ratio) is required to investigate the response of the helicase against to different base pairing energies.

For many substrates in single-molecule experiments, especially for DNA hairpin constructs, the ligation of ssDNA to dsDNA is required. The single stranded tails of the hairpins are ligated to longer and more rigid dsDNA handles. The ligation efficiency strongly depends on the length of the sticky end of the handle and is rather low for the typical 4 bp overhangs generated by restriction enzymes. Longer overhangs can be generated using Autosticky PCR [95], which supports efficient ssDNA to dsDNA ligation [96]. However, this method is restricted to 5´-overhangs only and requires rather expensive primers. A simpler alternative, which allows to generate both 3´ and 5´ overhangs, which recently was published [53] will be presented.

The methods for DNA hairpin construct preparation developed for this work are presented in the first sections of this chapter. Experiments to calibrate forces with DNA hairpin constructs are shown in the second part of this chapter.

3.1 Methods to assemble DNA hairpin constructs

There are a number of properties common to all the DNA hairpin constructs used. A sketch of the DNA hairpin constructs in open and closed conformation was already presented in section 2.3.4, Figure 2.9. All of the DNA hairpin constructs need modified bases at their ends. The strong non-covalent bindings between biotin and streptavidin as well as between digoxigenin and anti-digoxigenin are used to link the DNA to the microsphere and to the surface of the flow cell, respectively. A certain distance between the flow cell surface on the microsphere is desired to assure low surface effects (e.g. chemical reactions between the surfactants or mechanical influences). Therefore, DNA spacers between the microsphere and the hairpin and the hairpin and the flow

cell surface are required. For all DNA hairpin constructs, these spacers are formed by non-homologous ssDNA ends of the hairpin, i.e. these non-homologous ssDNA ends cannot hybridize with each other and do not contribute to the actual hairpin region. Beside keeping, the ssDNA spacers also provide a start site for the helicases to bind and initiate the unwinding of the DNA hairpin. As the helicases used in this thesis translocate on ssDNA only in 3´ to 5´ direction, the strand polarity of the start site is required to have the corresponding polarity so that the helicase translocates towards the DNA hairpin. These desired properties are considered in the design of the DNA hairpin constructs.

The different methods to prepare DNA hairpin constructs in this section are required to achieve different hairpin lengths. The used enzymes to modify and purify the DNA are given in the appendix 6.3. The DNA sequences of the final hairpins can be found in the appendix 6.1.

3.1.1 Making long DNA hairpins by thermal denaturation

A 2000 bp DNA hairpin construct (P2000) was prepared by thermal denaturation of a dsDNA construct containing a palindromic sequence. A palindromic sequence is a inverted repeat of identical sequences. This allows each of the top- or bottom-strand to fold back on itself to form a hairpin. Adjacent to this palindromic sequence non-palindromic spacer sequences (Fig. 3.1a) cannot fold on themselves, but rather create ssDNA-ends. These serve as start-site for the enzyme and form spacers between the hairpin and its attachment to the surface of the flow cell and the microsphere. Thermal denaturation is used to separate the strands, allowing the folding of the DNA hairpin construct during subsequent cooling (Fig. 3.1a).

The different fragments of the complete dsDNA were created by PCR using both self-cloned and commercial plasmids. The sub-steps of the procedure were monitored by agarose gel electrophoresis (1%, TAE buffer, 1 h, 60 V) and ethidium bromide staining (Fig. 3.1b). Fragments 1 and 4 were obtained by PCR in presence of 10% modified dUTPs to create dsDNA with several biotin modified bases on one end of the construct and digoxigenin on the other end (see appendix 6.3 for protocol).

Fragments 2 and 3 were created by PCR using two plasmids that contain a sequence of lambda phage DNA. The PCRs for fragments 2 and 3 amplify equal lambda sequences in both plasmids as well as some different, plasmid-specific sequences. Ligation of fragment 2 to fragment 3 through the same restriction site overhangs (XhoI) in the lambda sequences will form the palindromic sequence (green area in Fig. 3.1a). The plasmid-specific sequences at both ends of fragment 2 and fragment 3 will not hybridize after strand separation by thermal denaturation and serve as spacers (bright blue in Fig. 3.1). Fragments 2 and 3 are digested (Fig. 3.1b) and ligated (Fig. 3.1c) to the anchors to form the dsDNA construct as sketched in Figure 3.1a. The final ligation product is purified from gel and stored at $-20°C$.

Before an experiment, the 2000 bp DNA hairpin is denatured at 99°C for 5 min and directly put on ice to favour the folding of the single DNA strands into hairpins over the reannealing to dsDNA. After thermal denaturation both strands (top- and bottom-strand both fold into hairpins) can attach to the flow cell and the microsphere.

The helicases used for this construct have a footprint of ≈ 20 bp on the ssDNA. Therefore the start site of the helicase is always the 360 nt spacer (left spacer in Fig. 3.1a). Thus, only the bottom strand construct is useful for the experiments, because it maintains the correct polarity for the used helicases (3´ to 5´). Therefore half of the constructs cannot be used for helicase experiments and can also not be distinguished. The 500 bp DNA hairpin construct presented in the next section was designed and prepared in a more efficient manner.

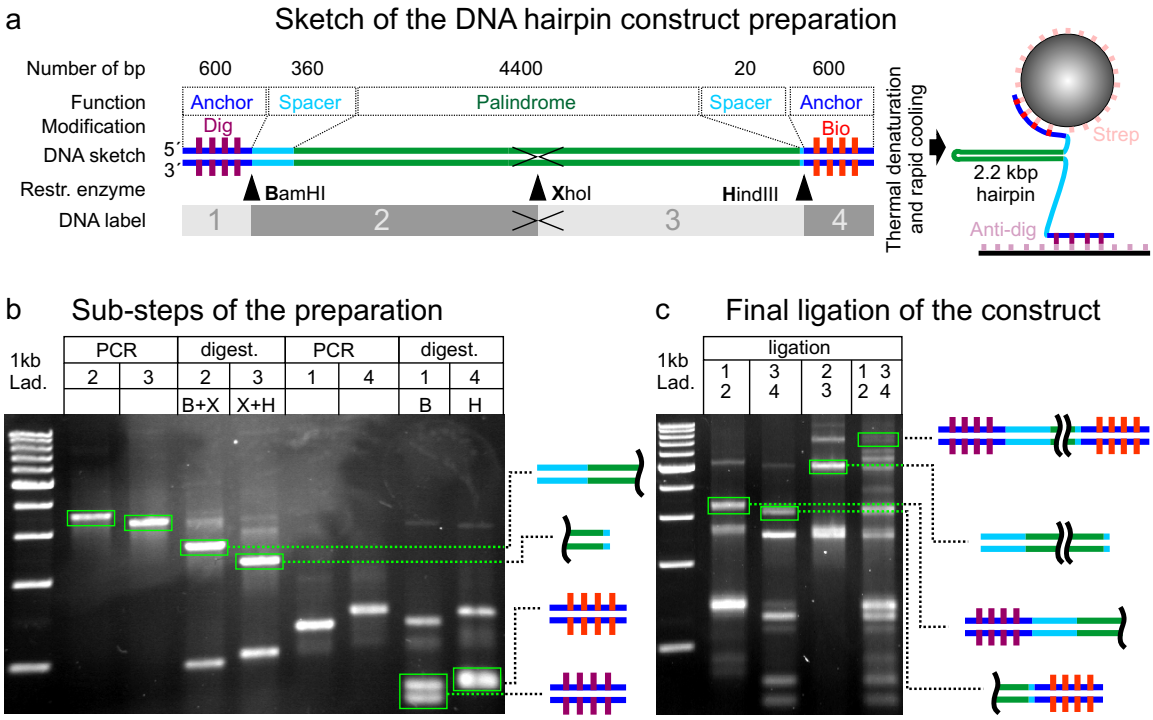

Figure 3.1 Design and preparation of a 2000 bp DNA hairpin construct (P2000). (**a**) Composition of the dsDNA, which folds into a DNA hairpin construct after thermal denaturation followed by rapid cooling. Numbers indicate the lengths of the indicated functional units in base pairs (bp). The DNA anchors contain modified bases for attachment to the microsphere and the flow cell surface (Bio: biotin, Dig: digoxigenin, Strep: streptavidin, Anti-dig: Antidigoxigenin). Black triangles point towards the restriction site of the indicated enzyme. DNA fragments indicated by gray boxes are labeled 1-4. The sketch on the right shows the folded and attached 2000 bp DNA hairpin construct as used for the experiments. (**b**) Ethidium bromide stained fragments visualized by agarose gel electrophoresis. The header specifies the performed modification, the number of the fragment as shown in (a) as well as the initial of the used restriction enzymes. The first lane contains a 1 kbp dsDNA step ladder. The bands with the main reaction intermediates are highlighted. Sketches indicate the final fragments used for ligation. (**c**) Ligation of the DNA segments specified in the header. Sketches indicate the ligated fragments.

3.1.2 Making long DNA hairpins using Lambda exonucleases

The 500 bp DNA hairpin construct (P500) was prepared with several improvements compared to the 2000 bp DNA hairpin construct presented in the last section. Firstly, the hairpin is not created by thermal denaturation of palindromic dsDNA, but by digestion of the bottom strand with an exonuclease. This leaves just the one single DNA strand with the required strand polarity for the used helicase (3´ to 5´). Secondly,

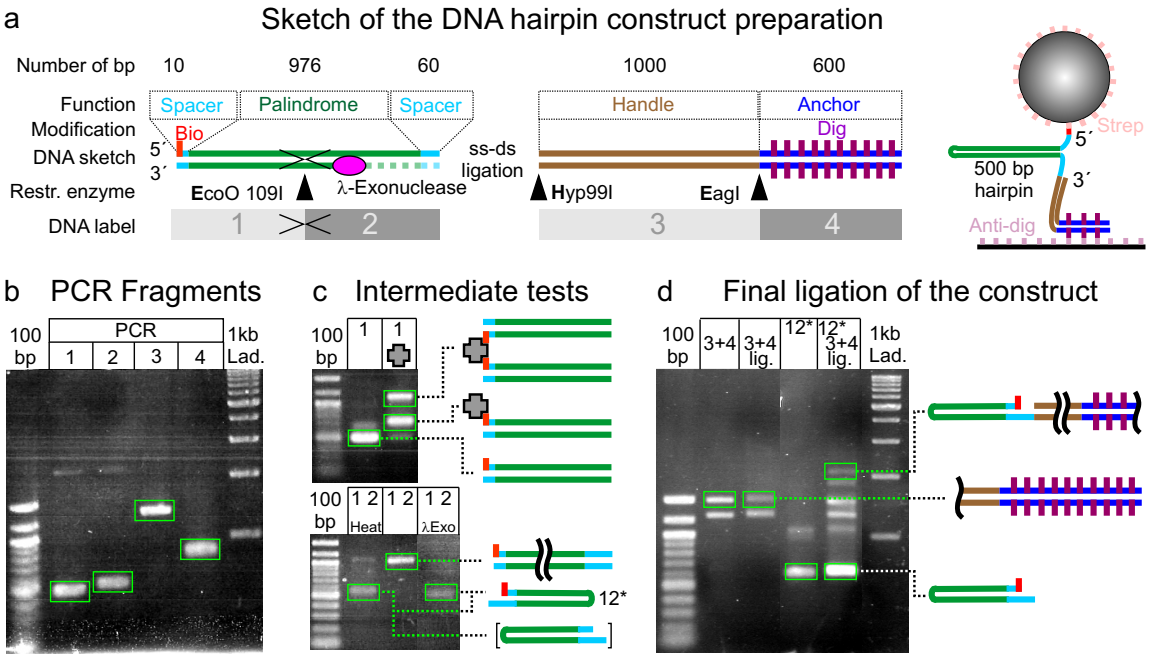

Figure 3.2 Design and preparation of a 500 bp DNA hairpin construct (P500). (**a**) Sketches the assembly of different parts of the DNA hairpin construct. Numbers indicate the lengths of the indicated functional units in base pairs (bp). DNA ends contain digoxigenin and biotin modified bases for attachment to the microsphere and the flow cell surface (Bio: biotin, Dig: digoxigenin, Strep: streptavidin, Anti-dig: Antidigoxigenin). Black triangles point towards the restriction site of the indicated enzyme. DNA fragments indicated by gray boxes are labeled 1-4 for the gel images. The sketch on the right shows the folded and attached 2000 bp DNA hairpin construct as used for the experiments. The hairpin is created by digesting the bottom strand of the ligation product of fragment 1 to 2 using lambda exonuclease. Afterwards the 3´ end of the resulting 60 nt ssDNA spacer is ligated to the sticky end of the handle (Hyp99I restriction site). (**b**) Agarose gel electrophoresis of the PCR products for the four fragments. First lane contains a 100 bp, last lane a 1 kbp dsDNA step ladder. (**c**) *top*: Streptavidin shift assay to verify biotinylation of PCR fragment 1. Lanes contain fragment 1 only and fragment 1 with 10-fold excess of streptavidin. Streptavidin is depicted by the large gray symbol, where every corner allows for binding of one biotin. *bottom*: Comparison of hairpin formation by thermal denaturation (Heat) and lambda exonuclease (λ Exo). The purified product of the lambda exonuclease method is labeled 1 2*. Sketches indicate the fragments used for ligation. (**d**) Test for self-ligation of fragment 3 to 4 and final ligation. The header indicates where ligase (lig.) was used. The bands with the correct DNA fragments are highlighted.

instead of using a long ssDNA spacers between hairpin and the surface of the flow cell a dsDNA handle was introduced. This increases the stiffness of the construct for better spatial resolution along the vertical direction (z direction). Thirdly, to reduce the number of purification steps (which is always accompanied by considerable loss of DNA product), the 600 bp biotin anchor (as used for the 2000 bp DNA hairpin construct) was replaced by a single biotinylated nucleotide. Fourthly, two asymmetric restriction sites (EcoO109I, Hyp99I) were used to prevent self-ligation of the fragments, which increases the efficiency for the desired ligation.

At first fragments 1 and 2 in Figure 3.2a are obtained by PCR (this PCR requires special attention, explained later in the text) . After digesting fragments 1 and 2 with EcoO109I, the fragments were ligated to form a palindromic sequence. The resulting dsDNA fragment is digested with 5´ lambda exonuclease (see appendix 6.3). The lambda exonuclease digests the bottom strand in 5´ to 3´ direction, which forces the top strand to fold into a hairpin, because of the palindromic sequence. This 500 bp DNA hairpin is ligated to the prepared dsDNA fragment of handle and anchor, via a ssDNA to dsDNA ligation to form the final 500 bp DNA hairpin construct.

Now some steps of the method are considered in more detail.

The forward primer of PCR fragment 1 contains a 5´ biotinylated base serving as anchor for the streptavidin coated microspheres (Fig. 3.2a). To prove the binding ability a streptavidin shift assay was performed (Fig. 3.2c upper gel). The 16.5 kDa protein streptavidin slows the migration velocity of the attached DNA during gel electrophoresis (see sketch). The resulting second band in presence of streptavidin appears because two of its four binding sites are connected to fragment 1 as sketched on the right side of Figure 3.2c (upper gel).

The DNA fragments 1, 3 and 4 are obtained by PCR using Taq polymerase (see appendix 6.3). Fragment 2 is obtained by PCR using Phusion polymerase. This is done because Phusion polymerase does not add an additional base to the end of its template sequence as Taq polymerases do. Usually this is not of importance for the constructs used here, because the PCR fragments are subsequently digested with restriction enzymes to create sticky ends to ligate them to other fragments, i.e. the ends of the PCR fragments (with the additional base) are cut off. In contrast, the 500 bp DNA hairpin does not provide a sticky end to ligate it to fragment 3, but a 3´ ssDNA-end (the spacer on the right end in Figure 3.2a). This ssDNA end is ligated to the sticky end of fragment 3, created by digestion with Hyp99I (see ss-ds ligation in Figure 3.2). To be able to ligate the 3´ end of the hairpin to the sticky end of fragment 3 with the Hyp99I sequence, the reverse primer of fragment 2 offers the inverted sequence of the Hyp99I site. Taq polymerase would add an additional base to this inverted sequence upon PCR and subsequently the 3´-end of the hairpin would not match the sticky end of fragment 3. To maintain the inverted sequence of the Hyp99I site during PCR and therewith the created 3´-end of the hairpin, Phusion polymerase, instead of Taq is required for PCR of fragment 2. All PCR fragments were visualized by gelelectrophoresis (Fig. 3.2b).

To use the 5´ lambda exonuclease the DNA need to be phosphorylated using T4 polynucleotide kinase (see appendix 6.3). The top strand of the ligated PCR fragments 1 and 2 is not digested by the exonuclease, because the biotinylated 5´-base cannot

be phosphorylated by the kinase and prevents the initiation of lambda exonuclease. To evaluate the success of this method the hairpin was compared to a hairpin created by thermal denatured (as done for the 2000 bp hairpin in the last section) (Figure 3.2c, lower gel). The bands for the hairpins produced with both methods were found at the same length, indicating that the method of strand digestion using lambda exonuclease is working. While thermal denaturation creates two hairpins (one from the top-strand, one from the bottom-strand) the method using lambda exonuclease creates only the biotinylated hairpins. This is a large advantage compared to the thermal denaturation, because only DNA hairpin constructs with the correct strand polarity are produced for the experiment.

PCR fragments 3 and 4 are digested with the restriction enzyme EagI and subsequently ligated. The resulting DNA fragment (3+4) was digested with Hyp99I to produce a sticky end to ligate it to the ssDNA 3´-end from the hairpin. The Hyp99I site was chosen, because the produced sticky end has an asymmetic base pair sequence. This prevents self-ligation of fragment 3+4, resulting in no ligation byproducts (Fig. 3.2d compare fragment 3+4 with and without added ligase). Finally the ssDNA to dsDNA ligation between the hairpin and the fragment 3+4 is performed at 4°C over 72 h and the product gel purified and stored at −20°C.

This method efficiently creates very stable DNA hairpin constructs. The stiff dsDNA handle increases the spatial resolution in vertical direction compared to the ssDNA spacer of the 2000 bp DNA hairpin construct. This is because dsDNA is much stiffer than ssDNA and because in contrast to dsDNA the long ssDNA spacer can form instable secondary structures (for example little hairpins, which open and close when a force is applied were the two states are in equilibrium) which adds vertical fluctuations. Additionally all 500 bp DNA hairpin constructs found in the flow cell have the correct strand polarity and are suited for an helicase experiment.

3.1.3 Preparing short DNA hairpins by ssDNA hybridization

DNA hairpin constructs with short hairpins are desired for experiments with helicases which unwind only several tens of base pairs. Short hairpins are created by folding of ssDNA oligomers containing inverted repeats. Oligomers which can be synthesized are limited in length (usually < 100 nt). For the shortest DNA hairpin design in this thesis, which contains 40 bp already 143 nt are required including the ssDNA spacers. Therefore the DNA hairpin is produced by hybridization of two ssDNA oligomers.

The two oligomers are sketched in Figure 3.3a (see appendix 6.1.3 for sequences). Once the two oligomers are ligated, the green parts of both oligomers in the sketch will form the hairpin. As seen in the sketch of the folded hairpin, oligomer 2 creates already the hairpin partially, because of its inverted repeat (the center of the repeat is indicated by the two arrows pointing towards each other in the DNA sketch). Oligomer 1 is hybridized to oligomer 2. The hybridization reaction is carried out in presence of 5 mM $MgCl_2$ and 200 mM NaCl by cooling an stoichiometric amount of oligomer 1 and 2 from 95°C to 10°C. Every 150 s the temperature is reduced by 1°C with a rate of 3°C/s. Afterwards the hybridized hairpin has to be ligated, therefore oligomer 2 contains a phosphate at the 5´-end. Oligomer 1 additionally contains a

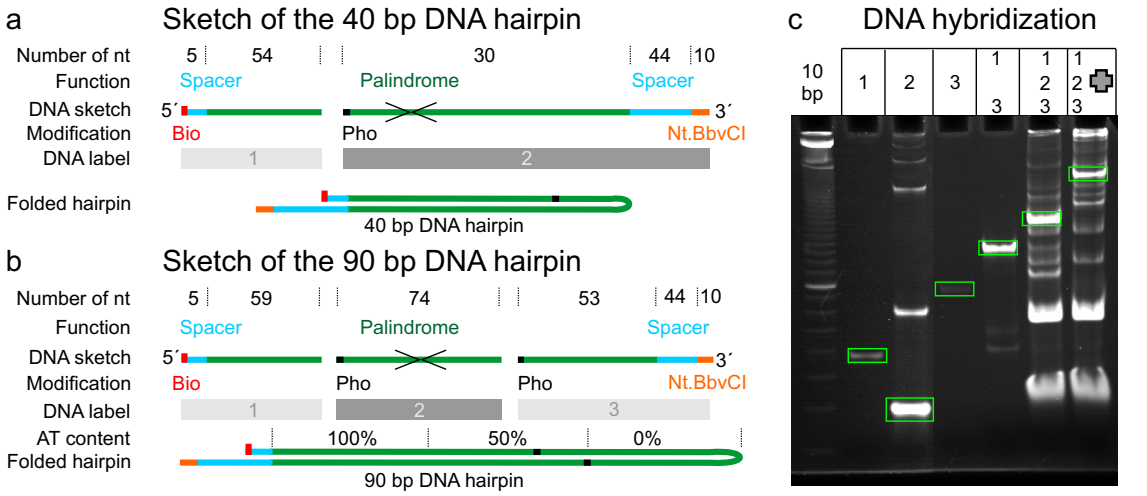

Figure 3.3 Short DNA hairpins created by ssDNA oligomer hybridization. (**a**) Sketch of the oligomers used for a 40 bp DNA hairpin. Numbers indicate the lengths of the indicated functional units in nucleotides (nt). Oligomers are labeled as indicated by gray boxes. Oligomer 1 contains a 5´ biotin modification, oligomer 2 contains a 5´ phosphorylation and the 3´ end has a special base pair sequence which allows for very efficient ssDNA to dsDNA ligation (which will be explained in detail in the next section). The sketch at the bottom shows the folded DNA hairpin. (**b**) Sketch of the oligomers for a 90 bp hairpin, as shown in a. Additionally the content of AT bases in the DNA sequence is indicated. (**c**) 8% polyacrylamide gel of the three oligomers for the 90 bp DNA hairpin. The header indicates the single oligomers or their hybridization. Streptavidin is depicted by the large gray symbol in the last lane. The main reaction intermediates are highlighted.

biotinylated base at the 5´-end as anchor for the microsphere. The 3´-end of oligomer 2 is complementary to the 3´-overhang created at the dsDNA handle (fragment 2 in Fig. 3.3a) which will be ligated to the hairpin. The strategy of creating 3´-overhangs instead of 3´ sticky ends (as done for the 500 bp DNA hairpin construct), provides a highly efficient ssDNA to dsDNA ligation. This method will be presented in detail in the following section. Finally the hybridized oligomers are ligated.

Another DNA hairpin construct, with a 90 bp long hairpin was prepared with the same hybridization method (Fig. 3.3b). To keep the individual lengths of the oligomers small, this hairpin was prepared using three oligomers (see appendix 6.1.3 for sequences). The DNA hairpin is designed to contain 90 bp with three 30 bp segments of 100%, 50% and 0% of AT bases. The hybridization reaction was carried out using stoichiometric amount of all three oligomers. The three single oligomers 1-3 are shown in a 8% polyacrylamide gel (Fig. 3.3c). oligomers 1 and 3 show a weak signal, because ssDNA can only be very inefficiently be stained with ethidium bromide. Oligomer 2 shows many bands from either secondary structures or synthesis problems which could not be reduced by thermal denaturation and rapid cooling down (data not shown). First oligomer 1 and 3 are hybridized with the same reaction conditions as for the 40 bp hairpin. This creates a 10 nucleotide 5´-overhang. This overhang is located in the 50% AT segment of the hairpin and designed to have a low probability

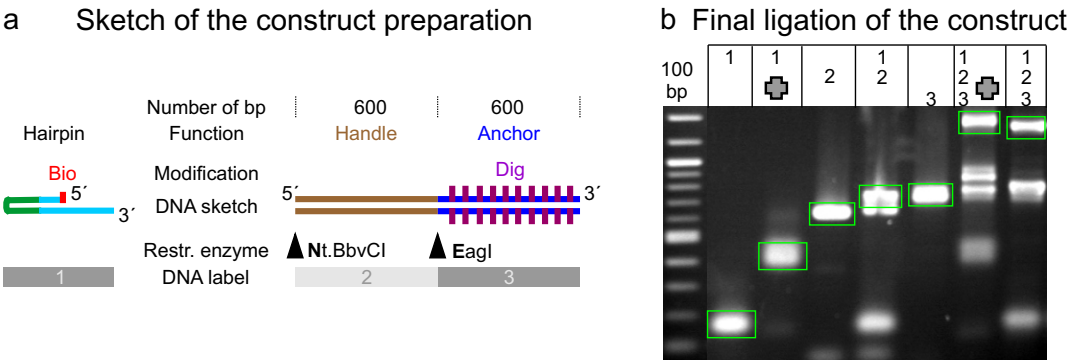

Figure 3.4 Design and preparation of short DNA hairpin constructs. (**a**) Sketches the assembly of different parts of the DNA hairpin construct. Left side sketches a hairpin prepared as shown in Figure 3.3. Right side sketches handle and anchor. Numbers indicate the lengths of the handle and the anchor in base pairs (bp). Anchor contains digoxigenin modified bases (Dig) for attachment the flow cell surface, the hairping contains a biotinylated base (Bio) for attachment to the microsphere. Black triangles point towards the restriction/ nicking site of the indicated enzyme. DNA fragments indicated by gray boxes are labeled 1-3. (**b**) 2% agarose gel to monitor the sub-steps and the final ligation of the DNA hairpin construct preparation. The header indicates the DNA fragments as labeled in (a). A streptavidin shift assay verifies the band with the final ligation product. Streptavidin is depicted by the large gray symbol. The main reaction intermediates are highlighted.

of forming secondary structures. The complementary overhang appears when oligomer 2 folds into a hairpin as designed. To connect the preformed fragment of oligomer 1 and 3 with oligomer 2 a second hybridization is carried out. This hybridization reaction starts only at 50°C to avoid destabilization of the preformed fragment of oligomer 1 and 3. The hybridized oligomers are finally ligated. The results of the hybridization are analyzed on a 8% polyacrylamide gel (Fig. 3.3c). A streptavidin shift assay identifies the correct band, which was subsequently purified from the gel (see appendix 6.3).

To prepare a final DNA hairpin construct, the created hairpins need to be ligated to the DNA handle and the DNA anchor (Fig. 3.4a). Handle and anchor are prepared as explained for 500 bp DNA hairpin construct (see previous section) and attached to the hairpin by ssDNA to dsDNA ligation. The intermediate products of the DNA hairpin preparation as well as the final ligation were visualized by agarose gel electrophoresis (Fig. 3.4b).

The ssDNA to dsDNA ligation (hairpin to handle) during the preparation of the 500 bp DNA hairpin construct was efficient (see Figure 3.2d). In contrast, ssDNA to dsDNA ligation with the same method was much more inefficient during the preparation of the short 40 and 90 bp hairpins. The reason could not be clearly identified, but may have been due to formation of secondary structures which reduced the accessability of the 3´-end of the hairpins. To overcome these problems, an improved method for the ligation of ssDNA to dsDNA was developed and will be presented in the following section.

3.2 Improving ssDNA to dsDNA ligation

The efficiency of hybridization of two complementary ssDNA strands depends on the number of complementary bases which can hybridize. The hybridization of a ssDNA-end to the complementary overhang of a sticky-end (created by digesting dsDNA with a restriction enzyme) is an equivalent problem. The question adressed in this section is how much the ligation efficiency of ssDNA to dsDNA is effected by the number of complementary bases. This is of importance to improve the construction of DNA hairpin constructs as mentioned in the previous sections.

A bulk experiment was performed to test the ssDNA to dsDNA ligation efficiency. The ssDNA-end is the 3´-end of a 40 bp DNA hairpin (previous section, Fig. 3.3a, spacer on the 3´-end) and is designed to contain the complementary sequence to a sticky end. The sticky end is created by digesting a dsDNA handle (previous section, Fig. 3.4a, restriction site on the left side of the handle). First, a 4 nucleotide 3´-overhang generated by digesting the handle with the restriction enzyme BstXI was tested. (The BstXI site is variable, i.e. several bases of the restriction site can be exchanged without affecting its activity. The restriction site was designed such that no self-ligation can occur.) Therefore the hairpins and handles were ligated with a 10-fold molar excess of hairpins over the handles. The ligation was carried out for 1 h at room temperature. The results are shown in Figure 3.5a, lanes 1-5. Lane 1 shows the 40 bp DNA hairpin only, lane 2 a shift of the DNA hairpin band, induced by adding streptavidin and lane 5 shows the handle only. In lanes 3 and 4, hairpin and handle are mixed and ligated. Lane 4 in Fig. 3.5a shows no streptavidin induced shift of the ligated product. This means either hybridization or the subsequent ligation failed when using a 4 nucleotide overhang.

In a second test of ssDNA to dsDNA ligation a longer 3´-overhang at the handle was created. A BbvCI site was incorporated into the primer that is used to produce a dsDNA handle by PCR. After nicking the handle using Nt.BbvCI followed by a 5 min heat denaturation at 50°C to displace the small fragment, a 10 nucleotide long 3´-overhang formed (Fig. 3.5b). The 3´-end of the 40 bp DNA hairpin is designed to contain the complementary sequence to this overhang. This overhang supports highly efficient hybridization and subsequent ligation of the 3´-end of the 40 bp hairpin. The success of the ssDNA to dsDNA ligation was confirmed by gel electrophoresis (Fig. 3.5a, lanes 6-10). Lanes 6 and 7 shows the streptavidin shift for the 40 bp hairpin only, lane 10 shows the handle only. Lanes 8 and 9 shows that the desired ligation product specifically shifted. This means the 10 nucleotide overhang shows a much higher ligation efficiency, compared to the 4 nucleotide overhang.

The correct covalent attachment of the hairpin to the dsDNA handle was also verified in a magnetic tweezers experiment. To support the tethering of the molecule, a 600 bp anchor with digoxigenin modified bases was ligated to the dsDNA handle and a biotin was added to the 5´-end of the hairpin (see Figure 3.4). A sufficiently high force was applied on the hairpin construct, which allowed its transient unfolding and the folded and unfolded state to be approximately equally populated (Fig. 3.5c). The difference in DNA extension between the two states was 38 nm corresponding to ≈ 80 nucleotide as expected for a 40 bp hairpin.

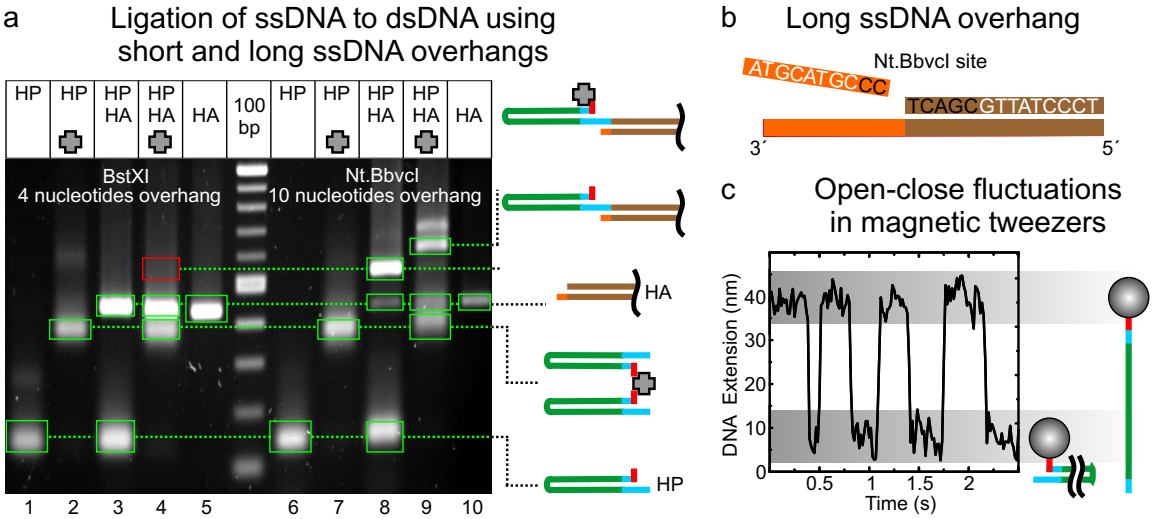

Figure 3.5 Improved ssDNA to dsDNA ligation using long ssDNA overhangs. (**a**) 2% Agarose gel of DNA fragments, ligation products and streptavidin-induced band shifts. Lanes 1-5 contain the reaction products for the 4 nt overhang generated by BstXI. Lanes 6-10 contains reaction products for the 10 nt overhang generated by Nt.BbvCI. The lane in the middle is a 100 bp DNA step ladder. The header indicates where the biotinylated 40 bp hairpin (HP), the 430 bp dsDNA handle (HA) and streptavidin (gray symbol) were used in the reaction. The bands with the main reaction intermediates are highlighted. Sketches on the right represent the fragments in the band. (**b**) Schematic representation of overhang generation. A BbvCI recognition site (black letters) was incorporated near the DNA end in such a way that nicking with Nt.BbvCI generates a 10 nt fragment at the 5´-end. (**c**) Magnetic tweezers experiment with the prepared hairpin construct. The molecule was held at the critical force where the closed and the opened states of the hairpin (as illustrated by the sketches) were equally populated. The change in height between the two states was $\approx$ 38 nm as expected for a 40 bp hairpin.

3.3 Determining the unzipping force of DNA hairpin constructs

Knowing the applied forces in an helicase experiment is important, because the force influences the DNA junction where the helicase is acting. The forces in magnetic tweezers can be measured for a certain magnet position (see section 2.3.1). Usually the applied force at any given distance of the magnets from the flow cell surface is estimated from a force-distance calibration curve. It is obtained by measuring forces for different magnet positions and extrapolating the forces for all magnet positions by fitting a function to the forces (the force-distance calibration curve, see section 2.3.2). This method usually takes up to 30 min. A faster way to determine the force-distance calibration curve is explained in the following section.

The force-distance calibration curve is determined by a decay and the absolute value of the force. The decay is the same for a specific set of magnets and microspheres and is found by averaging all determined decays of all experiments using the same magnets and microspheres (independent of the DNA construct, buffer conditions, etc.). The absolute force values vary due to variabilities between individual microspheres

(see section 2.3.2). Instead of measuring the forces to determine the force-distance calibration curve we use the property of DNA hairpins, that under the same conditions (ionic strength, temperature) a specific DNA hairpin will always unzip at the same force. Thus to determine the force-distance calibration curve for every experiment the decay and at least one magnet position. The corresponding force is required (one point of force-distance calibration curve). The decay is known as mentioned above. For a magnet position and the corresponding force we choose the magnet position where the hairpin unzips. The corresponding force where the hairpin unzips need to be determined for every DNA hairpin in every used buffer, because the unzipping force is DNA sequence dependent [97, 98] and depends on ionic strength of the surrounding buffer. In the following two sections these unzipping forces are determined. The force-distance calibration for these experiments has been performed by measuring forces as explained in section 2.3.4. The compositions of the used buffers can be found in the appendix 6.2.2.

In the first section the unzipping forces of long DNA hairpins are determined. In the second section the unzipping forces of short DNA hairpins are determined. In the last section the DNA hairpin unzipping is decribed theoretically to support the determined unzipping forces.

3.3.1 Unzipping forces of long DNA hairpins

The unzipping force can be found by slowly approaching the magnets (increasing force) to the flow cell to find the magnet position where the hairpin unzips. The energy landscape of the DNA sequences tilts under application of force which changes the free energy difference between open and close state. The used long DNA hairpins (500 and 2000 bp) unzip in several steps, i.e. the several intermediate states between close and open hairpin are sufficiently stable over time to be detected (Fig. 3.6a). This unzipping pattern is characteristic for every DNA hairpin and depends on the approaching velocity of the magnets. A fast approach of the magnets will cause the DNA hairpin to unzip at a higher magnet position, than a slower approach of the magnets (Fig. 3.6a). Additionally, a fast approach of the magnets causes a larger variance of the mean magnet position at which the unzipping occurs (Fig. 3.6a compare gray curves). Equilibrium conditions for the relaxation of the base pairs would only be achieved with an infinitly slow velocity of the magnets. The finite velocity of the magnets in the experiment will shift this equilibrium, i.e. while approaching with the magnets the opened state of the base pairs is favoured and while withdrawing the magnets the closed state of the base pairs is favoured (compared to the equilibrium state). This causes different patterns for unzipping and rezipping of the DNA hairpin as well as a hysteresis between the mean magnet position of unzipping and rezipping (Fig. 3.6b). To define the magnet position which will be used to determine the unzipping force, the patterns were investigated for reproduceable features. Therefore the constructs with long DNA hairpins were slowly (0.005 mm/s velocity of the magnets) unzipped and rezipped in repeated cycles (Fig. 3.6b shows the data for the 500 bp DNA hairpin construct). The most reproduceable feature in the unzipping pattern is the last step of hairpin opening (Fig. 3.6b upper plot,

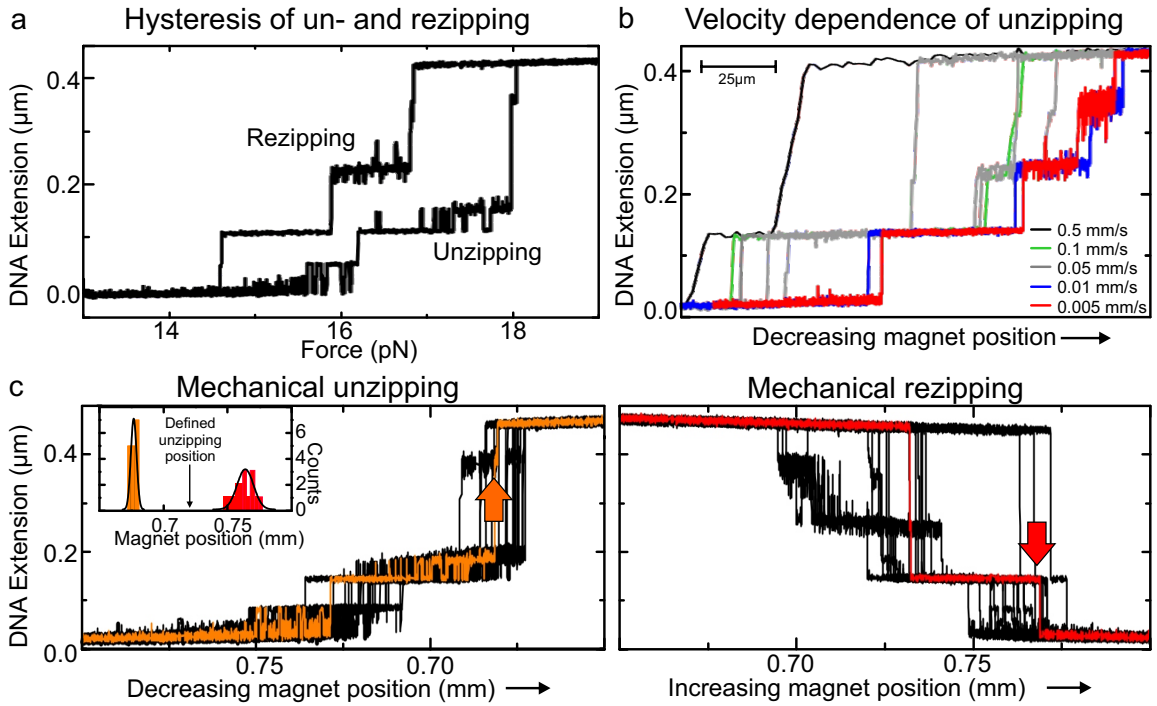

Figure 3.6 Mechanical unzipping of the 500 bp DNA hairpin construct. (**a**) Hysteresis between unzipping and rezipping. (**b**) Hairpin unzipping patterns for different approaching velocities of the magnets as indicated. The three gray curves (all 0.05 mm/s) demonstrate the possible variations when the velocity is too fast. The patterns for 0.01 and 0.005 mm/s are similar in repeated runs. (**c**) *Left*: Repetitive mechanical unzipping of a single 500 bp DNA hairpin at a velocity of the magnets of 0.005 mm/s. Black traces are 17 repetitions, orange is an individual unzipping trace. Arrow indicates the last step of hairpin opening. *Right*: Repetitive mechanical rezipping of the same DNA hairpin construct as in (a). Black traces are 17 repetitions, red is an individual rezipping trace. Arrow indicates the final rehybridization step of the DNA hairpin closing. *Inset*: Distribution of the 17 magnet positions of the last step of hairpin opening (orange) and the last step of hairpin closing (red) and the defined magnet position used to determine the unzipping force.

indicated by an arrow). For the rezipping pattern the final rehybridization step to the completely closed hairpin shows a rather narrow distribution (Fig. 3.6b lower plot, indicated by an arrow). The distribution of the rezipping intermediates are considerably broader than for unzipping. This maybe caused by the formation of secondary structures in the free ssDNA. During rezipping these secondary structures might occur just along one of the single strand and thus result in mismatches along the rest of the hairpin sequences. The energetically more favourable conformation of the matching dsDNA might be formed slower at random times, thus resulting in different rehybridization patterns. The magnet position which is used to determine the unzipping force was defined to be the average of the mean values of the last step of hairpin unzipping and the final rehybridization step of hairpin rezipping (Fig. 3.6b inset). Now the unzipping force for the DNA hairpin can be extrapolated by using the (afore measured) force-distance calibration curve (Equation 2.21 in section 2.3.2)

and the just determined magnet position for DNA hairpin unzipping.

The mean unzipping force of 19 of the 500 bp DNA hairpin constructs was found to be 16.6 ± 1.4 pN in the buffer RBTAg. The error of ≈10% (standard deviation) of the unzipping force might occur due to varying temperatures or propagated errors from the force-distance calibration. Additionally the error might be caused by varying ion concentrations between the measurements [99]. The DNA hairpin stability depends on the ionic conditions of the surrounding buffer [100, 101]. Therefore the unzipping force needs to be determined for the particular reaction buffer used. The two buffers used most often are the reaction buffers for the helicase experiments RBTAg and RBRecQ (see appendix 6.2.2). The same procedure was performed to determine the unzipping force of the 2000 bp DNA hairpin. The following values for the unzipping force have been determined:

Buffer	P500	P2000
RBRecQ	15.8±1.2	-
RBTAg	16.8±1	17.2±1.5

Table 3.1 Unzipping forces for the used long DNA hairpins in different buffers. The error is the standard deviation.

These values of the unzipping forces of the 500 and 2000 bp DNA hairpin construct have been used for rapid calibration of the DNA-microsphere systems before an experiment. The procedure is to slowly mechanical un- and rezip the hairpin in the used reaction buffer and determine the magnet positions where the hairpin opens and closes, respectively. Then the defined position for DNA hairpin unzipping is determined by finding the mean of un- and rezipping as mentioned above. This magnet position together with the corresponding force from table 3.1 provide one point in the force-distance calibration curve (Equation 2.21). The average decay of the used magnets-microsphere combination, which has been determined during several different force measurements (it is independent of the DNA construct or the buffer) are used to complete the determination of the force-distance calibration. The used values for the decays are:

Magnets	MagSense	M280
N50 magnets	5.3±0.2	4.2±0.1

Table 3.2 Mean decay values (d in Equation 2.21) of the force change upon moving the magnets by 1 mm. Error is the standard error of the mean.

The procedure to determine the unzipping forces of short DNA hairpins is different, because the DNA hairpin opens and closes without detectable intermediate steps. This allows to describe the hairpin dynamics as a simple two state system as shown in the following section.

3.3.2 Unzipping forces of short DNA hairpins

The flat energy landscape of the sequence of the 40 bp DNA hairpin construct provides that the hairpin does not unzip over a range of forces (with intermediate pauses causing a pattern as displayed by long DNA hairpins, see previous section). The 40 bp DNA hairpin rather opens and closes completely in a single transition (Fig. 3.7a). The first four base pairs of the hairpin are only GC bases and act as a clamp to stabilize the closed state (see Appendix 6.1 for the base pair sequence). The four T nucleotides in the hairpin loop help to stabilize the open state. Thermodynamic fluctuations cause continuous switching between the two states (Fig. 3.7a). The population of the open and closed state depend on the applied force. The force where the open and closed state are equally populated is defined as the unzipping force. It can be

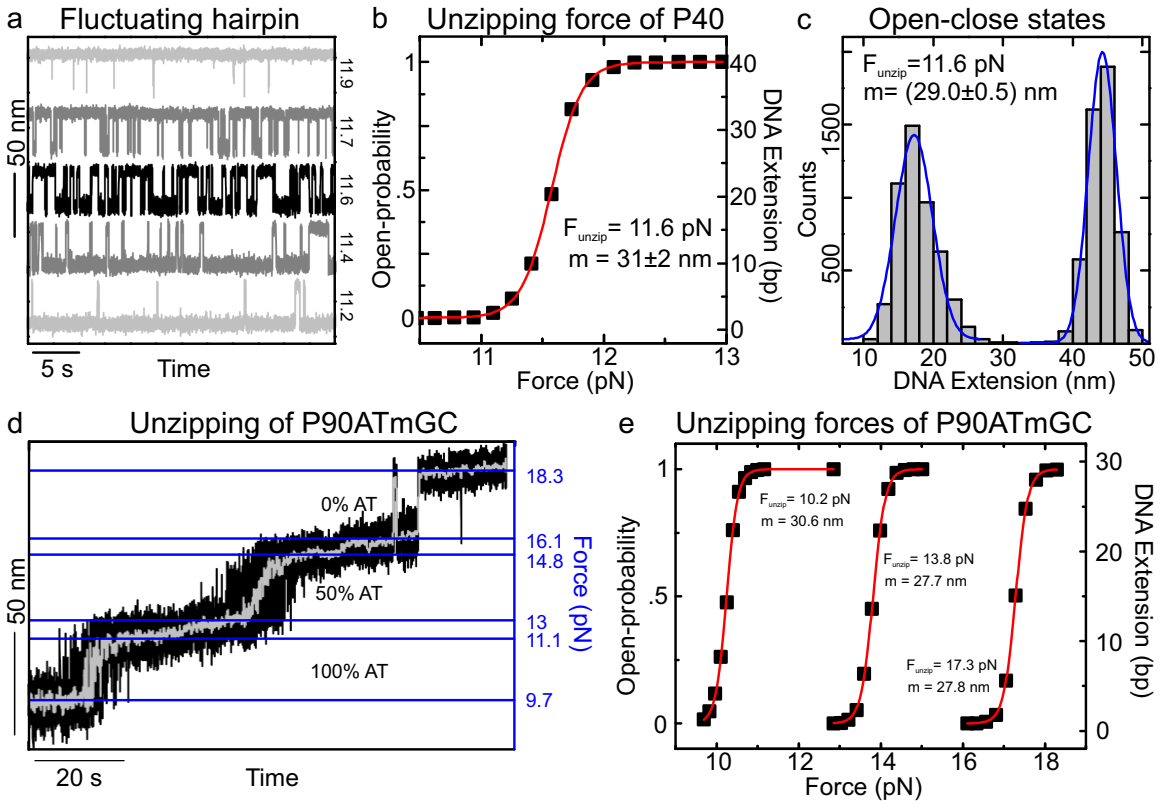

Figure 3.7 Unzipping forces of the 40 and 90 bp DNA hairpin. (**a**) DNA extension of the 40 bp DNA hairpin around the unzipping force. Forces are indicated next to each trajectory. Open and close state are equally populated (50% of the time in open state and 50% of the time in the close state) at the unzipping force (black curve). (**b**) Probability of the hairpin to be open fitted with equation 3.1 to determine the unzipping force and the distance between close and open state. Fitvalues are indicated. (**c**) Distribution of DNA extension in open (right peak) and close (left peak) states of the black curve in a. The centers of the fitted gaussians have a distance of 29 ± 0.5 nm. (**d**) Unzipping of the 90 bp DNA hairpin construct. Forces on the right indicate the limits of each regions of different AT content as indicated. (**e**) Probabilities of the three regions with different AT content to be open fitted with equation 3.1. Fit values are indicated.

determined by fitting the probability of the hairpin to be in the open state $P_{\text{open}}(F)$ with a Boltzmann relation for a two state system [102]:

$$P_{\text{open}}(F) = \frac{1}{1 + \exp\left(\frac{(F_{\text{unzip}} - F)m}{k_{\text{B}}T}\right)}. \tag{3.1}$$

The probability is determined from the experimental time trajectories (Fig. 3.7a). Therefore a threshold between open and close state for each trajectory is defined by the center between the two populations. The probability of the hairpin to be open is then defined by the time the hairpin spends above the threshold devided by the measurement time. The probabilities of the 40 bp DNA hairpin are shown in Figure 3.7b with a fit using equation 3.1. The fitted unzipping force is 11.6 pN. Additionally to the unzipping force the distance between the open and close state m is found (see Equation 3.1). The fitted distance is 31 ± 2 nm.

An independent test to verify the unzipping force and the distance between open and close state is conducted. The distribution of the open and close state at the unzipping force (equally populated states) are fitted with Gaussian distributions to find the DNA extension in the corresponding state (Fig. 3.7c). The difference between the DNA extensions at the open and close state correspond to the ssDNA extension of 83 nucleotides (40 bp+3 nucleotides loop) at the unzipping force. The ssDNA extension of 83 nucleotides at a tension of 11.6 pN can be calculated with the extensible freely jointed chain (FJC) model [103]:

$$z(F) = L_0 \left[\coth\left(\frac{Fb}{k_{\text{B}}T}\right) - \frac{k_{\text{B}}T}{Fb}\right]\left(1 + \frac{F}{S}\right) \tag{3.2}$$

where L_0 is the contour length of the ssDNA, b the segment-length and S the elastic stretching modulus. The values of the parameters b and S were fixed during the fitting and have been adapted from reference [39] with $b = 1.594$ nm, $S = 530$ pN. The ssDNA extension of 83 nucleotides at 11.6 pN was found to be 29 ± 0.5 nm in agreement with the fitted distance m using Boltzmann statistics (Equation: 3.1).

A 90 bp DNA hairpin construct was characterized in a similar way. The 90 bp DNA hairpin contains three DNA sequence regions, where 33 bp contain only AT base, 30 bp contain 50% of AT bases and 30 bp contain no AT bases (see section 3.1.3). This DNA hairpin does not unzip in one step, because the different base pairing energies of the three sequence regions result in three different unzipping forces (Fig. 3.7d). The three regions can be investigated independently, because the forces where the regions become unstable and start to fluctuate are sufficiently distant (e.g. in Figure 3.7d at 12 pN the 100% AT region is already stably open and the 50% AT region is still stably closes). The probability of the different regions to be open is determined similarly to the 40 bp DNA hairpin (Fig. 3.7e). The probabilties of the regions to be open were fitted with equation 3.1. The extensions of the individual regions were tested as shown for the 40 bp DNA hairpin and were found to be in agreement with the expected extension using equation 3.2 (100% AT: 33 bp at 10.2 pN yields 28.2 nm, 50 % AT: 30 bp at 13.8 pN yields 28.3 nm, 0 % AT: 30 bp+4 nucleotides loop at 117.3 pN yields 31.9 nm). The results of the unzipping force calibration for the 40 and 90 bp DNA hairpin in the buffer RBRecQ (see Appendix 6.2.2 for composition) are:

Buffer	P40	P90ATmGC
RBRecQ	11.6±0.8	(100% AT) 9.8±1.7/(50% AT) 13.2±1.2/(0% AT) 17.2±2.1

Table 3.3 Unzipping forces for the used short DNA hairpins in buffer RBRecQ (see Appendix 6.2.2 for composition). Errors indicate the standard deviation.

3.3.3 Mechanical DNA unzipping - theory

The large variations of the determined unzipping forces for all used DNA hairpin constructs can originate from heterogenity between individual hairpin constructs, variations in temperature or ionic strength between measurements or variations in the force determination. Additionally the large hysteresis ($\approx$ 2 pN) between unzipping and rezipping of the long DNA hairpins as well as the large range of forces to completely unzip and rezip long DNA hairpins can cause variations in the determined unzipping force between individual constructs. To verify the determined unzipping forces obtained in the previous section, the unzipping behavior is theoretically predicted in analogy to reference [104] for optical tweezers measurements.

The probability $p(j)$ of the DNA hairpin to be open at the base pair with index j (starting from the beginning of the hairpin, see fig. 3.8a) depends on the total free energy of the system $E_{\mathrm{total}}(j, F)$. The theory is an equilibrium approach and neglects dynamic contributions (e.g. varying force over time, non-equilibrium intermediate states), temperature variations or any drag forces of the DNA construct or the microsphere. Additionally the dsDNA handles are neglected, because of their high stiffness compared to the ssDNA [104]. The probability $p(j)$ is calculated with Boltzmann statistics:

$$p(j, F) = \frac{1}{\mathbf{Z}} e^{\frac{-E_{\mathrm{total}}(j,F)}{k_{\mathrm{B}}T}} \tag{3.3}$$

with the partition function $\mathbf{Z}$ to normalize the probability:

$$\mathbf{Z} = \sum_{\mathrm{states}} e^{\frac{-E_{\mathrm{total}}(j,F)}{k_{\mathrm{B}}T}}. \tag{3.4}$$

The states of the system will be derived in the following way. The total free energy of the system depends on the base pairing energy in the DNA hairpin sequence ΔG_{bp} (which itself depends on the ionic conditions of the sourrounding buffer), the applied external force (which extends the already unzipped ssDNA) ΔG_{el} and the temperature. Additionally thermal fluctuations of the free ssDNA $\Delta G_{\mathrm{therm}}$ will contribute to the total free energy. The different energetic terms in detail are firstly, the base pairing energy, which is the energy gained when opening the bases from 1 to j:

$$\Delta G_{\mathrm{bp}}(j) = \sum_{n=1}^{j} \Delta G_{\mathrm{ATGC}}(n) \tag{3.5}$$

where the $\Delta G_{\mathrm{ATGC}}(n)$ is the energy of the specific AT or GC base at position n. These energies are obtained using the online server *mfold* [105]. It calculates the base

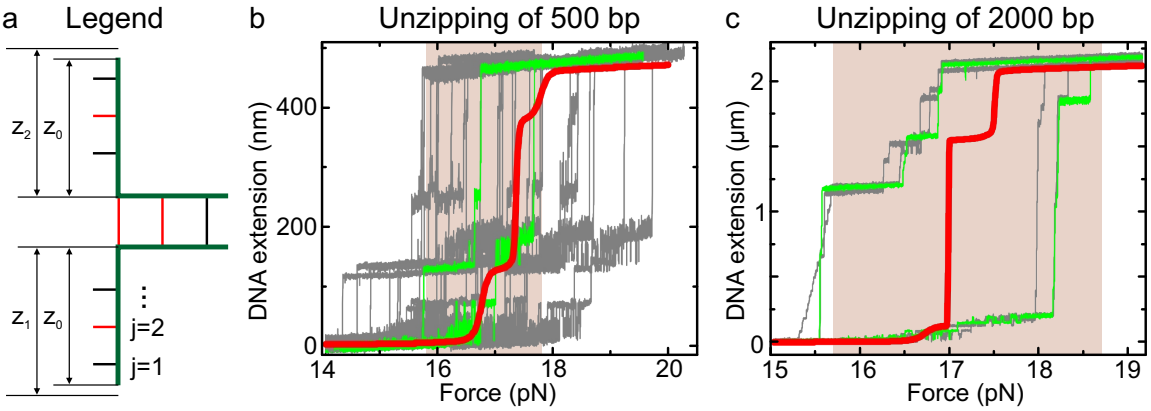

Figure 3.8 Prediction of the unzipping pattern of the 500 and 2000 bp DNA hairpin. (**a**) Sketch of the DNA hairpin junction. The distance z_0 is the ssDNA extension at the current force, z_1 and z_2 are the distances due to thermal fluctuations in both ssDNA linkers and j counts the base pairs. (**b**) 13 representative un- and rezipping traces of the 500 bp DNA hairpin in the buffer RBTAg (gray) (see appendix 6.2.2 for buffer composition). A single trace is highlighted in green. The center of the brown area indicates the experimentally determined mean unzipping force and its width corresponds to the standard deviation. The red curve shows the predicted mean number of unzipped base pairs using equation 3.14. Parameters for the base pairing energy determined using *mfold*: $T = 23°\mathrm{C}$, 50 mM Na ions, 2.013 mM Mg ions. (**c**) Same as in (b) for the 2000 bp DNA hairpin construct with 3 representative un- and rezipping traces.

pair energies according to the nearest neighbor model [106] and considers corrections for some ionic condition [107] (details at the end of this section).

Secondly, the elastic energy to stretch the (already unzipped) ssDNA of j nucleotides to an extension of z_0 at the given force (see Fig. 3.8a):

$$\Delta G_{\mathrm{el}}(j, F) = \int_0^{z_0(F)} F(z_0)\mathrm{d}z_0' = F(z_0)z_0 - j\int_0^{F(z_0)} z_0(F')\mathrm{d}F' = G_{\mathrm{el}}(j, z_0) \qquad (3.6)$$

where the ssDNA extension is described with a FJC model (see equation 3.2). The inversion of the FJC model is done numerically. Thirdly, the gain in potential energy due to the increasing ssDNA, which is simply $F_{\mathrm{mag}}(z_0)z_0$, with F_{mag} beeing the applied magnetic force. Fourthly, the free energy change due to thermal fluctuations in the free ssDNA:

$$\Delta G_{\mathrm{therm}}(j, z_1, z_2) = \frac{1}{2}\frac{\partial F}{\partial z_0}\left((z_1 - z_0)^2 + (z_2 - z_0)^2\right) \qquad (3.7)$$

where we assume a harmonic potential for small fluctuations of the ssDNA with a spring constant of $k = \partial F(z)/\partial z$ (F(z) is the inverse FJC model, a detailed derivation of k will follow). In thermal equilibrium $z_1 = z_2 = z_0$ and so the term to describe the thermal fluctuations vanishes.

Thus, the total free energy of the system with small thermal fluctuations in the

ssDNA is:

$$E_{\mathrm{total}}(j,z_1,z_2) = \Delta G_{\mathrm{bp}}(j) + 2\Delta G_{\mathrm{el}}(j,z_0) - 2F_{\mathrm{mag}}(z_0)z_0 + \frac{1}{2}\frac{\partial F}{\partial z_0}\left((z_1-z_0)^2+(z_2-z_0)^2\right). \tag{3.8}$$

In the second and third term of this equation we assume the ssDNA length z_1 and z_2 to be similar to z_0 (small displacements). The factors of two in the second and third term of this equation considers that for one unzipped base pair two nucleotides are released. The total free energy at a given force now depends on the position of the DNA junction j and the displacements z_1 and z_2. To calculate the probability of the system to be at the base pair with index j the energies of all displacement states of the system are summed up, i.e. integrate analytically over the displacements z_1 and z_2:

$$p(j,F,z_1) = \int_{-\infty}^{+\infty} e^{\frac{-E_{\mathrm{total}}(j,z_1,z_2)}{k_{\mathrm{B}}T}}\,\mathrm{d}z_2 = \frac{\sqrt{2\pi k_{\mathrm{B}}T}\,e^{\frac{-\Delta G_{\mathrm{bp}}-2\Delta G_{\mathrm{el}}+2F_{\mathrm{mag}}z_0-1/2((z_0-z_1)^2k)}{k_{\mathrm{B}}T}}}{\sqrt{k}} \tag{3.9}$$

and

$$p(j,F) = \int_{-\infty}^{+\infty} e^{\frac{-E_{\mathrm{total}}(j,z_1)}{k_{\mathrm{B}}T}}\,\mathrm{d}z_1 = \frac{2\pi k_{\mathrm{B}}T\,e^{\frac{-\Delta G_{\mathrm{bp}}-2\Delta G_{\mathrm{el}}+2F_{\mathrm{mag}}z_0}{k_{\mathrm{B}}T}}}{k} \tag{3.10}$$

with the spring constant k as introduced above. The spring constant is the derivative of the force-distance dependence of ssDNA $k = \partial F(z)/\partial z$. Because the spring constant is the denominator k^{-1} and $\mathrm{d}x/\mathrm{d}y = 1/\mathrm{d}y/\mathrm{d}x$, one can differentiate the FJC model $\partial z(F)/\partial F = k^{-1}$ (equation 3.2) and this yields:

$$k(j,F)^{-1} = jL_0\left[\frac{\left[1-\coth\left(\frac{Fb}{k_{\mathrm{B}}T}\right)^2\right]b}{k_{\mathrm{B}}T} + \frac{k_{\mathrm{B}}T}{F^2b}\right]\left(1+\frac{F}{S}\right) + \frac{jL_0\left[\coth\left(\frac{Fb}{k_{\mathrm{B}}T}\right)-\frac{k_{\mathrm{B}}T}{Fb}\right]}{S}. \tag{3.11}$$

The total free energy of the system in equilibrium is:

$$E_{\mathrm{total}}(j) = -\Delta G_{\mathrm{bp}} - 2\Delta G_{\mathrm{el}} + 2F_{\mathrm{mag}} \tag{3.12}$$

Finally the probability to find the DNA hairpin under the tension F opened at the base pair j is:

$$p(j,F) = \frac{k(j,F)^{-1}e^{\frac{-E_{\mathrm{total}}(j)}{k_{\mathrm{B}}T}}}{\sum_j k(j,F)^{-1}e^{\frac{-E_{\mathrm{total}}(j)}{k_{\mathrm{B}}T}}} \tag{3.13}$$

with $E_{\mathrm{total}}(j) = -\Delta G_{\mathrm{bp}} - 2\Delta G_{\mathrm{el}} + 2F_{\mathrm{mag}}z_0$. To obtain the mean number of unzipped base pairs N_{unzip} at the force F the probabilities of the hairpin to be at the positions j are summed up:

$$N_{\mathrm{unzip}} = \sum p(j,F)\; j. \tag{3.14}$$

Fig. 3.8b,c compares the calculated unzipping patterns using equation 3.14 to the measured unzipping patterns of the long (500 and 2000 bp) DNA hairpins from section

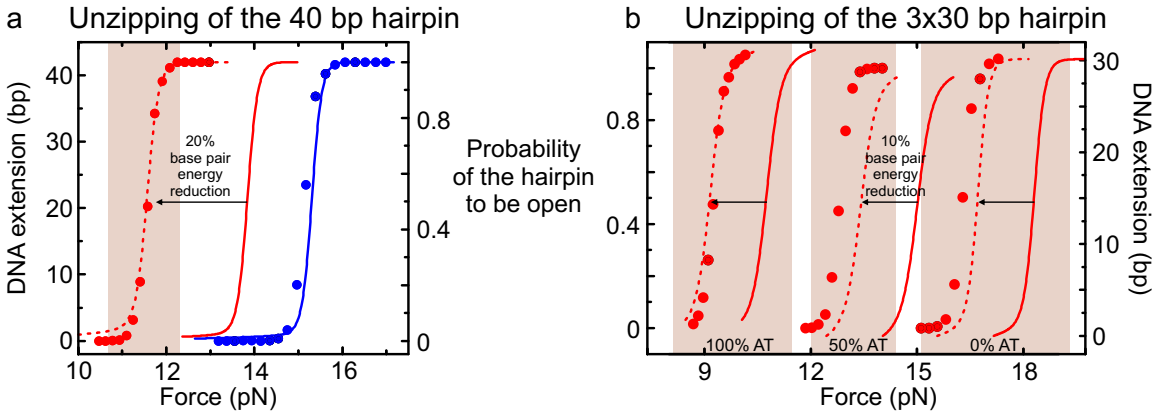

Figure 3.9 Prediction of the of the probability of the 40 and 90 bp DNA hairpin to be open. (**a**) Probability of a representative 40 bp DNA hairpin to be open as a function of applied force. Probabilities (filled circles) were determined as explained in section 3.3.2 where measured in three buffers of different ionic strength (blue: test buffer, red: RBRecQ, see appendix 6.2.2 for buffer composition). The center of the brown area indicates the experimentally determined mean unzipping force in RBRecQ and its width corresponds to the standard deviation. Solid lines are the theoretical prediction to the correspondingly colored measurement. Parameters for the base pairing energy determined using *mfold*: $T = 23°C$, 100 mM Na, 10 mM Mg (test buffer), $T = 23°C$, 10 mM Na, 0.27 mM Mg (RbRecQ). Red dashed line is a shift of the theoretical prediction in buffer RBRecQ by reducing the base pairing energies determined with *mfold* by ≈20% indicated by the arrow (see text). The left axis is obtained by assigning 42 bp (40 bp hairpin and 4 nucleotides hairpin loop) to the probability of 1. (**b**) Probability of the three 30 bp regions of a representative 90 bp DNA hairpin and the corresponding theoretical prediction as in (a). The centers of the brown areas indicate the experimentally determined mean unzipping forces in RBRecQ and their widths correspond to the standard deviations. The base pairing energy determined with *mfold* was reduced by ≈10% indicated by the arrows (see text). The calculations were done on the complete 90 bp DNA hairpin sequence. The calculated curve was split afterwards (see text). The left axis is obtained by assigning 33 bp to the 100% AT, 30 bp to the 50% AT and 32 bp to the 0% AT region (see short DNA hairpin section 3.1.3) to the probability of 1.

3.3.1. The measurements were done in the reaction buffer of T-Antigen (RBTAg, see appendix 6.2.2), because the long DNA hairpins are mainly used for experiments with this helicase (presented in the following chapter). The ionic strength of the buffer is considered in the calculation of the base pairing energy (see Fig. 3.8b). Although the variations in the unzipping traces are rather large, the theoretical curve largely matches the defined mean unzipping force (most of the red curve lies in the brown shaded area). Additionally some features of the unzipping pattern match the theoretical prediction (especially some of the intermediate stable unzipping states).

Fig. 3.9a,b compares the the measured probability of the short hairpins to be in the open state (section 3.3.2) to the calculated probability $p(j)$ of the DNA hairpin to be open at the base pair with index j using equation 3.13. The 40 and 90 bp DNA hairpins were unzipped in the reaction buffer of AtRecQ2 and AtRecQ3 (RBRecQ,

see appendix 6.2.2), because the short DNA hairpins are mainly used for experiments with RecQ helicases (presented in the chapter after the following). Since the exact ionic strength of the buffer RBRecQ cannot be set in *mfold* (only Na and Mg ions are considered), the 40 bp DNA hairpin was unzipped in a test buffer (containing 100 mM Na and 10 mM Mg ions) (Fig. 3.9a). The experimentally determined probability of the 40 bp DNA hairpin to be open in the test buffer is well described by the theoretical prediction using equation 3.13 (compare solid blue line to filled blue circles in Figure 3.9a). In contrast a measurement on the same DNA hairpin in the buffer RBRecQ cannot be well predicted (compare solid red line to filled red circles in Figure 3.9a). The forces are overestimated by ≈2 pN, which is not within the standard deviation of the measured unzipping forces (see table 3.3). The real ionic strength of the buffer RBRecQ (compared to the settings used in *mfold*) obviously reduces the base pairing energy further. The base pairing energies were reduced by ≈20% to match the mean measured probability of the 40 bp DNA hairpin to be open. The DNA hairpin unzipping theory was also applied to the 90 bp DNA hairpin with three areas of different AT content (Fig. 3.9b). The probabilities of the 90 bp to be open using equation 3.13 were calculated with the full 90 bp sequence instead of calculating every area separately. This was done to include the correct length of the created ssDNA and to consider influences of a neighboring base pair (although it might not belong to the same area of AT content) when calculating the base pairing energy using *mfold*. The resulting curve for the whole 90 bp DNA hairpin displays three steps, one for each area of different AT content. The curve was separated by cutting it at its two inflection points between these three steps. Figure 3.9b shows a representative measurement of the probability of the three areas to be open in the buffer RBRecQ, as explained in section 3.3.2. The theoretical prediction overestimates the mean forces, because of the wrong base pairing energy, as shown above for the 40 bp hairpin. By reducing the base pairing energies ≈10% the theoretical curve matches the mean experimental values (Fig. 3.9b). The difference of the base pair energy reduction between the 40 bp and the 90 bp DNA hairpin to match the theory (using slightly wrong buffer conditions for the base pairing energy) with the mean experimental values might arise from the different full lengths and the different base pair sequences of both DNA hairpins.

Nonetheless the theoretical predictions of the unzipping of the DNA hairpins fit well to the experimental values. This veryfies the use of the determined mean unzipping forces for all DNA hairpin constructs (tables 3.1 and 3.3) although the standard deviations are ≈10% (except for the AT area in the 90 bp hairpin which displays ≈17%).

4 DNA unwinding by Large Tumor Antigen from Simian Virus 40

4.1 Large Tumor Antigen - Structure and unwinding models

Simian Virus 40 (SV40) is a well studied polyomavirus which is hosted by monkeys and infects a variety of mammalian cells where it can cause tumors [108]. The very small genome of SV40 ($\approx$ 5 kbp, circular dsDNA) encodes a multifunctional enzyme, the so-called Large Tumor Antigen (T-Antigen). T-Antigen is a helicase [50, 109] involved in processes of DNA metabolism like replication, transcriptional regulation and transformation [110]. It is possibly a homologue to the minichromosome maintenance (MCM) complex and is therefore a model system for eukaryotic replication [111]. Most importantly it initiates and regulates replication of the virial genome by utilization of replication factors from the host cell [112].

Figure 4.1a shows the crystal structure of the core helicase domain of T-Antigen as a monomer [52]. T-Antigen consists of 708 amino acids (aa) where aa 1-82 form the J-domain (regulates tumor suppressor function), aa 131-250 the origin binding domain (OBD) (detects and binds the replication recognition sequence and participates in DNA unwinding), aa 251-627 the core helicase domain with three conserved motifs of the superfamily III and aa 628-708 the C terminal region (involved in host range determination).

In the presence of ATP T-Antigen forms a hexamer [22, 113], the active form of T-Antigen [114], with a central strongly positive charged channel [52] (Fig. 4.1b). It was shown that the monomers assemble subsequently around the origin of replication [115, 116] to form a double hexamer in a head-to-head [117] (C-terminI) orientation (Fig. 4.1c). The OBD is in a spiral configuration upon binding and enables threading of ssDNA out of its central channel [118] (in Fig. 4.1c only two OBD monomers of each T-Antigen hexamer are shown to depict the gap, which is formed by the spiral arangement of the OBD monomers). The helicase domain can be divided into two parts (small and large tiers [52]) which are able to rotate against each other and where the unwound ssDNA might exit the helicase domain. By distortion of the double hexamer complex, T-Antigen partially melts the dsDNA at the origin of replication [110, 51, 119].

Different conflictive models for the molecular mechanism of dsDNA unwinding by T-Antigen have been proposed [21, 122, 120, 121] (Fig. 4.1d). All of them include that at some point ssDNA is threaded outside the hexamer channel [123], which can be achieved during assembly of the hexamer complex or with the help of open and closed conformations of the ring-like J-domain and the OBD [124]. This creates a ssDNA to dsDNA fork (DNA junction) and initiates unwinding [125, 126, 118]. Magnesium ions and ssDNA stimulate ATP hydrolysis which drives conformational changes of a

beta-hairpin in every monomer facing into the channel (see also section 1.2, Figure 1.4) [127]. This causes translocation along the ssDNA backbone in the 3´ to 5´ direction [128, 129, 121].

Providing a preformed DNA junction as for the herein presented DNA hairpin experiments, most likely engages a single hexamer to unwind the DNA (Fig. 4.2) [130, 131, 122]. Different suggestions for the configuration of T-Antigen and the DNA junction are sketched in Figure 4.2, first row. The models *i*-*iv* are based on the dsDNA unwinding models which were proposed for dsDNA unwinding (Fig. 4.1d [21, 122, 120, 121]). These proposed unwinding models in Figure 4.1d differ in the location where the ssDNA exits T-Antigen (e.g. between OBD and small tier [121] or

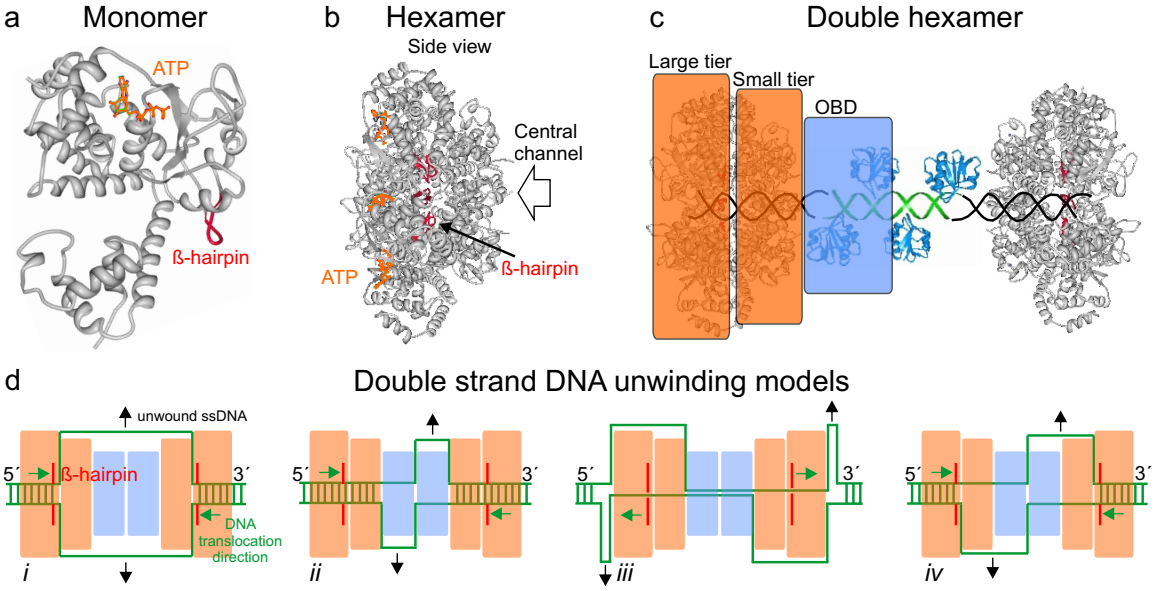

Figure 4.1 Large Tumor Antigen. Crystal structure and DNA unwinding models. (**a**) Monomeric structure of the T-Antigen helicase domain (aa 251-627, [21], PDB: 1SVM) visualized with proteinworkshop [20] with bound ATP (orange). The beta-hairpin, which is supposed to translocate the DNA upon an ATP hydrolysis cycle is shown in red. (**b**) Six monomers of T-Antigen (as shown in a) assembled to a hexameric structure. For front view see Figure 1.4 in section 1.2.1. The large arrow points into the inner hexamer channel, which is supposed to accommodate the DNA. (**c**) Cartoon of the assembled double hexamer on dsDNA in side view. The crystal structure of the OBD (with cocrystalized DNA in green) is taken from [120], PDB: 2NTC and merged with the side view of the hexamer in b. For the final picture one T-Antigen hexamer with OBD is mirrored. The additional dsDNA (black) is a copy of the cocrystalized dsDNA in the OBD (estimated localization). The colored squares represent the domains in the following representations. (**d**) After melting the dsDNA, the ssDNA is suggested to be routed outside the OBD or the helicase domain. Both hexamers unwind in opposite directions driven by conformational changes of the beta-hairpins (two beta-hairpins are representatively shown as red lines). The direction of ssDNA translocation is indicated with a green arrow. The extruding unwound ssDNA is indicated by black arrows. The unwinding models are adapted from *i* [21], *ii* [120], *iii* [121] and *iv* [122].

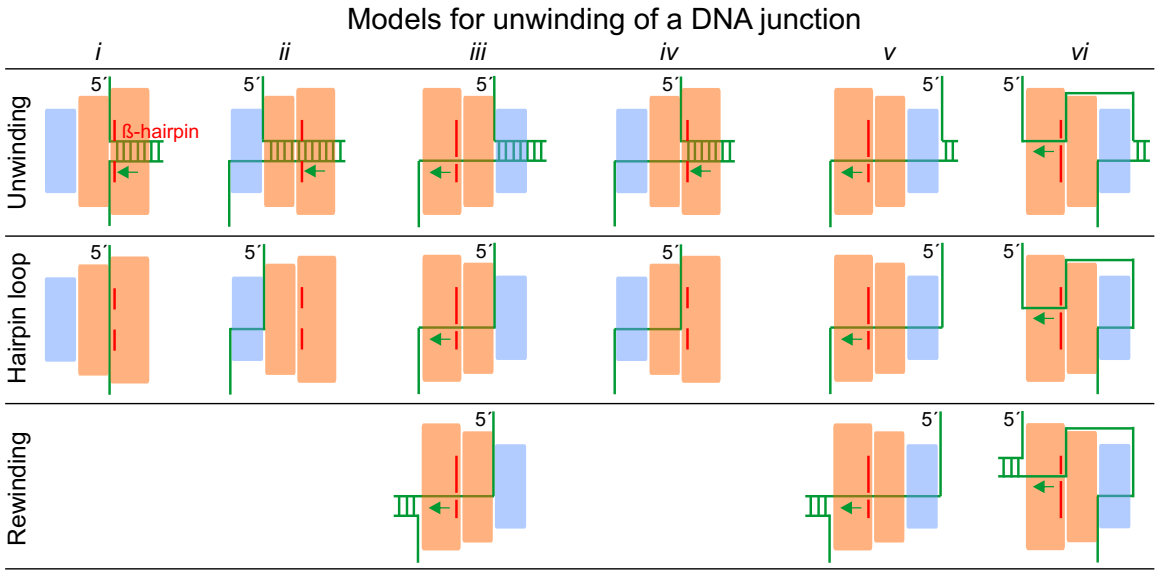

Figure 4.2 Unwinding of a DNA junction by a T-Antigen hexamer. In the columns six different unwinding models are presented (labeled *i*-*vi*). The squares are the large and small tier (orange) and the OBD (blue) as introduced in Figure 4.1. Two representative beta hairpins are shown in red. The green arrows indicate the direction of DNA translocation (5´ end indicated). The models *i*-*iv* are based on the dsDNA unwinding models in Figure 4.1. The models *v* and *vi* are two of several other possibilites of threading the ssDNA through a T-Antigen hexamer. The first row shows the possible threading configuration of the ssDNA through the T-Antigen hexamer during unwinding. The second row shows the ssDNA configuration (within the corresponding model) when the enzyme reaches the DNA hairpin loop, as given by the used DNA templates for the magnetic tweezers experiments in this thesis. The last row shows the ssDNA configuration when T-Antigen moved over the hairpin loop and rewinds the hairpin. For the models *i*, *ii* and *iv* rewinding cannot occur, because the beta-hairpins of T-Antigen, which translocate the ssDNA, might not be able to reach the ssDNA.

small and large tier [21]) as well as in the orientation of T-Antigen during translocation (with its C- or N-terminus in front). Beside these four configurations of helicase and DNA we found 28 additional models considering all possible configurations to thread ssDNA through a T-Antigen hexamer. Two of them are shown in Figure 4.2, first row, model *v* and *vi*. In model *v* the DNA junction is free, i.e. T-Antigen only translocates along the ssDNA and sterically disrupts the base pairs. Model *vi* shows a rather complicated threading of the ssDNA. Our data supports model *iii* given the available experimental results as presented in the first and in the last section of this chapter.

Magnetic tweezers allow to measure DNA lengths in real time and thus to investigate the unwinding- (v_{unw}) and ssDNA translocation- (v_{trans}) velocities of helicases. These parameters depend on the applied force, because the force may assist lowering the base pairing energy at the DNA junction. "Passive" helicases do not interact with the DNA junction and need to wait for base pair fraying due to thermal fluctuations to step forward into the DNA junction (see section 1.2.2). Energy from ATP hydrolysis is necessary to prevent the helicase to get pushed back by a rehybridizing base pair.

The unwinding velocity of a passive helicase strongly depends on the applied force, which shifts the probability of thermally fluctuating base pairs at the DNA junction towards an open state (see chapter 3.3.2). Hence, for a passive helicase the unwinding velocity will always be smaller than its ssDNA translocation velocity. This behaviour was shown for example for the helicases T4 gp41 [35] or T7 gp4 [39], where a 10-fold difference of the unwinding velocity between low and high forces was found.

Within this thesis the first single molecule unwinding data of T-Antigen was taken. The data presented in the next sections reveal a very slow and tremendously processive DNA unwinding of T-Antigen. In the first section, the force-dependence of DNA unwinding of T-Antigen will be presented. The unwinding velocity data could not be described by the current existing models. Therefore a new theoretical description was required and will be presented in the second section of this chapter.

The T-Antigen used in the following experiments was kindly provided by the groups of Hans Stahl (Medizinische Biochemie und Molekularbiologie, Universität des Saarlandes, 66421 Homburg, Germany) and Xiaojiang Chen (University of Southern California, USA). The purification protocols are described in [132] and [133]. The T-Antigen from Hans Stahl is the full enzyme aa 1-708, the T-Antigen from Xiaojiang Chen are truncated versions aa 1-627 (truncated C-terminus), aa 131-627 (truncated N- (J domain) and C-terminus) and aa 251-627 (helicase domain only) [52]. The results produced with the versions of T-Antigen: aa 1-708, 1-627 and 131-627 were not distinguishable from each other, i.e. we assume the same behavior of the three versions of T-Antigen for all investigated properties within our experiments.

4.2 Single molecule measurements with T-Antigen

Prior to the single molecule experiments, the enzyme was tested in a bulk assay to verify the functionality of the particular preparations of T-Antigen (Fig. 4.3a). In addition to forked DNA constructs also blunt ended dsDNA and DNA substrates with 3´- and 5´-overhangs were tested under the same reaction conditions as used for the subsequent single molecule experiments. As expected, T-Antigen only unwound DNA efficiently when a 3´-overhang was provided, because of its 3´ to 5´ strand polarity [50]. The bulk experiments were conducted when new batches of T-Antigen were used and assured functionality and correct storing conditions.

To set up single molecule unwinding measurements, DNA hairpins with attached microshpheres were flushed into the flow cell and incubated (see appendix 6.2.3). After finding an appropriate DNA hairpin construct the force-distance calibration was performed (see section 3.3). Afterwards 150 nM T-Antigen was flushed into the flow cell in reaction buffer (RBTAg, see appendix 6.2.2). The enzyme concentration was kept low to provide single molecule conditions. Initation of unwinding was found to take up to several hours. No particular reason was found to explain the different delays until unwinding is initiated. The time until DNA unwinding starts is used to test if T-Antigen assembles as a hexamer around the dsDNA region of the hairpin at an unspecific site (unspecific: without the sequence of the origin of replication) [134]. This is achieved by unzipping the DNA hairpin several times before enzyme

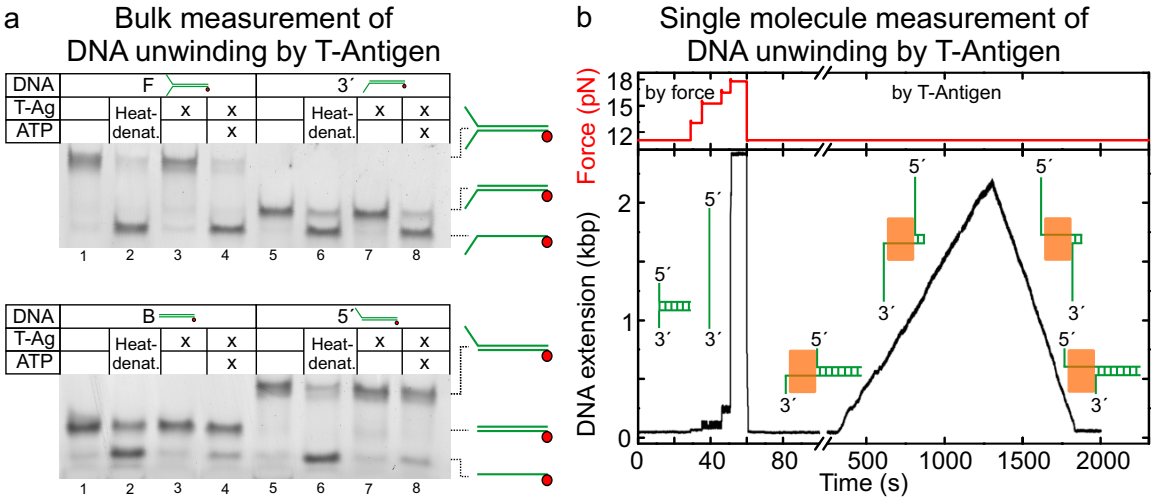

Figure 4.3 DNA unwinding measurements with T-Antigen. (**a**) For the bulk experiment four DNA constructs with a 50 bp long dsDNA stem and either 25 nucleotides 3´-, 5´-, both or no overhangs were hybridized (labeled 3´,5´,F,B, respectively) with a protocol explained in section 3.1.3 (DNA sequences in appendix: 6.1). The bottom strands were labeled at their 5´ ends with Rhodamine 6G to visualize the results with a laser scanner. Reactions were carried out at room temperature in reaction buffer RBTAg for 1 h. The reactions were stopped with 1.5% SDS, 0.2 mM EDTA and 50% glycerol and separated on a 8% TBE polyacrylamide gel for 1 h at 100 V. Lanes 1 and 5 in the upper and lower gel show the pure DNA construct corresponding to the DNA-label. Lanes 2 and 6 show the bottom strand only, created by heat denaturation (5 min at 95°C than on ice). In lane 3 and 7 T-Antigen is added without ATP, 4 and 8 with ATP. The upper gel reveals almost complete DNA unwinding compared to the lower, because of the 3´ to 5´ polarity of T-Antigen. (**b**) *left part*: Mechanical unzipping of the 2000 bp DNA hairpin before unwinding is detected. *right part*: After $\approx$ 6 min unwinding is observed by a slowly increasing DNA extension. The sketches indicate the state of the hairpin during unzipping and unwinding, the full enzyme is sketch undetailed as one orange square. Force: $\approx$ 10 pN, Buffer: RBTAg (see appendix 6.2.2).

activity is recognized (e.g. at the 2000 bp DNA hairpin construct shown in Fig. 4.3b, left). If T-Antigen assembled around the DNA hairpin (like a clamp around dsDNA) it might be detectable during mechanical unzipping of the hairpin by force, i.e. the unzipping would be stopped or delayed at the position where T-Antigen clamps the dsDNA. Those clamping effects have never been observed in the experiments and the unzipping patterns and unzipping forces do not differ from those one in the absence of T-Antigen. We conclude no measurable interaction with dsDNA at unspecific sites and that T-Antigen initiates DNA hairpin unwinding at the DNA junction.

After largely varying times unwinding is intitiated, seen by a slow increase in DNA extension (Fig. 4.3b). The helicase seperates the dsDNA creating two nucleotides per opened base pair, which add up to the DNA extension. Since no single stranded binding protein is used in the reaction buffer, a rehybridization of the newly created ssDNA behind the enzyme would be possible. The successively increasing DNA extension shows that rehybridization does not appear. Most likely the enzyme sterically prevents

the approach of the two strands supported by the applied force which routes them into opposite directions.

Although the experiment was performed under saturating ATP concentrations (3 mM ATP in the reaction buffer RBTAg, $k_M = 270\ \mu M$ [135]), the average unwinding velocity v_{unw} reaches only $1-2$ bp/s. This is very slow compared to other helicases under similar reaction conditions (compare e.g. NS3: $v_{unw} = 20-80$ bp/s [92], T4 gp41: $v_{unw} = 30-320$ bp/s [35], T7 gp4: $v_{unw} = 30-230$ bp/s [39]). Detailed investigations of the unwinding velocity follow below.

At some point the DNA unwinding turns into rewinding, i.e. the hairpin succesively closes again (Fig. 4.3b). This observation is in agreement with a mechanism where the helicase domain of T-Antigen encircles only a single DNA strand. The rewinding is then most likely caused by the enzyme moving over the DNA hairpin loop where it is directly transferred onto the formerly displaced strand. Processively the enzyme keeps on translocating in 3´ to 5´ direction while the DNA rehybridizes behind it. This idea is for example not applicable to the models *i* and *ii* in Figure 4.2 where the helicase domain encircles dsDNA instead of ssDNA which cannot be translocated through the helicase channel upon reaching the DNA hairpin loop, i.e. the observed rewinding cannot be explained within these models.

Fig. 4.4a shows the DNA extensions at the turning point from DNA unwinding to DNA rewinding of the 500 bp DNA hairpin under different forces. A comparison to the extensible FJC model (see section 3.3.2 equation 3.2) simulated with a contour length corresponding to the 500 bp DNA hairpin of $L_0 = 560$ nm $=$

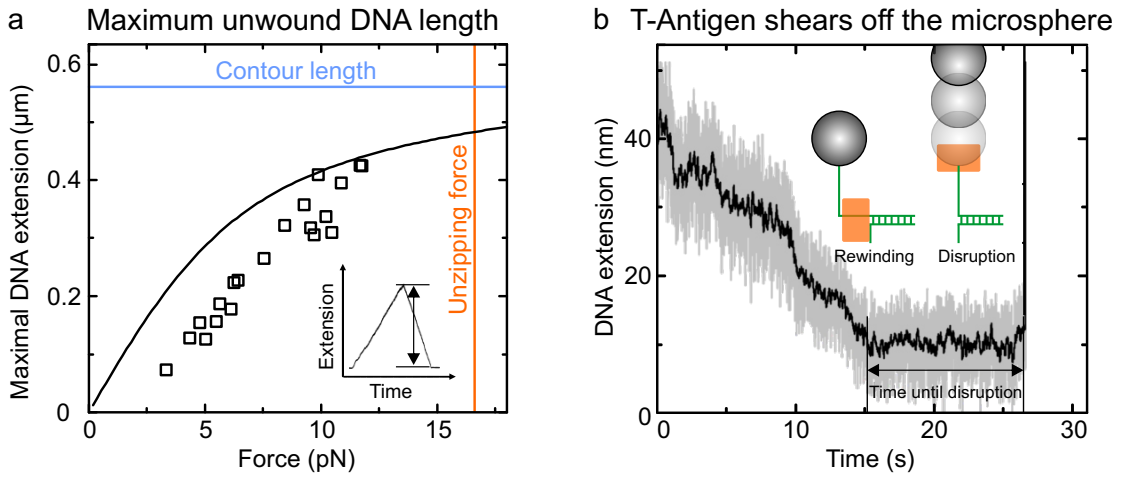

Figure 4.4 Maximum unwound DNA length before unwinding turns into rewinding and displacement of the microsphere by T-Antigen. (**a**) Maximum DNA extension during unwinding before rewinding occurs as function of the applied force (open squares). The black line is a prediction of the force-extension behavior of ssDNA using the FJC model (equation 3.2) with $L_0 = 560$ nm corresponding to the fully opened 500 bp DNA hairpin. For comparison L_0 is indicated by the solid blue line. The orange line indicates the determined unzipping force of the 500 bp DNA hairpin in RBTAg (see section 3.3.1). (**b**) After every rewinding the microsphere is sheared off the DNA. The time until disruption varies between $0-1500$ s.

$(2 \cdot 488\ \text{nt} + 3\ \text{nt}) \cdot 0.574\ \text{nm/nt}$ (488 bp hairpin plus 3 nt in the loop) reveals that the DNA extension at the turning point most likely corresponds to the fully unwound DNA hairpin. Deviations from the theory occur due to the formation of secondary structures below ≈ 10 pN, which reduce the DNA length. Assuming that T-Antigen always unwinds the DNA hairpin completely allows to recalculate the DNA extension from nanometer to base pairs, for different applied forces. Under all applied forces no extensive pausing, backward movement in 5´ to 3´ direction (would correspond to rewinding before the full DNA hairpin is unwound), slippage (helicase gets pushed back by the rehybridizing DNA hairpin) or dissociation of T-Antigen was observed. In all experiments the full hairpin was unwound (longest DNA hairpin construct contains 2000 bp). It can therefore be expected that T-Antigen can processively unwind much more than 2000 bp. This makes T-Antigen to be the most processive helicase known so far (compare e.g. NS3: $L_{\max} = 120$ bp [136], MCM4,6,7 $L_{\max} = 600$ bp [137], T7 gp4 $L_{\max} = 100 - 800$ bp [39]).

After every run of T-Antigen the microsphere is sheared off the DNA (see Fig. 4.4b). It is not clear at which point T-Antigen breaks the connection between DNA and microsphere (between DNA and biotin, biotin and steptavidin or streptavidin and microsphere). Thus no experiment can be repeated with the same helicase or the

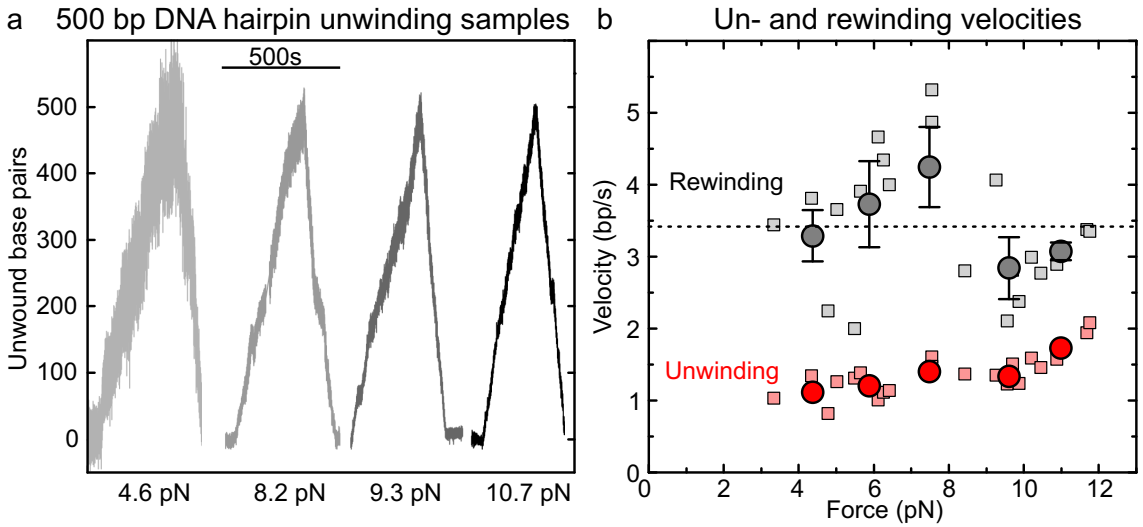

Figure 4.5 Force dependence of the un- and rewinding velocity of T-Antigen. (**a**) Four representative traces of the completely unwound 500 bp DNA hairpin. The DNA extension was recalculated from nm to bp. The force is indicated below the corresponding trace. The scale bar indicates a time period of 500 s. The average un- and rewinding velocity to each trace is simply evaluated by a global linear fit over the whole un- and rewinding period, respectively. (**b**) Unwinding (red squares) and rewinding velocities (gray squares) of T-Antigen. The force range is limited at the lower end due to a high signal to noise ratio and at the upper end due to the potential risk of hairpin unzipping. The data was binned (large circles), so that each bin contains a similar amount of data points. The standard error of the binned unwinding data is within the size of the circles. The rewinding error is much higher. The black line indicates the average rewinding velocity (3.4 ± 1 bp/s).

same DNA-microsphere system. This can cause variations between measurements as several helicases were shown to present static disorder [42], i.e. heterogenetic behavior in a homogenious group of enzymes. The ability of T-Antigen to disrupt biotin-digoxigenin bonds was already shown in bulk experiments [138] and is supported by our observations. The time until the microsphere is displaced varies largely (from immediatelly until 1500 s) and does not reflect the translocation velocity on the ssDNA spacer between the hairpin and the microsphere.

As mentioned in section 1.2.2 the force dependence of the unwinding velocity can provide insights into the degree of activity of a helicase. Thus, the unwinding velocity was measured as function of the applied force. Figure 4.5a shows a selection of unwinding events from T-Antigen acting on the 500 bp DNA hairpin at different forces. Neglecting the expected decrease of DNA length fluctuations at higher forces, no significant differences are observed in the unwinding behavior. The measurements reveal that the unwinding and the rewinding velocities are very weakly force dependent within the applied force range. The rewinding velocities ($2-5$ bp/s) are always significantly higher than the unwinding velocities ($1-2$ bp/s), most likely because no base pair has to be opened during rewinding (Fig. 4.5b). The variance of the rewinding velocity is somewhat higher than of the unwinding velocity. Assuming no active influence of the DNA junction in its wake, T-Antigen determines the DNA rewinding velocity with its translocation velocity. Thus the higher variance of rewinding velocities may be caused by a higher variance of the translocation on ssDNA. This idea will be discussed at the end of this chapter. The weak force dependence of the unwinding velocity of T-Antigen highly suggests that it is not a passive helicase. To get further insights into the unwinding characteristics of T-Antigen, the force dependence is modelled in the next section.

4.3 Modelling the unwinding velocity of T-Antigen

To identify passive or active unwinding behavior of T-Antigen, the force-dependent unwinding velocity was calculated on the basis of published theories [38, 139, 39] (see also section 1.2.2) to compare it to the measurements of the unwinding velocity in the previous section. Within these theories the observed unwinding velocity (v_{unw}) depends on the relative distance k (in base pairs) between the DNA junction and the helicase (Fig. 4.6a). Furthermore the junction presents an insurmountable energy barrier, so that the enzyme can only move when the DNA junction is open, more precisely, when the number of base pairs that are open correspond at least to the step size s of the helicase. This means the helicase moves with its translocation velocity v_{trans} and is stopped by the presence of a closed base pair at the DNA junction. Additionally the possibility of back stepping or pausing of T-Antigen is neglected, because these events are rarely observed (within the instrumental noise). The probability $p(j, F)$ of the DNA junction to be open at the base pair with index j (starting from the beginning of the DNA hairpin, see Figure 4.6a) was derived in section 3.3.3 (equation 3.3). This probability depends on the free energy of the system $E_{\mathrm{total}}(F)$ (see equation 3.3). The derived free energy of the system (section 3.3.3,

equation 3.12) is independent of the presence of the helicase, i.e. this probability can be used to describe a passive helicase $p(j, F) = p_{\text{pass}}(j, F)$. The observed unwinding velocity can be calculated as the average of the translocation velocities to all relative distances k between the DNA junction and the helicase:

$$v_{\text{unw}}(F, l) = \sum_{k=0}^{\infty} v_{\text{trans}}(k) \cdot p_{\text{pass}}(j, F) \tag{4.1}$$

with $j = k + l$ (see Fig. 4.6a) and the condition:

$$v_{\text{trans}}(k) = \begin{cases} 0 & \text{if } k < s \\ v_{\text{trans}} & \text{if } k \geq s. \end{cases}$$

The fitting parameters of the passive model are the translocation velocity v_{trans} and the step size s. For all following calculations the step size was not fitted, but fixed to s =1 or 2 nucleotides (indicated in the plot legends) to keep the number of parameters low. The passive unwinding model (equation 4.1) was used to simulate the unwinding velocity of T-Antigen for a step size of one nucleotide with a translocation velocity of the mean rewinding velocity (Fig. 4.6b, red solid line). The assumption that the rewinding velocity represents the translocation velocity was constituted in the last section. The force dependent unwinding velocities of T-Antigen cannot be desribed with this set of parameters (compare red filled circles and red solid line). The unwinding velocities are underestimated. A larger step size would predict even slower unwinding velocities. Furthermore the passive unwinding model was used to fit the unwinding velocity of T-Antigen with a fixed step size of one nucleotide using the Levenberg-Marquardt algorithm (Fig. 4.6b, blue solid line). Also the fit cannot describe the unwinding data well. Additionally the force dependence of the fitted curve is much higher than the force dependence of the measured velocities (fit: 4-fold, measurement: 1.5-fold increase of the velocity in the force range from $4 - 11$ pN). The fitted value of the translocation velocity $v_{\text{trans}} = 7.5$ nt/s is twice the mean rewinding velocity and is thus contradictory to the initial assuption $v_{\text{trans}} \approx v_{\text{rew}}$. A fit with a step size of two nucleotides deviates even more from the measured unwinding velocities (Fig. 4.6b, blue dashed line). Since the passive DNA unwinding model cannot describe the measured data, a model describing an active helicase was applied [38].

An active helicase reduces the base paring energy in a certain area ahead of the enzyme [14, 140]. To account for this effect, an additional contribution to the total free energy of the system was introduced (compared to the total free energy in absence of the helicase, see section 3.3.3, equation 3.3) [38]. This additional energetic contribution of the helicase ΔG_{heli} lowers the base pairing energy ΔG_{bp} at the DNA junction (see also section 1.2.2). This means that the probability of the DNA junction to be open is increased when the range M of this potential overlaps with the position of the DNA junction (Fig. 4.7a). The total free energy of the system is now:

$$E_{\text{total}}(j) = -\Delta G_{\text{bp}} - \Delta G_{\text{heli}} - 2\Delta G_{\text{el}} + 2F_{\text{mag}} \tag{4.2}$$

with the condition:

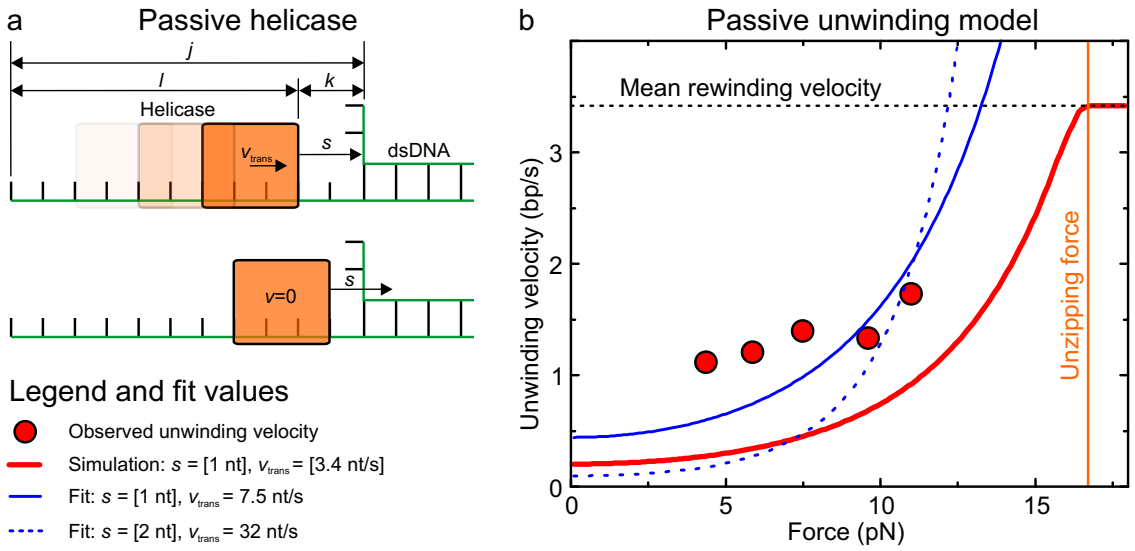

Figure 4.6 Passive DNA unwinding model applied to the unwinding velocity of T-Antigen. (**a**) Sketches illustrate the parameters and variables of the passive DNA unwinding model. The DNA is shown in green, the base pairs in black and the dsDNA area is labeled. The helicase is shown as orange square. The labels of the distances from the beginning of the hairpin to the helicase and to the DNA junction are indicated. In the sketch the helicase has a step size $s = 2$ nt. *Upper*: The helicase is at least one step size away from the DNA junction and translocates with the velocity v_{trans}. *Lower*: The helicase stalls when the DNA junction is closer than a step size. (**b**) Unwinding velocity of T-Antigen on the 500 bp DNA hairpin over the applied force. A figure legend is shown below a (numbers in brackets are fixed values, others are fit values). The observed unwinding velocities (red filled circles) are the average unwinding velocities, the black dashed line shows the mean rewinding velocity shown in Figure 4.5 in section 4.2. The orange line indicates the unzipping force of the 500 bp DNA hairpin (see table 3.1, section 3.3.1). The passive unwinding model (equation 4.1) was simulated and fitted to the data with the indicated values (see legend). RMS of the fits: blue solid line 0.39 bp/s, blue dashed line 0.73 bp/s.

$$\Delta G_{\mathrm{heli}} = \begin{cases} k\Delta G_{\mathrm{red}} & \text{if } \; 0 \leq k \leq M \\ M\Delta G_{\mathrm{red}} & \text{if } \; k > M \end{cases}$$

with ΔG_{red} beeing the strength of the reduction of the base pairing energy (per base pair). In equation 4.3 a linear decrease of the potential from the helicase which decreases the base pairing energy is considered [39]. The condition for the helicase to move forward is extended by the range of the potential M:

$$v_{\mathrm{trans}}(k) = \begin{cases} 0 & \text{if } \; k < s \\ v_{\mathrm{trans}} & \text{if } \; k + M \geq s. \end{cases}$$

In contrast to the full theory developed by Betterton and Jülicher the adapted theory neglects backward stepping of the helicase as well as the position of the energy barrier (formed by the base pairs) within a step size (in the theory of Betterton and Jülicher, this is considered with an additional parameter [38]). Now, the force

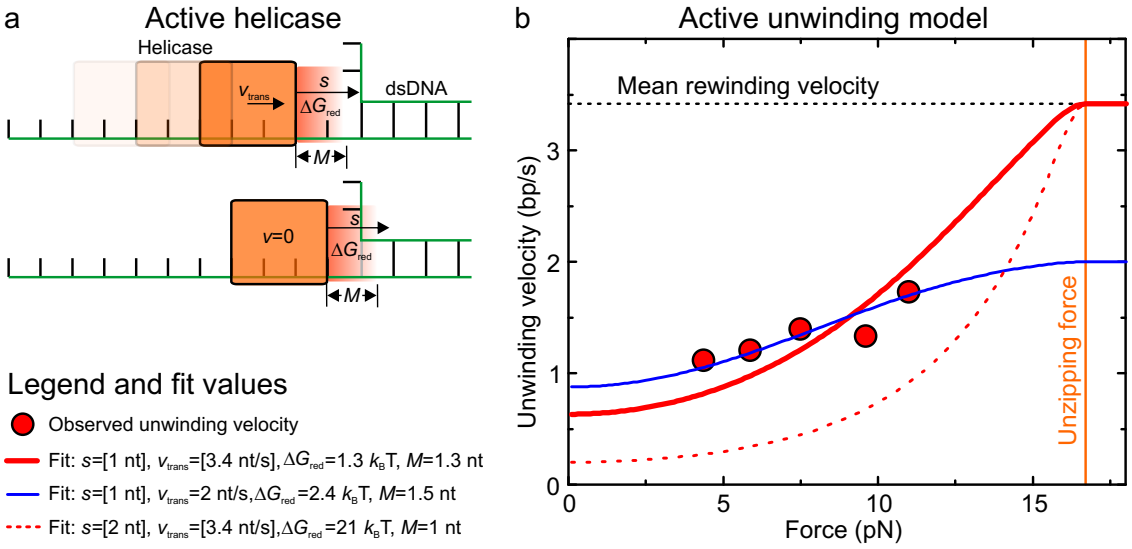

Figure 4.7 Active DNA unwinding model applied to the unwinding velocity of T-Antigen. (**a**) Sketches illustrate the parameters of the active DNA unwinding model. The DNA is shown in green, the base pairs in black and the dsDNA area is labeled. The helicase is shown as orange square. In the sketch the helicase has a step size $s = 2$ nt and its potential to reduce the base pairing energy (red gradient area in front of the enzyme) has a range of $M = 1.5$ nt. *Upper*: The helicase is at least one step size away from the DNA junction and translocates with the velocity v_{trans} and the base pairs at the DNA junction are not affected by the presence of the helicase. *Lower*: The helicase stalls when the DNA junction is closer than a step size and the potential of the helicase ΔG_{red} lowers the energy of the first base pair at the DNA junction (indicated by a gray base pair). (**b**) Unwinding velocity of T-Antigen on the 500 bp DNA hairpin over the applied force. A figure legend is shown below a (numbers in brackets are fixed values, others are fit values). The observed unwinding velocities (red filled circles) are the average unwinding velocities, the black dashed line shows the mean rewinding velocity shown in Figure 4.5 in section 4.2. The orange line indicates the unzipping force of the 500 bp DNA hairpin (see table 3.1, section 3.3.1). The active unwinding model (equation 4.1) was fitted to the data with the indicated values (see legend). RMS of the fits: red solid line 0.24 bp/s, blue solid line 0.1 bp/s, red dashed line 0.83 bp/s.

dependent unwinding data was fitted using equation 4.1 with the conditions for an active helicase (Fig. 4.7b). With a fixed step size of one nucleotide and a translocation velocity equal to the mean rewinding velocity (for the reasons mentioned above) the unwinding velocities of T-Antigen is not fitted well (Fig. 4.7b, red solid line). The fitted value for the free energy reduction of $\Delta G_{\mathrm{red}} = 1.3\ \mathrm{k_B T}$ is comparable to the determined value for the T7 helicase of $\Delta G_{\mathrm{red}} = 1 - 2\ \mathrm{k_B T}$ [39], while the range of the potential is shorter $M = 1.3$ nt (T7: $M = 6$ nt [39]). A fixed step size of two nucleotides increases the deviations between the unwinding velocities and the theory (Fig. 4.7b, red dashed line). Additionally the fitted free energy reduction of $\Delta G_{\mathrm{red}} = 21\ \mathrm{k_B T}$ is several times higher than the base pairing energy of a GC base pair ($\Delta G_{\mathrm{GC}} = 3.4\ \mathrm{k_B T}$ [39]). When only the step size is fixed, the active model fits the data well (Fig. 4.7b, blue solid line). However, the fitted translocation velocity is found to be approximatelly half of the mean rewinding velocity. A reason for the

rewinding velocity to be faster than the translocation velocity could be the additional energy of the rehybridizing DNA hairpin pushing the helicase during rewinding so that the rewinding velocity could indeed be faster than the translocation velocity. Against this hypothesis one result will be shown at the end of this section.

Both the passive and the active model cannot describe the weak force dependence of the unwinding velocity of T-Antigen. The problem might be the restriction that a closed base pair in front of the helicase is always considered to be an insuperable obstacle at which the helicase velocity is zero. To find a better description of the force dependent unwinding velocities, an intrinsic ability of the enzyme to break a closed base pair open was introduced to the theory. With this assumption the helicase has intrinsically an active character and hence the reduction of the base pairing energy by the helicase ΔG_{heli} is removed from the theory. If the helicase is not located at the DNA junction the enzyme moves with its translocation velocity v_{trans} (Fig. 4.8a). If the helicase is located directy at the junction we assume that the helicase moves with a non-zero velocity v_{dsDNA}. Now some of the energy from the ATP hydrolysis is necessary to break the base pair at the DNA junction open, which implies that the velocity upon reaching the DNA junction is lower than the translocation velocity $v_{\mathrm{dsDNA}} < v_{\mathrm{trans}}$. Therefore, equation 4.1 is adapted to:

$$v_{\mathrm{unw}}(F,l) = \sum_{k=0}^{\infty} \left[v_{\mathrm{trans}}(k) \cdot p_{\mathrm{pass}}(j,F) + v_{\mathrm{dsDNA}}(k) \cdot (1 - p_{\mathrm{pass}}(j,F)) \right] \tag{4.3}$$

with $j = k + l$ and the conditions:

$$v_{\mathrm{trans}}(k) = \begin{cases} 0 & \text{if } k < s \\ v_{\mathrm{trans}} & \text{if } k \geq s \end{cases} \qquad v_{\mathrm{dsDNA}}(k) = \begin{cases} v_{\mathrm{dsDNA}} & \text{if } k < s \\ 0 & \text{if } k \geq s \end{cases}$$

The alternative DNA unwinding model (equation 4.3) was fitted to the data. Fixing the step size to one nucleotide and the translocation velocity to the mean rewinding velocity, the data was fitted well (Fig. 4.8b, red solid line). The fitted velocity of the helicase upon encountering the DNA junction is 0.8 bp/s. Also without fixing the translocation velocity to the mean rewinding velocity resulted in a reliable fit of $v_{\mathrm{trans}} = 3.6$ nt/s (the mean rewinding velocity of T-Antigen is $v_{\mathrm{trans}} = 3.4$ nt/s) (Fig. 4.8b, blue solid line). Increasing step sizes creates somewhat larger deviations from the data (e.g. a step size of two nucleotides Fig. 4.8b, red dashed line). Thus the alternative model might also predict a step size of one nucleotide.

The alternative unwinding model implies a direct influence of the base pairing energy on the unwinding velocity, since the reduction of the velocity of the enzyme at the DNA junction is caused by the loss of the energy required to open the base pair. Thus it is expected to detect a difference in the DNA unwinding velocity when an AT or a GC base pair is opened. The detection would require base pair resolution of the setup. However, the average velocity to unwind a DNA sequence with a higher AT content can be distinguished from a DNA sequence with a lower AT content. Using equation 4.3 and the base pair energies of the DNA hairpin sequence (calculated using *mfold* [105], see section 3.3.3) the DNA unwinding traces can be simulated for a given

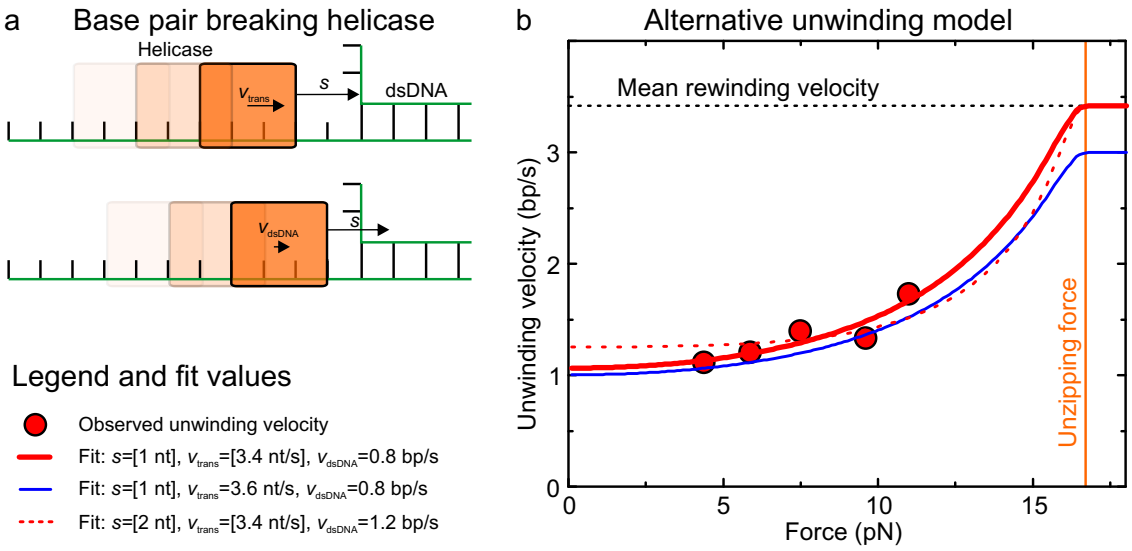

Figure 4.8 Alternative unwinding model describing T-Antigen as an active base pair breaker. (**a**) Sketches illustrate the parameters of the alternative DNA unwinding model. The DNA is shown in green, the base pairs in black and the dsDNA area is labeled. The helicase is shown as orange square. In the sketch the helicase has a step size $s = 2$ nt. *Upper*: The helicase is at least one step size away from the DNA junction and translocates with the velocity v_{trans}. *Lower*: The step size is larger than the distance between enzyme and DNA junction. The base pair at the DNA junction is opened for the price of a reduced velocity v_{dsDNA}. (**b**) Unwinding velocity of T-Antigen on the 500 bp DNA hairpin over the applied force. A figure legend is shown below a (numbers in brackets are fixed values, others are fit values). The observed unwinding velocities (red filled circles) are the average unwinding velocities, the black dashed line shows the mean rewinding velocity shown in Figure 4.5 in section 4.2. The orange line indicates the unzipping force of the 500 bp DNA hairpin (see table 3.1, section 3.3.1). The alternative unwinding model (equation 4.1) was fitted to the data with the indicated values (see legend). RMS of the fits: red solid line 0.09 bp/s, blue solid line 0.09 bp/s, red dashed line 0.13 bp/s.

force (Fig. 4.9a). High forces shift the equilibrium of the base pairs at the DNA junction to an open-state. Thus the difference between the base pairing energies of AT and GC base pairs is more pronounced than for low forces. This means the ratio between the unwinding velocity in the GC rich region and the unwinding velocity in the AT rich region $v_{\mathrm{GC}}/v_{\mathrm{AT}}$ is close to one at low forces and decreases with increasing forces (Fig. 4.9b, inset). A preliminary DNA hairpin unwinding experiment at 10 pN was performed using a 2000 bp DNA hairpin where the initial 1000 bp region contains 67% AT base pairs and the subsequent region contains 40% AT base pairs (Fig. 4.9b). A difference in the unwinding velocity between the 67% AT and the 40% AT region is detectable (Fig. 4.9b, the line indicates half of the hairpin unwound, i.e. the transition from 67% AT to 40% AT). The ratio of the unwinding velocities in the GC region to the unwinding velocities in the AT region at 10 pN fit well to the prediction (Fig. 4.9b, inset), although the absolute values differ by 20%.

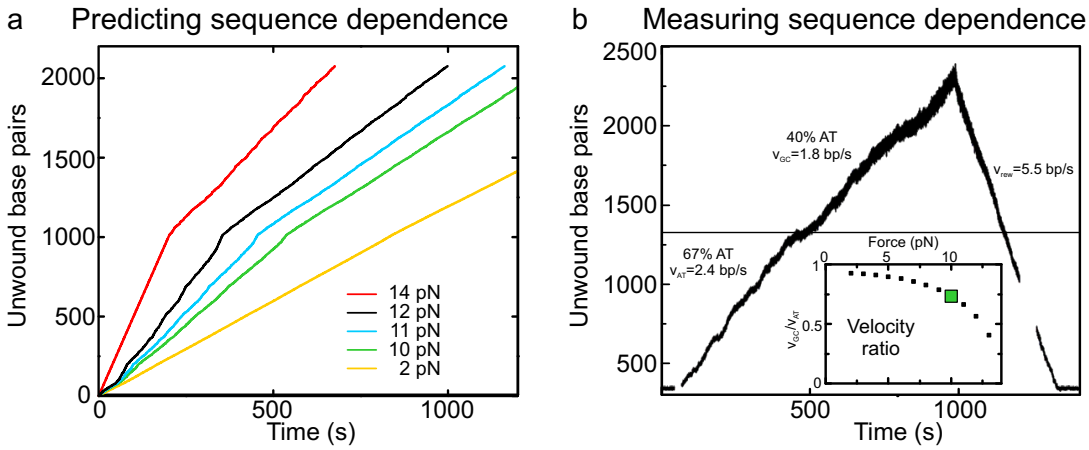

Figure 4.9 DNA sequence dependence of the unwinding velocity of T-Antigen. (**a**) Simulated unwinding traces using the alternative unwinding model which assigns the enzyme the ability to break a base pair (equation 4.3). The used forces are indicated. The DNA sequence contained initially 1000 bp with 67% AT base pairs and subsequent 1000 bp with 40% AT base pairs. (**b**) DNA unwinding measurement at 10 pN using the same DNA hairpin sequence as used in the simulations in a. The measured unwinding velocities are $v_{\mathrm{GC}} = 1.8$ bp/s and $v_{\mathrm{AT}} = 2.4$ bp/s. The theory predicts $v_{\mathrm{GC}} = 1.4$ bp/s and $v_{\mathrm{AT}} = 1.9$ bp/s. The inset shows the predicted ratio of $v_{\mathrm{GC}}/v_{\mathrm{AT}}$ over the applied force (black points). The measurment at 10 pN confirms the theoretical prediction (green filled square in the inset). The gap in the rewinding trace is caused by a short stop and restart of the tracking.

Furthermore, this experiments shows that the rewinding velocity cannot be faster than the translocation velocity due to an energy gain of the rehybridizing DNA hairpin as mentioned before. While the unwinding velocity of T-Antigen on this DNA hairpin clearly shows two different velocities in the two areas of different AT content, the rewinding velocity is constant over the whole hairpin. This is not expected if during rewinding the velocity would be influenced by the rehybridizing DNA hairpin, because the area with less AT base pairs would have a stronger rehybridizing energy, i.e. the rewinding would speed up. Since this is not observed the hypothesis that rewinding can be faster than translocation does not hold.

In the next chapter it is discussed how the assumptions and predictions of this theory as well as known properties from different biophysical experiments can be combined to develop a molecular model for DNA unwinding of T-Antigen.

4.4 Towards a molecular model for DNA unwinding by T-Antigen

In the following the DNA unwinding models for T-Antigen suggested in Figure 4.2 are discussed. T-Antigen rewinds the DNA hairpins after unwinding, which suggests that it translocates along the 3´ to 5´ single strand during un- and rewinding (as sketched in Fig. 4.3b). The DNA unwinding models *i*, *ii* and *iv* in Figure 4.2 cannot describe rewinding, because in these models the translocation finishes when the DNA hairpin loop is pulled into the helicase channel (see Fig. 4.2, second row). As a result

the DNA is not oriented along the beta hairpins in the channel of the helicase domain and the DNA cannot be translocated. No further translocation will occur and no rewinding would be detected. This excludes the models *i*, *ii* and *iv*.

In most of the models in Figure 4.2 both ssDNA strands are threaded into the T-Antigen hexamer (except for model *v*, where just one single strand is threaded into the hexamer). This property of T-Antigen could shield the DNA junction against the applied force, because the hexamer channel can be thought of as a movable clamp around the dsDNA. A result would be the observed low force dependence of the DNA unwinding velocity. In the suggested model *v* in Figure 4.2 the DNA junction is completely free, i.e. not threaded into the hexamer. If clamping of the DNA junction is required, than model *v* might be less likely. However, within the derived DNA unwinding theory shown in the previous section a mechanical clamp is not required to achieve the low force dependence of the unwinding velocity. Instead a smaller dsDNA velocity compared to the ssDNA velocity needs to be achieved.

In several studies of the unwinding of the origin of replication by T-Antigen it was shown that the enzyme assembles around the dsDNA and threads ssDNA out of the hexamer after melting the origin of replication [141] (see Fig. 4.1d for suggested models). With this mechanism T-Antigen creates a DNA junction and starts unwinding. The DNA hairpin constructs used for the experiments in this thesis already provide a DNA junction. The question arises if T-Antigen assembles on ssDNA at the DNA junction and threads the second single strand inside the hexamer channel or if it assembles on dsDNA and threads a single strand outside the hexamer channel. For the latter case it is necessary that the enzyme assembles around dsDNA. This is unlikely because the assembly would be DNA sequence unspecific (none of the DNA hairpins used in this thesis contain the origin of replication sequence for T-Antigen). Furthermore it would not explain why T-Antigen initiates the unwinding at the DNA junction. Also, we did not detect DNA sequence unspecific assembly of T-Antigen on dsDNA (Fig. 4.3b). If instead T-Antigen threads the ssDNA inside hexamer channel, this would require work against the applied force, which keeps the ssDNA streched in opposite directions. This hypothesis makes complicated threading of ssDNA like in model model *vi* in Figure 4.2 less likely.

We suggest that T-Antigen assembles on ssDNA and the OBD is in an open, spiral configuration as shown in [142]. The threading of ssDNA could be supported by a lock washer conformation of the OBD [142] when T-Antigen assembles on dsDNA, i.e. the OBD monomers are arranged spirally and form a gap (see Fig. 4.1c). Upon reaching the DNA junction, the second single strand might be captured in the gap of the OBD hexamer so that the dsDNA is encircled in the OBD [143]. The final configuration of the ssDNA threaded in the T-Antigen enzyme is sketched in model *iii* in Figure 4.2.

To further narrow down the possible DNA unwinding models for T-Antigen, experiments with a version of T-Antigen with a truncated OBD domain will be performed in future experiments. The first measurements are in agreement with the suggested model *iii*, but more data is required. Therefore the following results are just preliminary. Figure 4.10b sketches T-Antigen during unwinding (first row) and rewinding (second row) with (left column) and without the OBD domain (right column) within

the suggested model *iii*. The T-Antigen version with the helicase domain only (core helicase domain aa 251-627, without OBD, J-domain and C-terminus) was found to be able to unwind and rewind the 500 bp DNA hairpin. The unwinding velocity of the core helicase domain was found to be similar to the unwinding velocity of the full T-Antigen enzyme (Fig. 4.10b, compare red filled circles to red filled squares). The slightly higher values of the core helicase domain might arise from the different friction between DNA and enzyme because of the different lengths of the enzyme channel (compare sketches in left and right column in Figure 4.10b, first row). Also the first measurements of the rewinding velocity of the core helicase domain are within the mean rewinding velocity of the full T-Antigen (Fig. 4.10a, gray symbols). This is also in agreement with the suggested model *iii*, because the DNA junction is free to rehybridize behind T-Antigen with or without OBD domain (compare sketches in left and right column in Figure 4.10b, second row). Differences in the rewinding velocities could occur due to the different pathways of the ssDNA in the hexamer, but cannot be distinguished the variance of the rewinding velocity data. The similar un- and rewinding velocities suggested a similar un- and rewinding mechanism for T-Antigen with and without the OBD domain.

Additionally the model *iii* might explain the larger variance of the rewinding velocities of the full T-Antigen compared to the variance of its unwinding velocities (see section 4.2, Fig. 4.5) as follows. During rewinding by the full T-Antigen the 5´ end of the ssDNA can either stay located between the helicase hexamer and the OBD hexamer (compare the two pathways sketched in Fig. 4.10b, first column, second row). These two different pathways of rewinding might result in two different rewinding velocities. Occasional random switching or force dependent switching between these two pathways could result in the higher variance of the rewinding velocity compared to the unwinding velocity. In contrast, for the unwinding by the full T-Antigen just one pathway is possible (Fig. 4.10b, first column, first row). The possibility that rewinding has two pathways and unwinding just one pathway for the ssDNA could be also explained by the different direction the second single DNA strand is moving (Fig. 4.10b, compare blue arrows between first column, first and second row). During unwinding the 5´ ssDNA end is pushed out of the enzyme complex, while it is pulled into the enzyme complex during rewinding.

Furthermore, an experiment was performed to investigate the translocation velocity of the enzyme on ssDNA (Fig. 4.11a). To determine the translocation velocity of T-Antigen the DNA hairpin was completely mechanically unzipped by applying high forces ($F > F_{\mathrm{unzip}}$, see table 3.1 in section 3.3.1) while the enzyme actively unwinds (Fig. 4.11a, *A*-*D*) or rewinds (Fig. 4.11a, *E*-*H*) the DNA hairpin. The hairpin is kept open for a certain time (τ_{open}) and rezipped again by reducing the force back to its initial value. The rezipping of the hairpin stops at the location of the enzyme. A different DNA extensions before hairpin unzipping and after hairpin rezipping reveal that T-Antigen translocates on the ssDNA during the time the hairpin is kept open. The difference in DNA extension just before unzipping the hairpin and the DNA extension just after rezipping the hairpin ($h_m athrmssDNA$) divided by the time the hairpin was kept open reflects the corresponding translocation velocity on ssDNA (Fig. 4.11b). After rezipping of the DNA hairpin the unwinding and rewinding

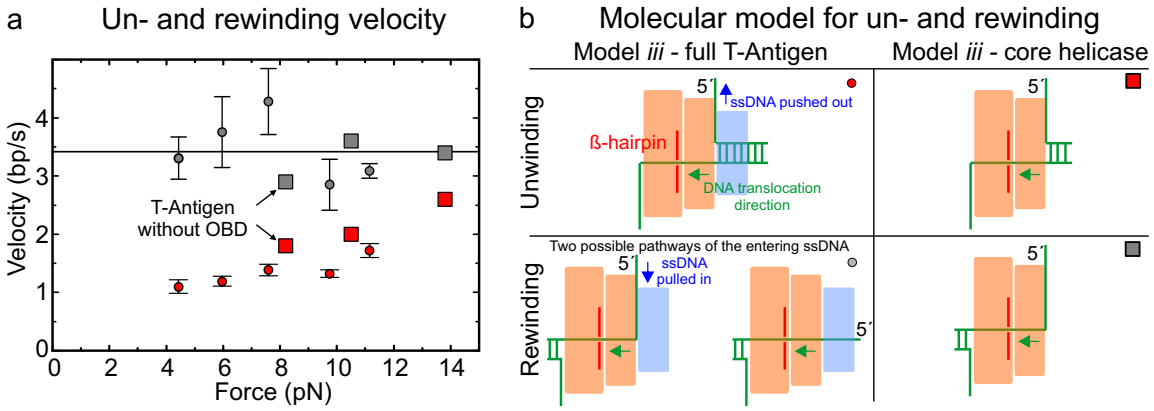

Figure 4.10 Molecular model for unwinding and rewinding of dsDNA by T-Antigen with and without the OBD. (**a**) Un- (red) and rewinding (gray) velocity of the full T-Antigen enzyme (circles) compared to the un- and rewinding velocity of the core helicase domain (squares) as function of force. The data from the full T-Antigen are the binned values shown previously in section 4.2, Figure 4.5b. The data of the core helicase are single measurements. (**b**) Sketches of the ssDNA threading through the full T-Antigen (left column) and core helicase domain (right column) during unwinding (first row) and rewinding (second row). The threading of the ssDNA corresponds to model *iii* from Figure 4.2. Two beta-hairpins are sketched in red. The 5´ end of the DNA is indicated. The green arrow indicates the translocation direction of the ssDNA. The blue arrow indicates the different direction of ssDNA movement between un- and rewinding. The second sketch of rewinding of the full T-Antigen (fist column, second row) shows an alternative pathway of the ssDNA during rewinding. The symbols in the upper left corner at each sketch are the legend to the plots in b where the corresponding velocity of T-Antigen is shown.

always restart, which shows that T-Antigen stays attached to the ssDNA. The single molecule conditions makes binding of another enzyme to the ssDNA, during the time the hairpin is kept open, unlikely.

The translocation velocity has not been investigated for its dependency on the force. The different stretching of ssDNA at different forces could have an influence on the translocation velocity of the enzyme, but is neglected in here. The first determined translocation velocities for the full T-Antigen as well as the core helicase domain during unwinding and during rewinding are shown in Figure 4.12a. Because of the assumption made in the last sections, that the rewinding velocity is similar to the translocation velocity, the rewinding velocity of the full T-Antigen is plotted in the same graph for comparison (Fig. 4.12a, upper graph).

To interpret the different translocation velocities, the sketches in Figure 4.12b, first column, show the suggested configuration of the ssDNA (within the suggested model *iii*) during the time when the DNA hairpin is unzipped. The first row shows the configuration of T-Antigen after unwinding, the second row shows the configuration of T-Antigen after rewinding. The activity of T-Antigen during the DNA hairpin is unzipped implies that one strand of ssDNA can be pulled out of the channel formed by the OBD domains (compare the threading of the ssDNA during unwinding Fig. 4.10b first column, first row to the threading of the ssDNA during translocation Fig. 4.12b

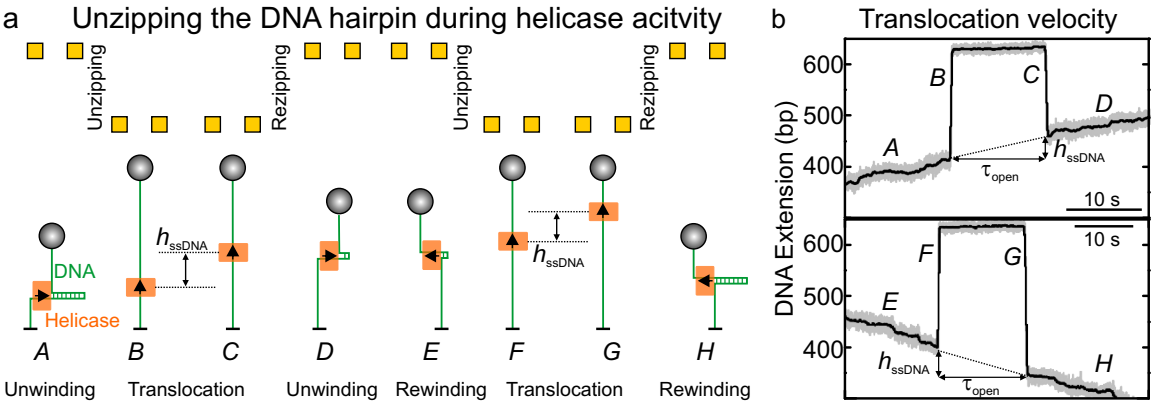

Figure 4.11 Experiment to determine the translocation velocity of T-Antigen. (**a**) Sketches depict the activity of the T-Antigen (orange) on the DNA hairpin (green) in the magnetic tweezers setup (magnets are yellow squares). T-Antigen moves into the direction of the black arrow. The high magnet position corresponds to force where the DNA hairpin is closed (usually $8-10$ pN), the low magnet position corresponds to force where the DNA hairpin is open (usually $20-24$ pN). The change of the magnet position induces DNA hairpin unzipping and rezipping as indicated. At low forces T-Antigen is unwinding or rewinding, at high forces it translocates along ssDNA (moved distance) as indicated. The letters *A*-*H* correspond to the labeled sections of the data shown in b. (**b**) *upper*: Sample trace of the experiment explained in a for the steps from *A*-*D* (during unwinding). The translocation velocity is determined by the slope of the dashed line. The time the hairpin is kept open is labeled τ_{open}, the distance the helicase moves within this time is labeled $h_m athrm ssDNA$. *lower*: Sample trace of the experiment explained in a for the steps from *E*-*H* (during rewinding).

first column, first row). The average translocation velocity, when the DNA hairpin is unzipped during unwinding (Fig. 4.12a, lower graph, red) is slightly higher than the average rewinding velocity (Fig. 4.12a, upper graph). This suggests that during rewinding of the DNA hairpin by the full T-Antigen the translocation on ssDNA is slightly hindered. Within the model *iii* it can be explained by the different pathways the ssDNA takes during rewinding and during translocation when the DNA hairpin is unzipped during unwinding (compare ssDNA threading in Fig. 4.10b first column, second row and Fig. 4.12b first column, first row).

Additionally the translocation velocity of T-Antigen, when the DNA hairpin is unzipped during rewinding (Fig. 4.12a, lower graph, blue) is significantly smaller than the rewinding velocity of the full T-Antigen enzyme (Fig. 4.12a, upper graph). Within the suggested model *iii* this could be explained by the application of high forces and the threading of ssDNA through the enzyme. Upon application of high forces to unzip the DNA hairpin, the ssDNA might be blocked, because of the threading of the ssDNA between the OBD and the core helicase domain. Another possibility could be that T-Antigen is distorted by the stretched ssDNA causing that the conformational changes during ATP hydrolysis are hindered. These effects can only occur when T-Antigen was rewinding before unzipping the DNA hairpin. In contrast it cannot occur when T-Antigen was unwinding before unzipping the DNA hairpin (compare

Fig. 4.12b first column, first to second row). We also observed that the translocation during rewinding can go into the opposite direction (Fig. 4.12a, lower graph, blue), which cannot be explained yet.

To test the influence of the OBD on the translocation velocity, the same experiment was performed on the core helicase domain (T-Antigen without the OBD). Sketches of the ssDNA threading and some data is shown in the right column of Figure 4.12b, second column. The first two measured translocation velocities are indicated in Figure 4.12a (green and orange). In contrast to the translocation velocites with the full T-Antigen, the first measurements with the core helicase only show that the translocation velocities are not dependent on the activity of T-Antigen before DNA hairpin unzipping. Also, the translocation velocities without OBD are in the range of the rewinding velocity of the full T-Antigen (compare orange and green data in Figure 4.10b, lower graph to Figure 4.12a upper graph). This means that the OBD influences the translocation and thus the un- and rewinding mechanism of T-Antigen. Also these preliminary results support the suggested unwinding model *iii* (without the OBD no blocking of the helicase at high forces can occur during translocation at high forces).

Although additional measurements are necessary to verify the data, the first results support the model *iii* from Figure 4.2 for the unwinding of forked DNA by T-Antigen. The data also shows that the ssDNA translocation velocity cannot necessarily be inferred from the rewinding velocity as it is suggested for other helicases [7].

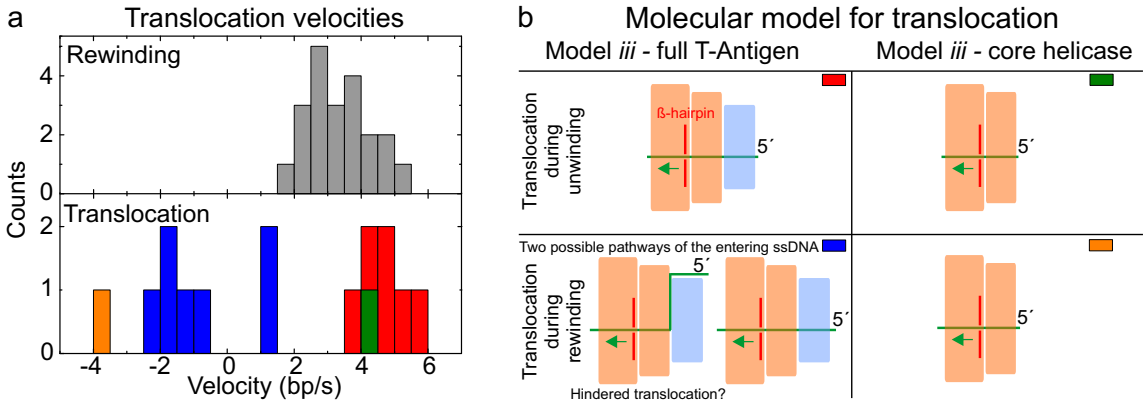

Figure 4.12 Molecular model for the translocation of ssDNA by T-Antigen with and without the OBD. (**a**) Translocation velocities of the full T-Antigen during unwinding (red), rewinding (blue) and of the core helicase domain during unwinding (green) and rewinding (orange). For comparison the average rewinding velocity is shown in the upper graph. The forces during the hairpin was closed are between $8 - 10$ pN. Forces when the hairpin was unzipped are between $20 - 24$ pN. (**b**) Sketches of the ssDNA threading through the full T-Antigen (left column) and core helicase domain (right column) during translocation (at high forces) when the DNA hairpin is unzipped during unwinding (first row) or when the DNA hairpin is unzipped during rewinding (second row). The threading of ssDNA corresponds to model *iii* from Figure 4.2. The green arrow indicates the translocation direction of the ssDNA. Two beta-hairpins are sketched in red. The colors at the upper right corner of each sketch correspond to the translocation velocities in a.

4.5 Summary, conclusion and discussion

The single molecule DNA hairpin unwinding experiments in this chapter showed that T-Antigen from Simian Virus 40 is an extremly slow ($1 - 2$ bp/s) enzyme compared to prokaryotic replicative helicases (Fig. 4.5). Furthermore, T-Antigen is very processive (unwinds thousand of base pairs without dissociation) and rarely stalls or steps backwards in contrast to other helicases [144, 64]. Additionally, T-Antigen was shown to rewind a DNA hairpin, faster than it is unwinding ($2 - 5$ bp/s) (Fig. 4.3). The observation of rewinding of the DNA hairpin, strongly suggests that T-Antigen translocates on ssDNA during unwinding and rewinding. Therefore the rewinding velocity is expected to be similar to the translocation velocity, given that the rehybridizing DNA hairpin behind the helicase has no strong influence on the rewinding process. This assumption could be confirmed. Firstly, because the rewinding velocity is not DNA sequence dependent (but the unwinding velocity is) (Fig. 4.9). The difference between unwinding and rewinding velocity arises from the work the helicase has to do against the base pairing energy while unwinding, which is not required during rewinding. Secondly, preliminary results of measurements of the translocation velocity at high forces are similar to the mean rewinding velocity (Fig. 4.12).

The unwinding velocity is weakly force-dependent compared to other studied helicases (NS3 [92], T4 gp41 [35], T7 gp4 [39]). This suggests that the unwinding behavior of T-Antigen cannot be decribed with a passive DNA unwinding model, which was confirmed (Fig. 4.6). Interestingly also active unwinding model failed to describe the force dependent unwinding velocities (Fig. 4.7) (with the premise that the translocation veloctiy is similar to the rewinding velocity). Additionally, it was recently shown that the active unwinding model predicts similar behavior for different sets of parameters [7]. Therefore, we described the unwinding behavior of T-Antigen with a physical model assigning T-Antigen the intrinsic ability to break base pairs open, which fits well to the experimental data (Fig. 4.8). The model includes that T-Antigen switches between two translocation modes depending on the presence or absence of a closed base pair within its step size. This means that T-Antigen is fast when it is translocating ssDNA (with 3.4 nt/s on averge) and slows down when it encounters dsDNA (to 0.8 bp/s), because the energy of the ATP hydrolysis cycle is now partially required to open the base pair. The active and passive unwinding model was shown to describe the behavior of prokaryotic helicases (e.g. T7 [39]). The main difference to the alternative model presented here is the ability of the enzyme to actively break base pairs bonds. Since SV40 infects eukaryotic cells the alternative model might be a general description for eukaryotic helicases. Recently, a very similar idea was used to describe the force dependence of the ribosome [145]. The predicted property of T-Antigen to break base pairs is supported by the preliminary result of the DNA sequence dependence of the unwinding velocity.

Beside the physical model to describe the unwinding velocity, the available data was used to develop a molecular unwinding model for T-Antigen (Fig. 4.10). In the following the main characteristics of T-Antigen, which were considered for the molecular unwinding model are summarized. 1. Many studies showed that T-Antigen

is required to form a double hexamer at the origin of replication [22]. Within the presented experiments no indication was found, that T-Antigen binds unspecifically to dsDNA and start unwinding within the DNA hairpin area (the DNA hairpin unzipping tests before unwinding is detected, would most likely have indicated such activity). Instead, T-Antigen uses the preformed DNA junction to initiate unwinding of dsDNA. Therefore, T-Antigen most likely assembles as sinlge hexamer at the DNA junction, which was also shown in other experiments [130]. 2. The ssDNA does not rehybridize behind the helicase, although no single stranded binding protein is used. Thus the enzyme sterically prevents the approach of the two single strands, i.e. the ssDNA exits the enzyme at different locations. 3. In the central channel of the helicase domain only ssDNA might be located (instead of dsDNA). This is supported by the possibility to unzip the DNA hairpin mechanically during T-Antigen is unwinding without loosing or destroying its ability to translocate. 4. The OBD is involved in the translocation process, because of the significantly different translocation velocities of T-Antigen with and without the OBD. In other studies the importance of the OBD during DNA unwinding was already shown (beside its task to locate the origin of replication [118, 124]). The OBD might form a clamp around the dsDNA area of the DNA junction, which is also supported by experiments, where the foot print of T-Antigen on the DNA junction was shown to cover the dsDNA area and both ssDNA ends at a DNA junction [130, 143]. Furthermore the clamping activity can explain the weak force dependence of the unwinding velocity, because the DNA junction is shielded against the applied force. 5. The developed alternative physical DNA unwinding model fits best for a step size of one nucleotide. This means the beta hairpins in the hexamer channel of T-Antigen seem to translocate the ssDNA subsequently (as for instance in the staircase model presented in section 1.2.1, Figure 1.4). These properties lead to the suggested molecular unwinding model for T-Antigen at a DNA junction (see Figures 4.10, 4.12). The threading of ssDNA within this model supports the suggested dsDNA unwinding model shown in reference [121]. However, the assembly of T-Antigen on dsDNA and on a DNA junction as well as the subsequent unwinding mechanism might differ. Additionally, it shall be noted, that *in vivo* T-Antigen binds to different cellular proteins such as topoisomerase, nucleolin, single stranded binding protein, polymerases or the tumor suppressors p53 and pRB [146, 147, 148] which influences the activity and the structural integrity of the enzyme. Therefore it is difficult to imply for example mechanisms of regulation of the replication *in vivo* from the data of T-Antigen only.

Finally, more data need to be produced to strengthen the hypothesis of the participation of the OBD and the sequence dependence of the unwinding velocity of T-Antigen. Additionally the step size of the enzyme need to be analyzed to evaluate another parameter of the alternative unwinding model.

5 DNA unwinding by RecQ from Arabidopsis thaliana

5.1 RecQ helicases - Structure and function

RecQ helicases are a subfamily of the superfamily 2 of helicases and are present in all eukaryotes and many bacteria [48]. An amino acid sequence alignment of several RecQ helicases shows the highly conserved domains within different organisms (Fig. 5.1a). The known specific tasks of the conserved domains are explained below. The important biological role of RecQ helicases is reflected by the fact that defects in three (HsBLM, HsWRN, HsRECQ4) of the five human RecQ homologous cause severe genetic diseases associated with pre-ageing and predisposition to cancer [48]. For instance, mutations in HsBLM (causing Bloom´s syndrome), can cause, amongst other clinical features, proportional dwarfism, sun-sensitive facial erythema, hyperpigmented skin lesions or male infertility [48]. Typically RecQ helicases are recruited for repair processes at replication and recombination intermediates. Such repair processes are initiated for example when a replication fork stalls at lesions or obstacles along the template DNA [149, 150]. Another example is the role of RecQ helicases in suppressing tumors by preventing sister chromatid exchange during homologous recombination (HR), which is potentially deleterious for genome stability [48]. HR is a mechanism of the cell, where a DNA sequence is utilized to repair a similar or equal broken sequence. HR is required to be carefully regulated, because uncontrolled it can promote tumorigenesis [48]. RecQ helicases are involved in several substeps of double strand break repair by HR, where they have a regulative role (Fig. 5.1b). For example Sgs1 might be involved in generating 3´ ssDNA overhangs to initate HR. In contrast, D-loops (an intermediate substrate during HR) can be disrupted by several RecQ helicases to abort the HR, i.e. they also have a regulatory role as anti-recombinases [48]. In a later stage of HR double Holliday junctions are generated, which HsBLM can resolve by dissolution. This results only in non-crossover recombinant products. If HsBLM is defect (like in Bloom´s syndrome) these double Holliday junctions are resolved by other Holliday junction resolvases, causing that a complete single strand of the DNA, which is utilized to repair the sequence, is exchanged (sister chromatid exchange). A high number of sister chomatid exchange is a potential danger for genetic stability and is likely to be related to tumor formation [48].

The direct role of individual RecQ helicases in repair processes is still widely unknown. Furthermore, the distinct tasks of different RecQ helicases within one organism are unclear yet.

The plant Arabidopsis thaliana has seven homologues of RecQ. In the following chapter single molecule experiments will be used to characterize RecQ2 (AtRecQ2) and RecQ3 (AtRecQ3) [153]. Although several amino acid sequence homologies between RecQ helicases of Arabidopsis thaliana and the human or bacterial RecQ helicases were identified (see Fig. 5.1a), it is not possible to infer functional homology

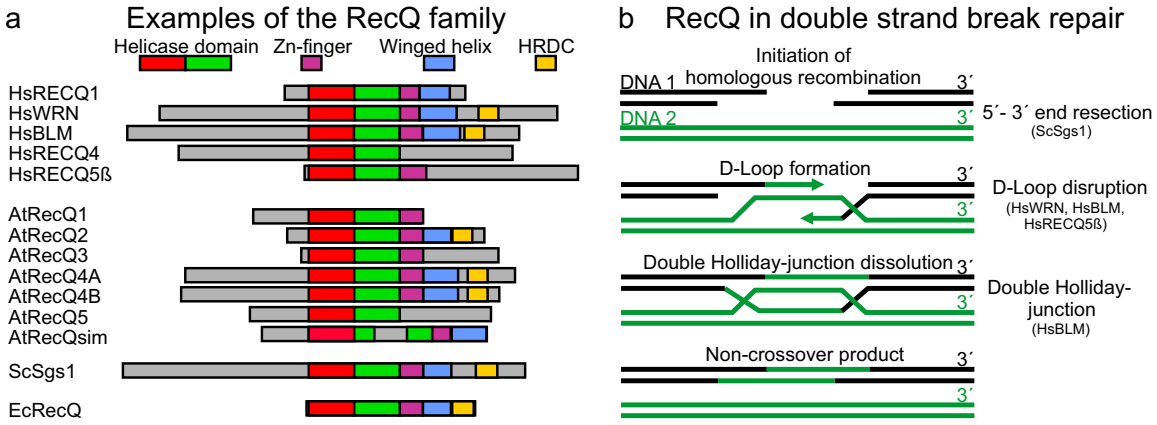

Figure 5.1 Structure of different RecQ helicases and one particular task in genome stability function. (a) Amino acid sequence alignment of some members of RecQ helicases from *Homo sapiens* (Hs...), *Arabidopsis thaliana* (At...), *Saccharomyces cerevisiae* (ScSgs1) and *Escherichia coli* (EcRecQ). The colored regions in the sequences show different conserved domains. The domain organization was adapted from Kobbe *et al.* [151] and Bennett *et al.* [152]. The sequences are aligned along the conserved helicase domain (red and green for the two subdomains (section 1.1.2)). Additionally the characteristic RecQ-C terminal domain (RecQ-Ct), consisting of a zinc-binding domain (Zn-finger, purple) and a helix-turn-helix domain (winged helix, blue), and the Helicase-and-RNase-D C-terminal (HRDC, yellow) are highlighted. The gray areas are mostly not conserved. (**b**) Scheme of several steps of double strand break repair by homologous recombination (HR) (sketch is adapted from Chu *et al.* [48]). Shown are steps where RecQ enzymes might be involved performing the tasks indicated to the right of each step. The dissolution of double Holliday junction results in non-crossover products (only the DNA sequence of DNA 2 (green) involved in the repair process is copied to DNA 1 (black), instead of sister chromatid exchange, see text).

[151]. For example AtRecQ4A might have a functional homology to HsBLM [153] (pro-recombinase), but AtRecQ4B, which has 70% amino acid secquence homology with AtRecQ4A, was shown to have an opposite function (anti-recombinase) [151]. On the other hand, the available strutural data of several RecQ helicases shows that the conserved domains as well as their structural arragement are similar. Unfortunately, no crystal structure of the helicases investigated in this thesis (AtRecQ2 and AtRecQ3) is available, but for comparison two examples of the crystal structures of EcRecQ [154] and HsRECQ1 (Pike *et al.*, to be published) are presented in Figure 5.2. The crystal structure of EcRecQ shows a bound ATPγS between the two RecA-like domains, which form the helicase domain (see also section 1.1.2). A ssDNA binding site is predicted between the two RecA-like domains, similar to Hel308 (see Fig. 1.2 in section 1.1.2), PcrA [26] or Rep [155], which were cocrystalized with dsDNA with single stranded overhangs [154]. The RecQ C-terminal domain (RecQ-Ct) is unique to RecQ helicases and important for the catalytic activity. One part of the RecQ-Ct contains four cystein residues, binding a zinc ion, which is highly conserved among RecQ helicases (purple in Fig. 5.2). Mutations in the cystein residues lead to Bloom´s syndrome and enhanced sensitivity to DNA-damage [156]. The RecQ-Ct of HsWRN was cocrystalized with DNA and the zinc binding was suggested to guide the unwound

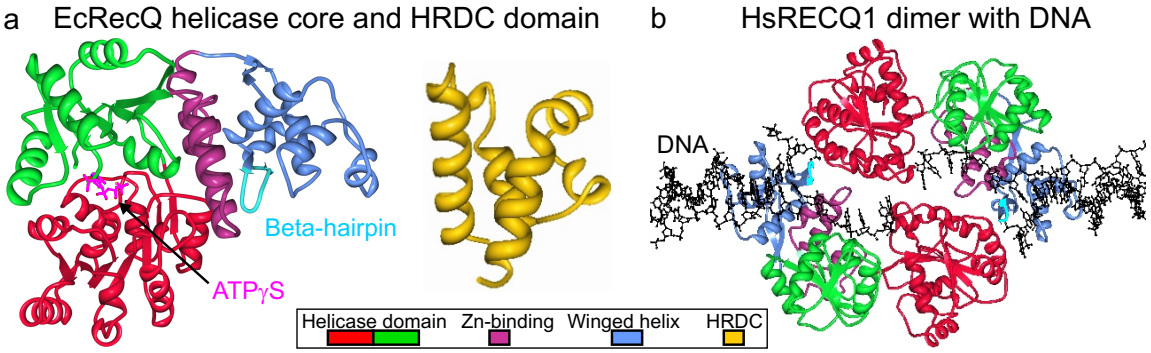

Figure 5.2 Crystal structure of EcRecQ and HsRECQ1. (a) Crystal structure of EcRecQ with ATPγS (pink) (PDB:1OYY, [154]) visualized with proteinworkshop [20]. The colors of the domains correspond to the colors in Figure 5.1a, except the additional highlighted beta-hairpin. RecA-like domain 1: aa 1-208, RecA-like domain 2: aa 209-340, Zn-binding domain: aa 341-406, winged helix: aa 484-496, beta-hairpin: aa 484-496. The HRDC domain (yellow) is shown seperately (PDB:1WUD, [159]). (**b**) Crystal structure of two HsRECQ1 helicases in an asymmetric unit with partially dsDNA (PDB:2WWY, Pike *et al.*, to be published) visualized with proteinworkshop [20]. RecA-like domain 1: aa 63-281, RecA-like domain 2: aa 282-418, Zn-finger: aa 419-480, winged helix: aa 481-592, beta-hairpin: aa 555-574.

ssDNA to the ATPase domain [157]. The second part of the RecQ-Ct is a winged helix domain (WH-domain) (blue in Fig. 5.2). Although this domain can be found at different positions and orientations in different RecQ helicases, it was shown to be important for dsDNA binding and unwinding in nearly all investigated RecQ helicases [156]. The most important feature of the winged helix domain is a beta-hairpin (cyan in Fig. 5.2), which was found in HsWRN [157] and Hel308 [11] to directly interact with the base pair at the DNA junction. Furthermore, mutations on the WH-domain leads to the inability of the most RecQ helicases to unwind DNA. Another conserved domain in several RecQ helicases is the Helicase-and-RNase-D C-terminal domain (HRDC-domain). It is suggested to be involved in nucleic acid binding, structural integrity and protein-protein interactions. HRDC is the most variable protein fold in RecQ helicases. Some RecQ helicases do not possess HRDC, while e.g. RecQ from Deinococcus radiodurans has three repeats of this domain [158]. Due to its very flexible linker to the RecQ-Ct a crystal structure of the HRDC domain of EcRecQ only exists isolated (yellow in Fig. 5.2). Figure 5.2b shows a dimer of HsRECQ1 cocrystalized with two pieces of partially dsDNA. The colored domains show the similarity to EcRecQ. This might be the configuration of HsRECQ1 to resolve Holliday junction substrates.

The crystal structures, amino acid sequences and the various studies of similar RecQ helicases might help to infer similar properties of the herein investigated RecQ heliacses. The major part of this chapter is dedicated to AtRecQ2. AtRecQ2 consists of 705 amino acids where amino acids 98-408 encode the helicase domain, 409-477 the RecQ-Ct domain and 591-670 the HRDC [160, 153]. It catalyses DNA unwinding in 3´ to 5´ direction, but at least 5 nucleotides of a 3´ ssDNA overhang are required

[151]. It can hydrolyse all (d)NTPs (highest efficiency for ATP) in the presence of Mg^{2+}, Mn^{2+} and Ca^{2+} [151]. As many other RecQ helicases AtRecQ2 is able to resolve D-Loops and induces branch migration of holiday junctions which are both intermediates of homologous recombination and repair processes as mentioned above [151].

AtRecQ2 and AtRecQ3 used in the following experiments was kindly provided by the collaborating groups of Daniela Kobbe and Holger Puchta (Karlsruher Institut für Technologie, Karlsruhe, Germany). The purification protocols are described in [151, 161].

5.2 Repetitive unwinding by a single AtRecQ2 enzyme

For the study of AtRecQ2 the 40 bp DNA hairpin construct was used (see chapter: 3.1.3). To observe unwinding of the hairpin by AtRecQ2 the force is set well below the unzipping force of the 40 bp hairpin ($F_{\mathrm{unzip}} = 11.6$ pN) and the enzyme added in reaction buffer (RBRecQ, see appendix 6.2.2). Fig. 5.3a (upper graph) shows a recorded unwinding event, which is illustrated in Fig. 5.3b (sketch). We observe characteristic events in which the DNA extension slowly increases in a processive manner. This indicates base pair opening by AtRecQ2. When the full 40 base pairs are unwound an abrupt reset to a partially or fully closed hairpin state is observed (Fig. 5.3b). The slow unwinding followed by a very fast resetting appears to be very characteristic for AtRecQ2, independent of the DNA template length, the base pair composition or the applied forces. Fig. 5.3a also shows that unwinding events typically occur in a highly repetitive fashion (graph in the middle). Such series of repetitive unwinding events occurs only in a confined time interval (lower graph), i.e. bursts of unwinding events are separated by long pauses of no unwinding activity. This strongly suggests that a single enzyme or enzyme-complex is responsible for the repetitive unwinding. At the end of an activity burst the enzyme dissociates. The long pause is then the time required until the next enzyme (complex) binds to the DNA hairpin. This explanation is the most simple model for the observed activity bursts. Additional evidence for single molecule conditions is provided by DNA hairpin unzipping experiments (see below).

The repetitive unwinding by AtRecQ2 is astonishing. It appears that the enzyme is able to frequently unwind DNA. The question however arises how a single AtRecQ2 accomplishes the successive unwinding events. Several possibilities will be briefly discussed in the following to establish a hypothesis for the mechanism of repetitive unwinding. A more detailed discussion of these possibilies follows in the next sections. 1. AtRecQ2 could dissociate after unwinding the DNA hairpin and a second AtRecQ2 enzyme binds to the ssDNA to fullfil the subsequent unwinding event. This explanation is ruled out by the above mentioned single molecule conditions. 2. As presented in the last chapter for T-Antigen, many helicases were shown to rewind DNA hairpins after unwinding (T7 gp4 [39], T4 gp41 [35], UvrD [64]), i.e. the DNA hairpin is slowly closed. This observation was explained by translocation of the helicase over the DNA hairpin loop when the full DNA hairpin is unwound. Then the helicase keeps on

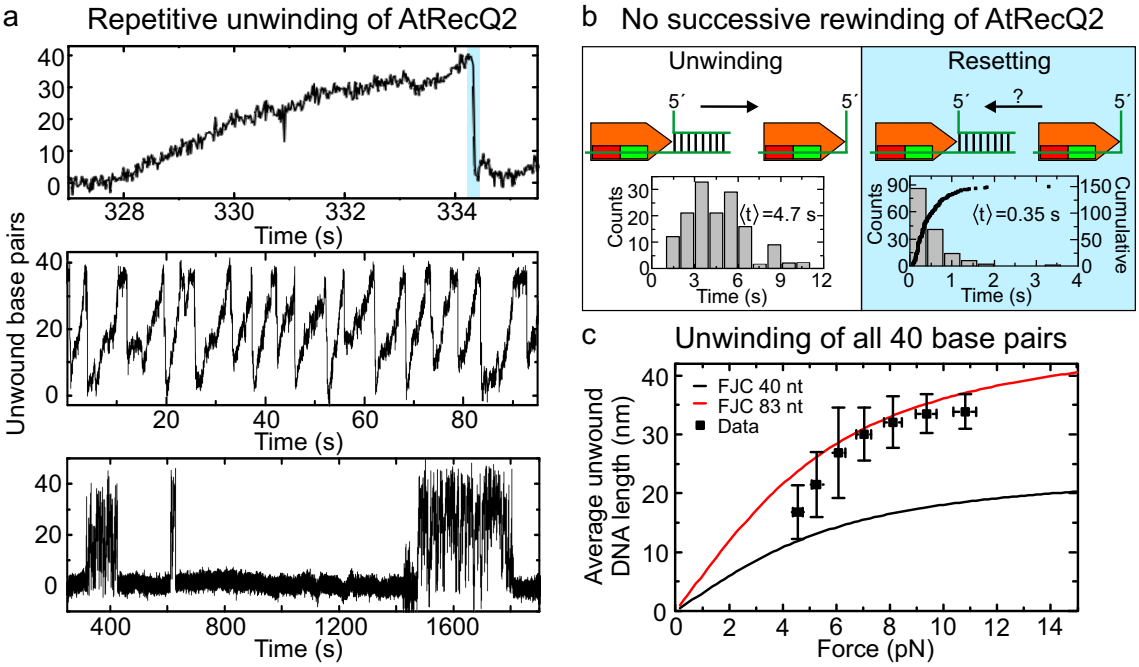

Figure 5.3 Repetitive unwinding events of a single AtRecQ2 helicase. (a) *top*: A single event of slow unwinding and fast resetting of the 40 bp DNA hairpin by AtRecQ2 at 10 pN. The DNA extension was recalculated from nanometers to base pairs assuming full unwinding of the hairpin. *middle*: Increasing time scales show that the characteristic behavior occurs in repetitive fashion. *bottom*: Bursts of repetitive unwinding events are separated by long pauses. (**b**) The slowly increasing DNA extension in (a) is caused by the unwinding of AtRecQ2 in 3´ to 5´ direction of the single strand it translocates along. A histogram as well as the mean unwinding time is shown. The resetting occurs much faster. Since AtRecQ2 is not able to translocate in 5´ to 3´ direction, it is unclear how the enzyme is reset to the beginning of the DNA hairpin. The values of the resetting times are shown as a histogram and as cumulative counts. (**c**) Average maximum unwound DNA hairpin length as function of force. The error bars display the standard deviation of the data. The black line is a calculation using the FJC model (see section 3.3.2 equation 3.2) with $L_0 = 40\ \text{nt} \cdot 0.574\ \text{nm/nt}$, the red line with $L_0 = 83\ \text{nt} \cdot 0.574\ \text{nm/nt}$.

translocating on the formerly displaced strand while the DNA hairpin rehybridizes in its wake (see sketches for T-Antigen in Fig. 4.3b). The same mechanism for AtRecQ2 seems not likely, because the nearly instant resetting from the open DNA hairpin to a closed conformation would require a tremendously faster rewinding velocity than the unwinding velocity. This is unlikely assuming the same translocation mechanism for un- and rewinding. 3. AtRecQ2 could move backwards (5´ to 3´ direction) on the tracking strand. This mechanism can be excluded due to various template specific bulk experiments shown by Kobbe *et al.* [151, 161] which define AtRecQ2 explicitly as 3´ to 5´ helicase. 4. Repetitive unwinding followed by fast resetting has been found for the RNA helicase NS3 [31]. There, the suggested mechanism includes a tight connection between the 5´ end of the displaced ssRNA and the NS3 enzyme, i.e. NS3 is put on a leash (ssRNA loop) during unwinding (explained in detail in

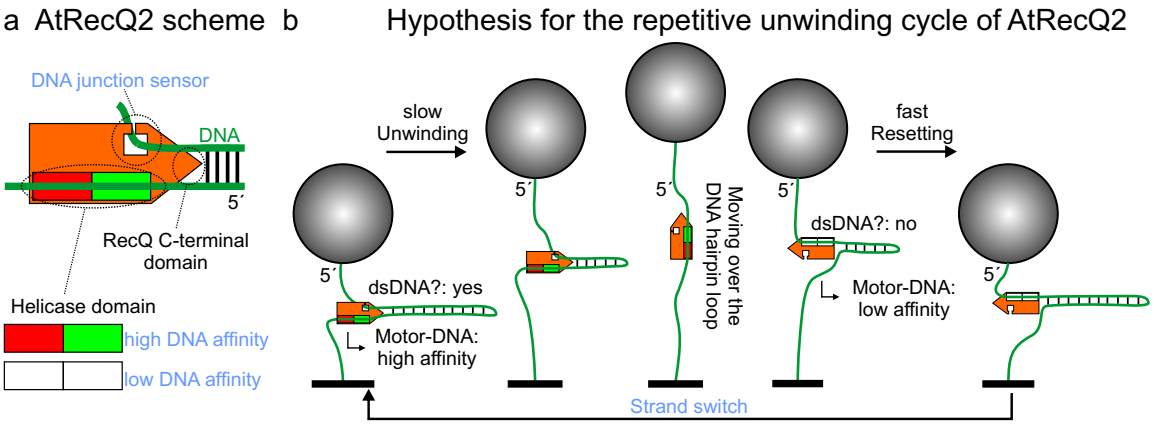

Figure 5.4 Hypothesis for the repetitive unwinding of AtRecQ2. (a) Schematic representation of AtRecQ2 (orange) with its helicase domain (red and green box for the two RecA-like domains, the green box always points towards the translocation direction, i.e. the 5´ end) unwinding dsDNA (the two dark green lines for the single strands connected by black lines for the base pairing). The RecQ-Ct is located towards the DNA junction and the beta-hairpin points on the first base pair as indicated. A dsDNA sensor (hole in the helicase) is required to detect the presence of the DNA junction. The helicase domain can have a low affinity to the DNA strand it is translocating (then presented as uncolored boxes). (**b**) Hypothesis for the unwinding and resetting cycle of AtRecQ2. (from left to right): AtRecQ2 at the DNA junction. The dsDNA sensor detects the junction which causes a high affinity of the helicase domain to the DNA. Upon ATP hydrolysis the hairpin is unwound. AtRecQ2 switches the tracking strand and hence, the dsDNA sensor does not detect the DNA junction which causes a low affinity of the helicase domain to the DNA. As a result the DNA hairpin can rehybridize, thereby rapidly pushing AtRecQ2 back to the beginning of the DNA hairpin. To restart the cycle, AtRecQ2 needs to switch the strand again. The properties of AtRecQ2 which will be investigated in the following are written in blue.

section 5.9, Fig. 5.14a). When NS3 releases the DNA after unwinding, it can be quickly repositioned to the beginning of the DNA hairpin to start the next unwinding event. This mechanism adapted to our DNA configuration would lead to an increase of the DNA extension corresponding only to one half of the DNA hairpin, i.e. the 40 nucleotides in the ssRNA loop would not contribute to the DNA extension. Fig. 5.3c shows however that for AtRecQ2 the measured average DNA unwinding length of the 40 bp DNA hairpin fits rather to the length of 83 nt (the full DNA hairpin) than to 40 nucleotides (half of the DNA hairpin). This excludes a loop formation and rules out a ridged connection between enzyme and DNA ends.

Neither multiple enzymes that successively unwind the DNA, dissociate and reassociate, nor a very fast rewinding, nor the proposed anchor model for NS3, are in agreement with our observations. Therefore, an alternative model is hypothesized (Fig. 5.4). For this hypothesis, AtRecQ2 has to be able to switch between a low and a high affinity to the ssDNA it is tracking along. For the model we sketch AtRecQ2 as shown in Figure 5.4. The helicase domain forms the contact to ssDNA which is either sketched red and green for high affinity to the ssDNA or uncolored for low

affinity. Figure 5.4b shows from left to right how one slow unwinding event followed by a fast resetting event is explained within this hypothesis. When AtRecQ2 has a high affinity to the DNA and the DNA junction is in front of the enzyme, it will unwind the dsDNA (in front means the DNA junction is located in the direction of AtRecQ2´s translocation direction (3´to 5´)). The RecQ-Ct is most likely also located in the translocation direction, as sketched in Fig. 5.4a, which is supported by experimental results showing a high dsDNA affinity of the RecQ-Ct [162, 163]. AtRecQ2 moves over the DNA hairpin loop, which will start to rehybridize behind the enzyme (behind means the DNA junction is located oppositely to the direction of AtRecQ2´s translocation direction (3´to 5´)). Now AtRecQ2 is oriented with the RecQ-Ct away from the DNA junction. This causes to switch the high affinity of AtRecQ2 to the DNA to a low affinity and the DNA hairpin can rehybridize. This reaction pushes AtRecQ2 (fast) back to the beginning of the DNA hairpin. To start the following unwinding cycle AtRecQ2 needs to switch from the single strand it was pushed along back to the original tracking strand. To verify this hypothesis, several properties of AtRecQ2 need to be investigated. First, the high and low affinity of AtRecQ2 to the ssDNA. Given a high affinity between AtRecQ2 and the ssDNA the position of the enzyme should influence the base pairing of the DNA, i.e. if the DNA junction is in the translocation direction of AtRecQ2, the high affinity causes dsDNA unwinding. In contrast, given a low affinity between AtRecQ2 and the ssDNA the base pairing influences the position of the enzyme, i.e. if the DNA junction is located oppositely of the translocation direction of AtRecQ2, the low affinity will cause the rehybridizing reaction to push the helicase. This will be investigated in the section 5.3. Second, it is required that AtRecQ2 is able to switch from one single DNA strand to the other. This will be investigated in section 5.4. Third, to explain that high affinity between AtRecQ2 and the ssDNA only occurs when the DNA junction is in front of the enzyme, a sensor is required to probe the location of the DNA junction. If the DNA junction is sensed in front of AtRecQ2 the enzyme switches to high affinity to DNA. If the DNA junction is sensed behind AtRecQ2 (or not sensed in front of AtRecQ2) the enzyme switches to low affinity to DNA. This would explain the asymmetry between slow unwinding and fast resetting. This will be investigated in section 5.5.

5.3 Two distinct contact modes in absence of a DNA junction

Different affinities between AtRecQ2 and the ssDNA might be reflected in varying translocation velocities on ssDNA. Therefore, an experiment to determine the translocation velocity of the enzyme on ssDNA was performed. This kind of experiment was already introduced in detail in section 4.4, Figure 4.11. Briefly, by unzipping and rezipping of a 500 bp DNA hairpin by force, the position of the helicase on ssDNA can be probed (representative trace in Fig. 5.5b). Unzipping of the DNA hairpin is achieved by applying forces well above the unzipping force of the 500 bp DNA hairpin ($F_{\mathrm{unzip}} = 15.8$ pN, see section 3.3.1). When AtRecQ2 unwinds the DNA hairpin during the unzipping, the DNA junction in front of the helicase dissolves and

AtRecQ2 faces pure ssDNA. After a certain time (τ_{open}) the force is reset and the DNA hairpin rehybridizes until the enzyme sterically hinders further annealing (see Fig. 4.11 *A*-*D*, in section 4.4). A change in the DNA extension before unzipping and after rezipping is detected, i.e. AtRecQ2 covers a distance on the ssDNA (h_{ssDNA}) during the time the DNA hairpin is open (τ_{open}). A unidirectional movement (3´ to 5´ translocation) of the enzyme along ssDNA would lead to only positive distances h_{ssDNA} (Fig. 5.5a). In contrast, in the experiment with AtRecQ2 also negative distances h_{ssDNA} are observed. (Evaluation of the distances the enzyme moved on ssDNA for different times the DNA hairpin is kept open are shown and discussed below.) In contrast to the bidirectional movement of AtRecQ2 on ssDNA, we always observe immediate, unidirectional dsDNA unwinding as soon as the DNA hairpin is rezipped.

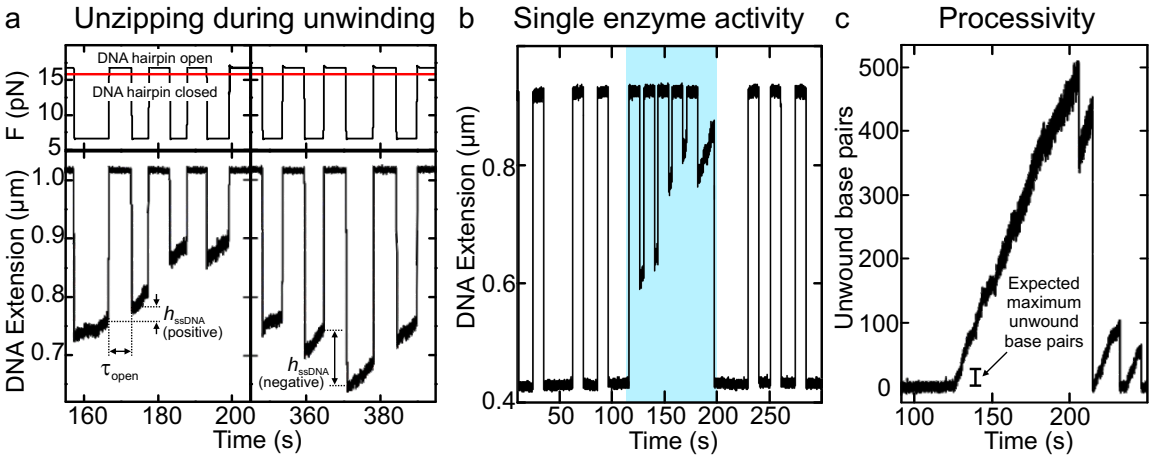

Figure 5.5 Probing the movement of AtRecQ2 on ssDNA. (a) Experiment to determine the translocation velocity of AtRecQ2 on ssDNA (explained in detail in Figure 4.11 in section 4.4). Therefore, the applied force is switched between 6.6 pN and 16.8 pN (top graph, red line indicates the unzipping force of the 500 bp DNA hairpin). This force switch unzips the DNA hairpin, seen as a sudden large extension of the DNA or rezips the DNA hairpin, seen as a sudden decrease in DNA extension (bottom graph). The DNA hairpin is kept open for a certain time (τ_{open}) until the force is switched back to close the DNA hairpin. This experiment is done in presence of AtRecQ2 in the unwinding reaction buffer (RBRecQ, see appendix 6.2.2). A difference in DNA extension when the DNA hairpin is opened and when it is closed again (h_{ssDNA}) indicates a different position of the enzyme on the DNA, i.e. the enzyme moved during the time the DNA hairpin was open. Assuming unidirectional translocation of AtRecQ2 on ssDNA, it would always result in a larger DNA extensions when the DNA hairpin is rezipped, compared to the DNA extension when it was unzipped (positive h_{ssDNA}, see also Fig. 4.11 in sec. 4.4 compare *A* to *D*). Suprisngly, also smaller DNA extensions are observed when the DNA hairpin rezipped (negative h_{ssDNA}). (**b**) Repeated unzipping and rezipping cycles to probe the presence of a helicase on the DNA hairpin. Activity of AtRecQ2 occurs only in a confined time interval (blue area) similar to the activity bursts in Figure 5.3a bottom graph. (**c**) AtRecQ2 is able to processively unwind several hundreds of base pairs at 10 pN applied force. This is in contrast to expectations from bulk experiments, where the activity of AtRecQ2 seems to be limited to a few tens of base pairs.

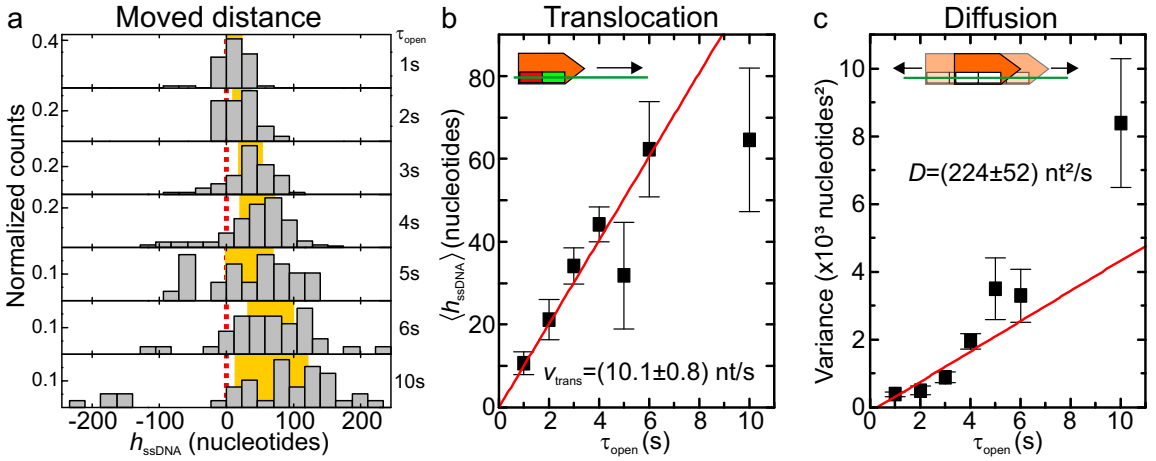

Figure 5.6 Translocation and diffusion of AtRecQ2 on ssDNA. (a) Evaluation of the experiment to determine the behavior of AtRecQ2 on ssDNA (Fig. 5.5a). The histograms show the distributions of the distances h_{ssDNA} AtRecQ2 moved during the DNA hairpin was unzipped for the indicated time τ_{open}. The red dashed line indicates the position where the distance before unzipping and after rezipping is the same ($h_{\mathrm{ssDNA}} = 0$ nt). The yellow areas indicate the standard error of the mean distances. (**b**) The linear increasing mean distance that AtRecQ2 moves with increasing time the DNA hairpin is kept open indicates a directional component of the movement on ssDNA. Such a behavior is expected for translocation. The sketch shows AtRecQ2 on ssDNA with a high affinity to the DNA in the style of Figure 5.4. The linear fit is weighted with the plotted standard error of the mean and was forced to intercept zero. The fitted translocation velocity is indicated. (**c**) The linear increasing variance of the distances that AtRecQ2 moves with increasing time the DNA hairpin is kept open indicates a diffusional component of the movement on ssDNA. The sketch shows AtRecQ2 on ssDNA with a low affinity to the DNA in the style of Figure 5.4. The linear fit is weighted with the plotted error of the variance ($\sqrt{2/N}$ times the variance). The calculated diffusion constant (Variance=$2D\tau_{\mathrm{open}}$) is indicated.

Thus, the dsDNA unwinding mechanism cannot be explained with a pure ssDNA translocation and steric disruption of the base pairs in front of the enzyme.

To rule out that the change in DNA extension is originated from dissociation and rebinding of different enzymes during the time the DNA hairpin is kept open a test experiment was performed. The 500 bp hairpin was repeatedly unzipped for a long time independent whether an enzyme actually unwinds it (Fig. 5.5b). When no enzyme is bound, the hairpin opens and closes completely. As soon as an enzyme is bound to the DNA the hairpin rezipping is stopped before the DNA hairpin is completely closed and dsDNA unwinding is detected. This activity is observed for a confined time interval (Fig. 5.5b, blue area). This observation is similar to the activity bursts observed during repetitive unwinding (Fig. 5.5a bottom graph) and is an independent verification of the detection of a single AtRecQ2 enzyme (or -complex).

Furthermore, it was tested if AtRecQ is able to unwind the complete 500 bp DNA hairpin (Fig. 5.5c). The finding that AtRecQ2 is able to unwind hundreds of base pairs is in contrast to bulk assays where the processivity of AtRecQ2 was tested. Bulk

experiments with short DNA templates of different lengths showed that the unwinding efficiency decreases rapidly, such that the maximum length AtRecQ2 can unwind would be thought to be rather limited to a few tens of base pairs (90% for 15 bp, 10% for 23 bp [151]). An obvious difference between the unwinding experiments in magnetic tweezers to the bulk experiments is the applied force. This will be discussed in section 5.7.

To investigate the type of movement on ssDNA we determined the distances between the DNA extension before unwinding and after rezipping the DNA hairpin in dependence of the time the DNA hairpin is kept open. Fig. 5.6a shows the distributions of these distances h_{ssDNA} for increasing times τ_{open} (indicated next to the graphs). The means of the distributions significantly increase linearly in agreement with unidirectional translocation (3´ to 5´) on ssDNA (Fig. 5.6b). The fitted translocation velocity is about 10 nucleotides per second. This value is in the order of magnitude for the translocation rate of HsBLM (30 nt/s [164]) and EcRecQ (90 nt/s [7]). Additionally the variances of the distances increase, suggesting a random bidirectional movement on ssDNA (Fig. 5.5c). The fitted diffusion coefficient is $D = 224 \pm 52$ nucleotides^2/s, which is similar to the diffusion coefficient of the restriction enzyme EcoRV on DNA (0.01 μm^2/s [165, 166]).

These results suggest that AtRecQ2 exhibits a mixed behavior on ssDNA. It is translocating and diffuses on ssDNA. For translocation the enzyme needs to be tightly coupled to the ssDNA, i.e. to have a high affinity for ssDNA. For diffusion the enzyme is loosely coupled to ssDNA, i.e. has low affinity for ssDNA. These findings support the hypothesis of a possible switch between high and low affinity of AtRecQ2 to ssDNA. In contrast, as soon as the DNA hairpin is rezipped in these experiments, AtRecQ2 always starts unidirectional dsDNA unwinding, i.e. always has a high affinity when a DNA junction is located in the direction of its translocation (in front of the enzyme).

The experiment revealed the affinity of AtRecQ2 to ssDNA and to dsDNA when a DNA junction is located in front of the enzyme. The question arises, how AtRecQ2 behaves when the DNA junction is located oppositely of the translocation direction of AtRecQ2 (behind the enzyme). To investigate this behavior it needs to be shoen that this situation (DNA junction behind AtRecQ2) can occur in our experiments at all. Two mechanisms could lead to this situation. First, as stated in the hypothesis, this situation can occur when AtRecQ2 translocates over the DNA hairpin loop after completely unwinding the DNA hairpin. Then the DNA hairpin will rehybridize behind the enzyme (see Fig. 5.4b, location of the DNA junction before and after moving over the hairpin loop). Second, the DNA junction can also be located behind the enzyme when AtRecQ2 is switching from its tracking strand to the formerly displaced strand during the unwinding of dsDNA. If these mechanisms apply to AtRecQ2 and how the enzyme behaves once the DNA junction is located behind it, is investigated in the next section.

5.4 AtRecQ2 can switch between single DNA strands

As mentioned above, the location of the DNA junction oppositely of the translocation direction of AtRecQ2 can be achieved by either strand switching during unwinding or translocation over the DNA hairpin loop. These activities were investigated by analysing the resetting events in more detail. The resetting events were investigated separately for different kinds of unwinding events: 1. the resetting events after complete unwinding of the 40 bp DNA hairpin (Fig. 5.7a), 2. the resetting events during a high force is applied (Fig. 5.7b), 3. resetting events which occur before complete unwinding of the 40 bp DNA hairpin (incomplete unwinding) (Fig. 5.7c).

For the first kind of unwinding events (full unwinding) most of the resetting events appear completely as a fast rehybridization (slip back) (Fig. 5.7a, *i*). Usually, translocation over the DNA hairpin loop leads to rewinding of the DNA hairpin (see for example T-Antigen, Fig. 4.3 in section 4.2). Detailed analysis of the characteristic fast resetting events after the DNA hairpin is completely unwound, indeed revealed a limited rewinding ability of AtRecQ2 (Fig. 5.7a, *ii*). This means AtRecQ2 is able to move over the DNA hairpin loop and is thereby directly transfered on the formerly displaced strand. Now the DNA junction is located behind the enzyme. In contrast to the dsDNA unwinding, the dsDNA rewinding occurs mostly for only a few base pairs before the rewinding event turns into a fast slip back. Of approximately 100 resetting events 83% of the resetting distances were overcome by a slip back, while 17% were reset by rewinding. For all used DNA constructs and applied forces rewinding appears not very stable and mostly turns into slip back after short distances.

The switch of unwinding into rewinding when the DNA hairpin is completely unwound is assisted by DNA hairpin loop. Supprisingly, also rewinding events were observed which directly switched from rewinding into unwinding again (Fig. 5.7a, *iii*). Compared to the event where unwinding switches into rewinding when the DNA hairpin is completely unwound, the switching of rewinding into unwinding is not assisted by a DNA hairpin loop. Thus, when rewinding turns into unwinding, the enzyme needs to switch from its actual strand to the other strand (the original tracking strand during it was unwinding). This finding supports the hypothesis of the repetivtive unwinding cycle in the previous section (Figure 5.4b, strand switch, written in blue, required to close the repetitive cycle).

The limited rewinding ability of AtRecQ2 was additionally verified by investigating resetting events during a high force is applied (Fig. 5.7b). Applied forces which are close to the unzipping force of the DNA hairpin destabilize the DNA hairpin when the enzyme has unwound several base pairs. This is seen by a sudden increase in the DNA extension (unzip) during unwinding (Fig. 5.7b, *i*). The increased probability for the hairpin to stay longer in the open conformation is seen as a plateau once the DNA hairpin is open. After a certain time the hairpin will rehybridize. A rewinding event is observed in Figure 5.7b, *ii*. During the open configuration of the DNA hairpin, the enzyme moves on average in 3´ to 5´ direction (see previous section) along the ssDNA and also passes the nucleotides of the DNA hairpin loop. During rehybridization of the DNA hairpin the translocating enzyme interrupts the closing of the hairpin which is seen as rewinding. As already observed before, the rewinding is not very stable and

mostly turns into a slip back. Also at high forces we observe strand switching which causes a direct switch from rewinding to unwinding (Fig. 5.7b, *iii*).

The last kind of investigated resetting events are the resettings which follow after incomplete DNA hairpin unwinding (Fig. 5.7c). The observed resetting events display the same characteristics as shown in the cases above (Fig. 5.7c, from left to right:

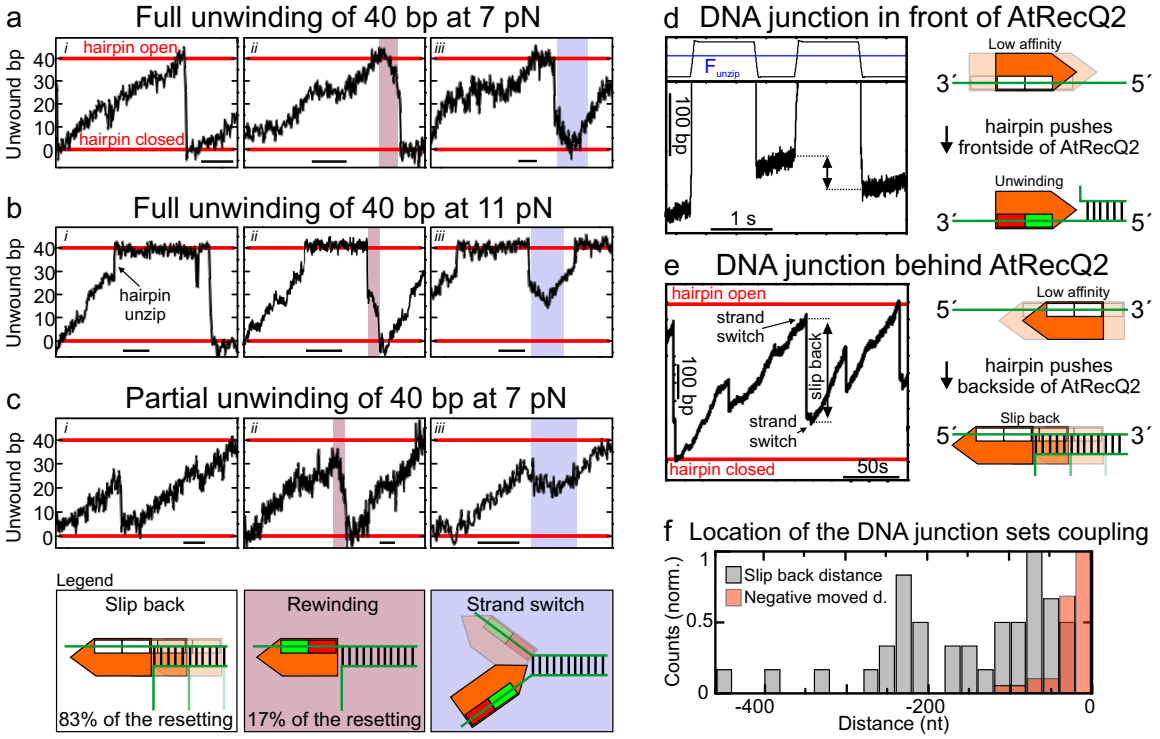

Figure 5.7 Limited rewinding and strand switching ability of AtRecQ2. In (a-c) selected unwinding events on the 40 bp DNA hairpin are shown. Red lines indicate the position of the fully closed and the fully open DNA hairpin. Special features of the resetting events are highlighted and the corresponding behavior of AtRecQ2 is sketched below. The bars indicate 1 s. The labels in the top left corner of each graph correspond to the following type of resetting event. *i*: full slip back of AtRecQ2. *ii*: partial rewinding and slip back. *iii*: direct switch from rewinding to unwinding. (a) Full DNA hairpin unwinding events at 7 pN. (**b**) DNA hairpin unwinding events at 11 pN. At a certain point the hairpin unzips (indicated abrupt jump) and stays unzipped (plateau). After random times the DNA hairpin rehybridizes. (**c**) Incomplete DNA hairpin unwinding at 7 pN. (**d**) Representative trace of the experiment performed in the previous section (compare Figure 5.5a). The switch between high and low force is shown in the top graph, the corresponding trace in the bottom graph. The arrow indicates a negative distance after the DNA hairpin is rezipped (see text). The sketch indicates the suggested affinity of AtRecQ2 to its tracking strand and orientation of the enzyme with respect to the DNA junction. *top*: during the DNA hairpin is unzipped. *bottom*: when the DNA hairpin is rezipped. (**e**) Representative trace of AtRecQ2 unwinding the 500 bp DNA hairpin. The measured intermediate slip back distance is indicated with an arrow. The position of the fully closed and the fully open DNA hairpin are indicated with red lines. (**f**) Normalized histogram of the distances measured in (d) (red) and (e) (gray).

full slip back, partial rewinding and direct switching from rewinding into unwinding). Interestingly, rewinding also occurs without the assistance of the DNA hairpin loop, i.e. the enzyme is not transfered to the formerly displaced strand by moving over the DNA hairpin loop. This means AtRecQ2 is not only able to switch from rewinding to unwinding (Fig. 5.7, all graphs with label *iii*), but also to switch from unwinding to rewinding. This finding shows that AtRecQ2 is able to switch its tracking strand, independent of the actual activity (unwind or rewinding). The question arises if also a full slip back event is induced by strand switching. Since a strand switch for a full slip back cannot be directly seen (because the orientation of the enzyme is not known in this case) an indirect measurement is required as explained in the following.

Instead of a strand switch, a resetting event, which occurs as a full slip back, could be argued to arise from a sudden low affinity of AtRecQ2 to its tracking strand during dsDNA unwinding. In this situation the rehybridizing hairpin would push against the frontside of AtRecQ2, causing it to slip back. This case is ruled out by the following argument. In the previous section an experiment was performed, where the DNA hairpin is unzipped and rezipped during AtRecQ2 unwinding of the DNA hairpin (see Fig. 5.5). Since the enzyme is assumed to be located on its tracking strand during the DNA hairpin is unzipped, the rezipping causes that the rehybridizing DNA hairpin hits the moving the enzyme from the frontside. AtRecQ2 was shown to have either a high or a low affinity to ssDNA as long as the DNA hairpin is unzipped (see previous section). When the rehybridizing DNA hairpin hits AtRecQ2 when it has apparently a low affinity to the ssDNA (Fig. 5.7d, sketch next to the graph, top), it should be pushed along the DNA and slip back. This could be a reason why negative distances are observed when the DNA hairpin is rezipped (Fig. 5.7d, sample of negative distance, indicated by the arrow). However, after DNA hairpin rezipping immediate DNA unwinding is always observed (Fig. 5.7d, sketch next to the graph, bottom). This situation (DNA hairpin pushes against the frontside of AtRecQ2 with low affinity) corresponds to the same situation as argued before, where the enzyme exhibits a sudden low affinity to its tracking strand during dsDNA unwinding (DNA hairpin pushes against the frontside of AtRecQ2 with low affinity). Hence, the average distances AtRecQ2 is pushed back during the experiments of the last section, should be comparble to the distances the enzyme slips back because of a sudden low affinity to the ssDNA during unwinding. Therefore, the slip back distances during AtRecQ2 unwinding of the 500 bp DNA hairpin were measrued (Fig. 5.7e, sample of slip back distance, indicated by the arrow). Only intermediate slip back events were measured, i.e. only when the slip back starts before the full DNA hairpin is unwound and stops before the the full hairpin is reset. This assures that neither the DNA hairpin loop (always inducing a resetting event), nor the stopped rehybridization of the DNA hairpin (mostly inducing new unwinding) could limit the distance of the slip back. The histogram of both distances clearly shows that the slip back during unwinding in average is considerably larger than the negative distances measured after rezipping the DNA hairpin (Fig. 5.7f). This indicates that both events do not have the same origin. In conclusion the argument above, that a full slip back could arise from a sudden low affinity of AtRecQ2 to its tracking strand during dsDNA unwinding, is disproved. Furthermore, this observation supports the idea, that also a full slip

back event is induced by a strand switch. Additionally, it shall be mentioned that mostly immediatelly after a slip back which completely closes the DNA hairpin a new unwinding event starts. This might indicate that the ability of AtRecQ2 to switch the strand when it exhibits a low ssDNA affinity is increased as soon as the DNA hairpin stops rehybridizing, i.e. the dynamics of the rehybridization might influence the strand switch ability. In conclusion AtRecQ2 is able to switch its tracking strand independent if it was unwinding, rewinding or pushed by the rehybridizing DNA hairpin before.

The characteristic properties of the resetting events (composition of DNA hairpin rewinding and slip back) are equivalent to the behavior of AtRecQ2 on ssDNA (composition of high affinity/translocation and low affinity/diffusion). This suggests that AtRecQ2 behaves during a resetting event as if it encounters pure ssDNA.

In summary, we provide evidence that before resetting AtRecQ2 switches from the original tracking to the displaced strand, which than becomes the new tracking strand. After strand switching the DNA junction is located behind the enzyme. In this situation we assume that AtRecQ2 behaves as on ssDNA, i.e. with high affinity to the ssDNA, causing rewinding, and low affinity causing it to slip back. Therefore, the enzyme needs to sense the presence or absence of the DNA junction in front of it in order to explain the observed asymmetric behavior (always high affinity with DNA in front, high and low affinity with the DNA junction behind). To further substantiate this hypothesis investigations on a possible DNA junction sensor were performed.

5.5 AtRecQ2 clamps both single strands at the unwinding junction

Our hypothesis includes the ability of AtRecQ2 to sense the DNA junction (see the dsDNA sensor in Figure 5.4 in section 5.2). This sensing most likely means that AtRecQ2 needs contact to its tracking strand and the displaced strand at the same time. Presuming that a contact to both ssDNA strands clamp the DNA junction, we investigated the difference of the force required to unzip the DNA hairpin in presence and absence of the enzyme.

The average force necessary to unzip the 500 bp DNA hairpin in the reaction buffer (RBRecQ, see appendix 6.2.2) is ≈ 16 pN (see section 3.3.1). Applying this force, the hairpin is unzipped in 88% of the attempts completely, while in 12% of the attempts it is only partially opened. Applying 18 pN unzips the 500 bp DNA hairpin in 100% of the attempts (Fig. 5.8a). At 10.4 pN the 500 bp DNA hairping is always completely closed.

The probability to unzip the 500 bp DNA hairpin changes in the presence of AtRecQ2 (Fig. 5.8b). After the initiation of dsDNA unwinding by AtRecQ2 at 10.4 pN the force was switched to 18 pN. In contrast to the observations in absence of AtRecQ2, the hairpin is now unzipped in only 65% of all attempts. In the other 35% of the attempts the dsDNA handle of the DNA hairpin construct (see Fig. 3.2a, sketch on the right) and the already unwound ssDNA are only slightly more streched due to the elevated force. Additionally, the DNA hairpin gets further unwound demonstrating

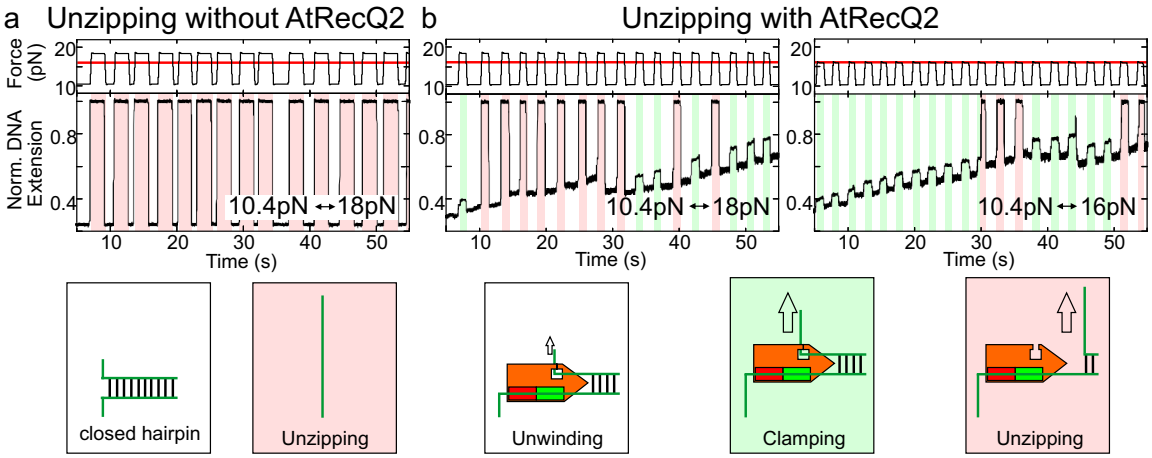

Figure 5.8 AtRecQ2 clamps the DNA junction. (**a**) Repeated unzipping and rezipping of the 500 bp DNA hairpin in absence of AtRecQ2. The force is switched between 10.4 pN, where the hairpin is completely closed and 18 pN where the hairpin is always open (top graph, red line indicates the average unzipping force of the DNA hairpin). The trace is highlighted in red where the force is high. DNA hairpin is sketched below. (**b**) *left*: The same experiment as in (**a**) in presence of AtRecQ2. 65% of the attempts to unzip the DNA hairpin were successful (red), while in 35% of the attempts, the DNA is only slightly more stretched (green). *right*: Force switch between 10.4 pN and 16 pN (which is the average unzipping force of the DNA hairpin determined in section 3.3.1, table 3.1). During the determination of the unzipping force, the probability to fully unzip the 500 bp DNA hairpin was 88% (data not shown). In presence of AtRecQ2 the probability of unzipping decreases to 20%. The enzyme migth have a domain to clamp the DNA junction (sketched as a hole) until a certain energy barrier is overcome (sketches are highlighted with the corresponding color of the traces)

the contact to the helicase. Switching the force between 10.4 pN and 16 pN changes the probability for complete hairpin unzipping to 20%, while the hairpin remains closed in 80% of the cases.

Different unzipping probabilities between presence and absence of AtRecQ2 for otherwise identical conditions must be attributed to AtRecQ2, which is clamping the tracking strand and the displaced strand together. Therefore, the dsDNA sensor, which was hypothesized before is drawn as a hole, where the diplaced strand is threaded through (Fig. 5.4a and Fig. 5.8). This hole represents a domain which is able to clamp the displaced single strand, but also the passage of the increasing displaced strand during unwinding. Additionally, the domain can release the displaced strand when for example the force is increased or the enzyme switches its tracking strand (therefore, the clamp is drawn to be open in Fig. 5.8, most right sketch, when the high force unzips the DNA hairpin).

The clamping effect should also be reflected in the force-dependence of the unwinding velocity, because the clamp could shield the force onto the DNA junction and therewith influence the unwinding assistance of force on the unwinding velocity (as explained in section 1.2.2). Simultaneously we investigated the sequence-dependence of the unwinding velocity by using a DNA hairpin construct with regions of different AT

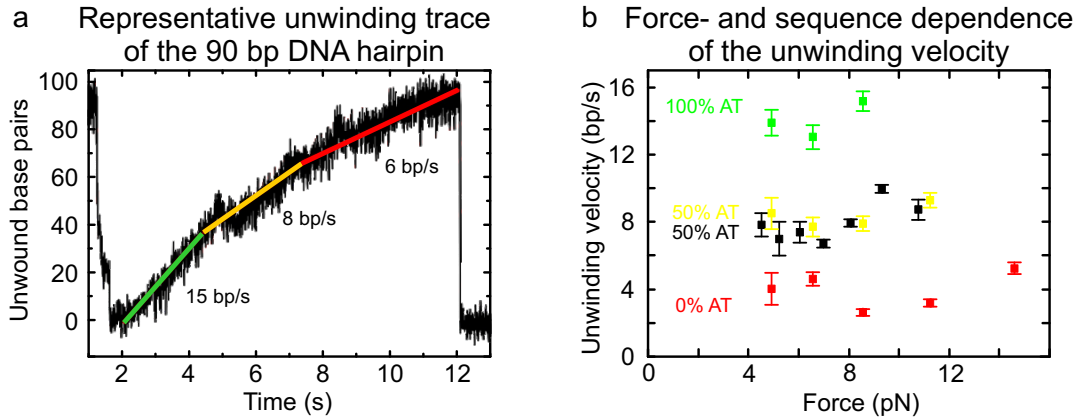

Figure 5.9 Force- and sequence-dependent unwinding velocity of AtRecQ2. (**a**) Representative trace of AtRecQ2 unwinding a DNA hairpin construct with three regions of different AT content (100% AT (green), 50% AT (yellow), 0% AT (red)). Many events clearly show different unwinding velocities for the different regions. To determine the slopes only unwinding events were chosen where the DNA hairpin is completely unwound. The unwinding trace was devided into three 30 bp areas and the data of each area fitted with a linear function. (**b**) Unwinding velocity in dependence of the applied force for each region of different AT content as indicated. The black data points are measurements of the 40 bp DNA hairpin (used in previous experiments with AtRecQ2, e.g. in Fig. 5.3) which also has 50% AT content. Error bars indicate the standard error of the mean.

base pair content (see Figure 3.3b in section 3.1.3). This DNA hairpin contains three regions: 30 base pairs with all being AT, 30 base pairs with an AT content of 50% and 30 base pairs with all being GC. These regions can be clearly distinguished during slow mechanical unzipping (see Figure 3.7d in section 3.3.2). Most importantly the three regions are also detected in individual unwinding events, i.e. the unwinding velocity in the 100% AT region is faster than in the 0% AT region (Fig. 5.9a). In addition to the sequence we also varied the forces in the measurements with this DNA hairpin construct between 4 pN to $9 - 16$ pN, depending on the DNA region (Fig. 5.9b). At forces above 8.6 pN the 100% AT region (green) is unzipped, at forces above 12.1 pN the 50% AT region (black) is unzipped and at forces above 16 pN the 0% AT region (red) is unzipped. At the lower end of the forces (below 4 pN) the determination of the unwinding velocity is limited by the low signal to noise ratio. Additionally it was observed that at low forces the DNA hairpin is less completely unwound, which will be discussed in more detail in the following section. The unwinding velocity does not strongly depend on the applied force, supporting the existence of a clamping domain of AtRecQ2 (Fig. 5.9b). In this respect the strong sequence dependence of the unwinding velocity is remarkable. While the 100% AT region is unwound with ≈ 14 bp/s, the 0% AT region slows the helicase down to ≈ 3 bp/s. This means the helicase is sensitive to the base pairing energy. Since the actual base pair opening mechanism stays rather unaffected by the applied force, AtRecQ2 might be classified as an active helicase. The force- and sequence-dependence as well as the clamping during rewinding can unfortunately not be investigated due to the very short appearance of rewinding

occurances.

However, the clamping of dsDNA by AtRecQ2 can be interpreted as sensing of the enzyme for the presence of the DNA junction. When the displaced strand is threaded into the clamp, AtRecQ2 is in its unwinding mode with a high affinity to its tracking strand. When no strand is present in the clamp, the enzyme is either in diffusion (high affinity) or in translocation mode (low affinity). This is particularly the case when only ssDNA is available or the DNA junction is located oppositely of AtRecQ2´s translocation direction. The findings of the last three section are summarized in the following section to establish a model for repetitive unwinding of AtRecQ2.

5.6 Model for repetitive unwinding of AtRecQ2

Based on the observations of the repetitive DNA hairpin unwinding by AtRecQ2 (Fig. 5.3) and exclusion of several known mechanisms, a working model for dsDNA unwinding of AtRecQ2 was developed (Fig. 5.4). To verify the working model, the investigation of three hypothesized features of AtRecQ2 was required. First, a high and low affinity of AtRecQ2 to the ssDNA was derived from mixture of translocation and diffusion on ssDNA (section 5.3). Second, the ability of AtRecQ2 to switch from its tracking strand to the displaced strand was found by detailded analysis of the resetting events (section 5.4). Third, a DNA junction sensing ability was inferred from the activity of AtRecQ2 to clamp the tracking strand and the displaced strand together (section 5.5). These results will now be combined to a model for repetitive DNA unwinding by AtRecQ2. Two additional features need to be assumed. The first assumption is that AtRecQ2 is not able to tranlocate along 5´ to 3´ direction. This is reasonable, because in bulk experiments DNA unwinding by AtRecQ2 was only detected for dsDNA containing 3´ but not 5´ overhangs [151]. Furthermore, the cocrystalized structure of the homologous HsRECQ1 with DNA with a 3´ overhang was also found in contact with the 3´ overhang such that the translocation is most likely only possible in 3´ to 5´ direction (Pike *et al.*, to be published). Finally all ATP-dependent translocation processes of helicases are unidirectional [26]. A second assumption is that AtRecQ2 is active as a monomer. This is supported by experiments for the homologous HsBLM, that was found to unwind dsDNA with 3´ overhangs as a monomer even under conditions that highly support multimerization [17].

These results lead to a model for repetitive DNA hairping unwinding by AtRecQ2 sketched in Fig. 5.10. *A*: The cycle starts with an AtRecQ2 enzyme bound with the helicase domain to its tracking strand. The affinity of AtRecQ2 to its tracking strand is controlled by the domain of the enzyme which clamps the displaced strand (the drawn hole in the enzyme). The displaced strand is threaded through the hole, i.e. the affinity is high (colored helicase domain). The polarity of the enzyme provides that the catalytic side always points to the 5´ end of the tracking strand (green RecA-like domain of the helicase domain always points to the 5´ direction). Upon ATP hydrolysis AtRecQ2 will unwind the dsDNA (*A*-*B*). The unwinding is finished as soon as the enzyme is transferred from its tracking strand to the displaced strand. The pathway after unwinding depends on the mechanism how this transfer is accomplished.

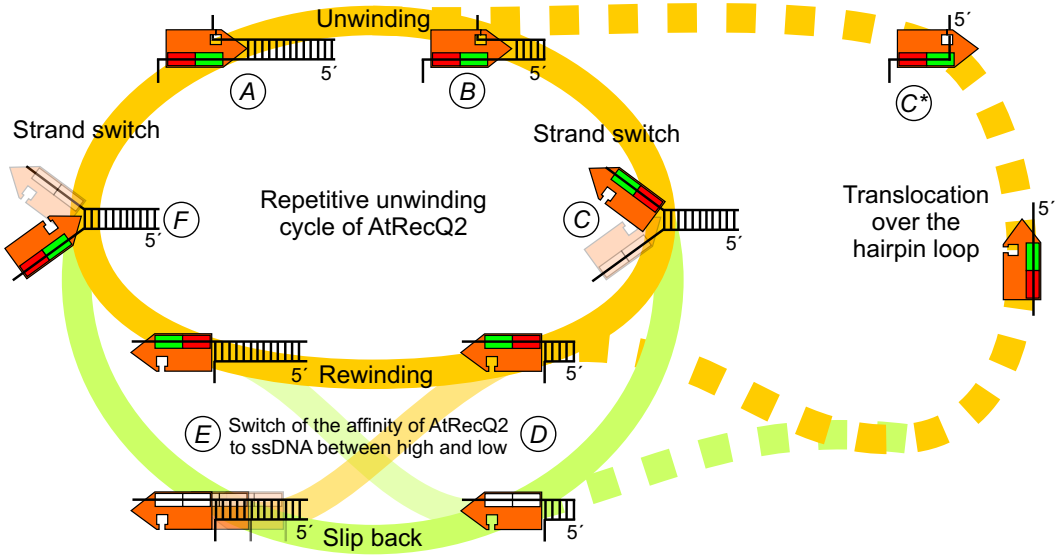

Figure 5.10 Model for repetitive unwinding cycle of AtRecQ2. The enzyme (orange) is sketched with three important features (as already introduced in Figure 5.4a). The tip represents the RecQ-Ct, where the base pair opening is catalyzed. The red and green rectangles represent the two RecA-like domains of the helicase domain, where enzyme translocates the ssDNA and the green one always points towards the 5´ end of the ssDNA to maintain the 3´ to 5´ strand polarity. When these two domains are drawn colored a high affinity to the ssDNA is symbolized. Uncolored domains symbolize low affinity to the ssDNA. During unwinding the DNA junction is clamped, symbolized by the displaced strand threaded through the squared hole. The yellow pathway represents a high affinity between enzyme and tracking strand, the green pathway represents low affinity. On the solid pathways AtRecQ2 switches its tracking strand to turn its translocation direction around. On the dashed pathway AtRecQ2 changes its tracking strand by moving over the DNA hairpin loop. The crossings in the lower part of the picture symbolize the ability of AtRecQ2 to switch its affinity to the ssDNA it is tracking along. The cycle is explained detailed in the text.

C: The solid yellow pathway is taken if AtRecQ2 performs a strand switch. The trigger for such a strand switch is not known and will be discussed at the end of this chapter. *C**: The yellow dashed pathway is taken if AtRecQ2 reaches the end of the DNA hairpin and moves over the DNA hairpin loop (the pathway is drawn dashed, because this is a more artificial pathway, caused by the used DNA hairpin templates, which most likely occurs much less *in vivo*). For both pathways the clamping domain looses the contact to the displaced ssDNA during the transfer, i.e. the DNA junction is not sensed. *D*: When the enzyme is located on the formerly displaced strand (which is now the new tracking strand), the strand polarity assures again that catalytic side of the enzyme points towards the 5´ direction of the new tracking strand. This means AtRecQ2 is turned around compared to its orientation before the transfer. In this configuration the data suggests that AtRecQ2 behaves as if it was located on ssDNA only. This might be caused by the location of the DNA junction oppositely to the translocation direction of the enzyme (behind the enzyme).

As shown, on ssDNA AtRecQ2 exhibit a high and low affinity to its tracking strand. Along the yellow pathway, the affinity is high, along the green pathway the affinity is low (colored and uncolored helicase domain, respectively). *D-E*: The data showed that the resetting events are composed of rewinding and slip back (yellow and green pathway, respectively). Mostly the rewinding has a short duration and turns into a slip back (path leading from the yellow to the green pathway). Additionally it was observed that a slip back event can be interrupted by a rewinding event (path leading from the green to the yellow pathway). In principle, the switching of the affinity of AtRecQ2 to its tracking strand during resetting is not restricted to appear just once (as inferred from the sketch), but might occur several times. However, due to fast resetting process, multiple affinity switches were rarely observed. The trigger to switch between a high and a low affinity to the tracking strand during a resetting event (when the DNA junction is not detected by the sensor) is not known. Apparent secondary structures of the free ssDNA might temporarily be detected by the sensor, which causes a transient high affinity. *F*: The resetting (either rewinding or slip back) is finished as soon as the enzyme is transferred from its tracking strand to the displaced strand. This is achieved by strand switching. It can occur intermediately, i.e. when the DNA hairpin is not completely close again or at the end, i.e. when the DNA hairpin is completely rehybridized. As soon as the DNA junction is sensed again by the clamping domain, the helicase domain switches to high ssDNA affinity and the next unwinding cycle starts.

The repeated strand switching could be a reason for the observed limited processivity in bulk experiments, i.e. although the enzyme is very processive, it fullfils complete unwinding only for short dsDNA pieces. The processivity of AtRecQ2 could be regulated by strand switching, but the question remains what regulates the strand switching. To investigate a possible regulation of the strand switching the processivity was measrued in dependence of the applied force. The results are presented in the following section.

5.7 The processivity of AtRecQ2 is limited by strand switching

In the following the processivity of AtRecQ2 is investigated. By processivity, the length of subsequently unwound base pairs without rewinding or slip back, is meant. As mentioned in the last section, the processivity might be regulated by the occurance of strand switching, which itself might also be triggered somehow. For HsBLM it was proposed that the enzyme has an intrinsic counter, such that it switches the strand after a certain distance or a certain number of base pairs unwound [167]. In contrast, DNA unwinding experiments with RecQ with magnetic tweezers showed that the processivity is limited to a certain time or unwound distance before a strand switch occurs (see for example Fig. 5.7e, where the slip back events on the 500 bp DNA hairpin occur at random distances and random times). One imaginable trigger for the strand switch could be the applied force, which will be discussed in the following.

We showed that the unwinding velocity barely depends on the applied force, explained with a mechanical shielding of the DNA junction by an intrinsic clamp (Fig.

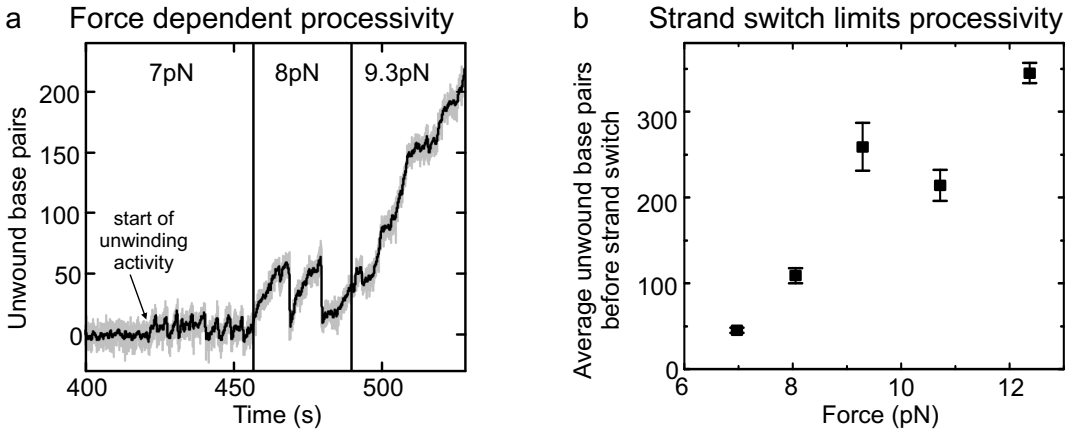

Figure 5.11 The processivity of AtRecQ2 is limited by the force-dependent strand switch. (**a**) AtRecQ2 unwinds parts of the 500 bp DNA hairpin. The processivity (the length of the subsequently unwound base pairs without strand switching) is highly force sensitive. (**b**) The average number of unwound base pairs before a strand switch occurs as a function of the applied force. The processivity increases approximately linearly, the error bars indicate the standard error of the mean.

5.9b). This causes the force-independence of the base pair opening mechanism of AtRecQ2. However, for strand switching this clamp needs to be opened to turn the enzyme around (within the suggested model of the previous section, Fig. 5.10). This means the clamping domain looses the contact to the displace strand and the mechanical shielding of the DNA junction is lost. Hence, the strand switching mechanism could be force dependent. To characterize the effect of force on the strand switching, the effect of force on the above defined processivity is investigated. Since we hypothesized that every directional change of the enzyme is caused by a strand switch, the processivity is simply the number of successively unwound base pairs before a resetting event occurs.

Figure 5.11a shows a representative trace of AtRecQ2 unwinding the 500 bp DNA hairpin. Obviously the processivity of AtRecQ2 is highly force sensitive. An increase in force of 2 pN results in a significantly larger number of unwound base pairs (Fig. 5.11b). In several experiments AtRecQ2 was shown to unwind hundreds of base pairs (e.g. Fig. 5.5c). This is in strong contrast to bulk strand displacement experiments, were only a few tens of base pairs are separated [151]. This was interpreted as limited processivity of AtRecQ2. Considering our results we suggest that at high forces the processivity is not increased, but the strand switch is suppressed. The molecular basis for the strand switching mechanism will be a subject for future investigations, but it could be imagined that a certain domain of the enzyme needs to reach for the second DNA strand to initiate strand switching. Higher forces might suppress this mechanism by lowering the probability for the enzyme to reach for the second strand.

The question remains which domains are responsible for the DNA sensor/clamping mechanism as well as the strand switch function. To narrow down the participation of individual domains of AtRecQ2, similar experiment on AtRecQ3 shall be performed. AtRecQ3 is another homologue RecQ helicase from Arabidopsis thaliana (see Fig.

5.1a). AtRecQ3 is missing some of the conserved domains, so that differences in the dsDNA unwinding properties may be related to those domains.

5.8 Repetitive unwinding by a single AtRecQ3 enzyme

A molecular difference for AtRecQ3 compared to AtRecQ2 is the absence of the conserved winged helix and the HRDC domain (see Fig. 5.1a) [153]. The winged helix is for example also missing in HsRECQ4, the HRDC domain is also missing in HsRECQ1. Both domains appears to be not essential for the general DNA unwinding mechanism of some RecQs, but might be involved in more elborate functions like strand switching or substrate specificity like Holliday junctions.

AtRecQ3 has also a 3´ to 5´ strand polarity. Compared to AtRecQ2 it requires 12 base pairs of a 3´ ssDNA overhang to unwind dsDNA fragments [161] and it hydrolyzes only ATP and dATP (compared to AtRecQ2 which can hydrolyze all available triphosphates) [161]. Furthermore, AtRecQ3 is able to processively anneal complemetary oligomers to dsDNA, a property that AtRecQ2 does not exhibit.

Differences in the unwinding properties between the two homologoue helicases were investigated. At first the ability of AtRecQ3 to unwind a 500 bp DNA hairpin was tested. AtRecQ3 displays a very different unwinding compared to AtRecQ2 under otherwise same conditions (Fig. 5.12a). An unwinding event is always followed by a full rewinding event. No fast rehybridization (like the slip back events of AtRecQ2) was observed. As previously discussed for T-Antigen and AtRecQ2, a rewinding event within the applied magnetic tweezers assay using DNA hairpin constructs can be initiated by a transfer of the enzyme over the DNA hairpin loop, a reverse translocation (in 5´ to 3´ direction) or a strand switch. Since AtRecQ3 was shown to be unable to unwind in 5´ to 3´ direction [161] and is also far away from the DNA hairpin loop when rewinding starts (only tens of base pairs of the 500 bp DNA hairpin are unwound, see Figure 5.12a), the data suggests that AtRecQ3 frequently performs strand switches.

The unwinding and rewinding events are separated by pauses, unlike shown for AtRecQ2 (Fig. 5.12a). These pauses showed random durations with a mean of three seconds (histogram in Fig. 5.12b). Thus the single events could be performed by different individual enzymes. In contrast, on a larger time scale, the activity of AtRecQ3 occurs in bursts of events indicating that a single enzyme or enzyme-complex is responsible for successive unwinding and rewinding events. These bursts of events were also observed with a 20-fold lower enzyme concentration (data not shown), with similar delay times between the single unwinding and rewinding events. Thus, multiple strand switches of AtRecQ3 are required to fulfill the repetitive unwinding.

The rewinding velocity does not differ significantly from the unwinding velocity (Fig. 5.12c). The unwinding velocity is faster than for AtRecQ2 and very surprisingly decreases with applied force onto the DNA hairpin junction. This is in contrast to any other investigated helicase to our knowledge so far. One might speculate, that the applied force distorts the enzyme such that its catalytic function is hindered. Another possibility could be that AtRecQ3 is slower in ssDNA translocation than in unwinding

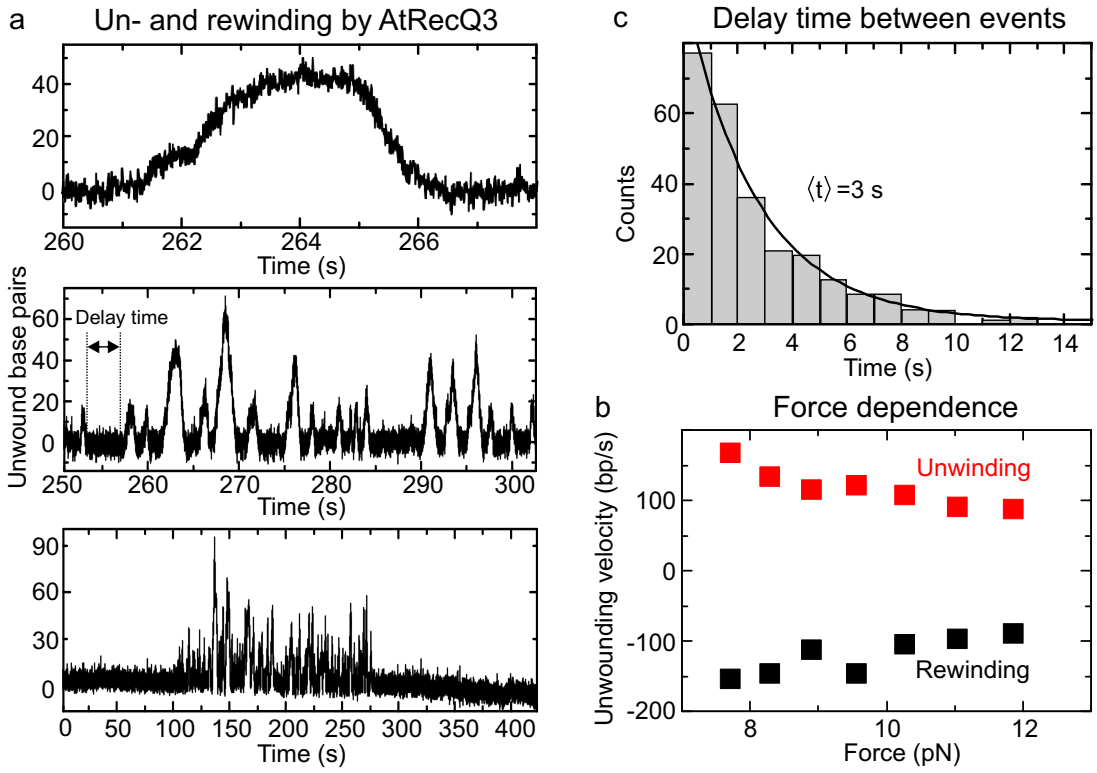

Figure 5.12 Unwinding and rewinding of a single AtRecQ3 helicase. (**a**) Single traces of activity of AtRecQ3 at the 500 bp DNA hairpin in reaction buffer RBRecQ (see appendix 6.2.2) at 10 pN. *top*: Single unwinding and rewinding event. The rewinding occurs long before the whole DNA hairpin is unwound. *middle*: Several unwinding and rewinding events are separated by pauses of different duration. *bottom*: Activity occurs in a confined time interval, indicating single molecule activity. The DNA extension in nanometers was converted to unwound base pairs using the FJC model (equation 3.2 in section 3.3.2). (**b**) Time between the single unwinding and rewinding events. The mean delay time (for the conditions as in (a) is indicated. (**c**) Mean unwinding- (red) and rewinding velocities (black). Supringly, the velocity decreases with increasing applied forces (see text). Standard error of the mean is within the size of the symbols.

or rewinding dsDNA. Higher assisting forces might increase the ssDNA area in front of the enzyme and thus slow down the unwinding or rewinding.

Similarly to AtRecQ2, we also performed experiments where the DNA hairpin is mechanically unzipped during the enzyme unwinds it, to gain more insight into the behavior of AtRecQ3 on ssDNA (detailed explanation of this experiment was shown in Figure 4.11 in section 4.4). In contrast to AtRecQ2, which was always directly unwinding after the DNA hairpin was rezipped (see for example Fig. 5.5a in section 5.3), AtRecQ3 starts immediate rewinding of the DNA hairpin after the DNA hairpin is rezipped (Fig. 5.13a, *top*). How the enzyme gets to the position where it is probed when the DNA hairpin is rezipped is not clear. Either an enzyme binds to the ssDNA during the DNA hairpin is unzipped or the currently active enzyme (unwinding and rewinding events indicate that an enzyme is active on the DNA hairpin) moves very

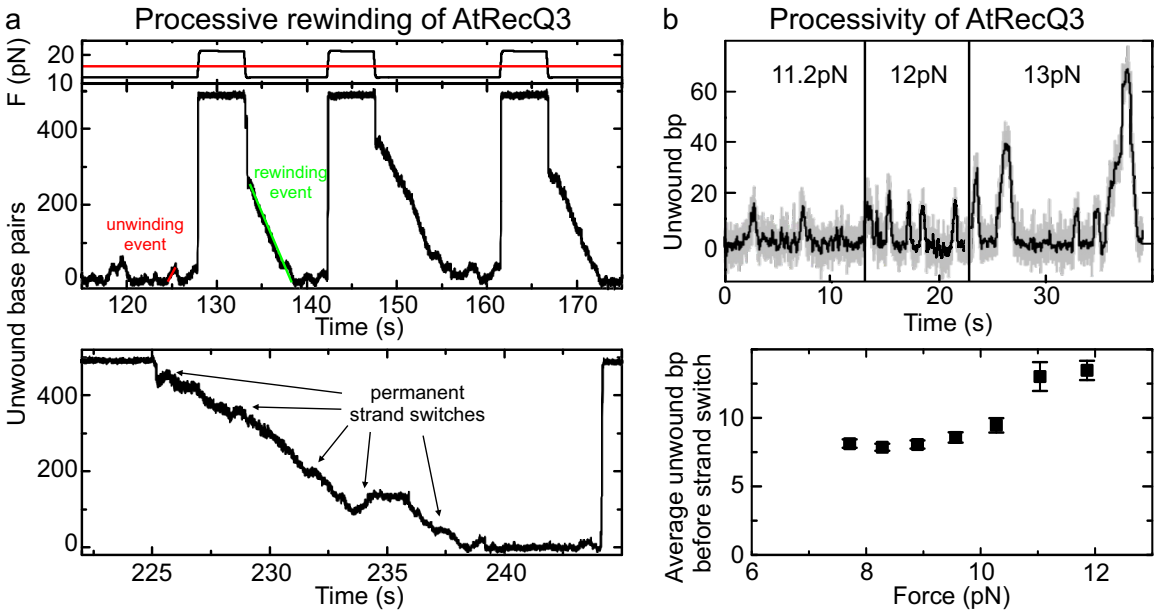

Figure 5.13 AtRecQ3 processively rewinds dsDNA. (**a**) Unzipping and rezipping the 500 bp DNA hairpin during activity of AtRecQ3 (force switch is shown above). *top*: In contrast to the very short unwinding distance, the DNA hairpin is processively rewound over hundreds of base pairs. *bottom*: Zoom of a rewinding event reveals permanent changes from unwinding to rewinding, most likely induced by strand switches. (**b**) Processivity of AtRecQ3 is force sensitive. *top*: AtRecQ3 unwinds only a few base pairs of the 500 bp DNA hairpin. The processivity (the length of the subsequently unwound base pairs without strand switching) can be increased by force. *bottom*: The average number of unwound base pairs before a strand switch occurs as a function of the applied force. The error bars indicate the standard error of the mean.

quickly along the ssDNA during the DNA hairpin is unzipped to the probed position (the latter suggestion is in contrast to the speculation before, that AtRecQ3 might translocate slower than it is unwinding or rewinding). The rewinding of the DNA hairpin by AtRecQ3 is much more processive than then the unwinding. Such activity has not been shown in single molecule experiments before. A zoom into a rewinding event shows that rewinding can also turn into unwinding (Fig. 5.13a, *bottom*). The unwinding is than again not very processive and turns back into rewinding after a few tens of base pairs. This is another support of the hypothesis of the permanent strand switching activity of AtRecQ3.

Furthermore, the processivity of unwinding (defined as the number of successively unwound base pairs before a strand switch occurs) was investigated in dependence of the applied force. As found for AtRecQ2, the number of unwound base pairs before a strand switch occurs, increases with the applied force (Fig. 5.13b, *top*). The strand switch of AtRecQ3 is less force dependent (processivity increases approximately two times between 8 and 12 pN, Fig. 5.13b, *bottom*) than the strand switch of AtRecQ2 (increases approximately four times between 8 and 12 pN, Fig. 5.11b).

The efficient rewinding activity and the observation that no slip back events occur,

may show that AtRecQ3, unlike AtRecQ2, cannot modulate its affinity to its tracking strand. The similar velocities of unwinding and rewinding suggest in this respect, that the location of the DNA junction is not important for the translocation of AtRecQ3 on ssDNA. On the other hand the strand switch is sensitive to the location of DNA junction, because the rewinding activity is highly preferred over unwinding activity. This might be also the origin of the delay times between single unwinding and rewinding events, because it shows that it takes longer for AtRecQ3 to switch the strand when the DNA junction is located oppositely to its translocation direction (i.e. the strand switch from rewinding to unwinding). Compared to the suggested model for AtRecQ2 this means that AtRecQ3 has no dsDNA sensor (see Fig. 5.10 for the function of the sensor of AtRecQ2). No sensitivity to the location of the DNA junction indicates that at least a part of the dsDNA sensor (the clamping domain) of AtRecQ2 is encoded by the HRDC domain or the winged helix domain which is missing in AtRecQ3. The HRDC domain of HsBLM was shown to preferentially bind to ssDNA and might therefore be a good candidate for the clamping-domain which holds the displaced ssDNA strand [168].

5.9 Summary, conclusion, discussion

In the previous sections it was shown that AtRecQ2 and AtRecQ3 repetitively unwind dsDNA. This is most likely achieved by a permantent strand switching mechanism. The characteristic behavior of AtRecQ2 with a slow unwinding followed by a fast resetting was also observed for the RNA helicase NS3 of the Hepatitis C virus [31]. The RNA template for the experiments on NS3 did not contain a DNA hairpin loop (see Fig. 5.14a), i.e. a transfer of the enzyme to the other strand cannot be induced by translocation over the DNA hairpin loop as shown for example for T-Antigen in this thesis. Myong *et al.* suggested a model for NS3 unwinding including a fixed contact between helicase and 5´ end of the displaced ssRNA to create an ssRNA loop during unwinding (Fig. 5.14a). This loop serves as an intrinsic anchor when the helicase releases the DNA after unwinding, i.e. the enzyme can be quickly repositioned to the beginning of the DNA hairpin after unwinding. In section 5.2, Figure 5.3c, this mechanism was ruled out for AtRecQ2, because of the observed maximum DNA extension before a resetting event. This extension corresponds to the full DNA hairpin, which would not be expected if part of the DNA hairpin would be fixed in a DNA loop to the enzyme.

Repetitive unwinding was also shown for HsBLM, also with a DNA template which does not contain a DNA hairpin loop (i.e. no transfer from one strand to the other by translocation over the DNA hairpin loop is possible). In the case of HsBLM unwinding and slow rewinding (not fast resetting) was observed as shown herein for AtRecQ3 [167]. To explain those results a strand switching mechanism was suggested (sketched in Fig. 5.14b). It was suggested that HsBLM intrinsically counts the number of unwound base pairs before strand switching. The strand switching mechanism of HsBLM is suggested to work independent of the DNA junction position.

NS3 and HsBLM were studied using FRET assays, i.e. without the application of

external forces (see section 1.3). The studies on AtRecQ2 and AtRecQ3 presented in this thesis are all done under external applied forces. We found repetitive unwinding for AtRecQ2 and AtRecQ3 to our knowledge for the first time under external tension. Two important differences between FRET and magnetic tweezers experiments shall be mentioned. First, the application of force on the ssDNA excludes the possibility of ssDNA loop formation (as for example suggested for NS3). Secondly, for FRET experiments the enzyme and the DNA need to be labeled with a fluorophore, which

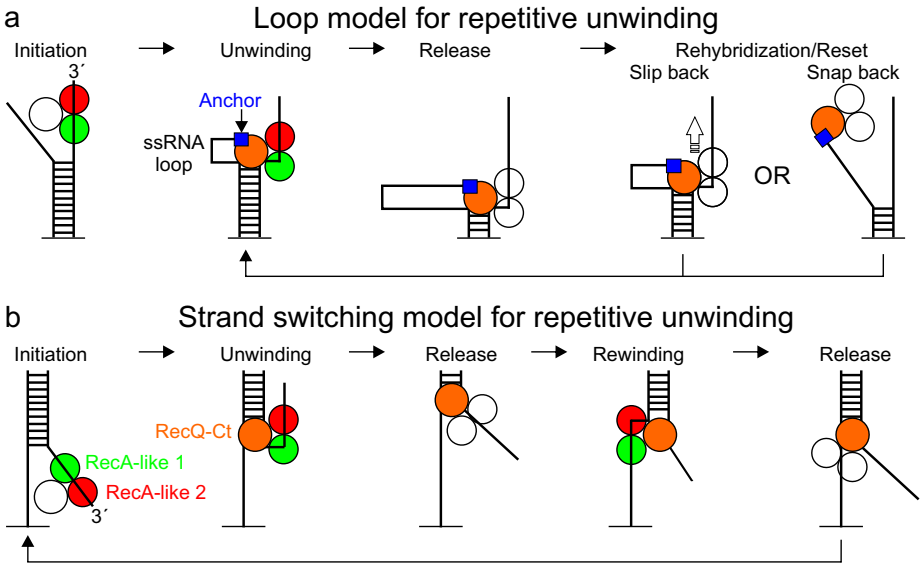

Figure 5.14 Models for repetitive DNA unwinding. (**a**) Model for repetitive RNA unwinding followed by a fast resetting by the helicase NS3 from Hepatits C virus (sketch is adapted from reference [31]). The circles correspond to different domains than introduced for RecQ helicases, because NS3 does not belong to this family of helicases. However, the sketched domains shall fulfill the same role in this model (translocation by the red and green circles, dsDNA opening by the orange circle) [92]. When the domains are colored they are in contact with the DNA. When they are uncolored, they are not attached to the DNA. The experiment is a FRET assay (see section 1.3), i.e. no external forces are applied. From left to right: The ssRNA of the displaced strand is fixed to the enzyme during unwinding. After full unwinding, the enzyme either slips back along its tracking strand or dissociates and snaps back. The anchor allows immediate repositioning of the enzyme to start another unwinding cycle. (**b**) Model for repetitive DNA unwinding (sketch adapted from reference [167]). The red an green filled circles represent the RecA-like domains of the helicase domain (green is always pointing into the translocation direction which is 5´ for HsBLM). The third circle represents the RecQ-Ct domain which opens the base pairs at the DNA junction. When the domains are colored they are in contact to the DNA. When they are uncolored, they are not attached to the DNA. The experiment is a FRET assay (see section 1.3), i.e. no external forces are applied. From left to right: After initial binding to the 3´ overhang and translocation (3´ to 5´), HsBLM unwinds the dsDNA. After a certain distance the helicase domain is released and switches the tracking strand. After rebinding translocation in 3´ to 5´ direction will lead to rewinding. Rewinding is terminated by another strand switch that finally leads to repetitive unwinding.

can influence the activity of the enzyme as well as the dynamics of the DNA hairpin [169].

We have shown that AtRecQ2 and AtRecQ3 both exhibit a limited unwinding distance before a stand switch occurs. The limited number of base pairs found to be unwound in bulk experiments might be observed because of the permanent strand switching of the enzymes. In this respect the definition of processivity of enzymes with repetitive unwinding behavior must be reconsidered. The regulation of the strand switch was found to be force dependent. *In vivo* this could be performed by enzymes and proteins that themselves exert forces onto the DNA junction. Indeed for many helicases it was shown that the limit of the unwound DNA length is increase in presence of single stranded binding proteins [151].

AtRecQ2 and AtRecQ3 perform the same kind of enzymatic activity. They both unwind DNA repetitively. However, the emphasis of AtRecQ2 is much higher on dsDNA unwinding than on rewinding. In contrast, AtRecQ3 has a much higher emphasis on the rewinding process than on unwinding. In this respect it shall be mentioned again, that AtRecQ3 was found to have a strong annealing activity in bulk experiments, while no such activity is observed for AtRecQ2. Although the DNA would rehybridize also in absence of AtRecQ3, the enzyme might be present to strip off single stranded binding proteins or resolves secondary structures in the ssDNA which could lead to mismatches during rehybridization. This antagonistic behavior between AtRecQ2 and AtRecQ3 might reflect either very different tasks of the two RecQ enzymes *in vivo* or both enzymes balance DNA unwinding processes.

We suggest that AtRecQ2 repeatedly switches strands that causes unwinding and resetting also under cellular conditions. Additionally, the sensing for DNA junctions of AtRecQ2 could be interpreted as a search for new DNA target structures, which than gets repeatedly unwound: On ssDNA the enzyme searches by translocation and diffusion for dsDNA. As soon as a DNA junction is detected AtRecQ2 starts unwinding. This mechanism could be effective to keep short DNA structures open. During repair processes, this mechanisms of AtRecQ2 could provide access to other proteins of the DNA repair pathway. Concerning the huge variety of DNA structures that AtRecQ2 can unwind, these properties might be also important for more complex tasks like dissolution of Holliday junctions.

6 Appendix

6.1 Sequences of the DNA hairpin constructs

6.1.1 Hairpin sequence of P2000

GAATTCGGTGACCCTTACGCGAATCCGCTTTCAGACGTTGACTGGTCGCGTCTGGCAAAAGTTAAAGA
CCTGACGCCCGGCGAACTGACCGCTGAGTCCTATGACGACAGCTATCTCGATGATGAAGATGCAGACT
GGACTGCGACCGGGCAGGGGCAGAAATCTGCCGGAGATACCAGCTTCACGCTGGCGTGGATGCCCGGA
GAGCAGGGGCAGCAGGCGCTGCTGGCGTGGTTTAATGAAGGCGATACCCGTGCCTATAAAATCCGCTT
CCCGAACGGCACGGTCGATGTGTTCCGTGGCTGGGTCAGCAGTATCGGTAAGGCGGTGACGGCGAAGG
AAGTGATCACCCGCACGGTGAAAGTCACCAATGTGGGACGTCCGTCGATGGCAGAAGATCGCAGCACG
GTAACAGCGGCAACCGGCATGACCGTGACGCCTGCCAGCACCTCGGTGGTGAAAGGGCAGAGCACCAC
GCTGACCGTGGCCTTCCAGCCGGAGGGCGTAACCGACAAGAGCTTTCGTGCGGTGTCTGCGGATAAAA
CAAAAGCCACCGTGTCGGTCAGTGGTATGACCATCACCGTGAACGGCGTTGCTGCAGGCAAGGTCAAC
ATTCCGGTTGTATCCGGTAATGGTGAGTTTGCTGCGGTTGCAGAAATTACCGTCACCGCCAGTTAATC
CGGAGAGTCAGCGATGTTCCTGAAAACCGAATCATTTGAACATAACGGTGTGACCGTCACGCTTTCTG
AACTGTCAGCCCTGCAGCGCATTGAGCATCTCGCCCTGATGAAACGGCAGGCAGAACAGGCGGAGTCA
GACAGCAACCGGAAGTTTACTGTGGAAGACGCCATCAGAACCGGCGCGTTTCTGGTGGCGATGTCCCT
GTGGCATAACCATCCGCAGAAGACGCAGATGCCGTCCATGAATGAAGCCGTTAAACAGATTGAGCAGG
AAGTGCTTACCACCTGGCCCACGGAGGCAATTTCTCATGCTGAAAACGTGGTGTACCGGCTGTCTGGT
ATGTATGAGTTTGTGGTGAATAATGCCCCTGAACAGACAGAGGACGCCGGGCCCGCAGAGCCTGTTTC
TGCGGGAAAGTGTTCGACGGTGAGCTGAGTTTTGCCCTGAAACTGGCGCGTGAGATGGGGCGACCCGA
CTGGCGTGCCATGCTTGCCGGGATGTCATCCACGGAGTATGCCGACTGGCACCGCTTTTACAGTACCC
ATTATTTTCATGATGTTCTGCTGGATATGCACTTTTCCGGGCTGACGTACACCGTGCTCAGCCTGTTT
TTCAGCGATCCGGATATGCATCCGCTGGATTTCAGTCTGCTGAACCGGCGCGAGGCTGACGAAGAGCC
TGAAGATGATGTGCTGATGCAGAAAGCGGCAGGGCTTGCCGGAGGTGTCCGCTTTGGCCCGGACGGGA
ATGAAGTTATCCCCGCTTCCCCGGATGTGGCGGACATGACGGAGGATGACGTAATGCTGATGACAGTA
TCAGAAGGGATCGCAGGAGGAGTCCGGTATGGCTGAACCGGTAGGCGATCTGGTCGTTGATTTGAGTC
TGGATGCGGCCAGATTTGACGAGCAGATGGCCAGAGTCAGGCGTCATTTTTCTGGTACGGAAAGTGAT
GCGAAAAAAACAGCGGCAGTCGTTGAACAGTCGCTGAGCCGACAGGCGCTGGCTGCACAGAAAGCGGG
GATTTCCGTCGGGCAGTATAAAGCCGCCATGCGTATGCTGCCTGCACAGTTCACCGACGTGGCCACGC
AGCTTGCAGGCGGGCAAAGTCCGTGGCTGATCCTGCTGCAACAGGGGGGGCAGGTGAAGGACTCCTTC
GGCGGGATGATCCCCATGTTCAGGGGGCTTGCCGGTGCGATCACCCTGCCGATGGTGGGGGCCACCTC
GCTGGCGGTGGCGACCGGTGCGCTGGCGTATGCCTGGTATCAGGGCAACTCAACCCTGTCCGATTTCA
ACAAAACGCTGGTCCTTTCCGGCAATCAGGCGGGACTGACGGCAGATCGTATGCTGGTCCTGTCCAGA
GCCGGGCAGGCGGCAGGGCTGACGTTTAACCAGACCAGCGAGTCACTCAGCGCACTGGTTAAGGCGGG
GGTAAGCGGTGAGGCTCAGATTGCGTCCATCAGCCAGAGTGTGGCGCGTTTCTCCTCTGCATCCGGCG
TGGAGGTGGACAAGGTCGCTGAAGCAG

6.1.2 Hairpin sequence of P500

GAATTCGGTGACCCTTACGCGAATCCGCTTTCAGACGTTGACTGGTCGCGTCTGGCAAAAGTTAAAGA
CCTGACGCCCGGCGAACTGACCGCTGAGTCCTATGACGACAGCTATCTCGATGATGAAGATGCAGACT
GGACTGCGACCGGGCAGGGGCAGAAATCTGCCGGAGATACCAGCTTCACGCTGGCGTGGATGCCCGGA
GAGCAGGGGCAGCAGGCGCTGCTGGCGTGGTTTAATGAAGGCGATACCCGTGCCTATAAAATCCGCTT
CCCGAACGGCACGGTCGATGTGTTCCGTGGCTGGGTCAGCAGTATCGGTAAGGCGGTGACGGCGAAGG
AAGTGATCACCCGCACGGTGAAAGTCACCAATGTGGGACGTCCGTCGATGGCAGAAGATCGCAGCACG
GTAACAGCGGCAACCGGCATGACCGTGACGCCTGCCAGCACCTCGGTGGTGAAAGGGCAGAGCACCAC
GCTGACCGTAGG

6.1.3 Oligos and hairpin of P40

To stabilize the closed state, the hairpin is designed to contain three GC base pairs at the beginning acting as a clamp (underlined italic letters). Four T bases in the hairpin loop stabilize the open state (italic letters). Bio* is a biotin labeled base, Pho* is a phosporylated base, R6G* is a rhodamine 6G labeled base.

Oligo 1:

Bio*TTTTT*GGG*AGCACTACGTTCGGACTAGTGTACTCTGACTTGAGAC*TTTT*GTCTCAAGTC

Oligo 2:

Pho*AGAGTACACTAGTCCGAACGTAGTGCT*CCC*TTTTTTTTTTTTTTTTTTTTTTTTTTTTTTTTTT
TTTTTTTTTTATGCATGCCC

Test oligo with BstI site for improved ss-ds ligation:
Oligo 2*:

Pho*AGAGTACACTAGTCCGAACGTAGTGCT*CCC*TTTTTTTTTTTTTTTTTTTTTTTTTTTTTTTTTT
TTTTTTTTTTATGC

Hairpin sequence:

*GGG*AGCACTACGTTCGGACTAGTGTACTCTGACTTGAGAC

6.1.4 Oligos and hairpin of P90ATmGC

Oligo 1:

Bio*TTTTT*GGG*ATTATTAAATTTAAATATTATTATATATATGGGAGCTCTACGTTCGGACTAGTGTA
CTCT

Oligo 2:

Pho*GCCGCCGGGGGCGCGCGCCGCCGCGGCCCC*TTTT*GGGGCCGCGGCGGCGCGCGCCCCCGGCGGC
AGAGTACACT

Oligo 3:

Pho*AGTCCGAACGTAGAGCTCCCATATATATAATAATATTTAAATTTAATAAT*CCC*TTTTTTTTTTT
TTTTTTTTTTTTTTTTTTTTTTTTTTTTTTTTTATGCATGCCC

Hairpin sequence:

*GGG*ATTATTAAATTTAAATATTATTATATATATGGGAGCTCTACGTTCGGACT
AGTGTACTCTGCCGCCGGGGGCGCGCGCCGCCGCGGCCCC

6.1.5 Oligos for the T-Antigen bulk measurements

Bottom strand for the 3´ overhang and the forked construct

R6G*CTTTAGCTGCATATTTACATCATCTTGACCTACAGCACCAGATTCA
GGTTGTTTGTTTGTTTGTTTGTTTGTTT

Top strand for the 5´ overhang and the forked construct

GTTTGTTTGTTTGTTTGTTTGTTTAACCTGAATCTGGTGCTGTAGGTCAA
GATGATGTAAATATGCAGCTAAAG

Top strand for the 3´ overhang and the blunt end construct

AACCTGAATCTGGTGCTGTAGGTCAAGATGATGTAAATATGCAGCTAAAG

Bottom strand for the 5´ overhang and the blunt end construct

R6G*CTTTAGCTGCATATTTACATCATCTTGACCTACAGCACCAGATTCAGGTT

6.2 Protocols

6.2.1 Flow cells

The glass cover slides are cleaned by 10 min sonication in isopropanol followed by aceton. The cover slide for the bottom of the flow cell is spin-coated (Polos Spin 150, Cpk Industries, Harleysville, PA, USA) with polysterene (100 kDa) to create a hydrophobic surface. Therefore 50 μl of 1% polystyrene solution in toluol is quickly pipetted onto the glass at 6000 rpm and dried by further spinning for 1 min. The holes in the top cover slide as well as the parafilm is cutted using a laser cutter (Speedy 100, Trotec, Marchtrenk, Austria) with modified settings for glass and rubber cutting. The cover slides and the parafilm are assembled and fused together by heat (150°C). To bind DNA to the bottom surface of the flow cell a 50 μg/ml anti-digoxigenin (Roche, Penzberg, Germany) solution in PBS buffer (appendix 6.2.2) is incubated over night at 4°C. Additionally, the flow cell is incubated with bovine serum albumin (NEB, Ipswich, MA, USA) over night at 4°C to prevent unspecific binding to the hydrophobic surface. Finally the flow cell is mounted into the holder (self-made), with an in- and outlet hole. The outlet is connected via tubings to a syringe pump system to provide constant, slow flows during exchange of the containing liquids.

6.2.2 Buffers

PBS buffer (pH7.4)
137 mM NaCl, 2.7 mM KCl, 10 mM $Na_2HPO_4 \cdot 2H_2O$, 2 mM KH_2PO_4

Phosphate buffer
10 mM PO_4, 10 mM NaN_3, 100 μg/ml BSA, 0.1 % Tween 20

Reaction buffer for T-Antigen
50 mM HEPES (pH 7.5), 3 mM $MgCl_2$ (2.0129 mM free magnesium ions), 1 mM DTT, 50 mM NaCl, 1 mM ATP, 500 ng/μl BSA

Reaction buffer for AtRecQ2 and -3
40 mM TrisAcetat pH 8.0, 50 mM K-Acetat, 6 mM DTT, 50 ng/μl BSA, 1.8 mM ATP, 1.8 mM $MgCl_2$ (0.2793 mM free magnesium ions)

Test buffer: 100 mm NaCl, 10 mm $MgCl_2$

The concentration of free magnesium ions depends on the Mg-ATP chelats and was calculated using WEBMAXCLITE
(http://www.stanford.edu/ cpatton/webmaxc/webmaxclite115.htm).

6.2.3 Setting up a force experiment

The superparamagnetic microspheres are washed prior usage to remove residual free streptavidin and rediluted in phosphate buffer (PB). To exchange the solution the superparamagentic microspheres are trapped in a tube using a magnetic rack. The desired DNA construct (see chapter: 3) is incubated ($\approx$ 5 min) with the desired microspheres in a 1:1 ratio. After a 1:300 dilution the mixture is flushed (at a slow velocity $\approx$ 150 μl/min) into the flow cell. During the flushing the external magnets should be far away from the flow cell to avoid magnetization and clustering of the microspheres (magnet position $>$ 6 mm for the configuration of the magnets used here). After $\approx$ 5 min incuation time the magnets are approached to the flow cell to remove unbound DNA-microsphere systems from the surface, which are then thoroughly flushed out of the flow cell with PB buffer.

After finding a field of view with a DNA tethered microsphere and a reference microsphere several tests were performed. Firstly, a quick verfication of the appropriate length of the DNA molecule by stretching and relaxing the DNA. Secondly, testing for a low offcenter attachment by magnet rotation (explained in section: 2.4.1). Thirdly, excluding molecules which unspecifically bind to the flow cell surface (sticking) and excluding microspheres with unexpected high fluctuations which are occasionally observed.

Recording the microsphere positions for preset magnet positions as well as the force determination is achieved with the graphical programming language LabView (National Instruments, Austin, USA).

6.3 DNA modification and purification

All enzymes used for DNA modification (all restriction enzymes, T4 DNA Ligase, Antarctic Phosphatase, T4 Polynucleotide Kinase, Lambda Exonuclease) in this section are from NEB (Ipswich, MA, USA) and were used as described in the corresponding protocols. All polymerase chain reactions (PCRs) were executed using Go-Taq (Promega, Fitchburg, Wisconsin, USA) or Phusion (Finnzymes, Vantaa, Finland) following the corresponding protocols. The PCR for the anchoring DNA fragments were performed in presence of modified dUTPs (Biotin-16-dUTP, Digoxigenin-11-dUTP, Roche, Penzberg, Germany) Primers were designed with pDraw and home written software and ordered at Sigma (St. Louis, Missouri, USA), IBA (Göttingen, Germany) or MWG (Huntsville, AL, USA). DNA purification after modification as well as gel purification was achieved using NucleoSpin Extract II (Macherey & Nagel, Düren, Germany) following the protocol. The size markers in all gel images are dsDNA ladders where the shortest fragments starts at the indicated unit which is mostly the size difference between all subsequent fragments. The loading buffer for agarose gels was always the 6x Blue/Orange Loading Dye (Promega, Fitchburg, Wisconsin, USA) and for PAGE gels 0.25% bromphenol blue w/v, 40% sucrose (g/ml).

6.4 Formulas

6.4.1 Coefficients to solve the cubic equation for DNA force-extension behavior

The WLC model (equation 2.18) without the correction terms (the sum) is written as cubic function of the form:

$$AF^3 + BF^2 + CF + D = 0 \tag{6.1}$$

with the coefficients:

$$\begin{aligned} A &= \frac{4}{S^3} + \frac{4p}{k_\mathrm{B}TS^2} && (6.2)\\ B &= -\frac{8pZ_\mathrm{r}}{k_\mathrm{B}TS} - \frac{12Z_\mathrm{r}}{S^2} + \frac{8p}{k_\mathrm{B}TS} + \frac{9}{S^2} && (6.3)\\ C &= \frac{6}{S} + \frac{12Z_\mathrm{r}^2}{S} + \frac{4pZ_\mathrm{r}^2}{k_\mathrm{B}T} - \frac{8pZ_\mathrm{r}}{k_\mathrm{B}T} - \frac{18Z_\mathrm{r}}{S} + \frac{4p}{k_\mathrm{B}T} && (6.4)\\ D &= -4Z_\mathrm{r} + 9Z_\mathrm{r} - 6Z_\mathrm{r}. && (6.5) \end{aligned}$$

with $Z_\mathrm{r} = L/L_0$ being the relative DNA extension.

Dividing by A and substituting $F = x - B/3A$ deletes the second order term and reduces the equation to:

$$x^3 + px + q = 0 \tag{6.6}$$

with

$$p = \frac{3AC - B^2}{3A^2} \qquad q = \frac{2B^3}{27A^3} - \frac{BC}{3A^2} + \frac{D}{A}. \tag{6.7}$$

6.4.2 Solving a system of coupled Langevin equations

The set of coupled, linear Langevin equations 2.48 is converted to:

$$F_2(t) = -\gamma_2 \dot{z_1} - (k_1 + k_2) z_1 + k_1 z_2 \tag{6.8}$$
$$F_1(t) = -\gamma_1 \dot{z_2} + k_1 z_1 - k_1 z_2 \tag{6.9}$$

with the following substitutions for the indices $k_{\mathrm{DNA}} = k_1$, $k_{\mathrm{rot}} = k_2$, $\gamma_{\mathrm{rot}} = \gamma_2$, $\gamma_{\mathrm{trans}} = \gamma_1$, $z_{\mathrm{rot}} = z_1$, $z = z_2$, $F_{\mathrm{rot}}(t) = F_2(t)$ and $F_{\mathrm{trans}}(t) = F_1(t)$. In matrix form the equations are expressed as:

$$\begin{bmatrix} \gamma_2 & 0 \\ 0 & \gamma_1 \end{bmatrix} \begin{bmatrix} \dot{z_1} \\ \dot{z_2} \end{bmatrix} + \begin{bmatrix} k_1 + k_2 & -k_1 \\ -k_1 & k_1 \end{bmatrix} \begin{bmatrix} z_1 \\ z_2 \end{bmatrix} = \begin{bmatrix} F_2 \\ F_1 \end{bmatrix} \tag{6.10}$$

and with $\begin{bmatrix} \gamma_2 & 0 \\ 0 & \gamma_1 \end{bmatrix} = \boldsymbol{\gamma}$ and $\begin{bmatrix} k_1 + k_2 & k_1 \\ -k_1 & k_1 \end{bmatrix} = \boldsymbol{k}$:

$$\boldsymbol{\gamma}\dot{\boldsymbol{z}} + \boldsymbol{k}\boldsymbol{z} = \boldsymbol{F}(t) \tag{6.11}$$
$$\dot{\boldsymbol{z}} = \boldsymbol{\gamma}^{-1}\boldsymbol{F}(t) - \boldsymbol{\gamma}^{-1}\boldsymbol{k}\boldsymbol{z}. \tag{6.12}$$

To decouple these equations the coordinate $\boldsymbol{z}$ is transformed to a new coordinate $\boldsymbol{\zeta}$ with the linear transformation $\boldsymbol{A}\boldsymbol{\zeta} = \boldsymbol{z}$. Now equation 6.12 is transformed to:

$$\boldsymbol{A}^{-1}\dot{\boldsymbol{z}} = \boldsymbol{A}^{-1}\boldsymbol{\gamma}^{-1}\boldsymbol{F}(t) - \boldsymbol{A}^{-1}\boldsymbol{\gamma}^{-1}\boldsymbol{k}\boldsymbol{z} \tag{6.13}$$
$$= \boldsymbol{A}^{-1}\boldsymbol{\gamma}^{-1}\boldsymbol{F}(t) - \boldsymbol{A}^{-1}\boldsymbol{\gamma}^{-1}\boldsymbol{k}\,\boldsymbol{I}\,\boldsymbol{z} \tag{6.14}$$
$$= \boldsymbol{A}^{-1}\boldsymbol{\gamma}^{-1}\boldsymbol{F}(t) - \boldsymbol{A}^{-1}\boldsymbol{\gamma}^{-1}\boldsymbol{k}\boldsymbol{A}\,\boldsymbol{A}^{-1}\boldsymbol{z} \tag{6.15}$$
$$\dot{\boldsymbol{\zeta}} = \boldsymbol{\Phi} - \boldsymbol{A}^{-1}\boldsymbol{\gamma}^{-1}\boldsymbol{k}\boldsymbol{A}\,\boldsymbol{\zeta} \tag{6.16}$$
$$\dot{\boldsymbol{\zeta}} = \boldsymbol{\Phi} - \boldsymbol{\lambda}\,\boldsymbol{\zeta} \tag{6.17}$$

with the unit matrix $\boldsymbol{I} = \boldsymbol{A}\boldsymbol{A}^{-1}$ and the transformed random forces $\boldsymbol{\Phi} = \boldsymbol{A}^{-1}\boldsymbol{\gamma}^{-1}\boldsymbol{F}(t)$. If the transformation matrix $\boldsymbol{A}$ is chosen in such way that

$$\boldsymbol{\lambda} = \boldsymbol{A}^{-1}\boldsymbol{\gamma}^{-1}\boldsymbol{k}\boldsymbol{A} \tag{6.18}$$

is diagonal, then equation 6.12 is decoupled. The columns of $\boldsymbol{A}$ are the eigenvectors of $\boldsymbol{\gamma}^{-1}\boldsymbol{k}$. Therefore the eigenvalues and eigenvectors of $\boldsymbol{\gamma}^{-1}\boldsymbol{k}$ are determined. The eigenvalues are calculated with the characteristic polynom, which is yielded from the determinant $\det(\lambda\boldsymbol{I} - \boldsymbol{\gamma}^{-1}\boldsymbol{k}) = 0$. The eigenvalues are:

$$\lambda_{\pm} = \frac{k_1 + k_2}{2\gamma_2} + \frac{k_1}{2\gamma_1} \pm \frac{1}{2}\sqrt{\left(\frac{k_1 + k_2}{\gamma_2} + \frac{k_1}{\gamma_1}\right)^2 - \frac{4k_2k_1}{\gamma_2\gamma_1}} \tag{6.19}$$

Before determining the corresponding eigenvectors, $\boldsymbol{\gamma}^{-1}\boldsymbol{k}$ is substituded to $\boldsymbol{r}$ for simplification:

$$\begin{bmatrix} \frac{k_1+k_2}{\gamma_2} & \frac{-k_1}{\gamma_2} \\ \frac{-k_1}{\gamma_1} & \frac{k_1}{\gamma_1} \end{bmatrix} = \begin{bmatrix} r_{11} & r_{12} \\ r_{21} & r_{22} \end{bmatrix} = \boldsymbol{r} \tag{6.20}$$

The eigenvectors $\vec{x}$ to the eigenvalues $\lambda_\pm$ are determined with $\boldsymbol{r}\vec{x} = \lambda_\pm \vec{x}$:

$$\begin{bmatrix} r_{11} & r_{12} \\ r_{21} & r_{22} \end{bmatrix} \begin{bmatrix} x_{11} \\ x_{12} \end{bmatrix} = \lambda_+ \begin{bmatrix} x_{11} \\ x_{12} \end{bmatrix} \qquad \text{and} \qquad \begin{bmatrix} r_{11} & r_{12} \\ r_{21} & r_{22} \end{bmatrix} \begin{bmatrix} x_{21} \\ x_{22} \end{bmatrix} = \lambda_- \begin{bmatrix} x_{21} \\ x_{22} \end{bmatrix}. \tag{6.21}$$

The elements of the eigenvectors $\vec{x}$ to the eigenvalues $\lambda_\pm$ are found to display the following dependence:

$$x_{12} = \frac{\lambda_+ - r_{22}}{r_{21}} x_{11} \qquad \text{and} \qquad x_{21} = \frac{\lambda_- - r_{11}}{r_{12}} x_{22}. \tag{6.22}$$

These eigenvectors can be multiplied by any constant c and still remain eigenvectors:

$$\vec{x}_+ = \begin{bmatrix} x_{11} \\ x_{12} \end{bmatrix} = c_1 \begin{bmatrix} 1 \\ \frac{\lambda_+ - r_{22}}{r_{21}} \end{bmatrix}, \quad \vec{x}_- = \begin{bmatrix} x_{21} \\ x_{22} \end{bmatrix} = c_1 \begin{bmatrix} \frac{\lambda_- - r_{11}}{r_{12}} \\ 1 \end{bmatrix}. \tag{6.23}$$

As mentioned before, the columns of the transformation matrix $\boldsymbol{A}$ are the eigenvectors of $\boldsymbol{r} = \boldsymbol{\gamma}^{-1}\boldsymbol{k}$:

$$\boldsymbol{A} = \begin{bmatrix} c_1 & c_2 x_{12} \\ c_1 x_{21} & c_2 \end{bmatrix} = \begin{bmatrix} c_1 & c_2 C \gamma_1 \\ -c_1 C \gamma_2 & c_2 \end{bmatrix} = \frac{1}{\sqrt{1 + C^2 \gamma_1 \gamma_2}} \begin{bmatrix} 1/\sqrt{\gamma_2} & C\sqrt{\gamma_1} \\ -C\sqrt{\gamma_2} & 1/\sqrt{\gamma_1} \end{bmatrix}. \tag{6.24}$$

with

$$C = \frac{\left(-\frac{k_1+k_2}{2\gamma_2} + \frac{k_1}{2\gamma_1} - \frac{1}{2}\sqrt{\left(\frac{k_1+k_2}{\gamma_2} + \frac{k_1}{\gamma_1} \right)^2 - \frac{4k_2k_1}{\gamma_2\gamma_1}} \right)}{k_1}. \tag{6.25}$$

The last matrix can be used because x_{12} and x_{21} differ only in their sign and the drag coefficients γ. In explicit terms x_{12} and x_{21} are:

$$x_{12} = \frac{\left(-\frac{k_1+k_2}{2\gamma_2} + \frac{k_1}{2\gamma_1} - \frac{1}{2}\sqrt{\left(\frac{k_1+k_2}{\gamma_2} + \frac{k_1}{\gamma_1} \right)^2 - \frac{4k_2k_1}{\gamma_2\gamma_1}} \right) \gamma_1}{k_1} \tag{6.26}$$

and

$$x_{21} = \frac{\left(\frac{k_1+k_2}{2\gamma_2} - \frac{k_1}{2\gamma_1} + \frac{1}{2}\sqrt{\left(\frac{k_1+k_2}{\gamma_2} + \frac{k_1}{\gamma_1} \right)^2 - \frac{4k_2k_1}{\gamma_2\gamma_2}} \right) \gamma_2}{k_1} \tag{6.27}$$

The constants c_1 and c_2 are chosen to normalize the transformation matrix, to fulfill the condition: $\boldsymbol{A^{-1}}(\boldsymbol{\gamma}^{-1})^T(\boldsymbol{A^{-1}})^T = \boldsymbol{I}$ [44]:

$$\boldsymbol{A^{-1}}(\boldsymbol{\gamma}^{-1})^T(\boldsymbol{A^{-1}})^T = \begin{bmatrix} \frac{1}{(1+C^2\gamma_1\gamma_2)c_1^2\gamma_2} & 0 \\ 0 & \frac{1}{(1+C^2\gamma_1\gamma_2)c_2^2\gamma_1} \end{bmatrix} = \begin{bmatrix} 1 & 0 \\ 0 & 1 \end{bmatrix} \tag{6.28}$$

with

$$c_1 = \sqrt{\frac{1}{(1 + C^2\gamma_1\gamma_2)\gamma_2}} \qquad \text{and} \qquad c_2 = \sqrt{\frac{1}{(1 + C^2\gamma_1\gamma_2)\gamma_1}}. \tag{6.29}$$

With these constants the transformation matrix $\boldsymbol{A}$ is determined. The matrix $\boldsymbol{\lambda}$ in equation 6.18 is now diagonal, decouples the linear Langevin equations 6.9 and the diagonal entries are the eigenvalues $\lambda_\pm$:

$$\boldsymbol{\lambda} = \begin{bmatrix} \lambda_+ & 0 \\ 0 & \lambda_- \end{bmatrix}. \tag{6.30}$$

Now the decoupled system of linear equations (Equation 6.17) can be solved. Because of the random nature of the forces $\mathbf{F}(\mathrm{t})$, the decoupled system of linear equations is solved in frequency space, i.e. the PSD is calculated (similar to the single equation 2.4 in section 2.3.1). The conditions for the random forces are [44] (compare to equation 2.5 in section 2.3.1):

$$\langle \boldsymbol{F}(t) \rangle = 0 \quad \text{and} \quad \langle \boldsymbol{F}(t) \times \boldsymbol{F}(\bar{t}) \rangle = 2k_\mathrm{B}T\boldsymbol{\gamma} \cdot \delta(t - \bar{t}) \tag{6.31}$$

The PSD for the coupled system is given in section 2.4.2, equation 2.50 as well as the solution in equation 2.52. In equation 2.52 all indices of the spring constants and drag coefficients, which were introduced for simplification at the beginning of this section, are resubstituted.

The influence of the coupling is shown in Figure 6.1.

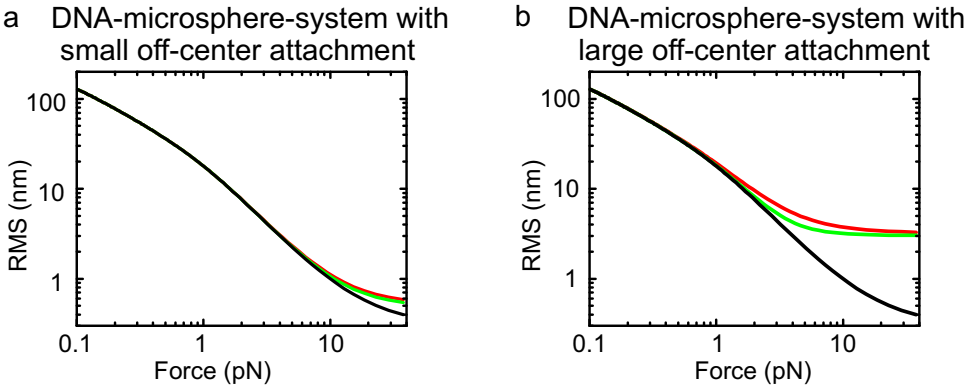

Figure 6.1 Influence of coupling between rotational and translational fluctuations on the noise along the vertical coordinate. (a) Small off-center attachment. Calculated noise for a 2 μm long DNA molecule, attached to a M280 microsphere with an off-center attachment of 0.2 μm and a torsional stiffness of 100 pN μm rad^{-1}. The sampling frequency was set to 60 Hz. RMS amplitudes as function of force were calculated for translational fluctuations only (black line, calculated according to equation 2.43), for uncoupled translational and rotational fluctuations (green line, calculated according to equation 2.43, for both types of fluctuations) and for coupled translational and rotational fluctuations (red line, calculated according to 2.54). (b) Large off-center attachment. Calculated noise as function of force with the same parameters as in (b) except the off-center attachment for which 1.2 μm was taken.

Bibliography

[1] N. Tuteja and R. Tuteja, *Prokaryotic and eukaryotic DNA helicases. essential molecular motor proteins for cellular machinery.*, Eur J Biochem **271**(10), 1835–1848 (2004)

[2] L. Wu and I. D. Hickson, *DNA helicases required for homologous recombination and repair of damaged replication forks*, Annual Review Of Genetics **40**, 279–306 (2006)

[3] N. Tuteja and R. Tuteja, *Unraveling DNA helicases. motif, structure, mechanism and function.*, Eur J Biochem **271**(10), 1849–1863 (2004)

[4] M. R. Singleton and D. B. Wigley, *Multiple roles for ATP hydrolysis in nucleic acid modifying enzymes.*, EMBO J **22**(18), 4579–4583 (2003)

[5] W. Yang, *Lessons learned from UvrD helicase: mechanism for directional movement.*, Annu Rev Biophys **39**, 367–385 (2010)

[6] T. M. Lohman, E. J. Tomko and C. G. Wu, *Non-hexameric DNA helicases and translocases: mechanisms and regulation.*, Nat Rev Mol Cell Biol **9**(5), 391–401 (2008)

[7] M. Manosas, X. G. Xi, D. Bensimon and V. Croquette, *Active and passive mechanisms of helicases.*, Nucleic Acids Res **38**(16), 5518–5526 (2010)

[8] J. G. Yodh, M. Schlierf and T. Ha, *Insight into helicase mechanism and function revealed through single-molecule approaches.*, Q Rev Biophys **43**(2), 185–217 (2010)

[9] J. Howard, *Mechanics of Motor Proteins and the Cytoskeleton* (Sinauer Associates, Sunderland, MA, 2001)

[10] J. E. Walker, M. Saraste, M. J. Runswick and N. J. Gay, *Distantly related sequences in the alpha- and beta-subunits of ATP synthase, myosin, kinases and other ATP-requiring enzymes and a common nucleotide binding fold.*, EMBO J **1**(8), 945–951 (1982)

[11] K. Büttner, S. Nehring and K.-P. Hopfner, *Structural basis for DNA duplex separation by a superfamily-2 helicase.*, Nat Struct Mol Biol **14**(7), 647–652 (2007)

[12] J. Y. Lee and W. Yang, *UvrD helicase unwinds DNA one base pair at a time by a two-part power stroke.*, Cell **127**(7), 1349–1360 (2006)

[13] N. K. Maluf, C. J. Fischer and T. M. Lohman, *A dimer of escherichia coli UvrD is the active form of the helicase in vitro.*, J Mol Biol **325**(5), 913–935 (2003)

[14] T. M. Lohman and K. P. Bjornson, *Mechanisms of helicase-catalyzed DNA unwinding.*, Annu Rev Biochem **65**, 169–214 (1996)

[15] I. Wong, K. L. Chao, W. Bujalowski and T. M. Lohman, *DNA-induced dimerization of the escherichia coli Rep helicase. allosteric effects of single-stranded and duplex DNA.*, J Biol Chem **267**(11), 7596–7610 (1992)

[16] Y. Yang, S.-X. Dou, H. Ren, P.-Y. Wang, X.-D. Zhang, M. Qian, B.-Y. Pan and X. G. Xi, *Evidence for a functional dimeric form of the PcrA helicase in DNA unwinding.*, Nucleic Acids Res **36**(6), 1976–1989 (2008)

[17] Y. Yang, S.-X. Dou, Y.-N. Xu, N. Bazeille, P.-Y. Wang, P. Rigolet, H.-Q. Xu and X. G. Xi, *Kinetic mechanism of DNA unwinding by the BLM helicase core and molecular basis for its low processivity.*, Biochemistry **49**(4), 656–668 (2010)

[18] M. J. Jezewska, S. Rajendran and W. Bujalowski, *Escherichia coli replicative helicase PriA protein-single-stranded DNA complex. stoichiometries, free energy of binding, and cooperativities.*, J Biol Chem **275**(36), 27865–27873 (2000)

[19] P. D. Morris, A. J. Tackett, K. Babb, B. Nanduri, C. Chick, J. Scott and K. D. Raney, *Evidence for a functional monomeric form of the bacteriophage T4 DdA helicase. Dda does not form stable oligomeric structures.*, J Biol Chem **276**(23), 19691–19698 (2001)

[20] J. L. Moreland, A. Gramada, O. V. Buzko, Q. Zhang and P. E. Bourne, *The molecular biology toolkit (MBT): a modular platform for developing molecular visualization applications.*, BMC Bioinformatics **6**, 21 (2005)

[21] D. Gai, R. Zhao, D. Li, C. V. Finkielstein and X. S. Chen, *Mechanisms of conformational change for a replicative hexameric helicase of SV40 large tumor antigen.*, Cell **119**(1), 47–60 (2004)

[22] I. A. Mastrangelo, P. V. Hough, J. S. Wall, M. Dodson, F. B. Dean and J. Hurwitz, *ATP-dependent assembly of double hexamers of SV40 T antigen at the viral origin of DNA replication.*, Nature **338**(6217), 658–662 (1989)

[23] F. Dong and P. H. von Hippel, *The ATP-activated hexameric helicase of bacteriophage T4 (gp41) forms a stable primosome with a single subunit of T4-coded primase (gp61).*, J Biol Chem **271**(32), 19625–19631 (1996)

[24] W. Bujalowski, M. M. Klonowska and M. J. Jezewska, *Oligomeric structure of escherichia coli primary replicative helicase DnaB protein.*, J Biol Chem **269**(50), 31350–31358 (1994)

[25] J. Sedman and A. Stenlund, *The papillomavirus E1 protein forms a DNA-dependent hexameric complex with ATPase and DNA helicase activities.*, J Virol **72**(8), 6893–6897 (1998)

[26] S. S. Velankar, P. Soultanas, M. S. Dillingham, H. S. Subramanya and D. B. Wigley, *Crystal structures of complexes of PcrA DNA helicase with a DNA substrate indicate an inchworm mechanism.*, Cell **97**(1), 75–84 (1999)

[27] C. J. Fischer, N. K. Maluf and T. M. Lohman, *Mechanism of ATP-dependent translocation of E.coli UvrD monomers along single-stranded DNA.*, J Mol Biol **344**(5), 1287–1309 (2004)

[28] G. T. Yarranton and M. L. Gefter, *Enzyme-catalyzed DNA unwinding: studies on escherichia coli Rep protein.*, Proc Natl Acad Sci U S A **76**(4), 1658–1662 (1979)

[29] I. Wong and T. M. Lohman, *Allosteric effects of nucleotide cofactors on escherichia coli Rep helicase-DNA binding.*, Science **256**(5055), 350–355 (1992)

[30] S. S. Patel and I. Donmez, *Mechanisms of helicases.*, J Biol Chem **281**(27), 18265–18268 (2006)

[31] S. Myong, M. M. Bruno, A. M. Pyle and T. Ha, *Spring-loaded mechanism of DNA unwinding by hepatitis C virus NS3 helicase.*, Science **317**(5837), 513–516 (2007)

[32] E. J. Tomko, C. J. Fischer, A. Niedziela-Majka and T. M. Lohman, *A nonuniform stepping mechanism for E.coli UvrD monomer translocation along single-stranded DNA*, Molecular Cell **26**(3), 335–347 (2007)

[33] B. Sun, D. S. Johnson, G. Patel, B. Y. Smith, M. Pandey, S. S. Patel and M. D. Wang, *ATP-induced helicase slippage reveals highly coordinated subunits.*, Nature (2011)

[34] M. D. Betterton and F. Julicher, *Opening of nucleic-acid double strands by helicases: Active versus passive opening (vol 71, pg 11904, 2005)*, Physical Review E **72**(2) (2005)

[35] T. Lionnet, M. M. Spiering, S. J. Benkovic, D. Bensimon and V. Croquette, *Real-time observation of bacteriophage T4 gp41 helicase reveals an unwinding mechanism.*, Proc Natl Acad Sci U S A **104**(50), 19790–19795 (2007)

[36] I. Rasnik, Y.-J. Jeong, S. A. McKinney, V. Rajagopal, S. S. Patel and T. Ha, *Branch migration enzyme as a brownian ratchet.*, EMBO J **27**(12), 1727–1735 (2008)

[37] M. K. Levin, M. Gurjar and S. S. Patel, *A brownian motor mechanism of translocation and strand separation by hepatitis C virus helicase.*, Nat Struct Mol Biol **12**(5), 429–435 (2005)

[38] M. D. Betterton and F. Julicher, *A motor that makes its own track: Helicase unwinding of DNA*, Physical Review Letters **91**(25) (2003)

[39] D. S. Johnson, L. Bai, B. Y. Smith, S. S. Patel and M. D. Wang, *Single-molecule studies reveal dynamics of DNA unwinding by the ring-shaped T7 helicase.*, Cell **129**(7), 1299–1309 (2007)

[40] M. Manosas, A. Meglio, M. M. Spiering, F. Ding, S. J. Benkovic, F.-X. Barre, O. A. Saleh, J. F. Allemand, D. Bensimon and V. Croquette, *Magnetic tweezers for the study of DNA tracking motors.*, Methods Enzymol **475**, 297–320 (2010)

[41] A. M. Pyle, *Translocation and unwinding mechanisms of RNA and DNA helicases.*, Annu Rev Biophys **37**, 317–336 (2008)

[42] J. Park, S. Myong, A. Niedziela-Majka, K. S. Lee, J. Yu, T. M. Lohman and T. Ha, *PcrA helicase dismantles RecA filaments by reeling in DNA in uniform steps.*, Cell **142**(4), 544–555 (2010)

[43] J. A. Ali and T. M. Lohman, *Kinetic measurement of the step size of DNA unwinding by escherichia coli UvrD helicase.*, Science **275**(5298), 377–380 (1997)

[44] J. R. Moffitt, Y. R. Chemla, D. Izhaky and C. Bustamante, *Differential detection of dual traps improves the spatial resolution of optical tweezers.*, Proc Natl Acad Sci U S A **103**(24), 9006–9011 (2006)

[45] J. R. Moffitt, Y. R. Chemla, K. Aathavan, S. Grimes, P. J. Jardine, D. L. Anderson and C. Bustamante, *Intersubunit coordination in a homomeric ring ATPase*, Nature **457**(7228), 446–U2 (2009)

[46] S. Marsden, M. Nardelli, P. Linder and J. E. G. McCarthy, *Unwinding single RNA molecules using helicases involved in eukaryotic translation initiation.*, J Mol Biol **361**(2), 327–335 (2006)

[47] C. Gosse and V. Croquette, *Magnetic tweezers: micromanipulation and force measurement at the molecular level.*, Biophys J **82**(6), 3314–3329 (2002)

[48] W. K. Chu and I. D. Hickson, *RecQ helicases: multifunctional genome caretakers*, Nature Reviews Cancer **9**(9), 644–654 (2009)

[49] L. K. Stanley, R. Seidel, C. van der Scheer, N. H. Dekker, M. D. Szczelkun and C. Dekker, *When a helicase is not a helicase: dsDNA tracking by the motor protein EcoR124I.*, EMBO J **25**(10), 2230–2239 (2006)

[50] H. Stahl, P. Dröge and R. Knippers, *DNA helicase activity of SV40 large tumor antigen.*, EMBO J **5**(8), 1939–1944 (1986)

[51] M. G. Gomez-Lorenzo, M. Valle, J. Frank, C. Gruss, C. O. S. Sorzano, X. S. Chen, L. E. Donate and J. M. Carazo, *Large T antigen on the simian virus 40 origin of replication: a 3D snapshot prior to DNA replication.*, EMBO J **22**(23), 6205–6213 (2003)

[52] D. Li, R. Zhao, W. Lilyestrom, D. Gai, R. Zhang, J. A. DeCaprio, E. Fanning, A. Jochimiak, G. Szakonyi and X. S. Chen, *Structure of the replicative helicase of the oncoprotein SV40 large tumour antigen.*, Nature **423**(6939), 512–518 (2003)

[53] N. Luzzietti, H. Brutzer, D. Klaue, F. W. Schwarz, W. Staroske, S. Clausing and R. Seidel, *Efficient preparation of internally modified single-molecule constructs using nicking enzymes.*, Nucleic Acids Res (2010)

[54] D. Klaue and R. Seidel, *Torsional stiffness of single superparamagnetic microspheres in an external magnetic field.*, Phys Rev Lett **102**(2), 028302 (2009)

[55] H. Brutzer, N. Luzzietti, D. Klaue and R. Seidel, *Energetics at the DNA supercoiling transition.*, Biophys J **98**(7), 1267–1276 (2010)

[56] T. R. Strick, J. F. Allemand, D. Bensimon, A. Bensimon and V. Croquette, *The elasticity of a single supercoiled DNA molecule.*, Science **271**(5257), 1835–1837 (1996)

[57] T. Strick, J. Allemand, V. Croquette and D. Bensimon, *Twisting and stretching single DNA molecules.*, Prog Biophys Mol Biol **74**(1-2), 115–140 (2000)

[58] T. R. Strick, J. F. Allemand, D. Bensimon and V. Croquette, *Behavior of supercoiled DNA.*, Biophys J **74**(4), 2016–2028 (1998)

[59] J. Gore, Z. Bryant, M. Nöllmann, M. U. Le, N. R. Cozzarelli and C. Bustamante, *DNA overwinds when stretched.*, Nature **442**(7104), 836–839 (2006)

[60] J. F. Allemand, D. Bensimon, R. Lavery and V. Croquette, *Stretched and overwound DNA forms a Pauling-like structure with exposed bases.*, Proc Natl Acad Sci U S A **95**(24), 14152–14157 (1998)

[61] R. Seidel, J. G. P. Bloom, J. van Noort, C. F. Dutta, N. H. Dekker, K. Firman, M. D. Szczelkun and C. Dekker, *Dynamics of initiation, termination and reinitiation of DNA translocation by the motor protein EcoR124I.*, EMBO J **24**(23), 4188–4197 (2005)

[62] M. Nollmann, M. D. Stone, Z. Bryant, J. Gore, N. J. Crisona, S. C. Hong, S. Mitelheiser, A. Maxwell, C. Bustamante and N. R. Cozzarelli, *Multiple modes of escherichia coli DNA gyrase activity revealed by force and torque*, Nature Structural & Molecular Biology **14**(4), 264–271 (2007)

[63] R. Amit, O. Gileadi and J. Stavans, *Direct observation of RuvAB-catalyzed branch migration of single Holliday junctions.*, Proc Natl Acad Sci U S A **101**(32), 11605–11610 (2004)

[64] M.-N. Dessinges, T. Lionnet, X. G. Xi, D. Bensimon and V. Croquette, *Single-molecule assay reveals strand switching and enhanced processivity of UvrD.*, Proc Natl Acad Sci U S A **101**(17), 6439–6444 (2004)

[65] O. Otto, F. Czerwinski, J. L. Gornall, G. Stober, L. B. Oddershede, R. Seidel and U. F. Keyser, *Real-time particle tracking at 10,000 fps using optical fiber illumination.*, Opt Express **18**(22), 22722–22733 (2010)

[66] K. C. Neuman and A. Nagy, *Single-molecule force spectroscopy: optical tweezers, magnetic tweezers and atomic force microscopy*, Nature Methods **5**(6), 491–505 (2008)

[67] K. Berg-Sørensen and H. Flyvbjerg, *Power spectrum analysis for optical tweezers*, Review Of Scientific Instruments **75**, 594 (2004)

[68] K. C. Neuman, T. Lionnet and J. F. Allemand, *Single-molecule micromanipulation techniques*, Annu. Rev. Mater. Res. **37**, 33–67 (2007)

[69] F. Gittes and C. F. Schmidt, *Signals and noise in micromechanical measurements.*, Methods Cell Biol **55**, 129–156 (1998)

[70] G. Fonnum, C. Johansson, A. Molteberg, S. Morup and E. Aksnes, *Characterisation of Dynabeads ® by magnetization measurements and mossbauer spectroscopy*, J Magn Magn Mater **293**(1), 41–47 (2005)

[71] D. R. Baselt, G. U. Lee, M. Natesan, S. W. Metzger, P. E. Sheehan and R. J. Colton, *A biosensor based on magnetoresistance technology.*, Biosens Bioelectron **13**(7-8), 731–739 (1998)

[72] M. D. Wang, H. Yin, R. Landick, J. Gelles and S. M. Block, *Stretching DNA with optical tweezers.*, Biophys J **72**(3), 1335–1346 (1997)

[73] C. Bouchiat, M. D. Wang, J. Allemand, T. Strick, S. M. Block and V. Croquette, *Estimating the persistence length of a worm-like chain molecule from force-extension measurements.*, Biophys J **76**(1 Pt 1), 409–413 (1999)

[74] S. Bronstein, *Taschenbuch der Mathematik* (1979)

[75] D. E. Segall, P. C. Nelson and R. Phillips, *Volume-exclusion effects in tethered-particle experiments: bead size matters.*, Phys. Rev. Lett. **96**(8), 088306 (2006)

[76] H. C. Bryant, D. A. Sergatskov, D. Lovato, N. L. Adolphi, R. S. Larson and E. R. Flynn, *Magnetic needles and superparamagnetic cells.*, Phys Med Biol **52**(14), 4009–4025 (2007)

[77] Y.-F. Chen, D. P. Wilson, K. Raghunathan and J.-C. Meiners, *Entropic boundary effects on the elasticity of short DNA molecules.*, Phys Rev E Stat Nonlin Soft Matter Phys **80**(2 Pt 1), 020903 (2009)

[78] Y. Seol, J. Li, P. C. Nelson, T. T. Perkins and M. D. Betterton, *Elasticity of short DNA molecules: theory and experiment for contour lengths of 0.6-7 microm.*, Biophys J. **93**(12), 4360–4373 (2007)

[79] M. T. Woodside, W. M. Behnke-Parks, K. Larizadeh, K. Travers, D. Herschlag and S. M. Block, *Nanomechanical measurements of the sequence-dependent folding landscapes of single nucleic acid hairpins*, Proceedings Of The National Academy Of Sciences Of The United States Of America **103**(16), 6190–6195 (2006)

[80] H. Brutzer, F. W. Schwarz and R. Seidel, *Scanning evanescent fields using a pointlike light source and a nanomechanical DNA gear.*, Nano Lett **12**(1), 473–478 (2012)

[81] D. J. Kauert, T. Kurth, T. Liedl and R. Seidel, *Direct mechanical measurements reveal the material properties of three-dimensional DNA origami.*, Nano Lett **11**(12), 5558–5563 (2011)

[82] E. Schäffer, S. F. Nørrelykke and J. Howard, *Surface forces and drag coefficients of microspheres near a plane surface measured with optical tweezers.*, Langmuir **23**(7), 3654–3665 (2007)

[83] A. J. Goldman, R. G. Cox and H. Brenner, *Slow viscous motion of a sphere parallel to a plane wall - motion through a quiescent fluid*, Chem Eng Sci **22**, 637–651 (1967)

[84] H. Faxén, *Der Widerstand gegen die Bewegung einer starren Kugel in einer zähen Flüssigkeit, die zwischen zwei parallelen, ebenen Wänden eingeschlossen ist*, Ann. Phys. **373**(10), 89–119 (1922)

[85] A. D. Maude, *The movement of a sphere in front of a plane at low reynolds number*, Br. J. Appl. Phys. **14**, 894 (1963)

[86] C. Caizer, C. Savii and M. Popovici, *Magnetic behaviour of iron oxide nanoparticles dispersed in a silica matrix*, Materials Science And Engineering B-Solid State Materials For Advanced Technology **97**(2), 129–134 (2003)

[87] D. Normanno, M. Capitanio and F. S. Pavone, *Spin absorption, windmill, and magneto-optic effects in optical angular momentum transfer*, Physical Review A **70**(5), 053829 (2004)

[88] C. Danilowicz, V. W. Coljee, C. Bouzigues, D. K. Lubensky, D. R. Nelson and M. Prentiss, *DNA unzipped under a constant force exhibits multiple metastable intermediates.*, Proc Natl Acad Sci U S A **100**(4), 1694–1699 (2003)

[89] G. Mihajlovic, K. Aledealat, P. Xiong, S. Von Molnar, M. Field and G. J. Sullivan, *Magnetic characterization of a single superparamagnetic bead by phase-sensitive micro-hall magnetometry*, Applied Physics Letters **91**(17), 172518 (2007)

[90] S. Kohout, J. Roos and H. Keller, *Novel sensor design for torque magnetometry*, Review Of Scientific Instruments **78**(1), 013903 (2007)

[91] W. Cheng, S. Dumont, I. Tinoco and C. Bustamante, *NS3 helicase actively separates RNA strands and senses sequence barriers ahead of the opening fork.*, Proc Natl Acad Sci U S A **104**(35), 13954–13959 (2007)

[92] S. Dumont, W. Cheng, V. Serebrov, R. K. Beran, I. Tinoco, A. M. Pyle and C. Bustamante, *RNA translocation and unwinding mechanism of HCV NS3 helicase and its coordination by ATP.*, Nature **439**(7072), 105–108 (2006)

[93] M. Manosas, M. M. Spiering, Z. H. Zhuang, S. J. Benkovic and V. Croquette, *Coupling DNA unwinding activity with primer synthesis in the bacteriophage T4 primosome*, Nature Chemical Biology **5**(12), 904–912 (2009)

[94] M. T. Woodside, *Direct measurement of the full, sequence-dependent folding landscape of a nucleic acid*, Science **315**(5813), 766–766 (2007)

[95] J. Gál, R. Schnell, S. Szekeres and M. Kálmán, *Directional cloning of native PCR products with preformed sticky ends (autosticky PCR).*, Mol Gen Genet **260**(6), 569–573 (1999)

[96] K. Kim and O. A. Saleh, *A high-resolution magnetic tweezer for single-molecule measurements.*, Nucleic Acids Res **37**(20), e136 (2009)

[97] B. Essevaz-Roulet, U. Bockelmann and F. Heslot, *Mechanical separation of the complementary strands of DNA.*, Proc Natl Acad Sci U S A **94**(22), 11935–11940 (1997)

[98] M. Rief, H. Clausen-Schaumann and H. E. Gaub, *Sequence-dependent mechanics of single DNA molecules.*, Nat Struct Biol **6**(4), 346–349 (1999)

[99] J.-B. Lee, R. K. Hite, S. M. Hamdan, X. S. Xie, C. C. Richardson and A. M. van Oijen, *DNA primase acts as a molecular brake in DNA replication.*, Nature **439**(7076), 621–624 (2006)

[100] Z.-J. Tan and S.-J. Chen, *Salt dependence of nucleic acid hairpin stability.*, Biophys J **95**(2), 738–752 (2008)

[101] Z.-J. Tan and S.-J. Chen, *Nucleic acid helix stability: effects of salt concentration, cation valence and size, and chain length.*, Biophys J **90**(4), 1175–1190 (2006)

[102] J. Liphardt, B. Onoa, S. B. Smith, I. Tinoco and C. Bustamante, *Reversible unfolding of single RNA molecules by mechanical force*, Science **292**(5517), 733–737 (2001)

[103] S. B. Smith, L. Finzi and C. Bustamante, *Direct mechanical measurements of the elasticity of single DNA molecules by using magnetic beads.*, Science **258**(5085), 1122–1126 (1992)

[104] U. Bockelmann, B. Essevaz-Roulet and F. Heslot, *DNA strand separation studied by single molecule force measurements*, Phys. Rev. E **58**, 2386–2394 (1998)

[105] M. Zuker, *Calculating nucleic acid secondary structure*, Curr. Opin. Struct. Biol. **10**, 303 (2000)

[106] J. SantaLucia, Jr, *A unified view of polymer, dumbbell, and oligonucleotide DNA nearest-neighbor thermodynamics.*, Proc Natl Acad Sci U S A **95**(4), 1460–1465 (1998)

[107] N. Peyret, *Prediction of nucleic acid hybridization: Parameters and algorithms*, Ph.D. thesis, Wayne State University, Department of Chemistry (2000)

[108] E. Fanning and R. Knippers, *Structure and function of simian virus 40 large tumor antigen.*, Annu Rev Biochem **61**, 55–85 (1992)

[109] M. Dodson, F. B. Dean, P. Bullock, H. Echols and J. Hurwitz, *Unwinding of duplex DNA from the SV40 origin of replication by T antigen.*, Science **238**(4829), 964–967 (1987)

[110] M. S. Wold, J. J. Li and T. J. Kelly, *Initiation of simian virus 40 DNA replication in vitro: large-tumor-antigen- and origin-dependent unwinding of the template.*, Proc Natl Acad Sci U S A **84**(11), 3643–3647 (1987)

[111] Z. Kelman, J. K. Lee and J. Hurwitz, *The single minichromosome maintenance protein of methanobacterium thermoautotrophicum deltah contains DNA helicase activity.*, Proc Natl Acad Sci U S A **96**(26), 14783–14788 (1999)

[112] D. T. Simmons, *SV40 large T antigen functions in DNA replication and transformation.*, Adv Virus Res **55**, 75–134 (2000)

[113] M. C. San Martín, C. Gruss and J. M. Carazo, *Six molecules of SV40 large T antigen assemble in a propeller-shaped particle around a channel.*, J Mol Biol **268**(1), 15–20 (1997)

[114] J. A. Borowiec, F. B. Dean, P. A. Bullock and J. Hurwitz, *Binding and unwinding - how T antigen engages the SV40 origin of DNA replication.*, Cell **60**(2), 181–184 (1990)

[115] F. B. Dean, P. Bullock, Y. Murakami, C. R. Wobbe, L. Weissbach and J. Hurwitz, *Simian virus 40 (SV40) DNA replication: SV40 large T antigen unwinds DNA containing the SV40 origin of replication.*, Proc Natl Acad Sci U S A **84**(1), 16–20 (1987)

[116] R. E. Parsons, J. E. Stenger, S. Ray, R. Welker, M. E. Anderson and P. Tegtmeyer, *Cooperative assembly of simian virus 40 T-antigen hexamers on functional halves of the replication origin.*, J Virol **65**(6), 2798–2806 (1991)

[117] G. Meinke, P. Phelan, S. Moine, E. Bochkareva, A. Bochkarev, P. A. Bullock and A. Bohm, *The crystal structure of the SV40 T-antigen origin binding domain in complex with DNA.*, PLoS Biol **5**(2), e23 (2007)

[118] D. K. Reese, G. Meinke, A. Kumar, S. Moine, K. Chen, J. L. Sudmeier, W. Bachovchin, A. Bohm and P. A. Bullock, *Analyses of the interaction between the origin binding domain from simian virus 40 T antigen and single-stranded DNA provide insights into DNA unwinding and initiation of DNA replication.*, J Virol **80**(24), 12248–12259 (2006)

[119] I. Cuesta, R. Nunez-Ramirez, S. H. W. Scheres, D. Gai, X. S. Chen, E. Fanning and J. Maria Carazo, *Conformational rearrangements of SV40 large T antigen during early replication events*, Journal of Molecular Biology **397**(5), 1276–1286 (2010)

[120] E. Bochkareva, D. Martynowski, A. Seitova and A. Bochkarev, *Structure of the origin-binding domain of simian virus 40 large T antigen bound to DNA.*, EMBO J **25**(24), 5961–5969 (2006)

[121] A. Kumar, G. Meinke, D. K. Reese, S. Moine, P. J. Phelan, A. Fradet-Turcotte, J. Archambault, A. Bohm and P. A. Bullock, *Model for T-antigen-dependent melting of the simian virus 40 core origin based on studies of the interaction of the beta-hairpin with DNA.*, J Virol **81**(9), 4808–4818 (2007)

[122] M. Valle, X. S. Chen, L. E. Donate, E. Fanning and J. M. Carazo, *Structural basis for the cooperative assembly of large T antigen on the origin of replication.*, J Mol Biol **357**(4), 1295–1305 (2006)

[123] N. V. Smelkova and J. A. Borowiec, *Synthetic DNA replication bubbles bound and unwound with twofold symmetry by a simian virus 40 T-antigen double hexamer.*, J Virol **72**(11), 8676–8681 (1998)

[124] E. C. Foster and D. T. Simmons, *The SV40 large T-antigen origin binding domain directly participates in DNA unwinding.*, Biochemistry **49**(10), 2087–2096 (2010)

[125] C. Wu, R. Roy and D. T. Simmons, *Role of single-stranded DNA binding activity of T antigen in simian virus 40 DNA replication.*, J Virol **75**(6), 2839–2847 (2001)

[126] A. I. Alexandrov, M. R. Botchan and N. R. Cozzarelli, *Characterization of simian virus 40 T-antigen double hexamers bound to a replication fork. the active form of the helicase.*, J Biol Chem **277**(47), 44886–44897 (2002)

[127] M. S. VanLoock, A. Alexandrov, X. Yu, N. R. Cozzarelli and E. H. Egelman, *SV40 large T antigen hexamer structure: domain organization and DNA-induced conformational changes.*, Curr Biol **12**(6), 472–476 (2002)

[128] J. Shen, D. Gai, A. Patrick, W. B. Greenleaf and X. S. Chen, *The roles of the residues on the channel beta-hairpin and loop structures of simian virus 40 hexameric helicase.*, Proc Natl Acad Sci U S A **102**(32), 11248–11253 (2005)

[129] E. J. Enemark and L. Joshua-Tor, *Mechanism of DNA translocation in a replicative hexameric helicase.*, Nature **442**(7100), 270–275 (2006)

[130] R. Wessel, J. Schweizer and H. Stahl, *Simian virus 40 T-antigen DNA helicase is a hexamer which forms a binary complex during bidirectional unwinding from the viral origin of DNA replication.*, J Virol **66**(2), 804–815 (1992)

[131] H. Uhlmann-Schiffler, S. Seinsoth and H. Stahl, *Preformed hexamers of SV40 T antigen are active in RNA and origin-DNA unwinding.*, Nucleic Acids Res **30**(14), 3192–3201 (2002)

[132] U. Ramsperger and H. Stahl, *Unwinding of chromatin by the SV40 large T antigen DNA helicase.*, EMBO J **14**(13), 3215–3225 (1995)

[133] V. Simanis and D. P. Lane, *An immunoaffinity purification procedure for SV40 large T antigen.*, Virology **144**(1), 88–100 (1985)

[134] J. Jiao and D. T. Simmons, *Nonspecific double-stranded DNA binding activity of simian virus 40 large T antigen is involved in melting and unwinding of the origin.*, J Virol **77**(23), 12720–12728 (2003)

[135] W. B. Greenleaf, J. Shen, D. Gai and X. S. Chen, *Systematic study of the functions for the residues around the nucleotide pocket in simian virus 40 AAA+ hexameric helicase.*, J Virol **82**(12), 6017–6023 (2008), michaelis menten and other kinetik parameters for t-antigen

[136] J. Yu, W. Cheng, C. Bustamante and G. Oster, *Coupling translocation with nucleic acid unwinding by NS3 helicase.*, J Mol Biol **404**(3), 439–455 (2010)

[137] J. K. Lee and J. Hurwitz, *Processive DNA helicase activity of the minichromosome maintenance proteins 4, 6, and 7 complex requires forked DNA structures.*, Proc Natl Acad Sci U S A **98**(1), 54–59 (2001)

[138] P. D. Morris, A. K. Byrd, A. J. Tackett, C. E. Cameron, P. Tanega, R. Ott, E. Fanning and K. D. Raney, *Hepatitis C virus NS3 and simian virus 40 T antigen helicases displace streptavidin from 5'-biotinylated oligonucleotides but not from 3'-biotinylated oligonucleotides: evidence for directional bias in translocation on single-stranded DNA.*, Biochemistry **41**(7), 2372–2378 (2002)

[139] M. D. Betterton and F. Jülicher, *Velocity and processivity of helicase unwinding of double-stranded nucleic acids.*, J Phys Condens Matter **17**(47), S3851–S3869 (2005)

[140] P. H. von Hippel and E. Delagoutte, *A general model for nucleic acid helicases and their "coupling" within macromolecular machines.*, Cell **104**(2), 177–190 (2001)

[141] W. Wang and D. T. Simmons, *Simian virus 40 large T antigen can specifically unwind the central palindrome at the origin of DNA replication.*, J Virol **83**(7), 3312–3322 (2009)

[142] G. Meinke, P. A. Bullock and A. Bohm, *Crystal structure of the simian virus 40 large T-antigen origin-binding domain.*, J Virol **80**(9), 4304–4312 (2006)

[143] W. S. Joo, H. Y. Kim, J. D. Purviance, K. R. Sreekumar and P. A. Bullock, *Assembly of T-antigen double hexamers on the simian virus 40 core origin requires only a subset of the available binding sites.*, Mol Cell Biol **18**(5), 2677–2687 (1998)

[144] M. Spies, I. Amitani, R. J. Baskin and S. C. Kowalczykowski, *RecBCD enzyme switches lead motor subunits in response to chi recognition*, Cell **131**, 694–705 (2007)

[145] X. Qu, J.-D. Wen, L. Lancaster, H. F. Noller, C. Bustamante and I. Tinoco, Jr, *The ribosome uses two active mechanisms to unwind messenger RNA during translation.*, Nature **475**(7354), 118–121 (2011)

[146] S. Seinsoth, H. Uhlmann-Schiffler and H. Stahl, *Bidirectional DNA unwinding by a ternary complex of T antigen, nucleolin and topoisomerase i.*, EMBO Rep **4**(3), 263–268 (2003)

[147] Y. Murakami and J. Hurwitz, *Functional interactions between SV40 T antigen and other replication proteins at the replication fork.*, J Biol Chem **268**(15), 11008–11017 (1993)

[148] S. H. Ali and J. A. DeCaprio, *Cellular transformation by SV40 large T antigen: interaction with host proteins.*, Semin Cancer Biol **11**(1), 15–23 (2001)

[149] N. Hunter, *The RecQ DNA helicases: Jacks-of-all-trades or master-tradesmen?*, Cell Research **18**(3), 328–330 (2008)

[150] C. Z. Bachrati and I. D. Hickson, *RecQ helicases: guardian angels of the DNA replication fork*, Chromosoma **117**(3), 219–233 (2008)

[151] D. Kobbe, S. Blanck, K. Demand, M. Focke and H. Puchta, *AtRECQ2, a RecQ helicase homologue from arabidopsis thaliana, is able to disrupt various recombinogenic DNA structures in vitro.*, Plant J **55**(3), 397–405 (2008)

[152] R. J. Bennett and J. L. Keck, *Structure and function of RecQ dna helicases.*, Crit Rev Biochem Mol Biol **39**(2), 79–97 (2004)

[153] F. Hartung and H. Puchta, *The RecQ gene family in plants.*, J Plant Physiol **163**(3), 287–296 (2006)

[154] D. A. Bernstein, M. C. Zittel and J. L. Keck, *High-resolution structure of the E.coli RecQ helicase catalytic core.*, EMBO J **22**(19), 4910–4921 (2003)

[155] S. Korolev, J. Hsieh, G. H. Gauss, T. M. Lohman and G. Waksman, *Major domain swiveling revealed by the crystal structures of complexes of E. coli Rep helicase bound to single-stranded DNA and adp.*, Cell **90**(4), 635–647 (1997)

[156] A. Vindigni, F. Marino and O. Gileadi, *Probing the structural basis of RecQ helicase function.*, Biophys Chem **149**(3), 67–77 (2010)

[157] K. Kitano, S.-Y. Kim and T. Hakoshima, *Structural basis for DNA strand separation by the unconventional winged-helix domain of RecQ helicase WRN.*, Structure **18**(2), 177–187 (2010)

[158] M. P. Killoran and J. L. Keck, *Three HRDC domains differentially modulate Deinococcus radiodurans RecQ DNA helicase biochemical activity.*, J Biol Chem **281**(18), 12849–12857 (2006)

[159] D. A. Bernstein and J. L. Keck, *Conferring substrate specificity to DNA helicases: role of the RecQ HRDC domain.*, Structure **13**(8), 1173–1182 (2005)

[160] F. Hartung, H. Plchová and H. Puchta, *Molecular characterisation of RecQ homologues in arabidopsis thaliana.*, Nucleic Acids Res **28**(21), 4275–4282 (2000)

[161] D. Kobbe, S. Blanck, M. Focke and H. Puchta, *Biochemical characterization of AtRECQ3 reveals significant differences relative to other RecQ helicases.*, Plant Physiol **151**(3), 1658–1666 (2009)

[162] K. Kitano, N. Yoshihara and T. Hakoshima, *Crystal structure of the HRDC domain of human werner syndrome protein, WRN.*, J Biol Chem **282**(4), 2717–2728 (2007)

[163] M. D. Huber, M. L. Duquette, J. C. Shiels and N. Maizels, *A conserved G4 DNA binding domain in RecQ family helicases.*, J Mol Biol **358**(4), 1071–1080 (2006)

[164] M. Gyimesi, K. Sarlos and M. Kovacs, *Processive translocation mechanism of the human bloom's syndrome helicase along single-stranded DNA*, Nucleic Acids Research **38**(13), 4404–4414 (2010)

[165] I. Bonnet and P. Desbiolles, *The diffusion constant of a labeled protein sliding along DNA.*, Eur Phys J E Soft Matter **34**(3), 1–10 (2011)

[166] V. C. Barsky, Laurence T. A., *Biophysics of DNA-protein interactions: From single molecules to biological systems* (M.C. Williams and L.J. Maher, 2011)

[167] J. G. Yodh, B. C. Stevens, R. Kanagaraj, P. Janscak and T. Ha, *BLM helicase measures DNA unwound before switching strands and hRPA promotes unwinding reinitiation.*, EMBO J **28**(4), 405–416 (2009)

[168] Y. M. Kim and B.-S. Choi, *Structure and function of the regulatory HRDC domain from human bloom syndrome protein.*, Nucleic Acids Res **38**(21), 7764–7777 (2010)

[169] W. Kügel, A. Muschielok and J. Michaelis, *Bayesian-inference-based fluorescence correlation spectroscopy and single-molecule burst analysis reveal the influence of dye selection on DNA hairpin dynamics.*, Chemphyschem (2012)

List of Figures

Abbreviations and nomenclature

aa	Amino acid
AFM	Atomic force microscopy
APO	Nucleotide-free state
AT	Adenine-thymine base pair
ATP	Adenosin triphosphate
AtRecQ2	RecQ2 from Arabidopsis thaliana
AtRecQ3	RecQ3 from Arabidopsis thaliana
Beta-hairpin	Structural motif of two beta sheets of amino acids. Essential element for the DNA unwinding mechanism of helicases
bp	Base pair
Bulk	Ensemle average
DNA	Desoxyribonucleic acid
DNA junction	Forked DNA structure where dsDNA separates to ssDNA
dNTP	Desoxy nucleoside triphosphate
dsDNA	Double stranded DNA
DTT	Dithiothreitol
dUTP	Deoxyuridine Triphosphate
EDTA	Ethylenediaminetetraacetic acid
FJC	Freely jointed chain
Force-distance	Determined force versus the distance of the magnets to the flow cell
Force-extension curve	Determined force versus the DNA extension
FRET	Förster resonance energy transfer
GC	Guanine-cytosine base pair
HRDC	Helicase-and-RNase-D C-terminal domain
LED	Light emitting diode
LUT	Look-up-table. Set of reference images of the microsphere diffraction ring pattern at different focal distances
M280 microsphere	Microsphere with 2.8 μm diameter (see also table 2.1)
MagSense microsphere	Microsphere with $\approx$ 1.2 μm diameter (see also table 2.1)
MyOne microsphere	Microsphere with 1 μm diameter (see also table 2.1)
NDP	Nucleoside diphosphate
nt	Nucleotide
NTP	Nucleoside triphosphate
OBD	Origin binding domain
p	Persistence length
P_i	Inorganic phosphate
P2000	2000 bp DNA hairpin construct

P40, P40long	40 bp DNA hairpin construct with a 600 bp handle and a 3000 bp handle
P500	500 bp DNA hairpin construct
P90ATmGC/P90, P90long	90 bp DNA hairpin construct with three 30 bp segments of 100%, 50% and 0% of AT bases with a 600 bp handle and a 3000 bp handle
PA	Polyacrylamide
PB	Phosphate buffer
PCR	Polymerase chain reaction
PSD	Power spectral density
RBRecQ	Reaction buffer for AtRecQ2 and -3, see appendix 6.2.2
RBTAg	Reaction buffer for T-Antigen, see appendix 6.2.2
RecA-like fold/domain	Amino acid fold which forms a unit of the motor domain of many helicases
RecQ-Ct	RecQ C terminal domain
Rewind	DNA base pair closing by a helicase
Rezip	DNA base pair closing by decreasing forces
RMSz	Root-mean-squarded displacements in vertical direction
RNA	Ribonucleic acid
ROI	Region of interest. Confined area around the microsphere image which is used for the positional analysis
SF	Superfamily
ssDNA	Single stranded DNA
Strand-/unwinding polarity	Unidirectional translocation of the helicase with respect to the ssDNA backbone
SV40	Simian Virus 40
T-Antigen	Large Tumor-Antigen from Simian virus 40
TBE	Tris-acetate EDTA
TBE	Tris-borat EDTA
Translocation	Shifting of the position of the helicase along the DNA
Unwind	DNA base pair opening by a helicase
Unzip	DNA base pair opening by increasing forces
WLC	Worm-like-chain
ΔG_{bp}	Base pairing energy
ΔG_{el}	Free energy in the elastic stretching of the free ssDNA
ΔG_{heli}	Interaction potential (free energy) of the helicase which influences the base pairing energy
ΔG_{red}	Strength of the reduction of the base pairing energy (per base pair)
γ, γ_{trans}, γ_{rot}	Drag coefficient, Translational drag coefficient, Rotational drag coefficient
$\vec{B}$	Magnetic flux density, in this thesis always named magnetic field
$\vec{m}$	Magnetic dipole moment
d	Decay of the magnetic field in the microsphere

f_{cam}	Camera acquisition frequency
f_{c}	Cutoff frequency of the Lorenzian curve
f_{Ny}	Nyquist frequency. Half of the camera acquisition frequency
f_{signal}	Frequency of any periodic signal
F_0	Maximum force. Force for the shortest distance between magnets and microsphere, i.e. when the magnets almost touch the flow cell
F_{mag}	Magnetic force excerted on the microsphere
F_{unzip}	Mean force to mechanically unzip a DNA hairpin
F_{x}, F_{y}	Force determined from the x, y fluctuations respectively
$k_{\mathrm{B}}T$	Boltzmann constant times temperature yields the thermal energy for which 4.11 pNnm was used
k_{DNA}	Spring constant of the DNA for small displacements
k_{M}	Michaelis Menten constant
k_{rot}	Rotational spring constant of the microsphere
k_{rot}	Spring constant spring constant of the rotational movement (linear spring constant)
k_{tor}	Torsional spring constant (angular spring constant)
k_{x}, k_{y}	Spring constant in x, y
L_0	Contour length of the DNA
m	Width of the influenced area of an active helicase
S	DNA stretching modulus for which 530 pN was always used
s	Distance between helicase and DNA junction
v_{trans}	Translocation velocity
v_{unw}, v_{dsDNA}	Unwinding velocity

Danksagung/Acknowledgments

Ohne der Erklärung auf der nächsten Seite zu widersprechen, möchte ich an dieser Stelle deutlich klarmachen, dass diese Arbeit keinesfalls meine alleinige Leistung ist! Viele Menschen haben Ihren Teil dazu beigetragen, dass diese Arbeit zu dem geworden ist, was Sie gerade in der Hand halten. Einigen möchte ich nun besonders danken.

Ein besonders großer Dank gilt meinem Chef Dr. Ralf Seidel, ohne den dieses Projekt nicht zustande gekommen wäre. Ich bedanke mich für die Betreuung, die Hilfe, die Geduld und das unzählbare vermittelte Wissen während meiner gesamten Promotionsphase.

Ich danke ebenso meiner Doktormutter Prof. Dr. Petra Schwille: zum einen für die Begutachtung dieser Arbeit und die Abnahme meines Rigorosums, zum anderen, weil ich ohne sie nicht zur Biophysik gekommen wäre.

Ich danke Prof. Dr. Holger Puchta und Dr. Daniela Kobbe für die fruchtbare Kollaboration, die im Laufe meiner Promotion zustande kam und für die Begutachtung dieser Arbeit.

Des Weiteren danke ich Prof. Dr. Hans Stahl und seiner Gruppe für die Versorgung mit T-Antigen. I also thank Prof. Dr. Xiaojiang Chen and Dr. Dahai Gai for the collaboration on the T-Antigen project.

Außerdem danke ich Prof. Dr. Stefan Diez für die Abnahme meines Rigorosums.

Ein außerordentlicher Dank gilt meiner Sylvi für ihre Liebe, Unterstützung, Motivation und vor allem für ihre unglaubliche Geduld.

Ich danke der gesamten DNA-Motors Gruppe für Diskussionen, Unterstützung und Teamwork. Insbesondere danke ich Sylvia Clausing fürs Bauen von DNA Konstrukten, Hergen Brutzer, Nicholas Luzzietti und Jasmina Dikić fürs Korrekturlesen dieser Arbeit, Alexander Huhle für die großartige Programmierleistung und Dominik Kauert für die unzähligen Crashkurse im Programmieren. Ganz besonderer Dank geht an Friedrich Schwarz, nicht nur für herausfordernde Diskussionen und konstruktive Kritiken, sondern auch für die gute Zeit abseits der Forschung. Außerdem danke ich den Hilfswissenschaftlern Ignacio Gonzalez, Ran Rong und Felix Kemmerich, die an Teilen dieser Arbeit beteiligt waren.

Ich danke meinem ewig treuen Weggefährtenbegleiter Bob, meinem wichtigsten Studiumsbegleiter Rho ($\tilde{J}_{\mathrm{sni}}^{\mathrm{pfeff}}$), dem Oli-olsen und der gesamten Grillrunde (Claudi, Sven, Klaudi, Jörg, Christoph, Stephanie, Friedrich, Kristin, Robert, Jenny). Jeder, der nicht namentlich genannt wurde, möge mir verzeihen.

Ein besonderer Dank gilt auch meiner Familie.

Für die tägliche Unterhaltung während der schier unendlichen Schreibphase danke ich Mary, Manson und meiner Serienplatte.

Zuletzt möchte ich es mir nicht nehmen lassen meine Arbeit mit einem, wie ich finde, sehr passenden Zitat zu beenden:

„Es gibt eine Theorie, die besagt, wenn jemals irgendwer genau herausfindet, wozu das Universum da ist und warum es da ist, dann verschwindet es auf der Stelle und wird durch etwas noch Bizarreres und Unbegreiflicheres ersetzt.

Es gibt eine andere Theorie, nach der das schon passiert ist.“ **D**ouglas **N**oël **A**dams

Erklärung

Hiermit versichere ich, dass ich die vorliegende Arbeit ohne unzulässige Hilfe Dritter und ohne Benutzung anderer als der angegebenen Hilfsmittel angefertigt habe; die aus fremden Quellen direkt oder indirekt übernommenen Gedanken sind als solche kenntlich gemacht. Die Arbeit wurde bisher weder im Inland noch im Ausland in gleicher oder ähnlicher Form einer anderen Prüfungsbehörde vorgelegt.

Die Dissertation wurde im Zeitraum vom 01. Januar 2006 bis 30. März 2012 verfasst und von Prof. Dr. Petra Schwille, Biotechnologisches Institut der Technischen Universität Dresden betreut.

Weiterhin versichere ich hiermit, dass keine früheren erfolglosen Promotionsverfahren stattgefunden haben.

Ich erkenne die Promotionsordnung der Fakultät für Mathematik und Naturwissenschaften, Technische Universität Dresden an.

Daniel Klaue Dresden, 30. März 2012